# Local probe microscopies for the study of photovoltaic materials and structures

Mattia da Lisca

THESE DE DOCTORAT

NNT : 2023UPAST225

université PARIS-SACLAY

# Local probe microscopies for the study of photovoltaic materials and structures

*Microscopies à sonde locale pour l'étude de matériaux et structures pour le photovoltaïque*

**Thèse de doctorat de l'université Paris-Saclay**

École doctorale n° 575, Electrical, Optical,Bio-Physics and Engineering (EOBE)
Spécialité de doctorat : Electronique, Photonique, et Micro-Nanotechnologies
Graduate School : Sciences de l'Ingénierie et des Systèmes. Référent : ENS Paris-Saclay

Thèse préparée dans le **laboratoire de Génie électrique et électronique de Paris**, **(Université Paris-Saclay, CentraleSupélec, CNRS)**
sous la direction de **Jean-Paul KLEIDER**, Directeur de recherche CNRS,
la co-direction de **José ALVAREZ**, Chargé de recherche CNRS

**Thèse soutenue à Palaiseau, le 18/12/2023, par**

**Mattia DA LISCA**

## Composition du Jury

Membres du jury avec voix délibérative

| | |
|---|---|
| **Pere ROCA I CABARROCAS**<br>Directeur de recherche CNRS, LPICM | Président |
| **Benjamin GRÉVIN**<br>Directeur de recherche CNRS, SyMMES | Rapporteur |
| **Tobias CRAMER**<br>Associate Professor, Università di Bologna | Rapporteur |
| **Simona BINETTI**<br>Professor, Università di Milano-Bicocca | Examinatrice |
| **Frédérique DUCROQUET**<br>Chargée de recherche CNRS, IMEP-LaHC | Examinatrice |
| **Heinrich DIESINGER**<br>Chargé de recherche CNRS, IEMN | Examinateur |

université PARIS-SACLAY | ÉCOLE DOCTORALE Physique et ingénierie : Electrons, Photons, Sciences du vivant (EOBE)

**Titre : Microscopies à sonde locale pour l'étude de matériaux et structures pour le photovoltaïque**

**Mots clés :** Microscopie à sonde de Kelvin, Microscopie à force atomique à pointe conductrice, photovoltaïque, section transversale, KPFM, interfaces

**Résumé :** La microscopie à sonde de Kelvin (KPFM) et la technique AFM à pointe conductrice (c-AFM) ont été étudiées pour la caractérisation des matériaux et des dispositifs photovoltaïques, en accordant une attention particulière aux analyses en coupe transversale. Dans cette thèse, nous présentons les résultats obtenus sur diverses structures développées à l'IPVF et dans les laboratoires partenaires: des structures multicouches et cellules solaires à base de III-V, des cellules solaires en pérovskite à différents stades de traitement, des cellules solaires en CZTGS et en CIS, ainsi que des hétérojonctions au silicium. Parmi les technologies PV existantes, les dispositifs solaires à base de III-V font partie de la technologie photovoltaïque des films minces. En conséquence, la démonstration expérimentale de la sensibilité de la technique KPFM aux couches plus minces peut jouer un rôle crucial dans l'investigation et la compréhension des propriétés de surface locales. En particulier, nous avons examiné une structure multicouche InP:S/InP:Fe ainsi qu'une structure multicouche InP:Zn/GaInAs:Zn comportant des couches de largeurs et de concentrations de dopage différentes. Pour cette analyse, nous avons défini différents objectifs: le premier était l'évaluation de la résolution spatiale de notre configuration KPFM dans des conditions ambiantes. Le deuxième était une compréhension complète des résultats de VCPD combinée à une description des principaux facteurs qui affectent les mesures KPFM avec l'application de la modélisation numérique de la sonde Kelvin. Une évaluation quantitative de la distribution des concentrations de défauts de surface a été proposée pour expliquer les résultats expérimentaux de VCPD. L'analyse C-AFM et KPFM a ensuite été poursuivie sur une structure multicouche et cellule solaire hétérojonction AlGaAs:Be/GaInP:Si. L'analyse C-AFM s'est avérée être une méthode fiable pour mesurer la résistance locale le long d'une structure multicouche, permettant ainsi l'identification de différentes couches. Une analyse approfondie a été effectuée pour élucider la nature du contact électrique entre la pointe de l'AFM et la surface de l'échantillon, qui s'est révélé être un contact de Schottky. Par conséquent, une barrière de potentiel sera toujours présente à l'interface pointe/échantillon, ce qui peut entraver la collecte de charges et affecter la résistance locale mesurée.
KPFM a été utilisée pour fournir une preuve expérimentale de la performance PV insatisfaisante du dispositif CZTGS sous éclairage. En particulier, KPFM a révélé la présence d'une couche épaisse de MoS2 qui agissait comme une barrière à une collecte efficace des porteurs de charge positifs. La KPFM a également été réalisée pour évaluer la variation du potentiel de surface à travers une hétérojonction n-cSi/i-aSi:H/p-µcSiOx. Une attention particulière a été consacrée à élucider la méthodologie permettant d'identifier le véritable bord de l'échantillon tout en atténuant la présence d'un artefact distinct en forme de V, susceptible de gêner et de fausser une interprétation précise des données.
KPFM a été utilisée pour la caractérisation d'une cellule solaire CIS. L'analyse SPV a permis de déterminer la VOC de l'échantillon, ce qui aurait été difficile à estimer en utilisant des techniques conventionnelles en raison de la haute résistivité de la couche CIS due à l'oxydation.
La technique KPFM a été efficacement utilisée pour évaluer le changement potentiel de FTO résultant de l'incorporation de couches de SnO2 et de SnO2/NaF. Les résultats ont montré une augmentation du potentiel de surface, signifiant une diminution de la fonction de travail induite par ces couches supplémentaires. Dans une expérience similaire, il a également été démontré qu'une fine couche d'Al2O3 est également capable de réduire la fonction de travail de la couche de SnO2. Ces méthodes pourraient être utilisées pour améliorer la collecte d'électrons dans les dispositifs à base de pérovskite.

**Title : Local probe microscopies for the study of photovoltaic materials and structures**

**Keywords :** Kelvin probe force microscopy, conductive-AFM, photovoltaics, cross-section, KPFM, interfaces

**Abstract :** Kelvin probe force microscopy (KPFM) and conductive-AFM (c-AFM) techniques have been investigated for the characterization of PV materials and devices, with particular attention for cross-section analyses. In this thesis we present results on a variety of structures developed at IPVF and partner laboratories: III-V-based multilayer structures and finalized solar cells, half and fully processed perovskite solar cells, CZTGS and CIS solar cells and Silicon heterojunctions have been studied. Among the existing PV technologies, III-V-based solar devices belong to the PV technology of thin and ultra-thin films in which layers with widths of the order of a few nm are often integrated for an optimal surface passivation or for better carrier extraction, considerably enhancing device efficiency. Consequently, the experimental demonstration of the sensitivity of the KPFM technique to the narrower layers can play a crucial role in the investigation and comprehension of the local surface properties and charge transport mechanisms at the interfaces. In particular, we have investigated an InP:S/InP:Fe and an InP:Zn/GaInAs(P):Zn multilayer structure with layers of different widths and doping concentrations. For this analysis we have set different objectives: the first objective was the evaluation of the spatial resolution of our KPFM setup in ambient conditions. The second objective was a full understanding of the VCPD results combined with a description of the principal factors that affect KPFM measurements with the application of Kelvin Probe (KP) numerical modelling. A quantitative evaluation of the distribution of surface defects concentrations was proposed to explain the experimental VCPD results. C-AFM and KPFM analysis was then continued on a p-AlGaAs:Be/n-GaInP:Si heterojunction multilayer structure and finalized solar cell. C-AFM analysis proved to be a reliable method for measuring the local resistance along a III-V based multilayer structure, enabling the identification of various layers and regions with different doping type. Nonetheless, a thorough analysis was performed to elucidate the true nature of the electrical contact between the AFM tip and the surface of the sample which resulted to be a Schottky contact. Therefore, a potential barrier will be always present at the tip/sample interface which can hinder (or facilitates) the collection of charges and in turn affect the local measured Resistance. .Furthermore, cross-sectional KPFM was used to offer experimental evidence of the unsatisfactory PV performance of the CZTGS device under illumination. In particular, KPFM revealed the presence of a bulky $MoS_2$ layer which acted as a barrier for an efficient collections of positive charge carriers.

Cross-sectional KPFM was also performed to evaluate the surface potential variation across a n-cSi/i-aSi:H/p-µcSiOx heterojunction. Special attention was dedicated to elucidating the methodology for identifying the real physical edge of the specimen while mitigating the presence of a distinctive V-shaped artifact, which has the potential to impede and mislead accurate data interpretation.

In addition, KPFM was used an effective tool for the characterization of an unfinalized Mo-detached CIS solar cell. Specifically, SPV analysis allowed to determine the VOC of the sample, which would have been challenging to estimate using conventional techniques due to the high resistivity of the CIS layer due to oxidation. KPFM technique was effectively employed to assess the potential change of FTO resulting from the incorporation of $SnO_2$ and $SnO_2$/NaF layers. The findings unambiguously demonstrated an increase in surface potential, signifying a decrease in work function induced by these additional layers. In a similar experiment, it was also demonstrated that a thin layer of $Al_2O_3$ is also capable of reducing the WF of the $SnO_2$ layer. These methods could be used for improving electrons collection in perovskite-based devices.

# Synthèse en français

La microscopie à sonde de Kelvin (KPFM) et la microscopie à force atomique (AFM) à pointe conductrice (c-AFM) ont été étudiées pour la caractérisation des matériaux et des dispositifs photovoltaïques, en accordant une attention particulière aux analyses en coupe transversale. Nous présentons les résultats obtenus sur diverses structures développées à l'IPVF et dans des laboratoires partenaires : des structures multicouches et cellules solaires à base de semi-conducteurs III-V, des cellules solaires à base de pérovskites à différents stades de traitement, des cellules solaires en CZTGS et en CIS, ainsi que des hétérojonctions de silicium. Ces structures mettent en jeu des couches minces d'épaisseur de l'ordre du micron et parfois nettement moins, pour lesquelles nous avons montré la sensibilité de la technique KPFM et c-AFM.

En plus, une modélisation 2D par éléments finis de la mesure du potentiel de surface et de la différence de potentiel de contact ($V_{CPD}$) telle qu'obtenue par la méthode de sonde de Kelvin (KP) a été utilisée pour appuyer l'interprétation des résultats expérimentaux. En particulier, une évaluation quantitative de la distribution des concentrations de défauts de surface a été proposée pour expliquer les résultats expérimentaux de $V_{CPD}$.

Après un premier chapitre introductif, le chapitre 2 décrit les méthodes expérimentales et numériques utilisées au cours de cette thèse. Il décrit en particulier la technique KPFM, dont le schéma de principe est représenté à la figure 1.

Le chapitre 3 est consacré à l'analyse d'une structure InP:S/InP:Fe et d'une structure InP:Zn/GaInAs:Zn comportant des couches d'épaisseurs et de concentrations de dopants différentes. Pour cette analyse, nous avons défini différents objectifs. Le premier était l'évaluation de la résolution spatiale de notre configuration KPFM dans des conditions de fonctionnement à l'air ambiant. Le deuxième était la compréhension des résultats de $V_{CPD}$ combinée à une description des principaux facteurs qui affectent les mesures KPFM grâce au déploiement d'une modélisation numérique de la technique KP.

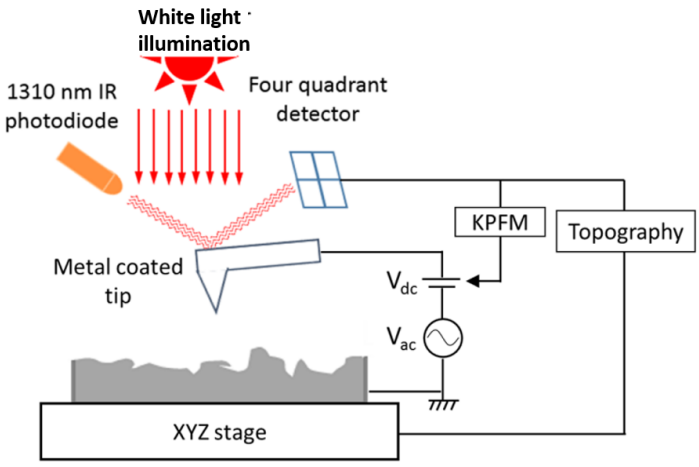


**Figure 1 :** Schéma de principe du système KPFM. Alors qu'une tension $V_{AC}$ + $V_{DC}$ est appliquée, la pointe KPFM balaye une surface. Le signal $V_{AC}$ est sinusoïdal avec une fréquence égale à la résonance mécanique du levier. Le détecteur à quatre quadrants fournit une rétroaction afin de minimiser l'oscillation du levier en modifiant le signal $V_{DC}$ pour fournir le potentiel de la surface de l'échantillon par rapport à celui de la pointe

Plus précisément, à partir de l'analyse de la structure multicouche InP:S/InP:Fe, nous avons réussi à démontrer la grande sensibilité de la technique KPFM à la concentration locale de dopants, puisque nous arrivons à détecter l'existence de couches d'épaisseur inférieure à quelques dizaines de nanomètres. De

plus, dans le cas de notre échantillon, en raison d'une concentration de dopants bien plus faible dans les couches d'InP:Fe par rapport à celle dans les couches contiguës d'InP :S et de leurs faibles épaisseurs (<100nm), la charge d'espace se développant autour des interfaces occupe toute l'épaisseur des couches d'InP:Fe. Un contraste de $V_{CPD}$ à travers les couches de différentes épaisseurs reste cependant possible. En outre, nous avons montré que l'application d'un éclairement par une lumière blanche d'intensité modeste sur la section transversale (obtenue par clivage) permettait une amélioration significative de ce contraste le long de toute la structure, ce qui s'explique par l'effet de l'éclairement sur la courbure des bandes en surface liée à la présence de défauts de surface. En raison de leur rôle central sur la détermination du profil de $V_{CPD}$, les aspects principaux de la théorie concernant les défauts de surface de semi-conducteurs est succinctement présentée.

Enfin, grâce à l'expertise acquise par l'étude de l'échantillon de multicouche d'InP:S/InP:Fe, une analyse KPFM en coupe transversale similaire a été réalisée sur une structure multicouche d'InP:Zn/GaInAs:Zn. Cette fois-ci, des distributions quantitatives de densités de défauts de surface sont proposées afin d'expliquer les profils expérimentaux de $V_{CPD}$. En particulier, la modélisation numérique et l'analyse ont indiqué que les défauts de surface sont responsables d'un écart significatif du profil de potentiel de surface par rapport à celui attendu en tenant compte des propriétés de volume (e.g. concentrations de dopants) des matériaux. De plus, nous avons montré que le profil de potentiel observé le long de la surface clivée de l'empilement n-InP/InP:nid/p-InP:Zn peut s'expliquer par de fortes densités de défauts de surface dans les couches fortement dopées n-InP et p-InP:Zn, avec une densité de défauts beaucoup plus faible dans la couche tampon non intentionnellement dopée d'InP :nid.

Le Chapitre 4 explore le cœur de notre recherche, présentant et analysant les résultats des mesures KPFM et c-AFM effectuées sur la section transversale de cellules de diverses technologies photovoltaïques, ainsi que les défis associés à ces caractérisations.

Après les résultats présentés dans le chapitre 3, l'analyse par c-AFM et KPFM a ensuite été poursuivie sur une structure multicouche et sur une cellule solaire à hétérojonction AlGaAs:Be/GaInP:Si. L'analyse c-AFM de la section transversale, telle que représentée à la figure 2, s'est avérée être une méthode fiable pour l'identification des différentes couches grâce la mesure de la résistance locale. Cependant, des différences substantielles dans les profils de résistance expérimentaux ont été observées en fonction de la polarité appliquée entre l'échantillon et la pointe AFM. Plus précisément, les polarités +1 V et -1 V ont été examinées en détail. Une analyse approfondie a été effectuée pour élucider la nature du contact électrique entre la pointe de l'AFM et la surface de l'échantillon, qui s'est révélé être un contact de type Schottky. Une barrière de potentiel sera ainsi toujours présente à l'interface pointe/échantillon, ce qui peut entraver la collecte de charges et affecter la résistance locale mesurée.

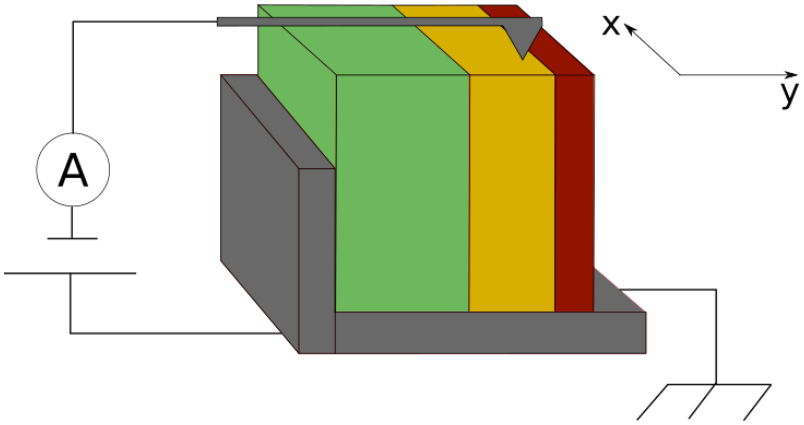


**Figure 2 :** Représentation schématique d'une mesure de Resiscope en coupe transversale. Le lac d'argent est généralement utilisé pour assurer un contact électrique raisonnable entre le porte-échantillon et l'échantillon.

L'analyse c-AFM de la cellule solaire AlGaAs:Be/GaInP:Si finalisée pour une polarité de -1 V appliquée entre l'échantillon (du côté du substrat fortement dopé p) et la pointe a révélé que l'application d'une illumination par laser (λ=488 nm) induit une diminution de la résistance apparente lorsque la pointe balaye la couche d'absorbeur la couche frontale de type n (émetteur) de la cellule . Ceci est interprété par un effet de photocourant généré par la cellule.
La cellule solaire finalisée AlGaAs:Be/GaInP:Si a également été caractérisée par KPFM en coupe transversale. L'analyse a été réalisée en utilisant également une sourcemètre, ce qui a permis de réaliser l'analyse dans différentes conditions expérimentales : court-circuit, circuit ouvert et sous une tension externe appliquée, à la fois dans l'obscurité et sous éclairement. Les résultats expérimentaux ont une fois de plus révélé l'impact des défauts de surface qui sont responsables d'une atténuation de la variation de potentiel par rapport à ce qui est attendu en se basant uniquement sur les concentrations de dopants en volume dans les couches.
Les caractéristiques typiques d'une jonction pn ont été observés dans nos résultats expérimentaux, où l'application d'une polarisation directe entraîne une réduction de la charge d'espace par rapport au cas sans polarisation. Cependant, selon la théorie, la barrière de potentiel interne devrait diminuer de la même quantité que la polarisation directe appliquée (si tant est que les chutes de potentiel en dehors de la zone de charge d'espace de la jonction restent négligeables). Les observations expérimentales ont révélé que l'application d'une polarisation de +1 V entraîne bien une différence notable, mais la valeur exacte de la tension n'est pas discernable à partir du profil $V_{CPD}$. De même, sous des polarisations inverses appliquées, on observe une augmentation de la charge d'espace et de la barrière de potentiel, mais une fois de plus, pas de la même quantité que la polarisation inverse appliquée. Enfin, nous avons mis en évidence que le profil $V_{CPD}$ obtenu sous une polarisation similaire à la tension en circuit ouvert ($V_{OC}$), permet d'obtenir un profil $V_{CPD}$ similaire à celui obtenu sous illumination avec l'échantillon en conditions de circuit ouvert. Cela est dû au fait que l'application d'une polarisation externe similaire à la tension en circuit ouvert est capable d'induire une séparation quasi-niveau de Fermi similaire à celle obtenue sous illumination.
Après l'analyse approfondie en KPFM et c-AFM en coupe transversale effectuée sur la cellule solaire AlGaAs:Be/GaInP:Si, afin de souligner l'intérêt et les potentialités de la technique KPFM pour le domaine du photovoltaïque, nous l'avons utilisée pour l'analyse d'autres PV structures.
En particulier, dans le cadre d'une collaboration avec l'université di Milano-Bicocca, nous avons pu fournir une explication expérimentale de la performance PV insatisfaisante de dispositifs CZTGS sous éclairement. En effet, nous avons révélé la présence d'une couche épaisse de $MoS_2$ qui agit comme une barrière à la collecte efficace des porteurs de charge positifs (trous). En fait, les trous se déplacent vers une énergie plus élevée, c'est-à-dire un potentiel plus bas. L'augmentation du potentiel enregistrée depuis le $MoS_2$ vers le Mo agit comme une barrière pour la collecte des trous et peut également induire l'accumulation d'électrons à l'interface Mo/$MoS_2$, favorisant ainsi les phénomènes de recombinaison. Une des problématiques des mesures en section transversale est l'identification précise du bord de l'échantillon (donc de la surface du dispositif qui va recevoir la lumière en utilisation photovoltaïque normale. Plus précisément, il existe bien souvent un artefact en forme de V dans le profil de $V_{CPD}$, susceptible de gêner et de fausser une interprétation précise des données. Dans le dernier paragraphe du chapitre 4, nous nous sommes servis de mesures du potentiel de surface en section transversale des couches utilisées dans la technologie des cellules PV à hétérojonctions de silicium, n-cSi/i-aSi:H/p-µcSiOx. Nous avons proposé une méthodologie permettant d'identifier le véritable bord de l'échantillon tout en atténuant la présence de cet artefact. En outre, l'acquisition de signaux supplémentaires à $V_{CPD}$ lors de l'analyse KPFM peut faciliter l'interprétation des données. En particulier, les signaux Mag, Phase et Dmag sont des mesures fondamentales qui fournissent collectivement des informations détaillées sur le

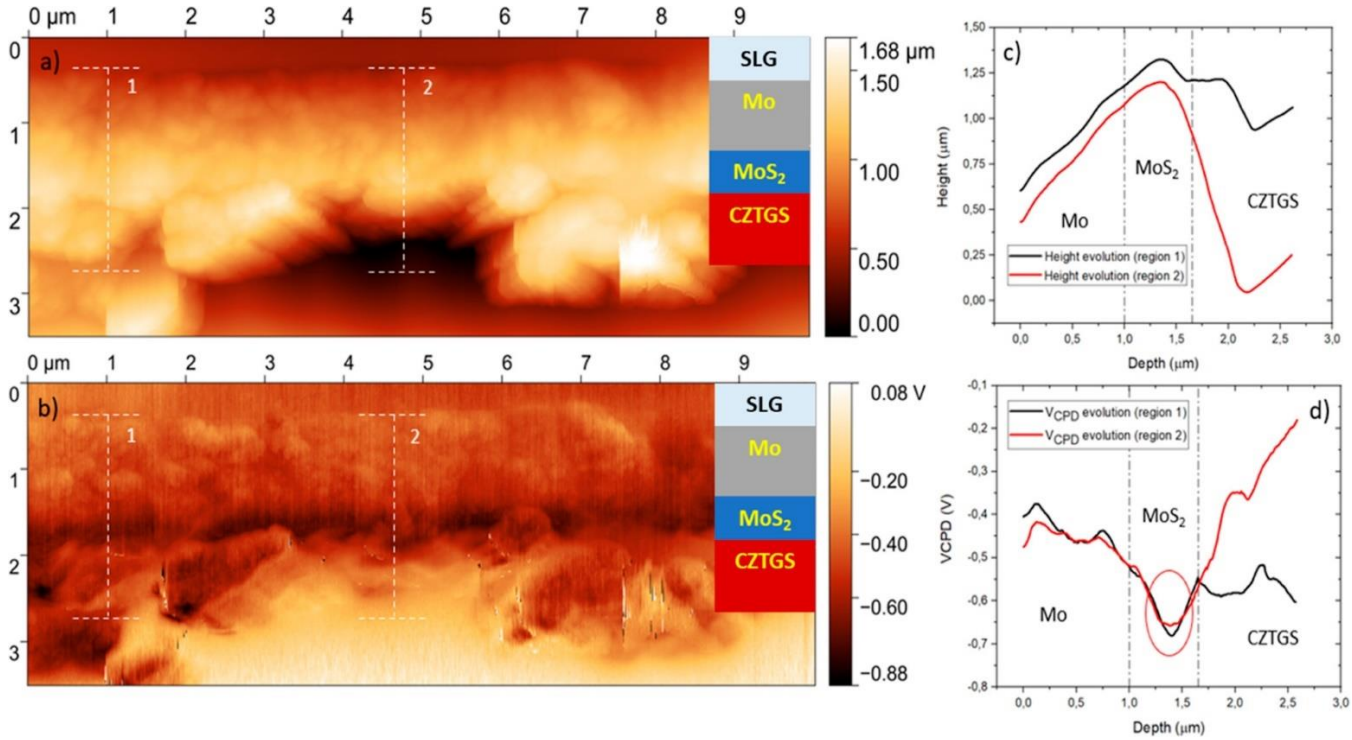


**Figure 3 :** Mesure FM-KPFM de la coupe transversale de la surface du dispositif CZTGS. La topographie (a) et l'image $V_{CPD}$ (b). Les profils en (c, d) montrent une valeur moyenne des données le long de la topographie et de l'image $V_{CPD}$, respectivement. Les profils correspondent aux deux régions identifiées par le segment blanc en pointillés.

potentiel de surface, les forces électrostatiques et les propriétés électroniques des matériaux à l'échelle nanométrique. Acquérir de la compétence dans l'acquisition et la compréhension de ces signaux peut améliorer l'interprétation des données expérimentales, ajoutant ainsi une valeur supplémentaire au seul profil de $V_{CPD}$ et aidant à l'identification précise du véritable bord de l'échantillon.

Afin de souligner l'intérêt et les potentialités de la technique KPFM pour le domaine du photovoltaïque, nous donnons dans le chapitre 5 deux exemples d'utilisation dans le cadre de projets supplémentaires entrepris au cours de la thèse de doctorat. Tout d'abord, la technique KPFM a récemment été reconnue comme une nouvelle méthode pour cartographier la tension de circuit ouvert locale avec une résolution spatiale nanométrique dans des dispositifs photovoltaïques. Lorsque le dispositif est éclairé, la tension de circuit ouvert peut être directement estimée à partir de la mesure de la photo tension de surface, SPV, i.e. en soustrayant la valeur de différence de potentiel de contact à l'obscurité, $V_{CPD/dark}$, de celle sous lumière, $V_{CPD/light}$,. Nous avons montré sur un exemple de cellule finalisée permettant une mesure simultanée de la tension de circuit ouvert macroscopique, que les valeurs de SPV correspondent de manière remarquable aux valeurs macroscopiques de $V_{OC}$. L'intérêt de la mesure SPV par KPFM se manifeste surtout pour l'étude de structures dont la fabrication n'est pas forcément entièrement finalisée (par exemple en l'absence de couche d'électrode supérieure), rendant impossible une mesure macroscopique fiable de $V_{oc}$.

Nous l'avons ainsi utilisée pour la caractérisation d'une cellule solaire CIS non pourvue d'électrode (terminée par une couche de CdS) détachée de son substrat de Mo, que nous sommes retournées afin d'analyser la surface de CIS ainsi mise à l'air. L'analyse de SPV a permis de déterminer la tension de circuit ouvert de l'échantillon, ce qui aurait été difficile à estimer en utilisant des techniques conventionnelles en raison de la haute résistivité de la couche CIS due qui peut être liée à un phénomène de création de défauts superficiels ou d'oxydation. L'échantillon, contacté par une laque à l'argent sur sa face CdS et

par une pointe macroscopique sur la surface du CIS présentait certes un effet redresseur dans sa caractéristique I-V ; cependant, ses performances photovoltaïques étaient très médiocres, avec un courant de court-circuit très faible et une tension de circuit ouvert mesurée à 0,20 V, également très faible. La valeur de courant extrêmement faible nous a par ailleurs empêchés de réaliser une analyse spectrale de rendement quantique externe (EQE), car le signal de l'échantillon était noyé dans le bruit.
Cependant, l'analyse du signal SPV effectuée avec trois lasers différents à 488 nm, 785 nm et 980 nm a révélé des valeurs de l'ordre de 0.6 V, ce qui correspond bien à la plage typique de $V_{OC}$ de 0.6 à 0.7 V rapportée pour les cellules solaires à base de CIS. Elle a aussi mis en évidence des dépendances avec la puissance lumineuse d'éclairement différentes selon la longueur d'onde, qui ont pu être interprétées en termes de défauts de surface, de non-homogénéité de la couche, et de longueur de diffusion des porteurs insuffisante au regard de l'épaisseur de la couche.
Enfin, la dernière partie du chapitre 5 présente deux méthodes différentes qui permettent de modifier le travail de sortie de la couche de transport des électrons utilisée dans les cellules solaires à base de pérovskite (PVK). En particulier, L'utilisation de FTO en tant qu'électrode conductrice transparente dans les cellules solaires en pérovskite pose un défi en raison de sa valeur élevée de travail de sortie. Cela conduit à un alignement des niveaux d'énergie défavorable avec la couche PVK, entravant l'extraction efficace des électrons et leur collecte. Pour remédier à cela, une couche d'extraction et de transport d'électrons (ETL) est utilisée. Les matériaux couramment utilisés pour l'ETL comprennent le dioxyde de titane ($TiO_2$), l'oxyde de zinc (ZnO) et l'oxyde d'étain ($SnO_2$).
Par l'analyse KPFM, nous avons pu évaluer des changements de travail de sortie résultant de l'incorporation de couches de $SnO_2$ et de $SnO_2$/NaF sur le FTO. Les résultats ont montré une augmentation du potentiel de surface, signifiant une diminution du travail de sortie induite par ces couches supplémentaires. Pour finir, dans une expérience similaire, il a été démontré qu'une fine couche d'$Al_2O_3$ est également capable de réduire le travail de sortie de la couche de $SnO_2$. Dans le futur, ces méthodes devraient être testées sur des cellules compètes et être utilisées pour améliorer la collecte d'électrons dans les dispositifs à base de pérovskites.

# Table of contents

## Chapter 1



## Chapter 2

## Chapter 3



## Chapter 4



## Chapter 5

# Chapter 1

# Context

Photovoltaic (PV) energy is a form of renewable energy that converts sunlight into electricity in a clean, quiet, and reliable way through PV systems (or modules) which consist of several PV devices (or solar cells) connected in series [1].
It is a relative newcomer technology, with the first functional PV devices demonstrated in the 50s. In particular, the merit of the development of PV technology must be attributed to the space industry in the 60s where cost was not a barrier since no other sources of electrical power are available [2]. These early devices were extremely more expensive than today and for this reason they did not find application on earth. Nonetheless, the interest in solar energy was renewed in the 1970s motivated by the first oil crisis [3]. At that time, the scientific community efforts were devoted to decreasing the fabrication costs and enhancing solar panels efficiency. In 1985 it was realized for the first time a silicon-based device with an efficiency of 20% which represented an initial substantial milestone in the PV community [4]. Nowadays, the research is still dedicated to the same principles of reducing costs and enhancing efficiency. In this regard, different materials have been explored and developed besides silicon, such as III-V (GaAs, InP, InGaAs), chalcogenide (CIGS, CdTe), perovskites, polymers etc. with the accomplishment of remarkable devices performances [5].

## 1.1 Illuminating the Future: an overview of photovoltaic energy and its potential

### 1.1.1 Global warming and renewable energies

The expression greenhouse (GH) effect has commonly been used for the role of the atmosphere in maintaining the surface of the earth warm. Recently, it has been progressively correlated to an increase of $CO_2$ in the atmosphere which is calculated to contribute about 50% to the anthropogenic GH effect. Furthermore, several other gases generated by the industrial and domestic activities such as $CH_4$, CFCs, halogens, $NO_x$, and ozone are also classified as greenhouse gasses (GHGs) and have an impact to the GH effect. The GH effect primarily contributes to the increase of the temperature of the Earth, as it is responsible for elevating the levels of trapped heat in the atmosphere [6]. This phenomenon gives rise to several secondary issues, including alterations in ecological systems and the accelerated erosion of coastlines due to rising sea levels.
According to the European Union (EU), climate change is taking place. Predictions indicate that if atmospheric concentrations of GHGs, mainly due to fossil fuel combustion, persist at the current rates, the temperature may rise by additional 2-4 °C in the next century [7]. If this prediction is actualized, the sea level could rise by 30–60 cm before the end of this century causing dramatic consequences for the environment.

Through the past two decades, the threat and consistency of environmental degradation have become more evident since the environmental impact of human activities has expanded drastically. This is due to the growth of the world population, energy consumption, and industrial activity. Therefore, a global and cohesive action is essential to regulate and limit the effect of human activities on earth. In this sense, many policies related to environment safeguard were supported and signed by nations from all over the world. The Kyoto Protocol signed in 1997 [8] is an international agreement with the aim of reducing GHGs emissions and slowing the pace of global warming. It is a legally binding agreement under the United Nations Framework Convention on Climate Change (UNFCCC) to which nearly all countries in the world are party. The essential principle of the Kyoto Protocol was that industrialized nations needed to diminish the amount of their $CO_2$ emissions.

Additionally, the European Climate Change Program (ECCP) was launched in 2000 by the European Union's European Commission, with the purpose of avoiding dangerous climate changes. The goal of the ECCP is to identify and develop all the necessary elements of an EU strategy to implement the Kyoto Protocol. Furthermore, the Paris Agreement is a legally binding international treaty adopted in 2015 by 196 Parties at COP21 with the goal of limiting global warming to below 2°C, preferably 1.5°C, compared to pre-industrial levels.

Accomplishing solutions to the environmental crises that humanity meets today necessitates protracted potential actions for sustainable development. Renewable energy resources seem to be one of the most efficient and effective solutions. Renewable energy resources are defined as sources of energy that are naturally replenished or regenerated over a relatively short period of time unlike non-renewable energy resources such as fossil fuels, which are depleted when extracted and consumed. Examples of renewable energy resources include solar energy, wind energy, hydroelectric energy, geothermal energy, and biomass [10].

Renewable energy resources are considered to be an important part of the solution to the problem of climate change, as they produce little or no GHGs when used. They also offer a more sustainable and secure source of energy, as they are not subject to the same price fluctuations or depletion risks as non-renewable energy resources.

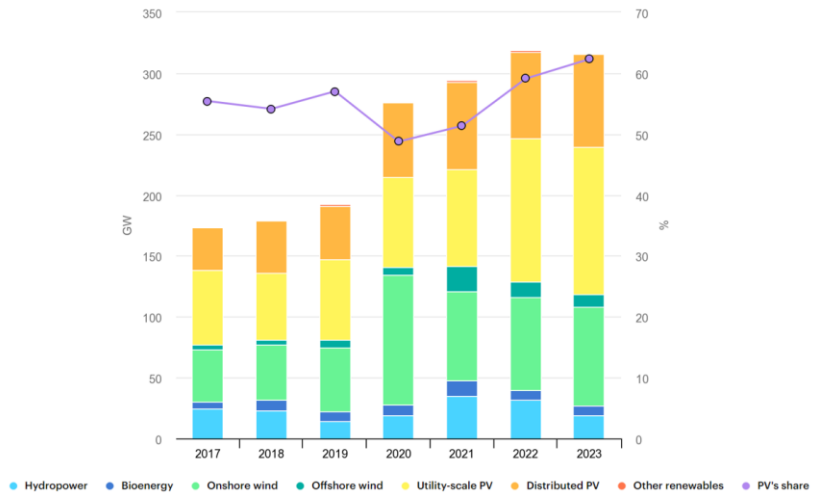


**Figure 1**: Net renewable capacity (GW) additions by the different renewable energy resources from 2017 to 2023 [11].

Although these resources have vast energy potential, they are poorly diffused and not fully available, and most of them are irregular and have definite regional variabilities. Lately, considerable progresses were achieved by improving collection and conversion efficiencies, reducing the initial and maintenance expenses, and increasing the reliability and applicability of renewable energy systems. The new renewable capacity provided by renewable energy resources is shown in Figure 1.

### 1.1.2 Solar energy

The quantity of sunlight continuously reaching the atmosphere of the earth is around $1.05 \times 10^5$ TW, considering a 60% transmittance through the atmospheric cloud cover. Hypothetically, if only 1% of the irradiance reaching the surface of the earth could be converted into electric energy with a 10% efficiency, it would furnish a resource base of $10^5$ TW, while the total global energy needs for 2050 are projected to be about 25–30 TW [12].

The current state of solar energy technologies is such that commercially available silicon solar cell efficiencies have achieved more than 20%, with concentrating PVs at about 20%-40%, and solar thermal systems provide efficiencies of 60–80%.

The countries with the most installed capacity of solar PV are China, the United States, Japan, Germany, and India. If the climate goal of 2 °C is to be achieved, solar PV should evolve from around 1% of total electricity generation in 2015 to 22% in 2050. That would mean an investment of roughly 5 trillion USD until 2050 in solar PV generation [13].

Although high initial investment costs constitute an important barrier for the upscaling of solar generation technologies, PV panels allow smaller installations with lower capital costs with respect to hydro or wind. The biggest advantage of solar energy compared with other forms of energy is that it is clean, and it can be provided without environmental pollution. Additionally, solar energy provides environmental benefits in comparison to electricity generation using conventional energy sources. The benefits arising from the installation and operation of solar energy systems fall into two main categories: *environmental* and *socioeconomical* issues [14].

From an environmental perspective, the use of solar energy technologies has several positive effects that comprise the reduction of the emission of the GHGs and of toxic gas emissions, renovation of degraded land, reduced necessity for transmission lines within the electricity grid, and improvement in the quality of water resources. The socioeconomic benefits of solar technologies involve the enhanced regional and national energy independence, creation of employment prospects, and diversification and security of energy supply [15].

On the other hand, no artificial project can entirely prevent some impact to the environment. The negative environmental aspects of solar energy systems include pollution as consequences of production, installation, maintenance, and demolition of the systems, and land displacement. Besides, the energy produced by solar systems should be used as soon as it is produced and, when this is not possible, solar energy must be stored. However, storage systems, such as batteries, can have negative environmental impacts due to the materials used in their manufacture and disposal. Additionally, storage systems for solar energy are quite expensive and the cost of storing energy is often higher than the cost of energy production [16].

### 1.1.3 Semiconductors

Semiconductor materials possess the capacity to conduct or impede electricity based on specific conditions, differentiating them from conductors and insulators. Through controlled manipulation of factors such as temperature and impurities, semiconductors enable the precise regulation of electrical conductivity, forming the foundational elements of modern electronic systems. Semiconductor materials have a number of unique properties that make them useful in electronic devices such as a tunable electrical resistance, a high melting point, and a high thermal conductivity. Semiconductor materials are used in a wide range of electronic devices, including transistors, solar cells, and diodes. PV devices are based on semiconductors materials due to the *light absorption* phenomenon which characterizes this class of materials. Specifically, absorption leads to generation of free charge carriers which can be collected through solar cells [17].

### 1.1.4 Photovoltaic effect

When a semiconductor material is exposed to light, the photons can be reflected, absorbed, or transmitted. When a photon is absorbed by a valence electron of an atom, the energy of the electron is increased by the amount of energy of the photon. If the energy of the photon is greater than the band gap of the semiconductor, the electron will jump into the conduction band, where it can move freely leaving in the valence band a positively charged carrier (hole). In order to efficiently collect the photogenerated carriers additional layers must be added to the semiconductor absorber. Specifically, a selective charge transport layer is defined as a component that is able to efficiently extract and transport photogenerated charge carriers, improving the efficiency of a solar cell energy by minimizing recombination losses. A charge transport layer is defined as Electron Transporting Layer (ETL) when it primarily facilitates the flow of electrons while impeding the transport of holes. Conversely, it is designated as a Hole-Transporting Layer (HTL) when its main function is to support the transport of holes while inhibiting the flow of electrons. Additionally, within a solar cell, the absorber material typically features a pn junction. The electric field generated by a pn junction [17] separates charge carriers by driving free electrons towards the n-side and holes towards the p-side.

If the two sides of the solar cell are connected through a load, an electric current will flow from the n-side to the p-side under sunlight irradiation. A basic schematic of the operation of a photovoltaic cell is shown in Figure 2. For instance, in the case of Si solar cells, when the absorber is p-type, a n-type Si layer is added in order to form a pn junction and a $p^+$ Si layer is added as an HTL. Note that the situation is reversed in case of a n-type absorber.

Generally, a PV cell consists of the active photovoltaic material, metal grids, antireflection coatings, and supporting material [18]. The complete cell is optimized to maximize both the amount of sunlight entering the cell and the power out of the cell. The PV material can be one of several compounds. The metal grids enhance the current collection from the front and back of the solar cell. The antireflection coating is generally deposited on to the top of the cell to reduce or minimize the amount of reflection of the incident light. As a result, PV cells range in color from black to blue. In some types of photovoltaic cells, the top of the cell is covered by a semi-transparent conductor that functions as both current collector and antireflection coating.

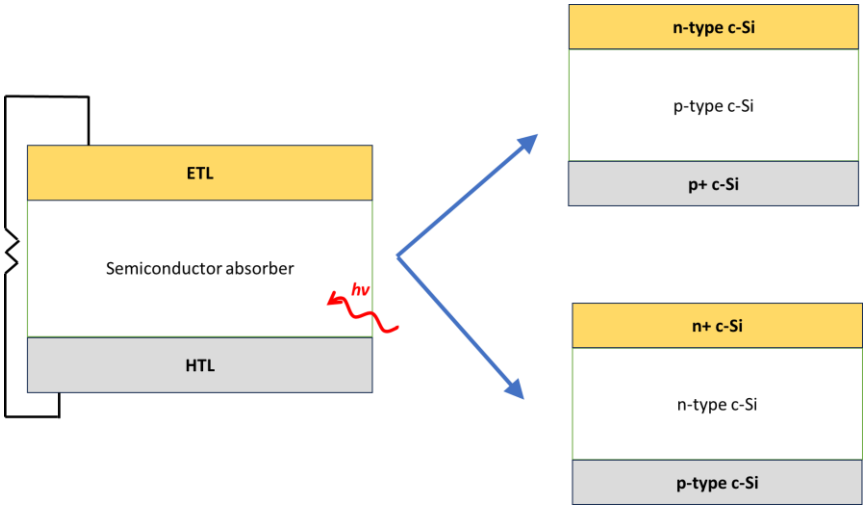


**Figure 2**: Schematic representation of a solar cell. The incident light is absorbed in the semiconductor and photo-generated charge carriers are collected thanks to selective charge transport layers (ETL and HTL). In order to improve PV performance, a pn junction is generally formed to facilitate charge carriers collections.

### 1.1.5 Recombination phenomena

Recombination is a mechanism that takes place in semiconductors to equilibrate excess charge carriers through the annihilation of oppositely charged carriers e.g., positively charged holes ($h^+$) and negatively charged electrons ($e^-$).

If the energy released through recombination is in the form of a photon, the process is known as radiative-recombination. Non-radiative recombination is often the result of material defects and intermediate energy levels in the band gap. Non-radiative recombination can be categorized as either Auger or defect level driven recombination [19]. A schematic of these principal recombination phenomena are shown in Figure 3 [20-23].

Non-radiative recombination: is a process in which an electron-hole pair recombines without emitting a photon. In a semiconductor, non-radiative recombination can occur through a variety of mechanisms, including trapping of charge carriers by impurities or defects in the crystal structure, recombination at grain boundaries, or recombination at the interface between the semiconductor and a metal contact.

Energy levels present within the band gap of a semiconductor material are known as recombination centers. After a carrier is captured by a recombination center there is a finite probability that a carrier of opposite charge will also be capable of occupying the same energy state, therefore resulting an electron-hole pair annihilation. This form of recombination is known as Shockley-Read-Hall (SRH) or defect level recombination. The energy released during non-radiative recombination phenomena is often in the form of thermal vibrations known as phonons, which are then absorbed into the material which results in heating. This heating occurs at the defect sites within the material and can be extremely detrimental to device efficiency.

Radiative recombination: is the mechanism responsible for photoemission in semiconductor light emitting diodes and is mainly associated with band-to-band recombination as a result of the high energy differences associated with a complete band gap transition. Direct band-to-band recombination is only possible in materials with extremely low defect concentrations.

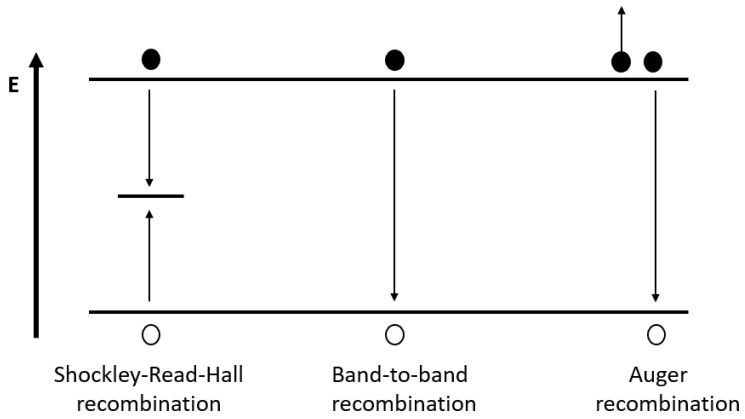


**Figure 3**: Schematic representation of the principal recombination phenomena that may occur in semiconductors material after light absorption.

Auger recombination: requires the interaction of three carriers. It happens when an electron and a hole recombine and the photoemitted energy is not transferred into heat energy or thermal vibrations, but it is transferred to an electron within the conduction band, which is then promoted to an energy higher in the conduction band. This electron then releases energy in the form of thermal vibrations as it returns to the lowest possible state within the conduction band. For this reason, Auger recombination is highly detrimental to the efficiency of extrinsic semiconductors with high concentrations of electron donor atoms. Additionally, the probability of Auger recombination increases with intensity of the input source (e.g., irradiation power) since an increased electron concentration will be present in the conduction band.

Understanding the distinction and controlling the dominating recombination mechanisms for materials is highly important for the optimization of semiconductor devices such as solar cells and light emitting diodes.

### 1.1.6 Solar cells

Photovoltaic energy conversion in solar devices involves two fundamental steps. The absorption of light which generates an $e^-/h^+$ pair and its collection to the respective metal contacts [24]. The electron and hole are separated by the structure of the device: electrons are drifted to the positive terminal and holes to the negative terminal generating electrical power. The equivalent circuit of an ideal solar cell can be exemplified by a current source connected in parallel, as shown in the equivalent circuit of Figure 4.

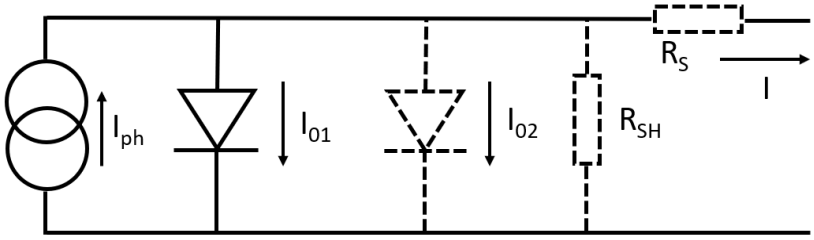


**Figure 4**: The equivalent circuit of an ideal solar cell (full lines). Non-ideal components are shown by the dotted lines.

The corresponding I–V characteristic is expressed by the Shockley solar cell equation [25]:

$$I = I_{ph} - I_0\left(e^{\frac{qV}{nk_BT}} - 1\right), (1)$$

where $k_B$ is the Boltzmann constant, $T$ is the absolute temperature, $q\ (>0)$ is the fundamental electric charge, and $V$ is the voltage at the terminals of the cell. $I_0$ is defined as the diode saturation current and $n$ is the ideality factor. Figure 5a shows the I–V characteristic (Eq. 1) of a generic diode.

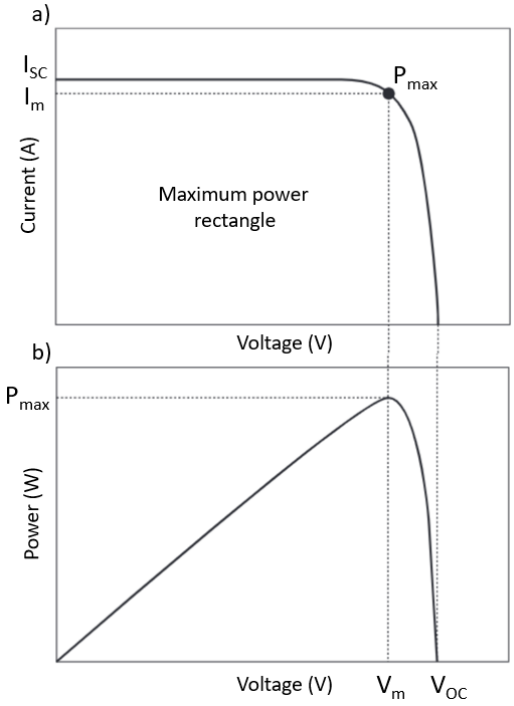


**Figure 5**: The I–V characteristic of an ideal solar cell a) and the power produced by the cell b). The power generated at the maximum power point is equal to the shaded rectangle in a).

The photogenerated current $I_{ph}$ depends on the photon flux incident on the solar device, and it is generally independent of the applied voltage. In an ideal solar cell, the short-circuit current $I_{sc}$ is equal to the photogenerated current $I_{ph}$, and the open-circuit voltage $V_{OC}$ is given by:

$$V_{OC} = \frac{k_BT}{q}\ln\left(1 + \frac{I_{ph}}{I_0}\right). (2)$$

The power $P$, which is expressed in Watt (W), is defined as the product between the current and the voltage ($P = IV$), generated by the solar cell is shown in Figure 3b. The cell delivers the maximum power ($P_{max}$) at a voltage $V_m$ and current $I_m$.
Having defined these parameters, it is then possible to provide the equation of the third fundamental PV parameter after the $I_{sc}$ and $V_{OC}$, which is the fill factor (FF):

$$FF = \frac{I_mV_m}{I_{SC}V_{OC}} = \frac{P_{max}}{I_{SC}V_{OC}}, (3)$$

Finally, it is worth mentioning that the I–V characteristics of an ideal solar cell complies with the superposition principle. Hence, Eq. 1 not only represents the characteristic of a dark diode but also the corresponding behavior of an illuminated diode by displacing the dark I-V curve along the current axis by $I_{ph}$, as depicted in Figure 6.

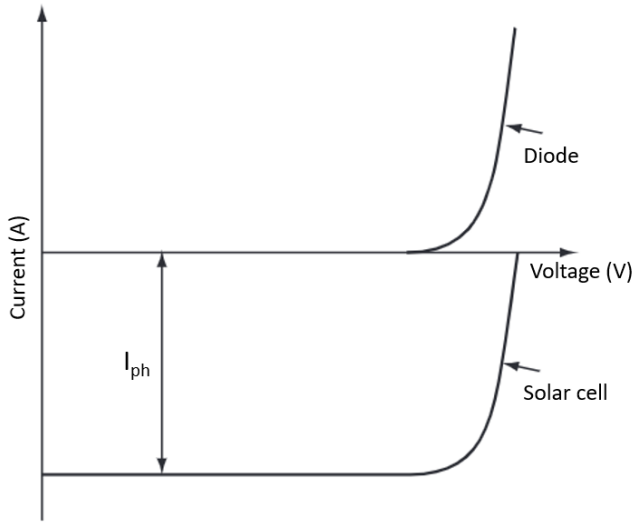


**Figure 6**: Superposition principle for solar cells.

To get into more details, it is important to mention that the I–V characteristic of an actual working solar device usually differs from the ideal characteristic expressed in Eq 1. As a matter of fact, a two-diode model is often used to fit an experimental I-V curve. In order to account for non-ideal behavior of a solar cell, to the second diode is generally attributed an ideality factor of 2. Additionally, series ($R_S$) and parallel (or shunt, $R_{SH}$) resistances can be also included in the equivalent circuit of solar cell, as a consequence the I-V characteristic of a real solar cell can be expressed as follows:

$$I = I_{ph} - I_{01}\left(e^{\frac{V+IR_S}{k_BT}}\right) - I_{02}\left(e^{\frac{V+IR_S}{2k_BT}} - 1\right) - \frac{V + IR_S}{R_{SH}}, (4)$$

These features were already shown in the equivalent circuit of Figure 4 and represented by the dotted lines.
Figures 7 depicts the effects of the second diode and the series and parallel resistances on the I-V characteristic of the solar cell, respectively [24,25].

### 1.1.7 The quantum efficiency and spectral response

The quantum efficiency (QE) of a solar cell is defined as the ratio of the number of charge carriers (electrons) in the external circuit (solar cell) produced by an incident photon of a given wavelength. Thus, one can define external and internal quantum efficiencies denoted by $EQE(\lambda)$ and $IQE(\lambda)$, respectively [26]. They differ in the treatment of photons reflected from the cell: all photons impacting on the cell surface

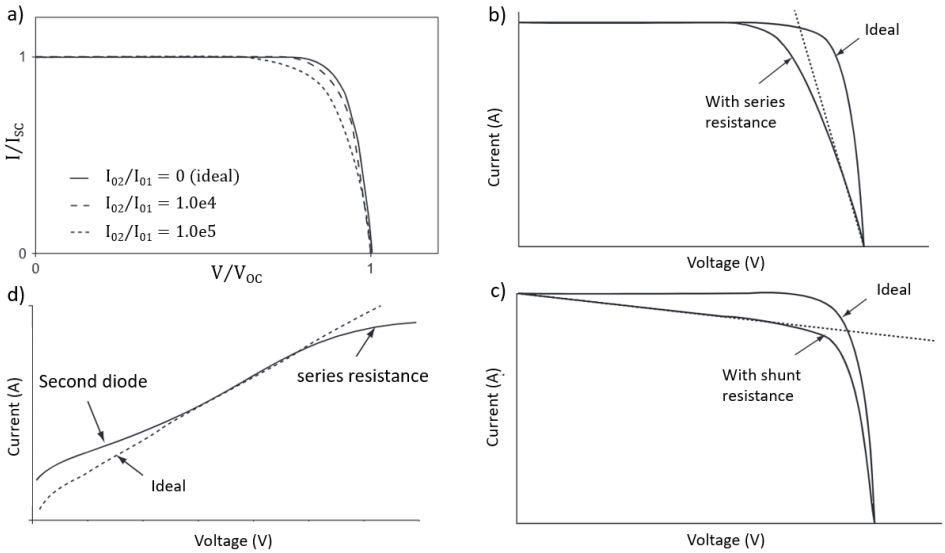


**Figure 7**: a) The I–V characteristic of the solar cell in the two-diode model for three values of the ratio $I_{02}/I_{01}$.The effect of series b) and parallel c) resistance on the I–V characteristic of the solar cell. d) The dark I–V characteristic of a solar cell for the two-diode model including the series resistance since the shunt resistance has a similar effect to the second diode. Note that, the y-axis of Figure d) is in log scale.

are considered in the value of the $EQE(\lambda)$, but only photons that are absorbed are considered in the value of the $IQE(\lambda)$. If the $EQE(\lambda)$ is known, the total photogenerated current can be calculated as:

$$I_{ph} = q \int_{(\lambda)} \phi(\lambda)[1 - R(\lambda)]EQE(\lambda)d\lambda\,, (5)$$

where $\phi(\lambda)$ is the photon flux incident on the cell at wavelength $\lambda$, $R(\lambda)$ is the reflection coefficient from the top surface, and the integration is carried out over all wavelength ($\lambda$) of light absorbed by the solar cell. The values of the internal and external quantum efficiency are regularly measured to assess the performance of a solar cell by using interference filters or monochromators.

Generally, $EQE(\lambda)$ measurements are a valuable tool for evaluating and optimizing the performance of a solar cell. As shown in Figure 8, the ideal quantum efficiency has a square shape, however, the quantum efficiency for most solar cells is reduced due to recombination effects. The same mechanisms which affect the collection probability also affect the quantum efficiency. For instance, front surface passivation affects carriers generated near the surface, and since blue light is absorbed very close to the surface, high front surface recombination will affect the "blue" portion of the quantum efficiency. Similarly, green light is absorbed in the bulk of a solar cell and a low diffusion length will affect the collection probability from the solar cell bulk and reduce the quantum efficiency in the green portion of the spectrum. Therefore, in principle, the quantum efficiency can be viewed as the collection probability due the generation profile of a single wavelength, integrated over the device thickness, and normalized to the incident number of photons at that wavelength. Additionally, the spectral response (denoted by $SR(\lambda)$, with the units A/W) is defined as the ratio of the photocurrent generated by a solar cell under monochromatic illumination of a given wavelength to the value of the spectral irradiance at the same wavelength; in other terms the capability of a solar cell to convert light energy into electrical energy, as a function of the

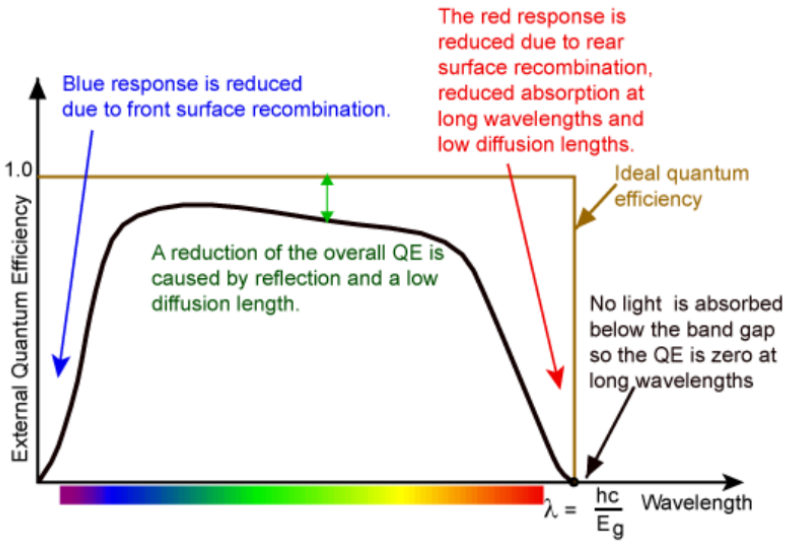


**Figure 8:** *The quantum efficiency of a silicon solar cell. Quantum efficiency is usually not measured much below 350 nm as the power from the AM1.5 spectrum contained in such low wavelengths is low [27].*

wavelength of the light. Since the number of photons and irradiance are related, the spectral response can be written in terms of the $QE(\lambda)$ as [28]:

$$SR(\lambda) = \frac{q\lambda}{hc} QE(\lambda), (6)$$

where $\lambda$ is generally expressed in micrometers. $SR(\lambda)$ expressed in equation 6 can be either internal or external, depending on whether $EQE(\lambda)$ or $IQE(\lambda)$ is used for $QE(\lambda)$.

### 1.1.8 Single and multi-junctions solar cells

The solar device scheme presented in paragraph 1.1.6 refers to single junction solar cell (Figure 4). However, for single junction solar cell there is an upper limit to the light-to-electrical power conversion efficiency that is determined by the Shockley–Queisser (SQ) model [29]. In particular, within the SQ formalism, it is postulated that all photons with energies above the bandgap ($E_g$) create free electrons and holes, which, with perfect charge-selective contacts (e.g., contacts that efficiently separate and collect electrons or holes), yields one electron per absorbed photon to contribute to the electrical current. The SQ model also stipulates that all electron–hole recombination events, which occur when the solar cell is generating power, are the inverse process to light absorption and therefore radiative. The SQ limit is based purely on thermodynamic considerations and takes the optical absorption edge, the solar spectrum, and the operating temperature of the solar cell as the only inputs for the calculation of efficiency.

As an example, for a silicon solar cell, the Shockley-Queisser limit is approximately 32% due to efficiency limitations caused by Auger recombination. It follows that for an ideal single pn junction silicon solar cell cannot convert more than 32% of incident sunlight into electrical energy, regardless of the quality of the material or the manufacturing process used to fabricate the cell. In practice, however, the actual efficiency of silicon solar cells is typically much lower than the Shockley-Queisser limit, due to various losses such as recombination of charge carriers, reflection of light, and parasitic resistances [30].

One possibility to overcome the efficiency limitation dictated by the SQ model lies in the use of multi-junction solar cells [31]. Multi-junction solar cells are an exciting technology that may provide increased efficiencies in the solar panels of the future. Multi-junction solar cells are capable of absorbing different wavelengths of incoming sunlight by using two or more photoactive layers, making them more efficient at converting sunlight into electricity than single-junction cells thanks to the mitigation of thermal losses. Nonetheless, the high production costs and continuing research and development means that multi-junction cells are not currently commercially available.
As the name suggests, a multi-junction solar cell is a solar cell with more than one photoactive junction. In practice, this means that there are multiple layers of different semiconductor materials, each of which produces electric currents in response to different wavelengths of light.
The highest efficiency devices incorporate multiple solar cells in a vertically connected stack for peak efficiency at various wavelengths within the solar spectrum. These multi-junction devices require a transparent and conductive layer to join them, most commonly in the form of tunneling junctions. One of the first monolithic multi-junction solar cell was grown in 1980 by Bedair et al. at NCSU [32].
Tunnel junctions are conductive, optically transparent semiconductor layers used to join different semiconductor materials in order to facilitate the efficient flow of charge carriers and increase overall device efficiency.

### 1.1.9 PV technologies

Solar cells are typically divided into three main categories referred also as generations [33]. The first and second generation have reached the industrial production, even though the active material in second generation solar cell contains precious or toxic elements (In, Ga, Cd) and therefore the fabrication is limited. The term third generation is used referring to solar cells that have the potential to be efficient and economical. Most technologies in this generation are not yet commercial, but there is a lot of research going on in this area, especially in the perovskite-based solar cells. Mainly, the purpose of the researchers is to make third generation solar cells stable along reasonable periods of time.
The first-generation of solar cells comprises two main types: single crystal Si solar cells, which are made from wafers consisting of a single crystal, and multi-crystal Si solar cells, which are produced from wafers composed of multiple crystal grains. These are the oldest and the most distributed technology due to high efficiencies. 1st generation solar cells are fabricated on wafers. Each wafer can supply 2–3-watt power. To increase power, solar modules, which comprise of many cells, are utilized. Although efficiency of mono crystal solar cells is higher than multi-crystal solar cells, production of multi-crystal wafer is easier and cheaper. Thus, they are competitive with monocrystals.
The second-generation of solar cells include amorphous Si (a-Si) based thin films solar cells, Cadmium Telluride/Cadmium Sulfide (CdTe/CdS) solar cells and Copper Indium Gallium Selenide (CIGS) solar cells and it is also known as thin-film generation. Their efficiencies are reduced than 1st generation, but their costs are also minor than 1st generation. Moreover, they have a benefit in visual aesthetic since there are no fingers in front of the thin film solar cells for metallization, they are much more applicable on windows, cars, building integrations etc. Plus, thin films can also be grown on flexible substrates and on large areas up to 6 $m^2$.

The third generation of cells are less commercially advanced *emerging* technologies. It is based on thin-film technologies developing organic and hybrid materials. Third generation solar cells comprise organic, dye-sensitized, polymer, copper tin zinc sulfide (CZTS), nanocrystals, quantum dots and perovskite solar devices. During the last years, the improvement of performance for perovskite solar cells was extraordinarily rapid and this has drawn considerable interest and attention of the researchers.
Figure 9 (here below) shows a chart of the highest confirmed conversion efficiencies for research cells for a range of PV technologies, plotted from 1976 to the present [34].

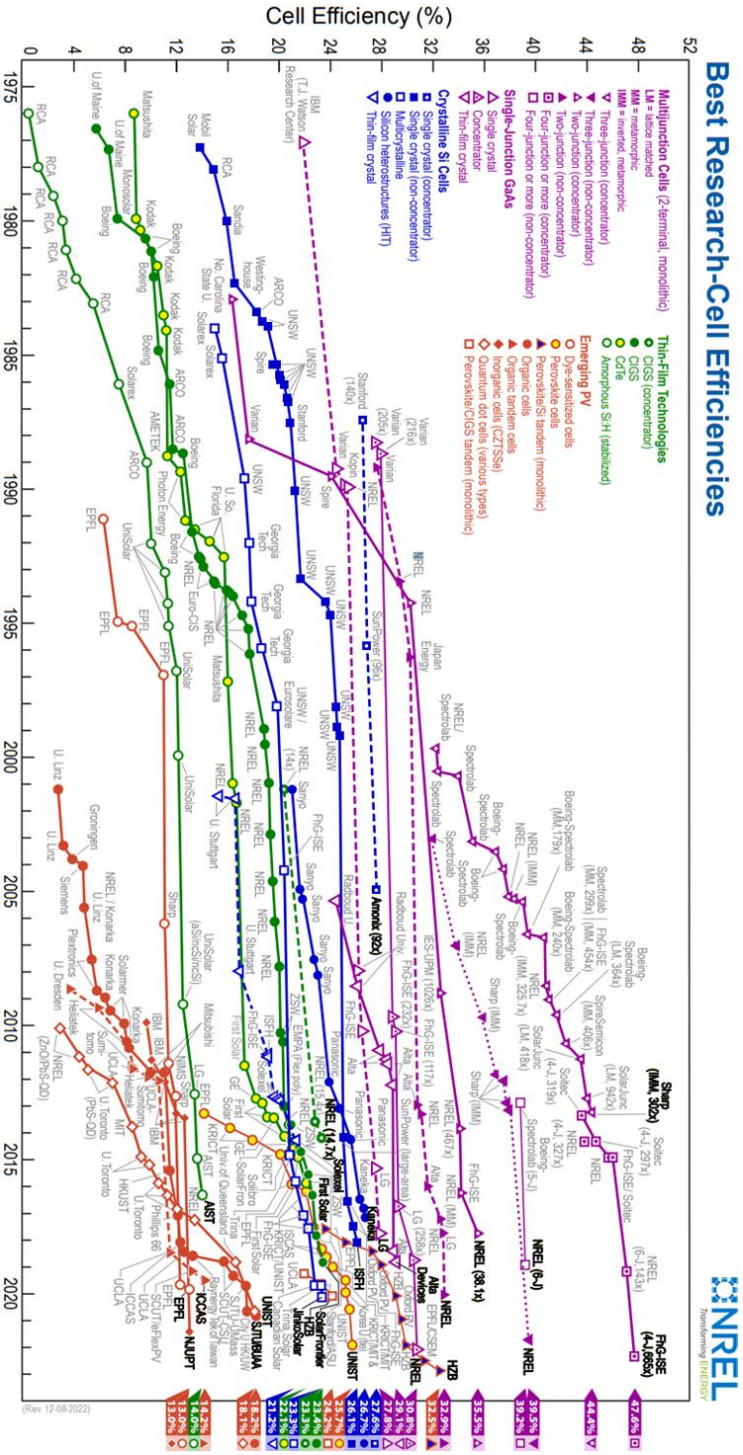

## 1.2 The power of imaging at the nanoscale: Scanning Probe Microscopy Techniques

The development of Scanning Probe Microscopy (SPM) in the 1980s was largely influenced by two key factors: the invention of the Scanning Tunneling Microscope (STM) [35] and the availability of piezoelectric devices [36].

The STM was invented in 1981 by Gerd Binnig and Heinrich Rohrer at IBM's Zurich Research Laboratory who received the Nobel Prize in 1986. The STM works by scanning a sharp metal tip across a surface, maintaining a small distance between the tip and the surface which is regulated by a feedback loop. A voltage is applied between the tip and the surface, and as the tip moves closer to the surface, electrons can tunnel from the surface to the tip. The resulting tunneling current is measured, and this current can be used to create an image of the surface with atomic resolution.

Piezoelectric materials are a class of materials that have the ability to generate an electrical charge in response to an applied mechanical stress, or to generate mechanical deformation in response to an applied electric field. The most commonly used piezoelectric ceramics materials are quartz and lead zirconate titanate. Thanks to this property, piezoelectric materials are used as actuators that allow small and precise movements in mechanical devices, as for instance the tip of a microscope.

These two factors together allowed the development of the SPM with the introduction of two new techniques: the scanning near field optical microscopy [37] and the Atomic Force Microscopy (AFM) [38]. The AFM uses a piezoelectric actuator to move the probe across a sample surface while monitoring the force generated between the tip and the surface which enables the acquisition of topographical images. Additionally, through the utilization of specific electrical extensions, AFM can investigate other surface properties, including magnetic, electrical, and mechanical properties [38].

AFM and its electrical extensions proved to be highly effective for the characterization of solar cells. In particular, the development of PV technologies has progressed significantly over the past twenty years as a result of considerable advancements in solar cell device engineering and material science. As a consequence, solar cells have turned into complex structures constituted of numerous layers and interfaces. J-V and EQE characterization (presented in the previous paragraphs) provide general information on the overall electrical performance of solar devices. However, the capability to conduct local investigations at the nanoscale level that provide information on the electrical properties of materials and along physical interfaces is becoming crucial for solar device efficiency improvement [2].

For this reason, AFM electrical extensions have revolutionized our ability to study the electrical properties of PV materials and devices. Kelvin probe force microscopy (KPFM), for instance, can be used to map the surface potential providing insight into the local charge distribution and the presence of energy barriers that may hinder charge transport. Additionally, conductive AFM (c-AFM) can be used to measure the local conductivity allowing the identification of defects or variations in the electrical properties.

In this PhD project the principal objective is to use electrical AFM extension to investigate materials and devices for photovoltaic applications. In particular, the use of KPFM and c-AFM was of primary interest throughout the doctorate as it will be described along the manuscript.

### 1.2.1 Atomic Force Microscopy (AFM)

Atomic Force Microscopy (AFM) is classified as a near-field microscopy since these measurements are performed directly on the very surface of the sample. In order to acquire topographical information a nano-sized probe is used. The probe comprises of different parts: a millimeter-scale chip, a cantilever, and a tip with a nano-scale radius. The cantilever and the tip are shown in Figure 10.

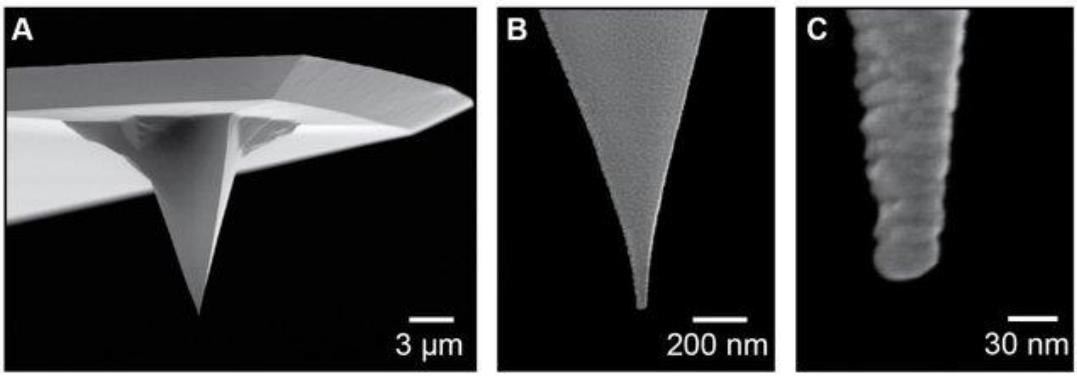


**Figure 10:** SEM images of a Pt/Ir coated silicon tip generally used for KPFM analysis. a) shows the cantilever and the tip, b) and c) shows zooms at different scales of the tip.

The cantilever is typically 200 µm long. The length of the cantilever characterizes its stiffness: shorter cantilevers are generally stiffer than longer ones. The tip is located under the cantilever, and it represents an essential part since its radius affects the lateral resolution of measurements.
There are several commercially available materials used for AFM tips, e.g., silicon nitride or silicon. For electrical measurements purposes, a conductive tip must be used to be sensitive to the electrical surface properties of the sample. Hence, tips are either coated with conductive materials, such as highly-doped diamond, or are directly composed of a bulk conductive material. Generally, AFM tips need to be changed regularly since they are fragile, and the conductive coating tends to wear off after several scans.
The tip is brought at a nano-scale distance from the sample in order to perform AFM measurements. The probe is sensitive to the attractive and repulsive forces present between the tip and the sample. The type of force depends on the tip/sample distance as shown in Figure 11.

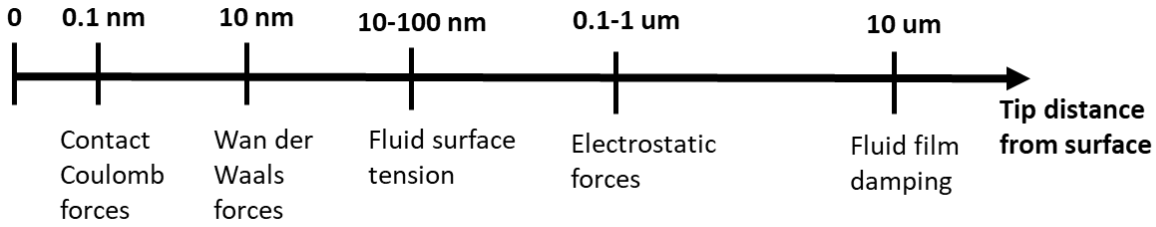


**Figure 11:** Different forces generated between the tip and surface of sample in function of the tip/sample distance. The schematic is not to scale.

Contact forces result to be prevalent at very small tip-sample distance (≈Å). This force is extremely repulsive due to the overlap of the electronic orbitals that occurs at atomic distances. For distances between 1 nm and 10 nm, Van der Walls forces become relevant. They act as weak attractive forces that derive from the interaction between molecules and groups of atoms. Fluid surface tension starts to arise between 10

and 100 nm leading to an attractive force which is derived from the nano-scale water film at the surface of the sample producing a water meniscus beneath the tip. Additionally, between 100 nm and 1 µm, electrostatic and magnetostatic forces, depending on the properties of materials, generate attractive or repulsive forces between the sample and the tip. Finally, moving away from the surface, at distances about 10 µm, fluid film damping forces can be considered [39].
The effect of the different forces defines an interaction between the tip and the sample which causes a mechanical bending of the cantilever. Consequently, the interaction between the tip and the sample can be observed by evaluating the motion of the cantilever which can be achieved with a laser focused on the extremity of the cantilever and reflected to a photo-detector. The position of the reflected laser magnifies the motion of the cantilever. A general AFM setup is shown in Figure 12.
The AFM requires a feedback signal to quantify the topography height at the nano-scale. In particular, when the AFM is operated in contact mode the deflection of the cantilever can be used, whereas in non-contact mode the amplitude or the frequency shift of the cantilever oscillation can be suitable to this purpose. During the measurements, a setpoint target value is established for the signal, which must remain constant. In the event of any deviation from the target, a vertical piezoelectric actuator, controlled by a proportional-integral-derivative (PID) controller, is employed to correct the error.

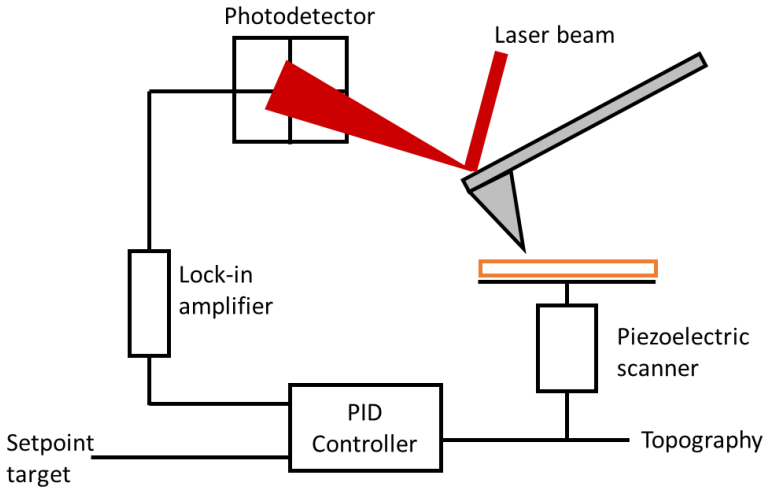


**Figure 12:** The setup for Atomic Force Microscopy involves monitoring the motion of the cantilever through laser beam reflection on the photodetector. This motion is then amplified using a lock-in amplifier and compared to a setpoint target. Any discrepancies are corrected by adjusting the Z position of the piezoelectric actuator through a PID controller.

During a scan of the surface, either the tip or the sample is moving utilizing lateral piezoelectric actuators in a micro-controller allowing the image acquisition of the topography. The piezoelectric actuators are at the base of the AFM spatial resolution since a considerable voltage is necessary to perform a small spatial motion. Voltages between 250 V and -250 V are used to achieve vertical displacements of about 50 µm, making AFM an uncontested technique for vertical resolution.
AFM measurements can be performed in three different modes: contact mode, tapping mode, and non-contact mode, as shown in Figure 13.

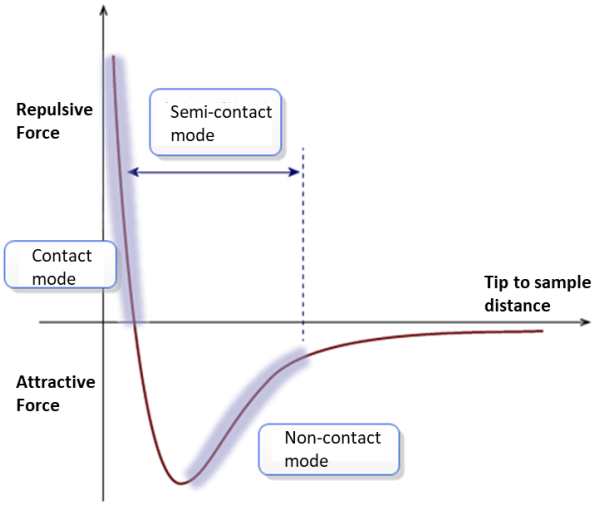


**Figure 13:** Plot of the tip-surface force versus the tip-surface distance for an AFM tip and a surface showing the approximate regions corresponding to contact mode, semi-contact mode, and non-contact mode.

The contact mode date back to 1986 and it was used in the first AFM [40]. In this mode, the tip is constantly in contact with the surface of the sample. In this mode, the feedback signal is the bending (or *deflection*) of the cantilever. The movement of the cantilever can be comprehended mechanically as that of a semi built-in beam and can be modeled using Hooke's law. The surface can be nano-indented if the force applied by the tip on the surface is strong, nonetheless, this can be advantageous in some specific cases (e.g., conductive AFM) but mostly it represents a downside to the achievement of precise topography images. Various AFM extensions operate using contact mode, which includes techniques such as lateral force microscopy (LFM), scanning capacitance microscopy (SCM), piezo-response force microscopy (PFM), and chemical force microscopy (CFM). For the extensions designed for electrical measurements, conducting AFM (c-AFM) also employs contact mode, which will be discussed in more detail in Chapter 2.
Just one year after the introduction of contact mode, non-contact mode was developed [41]. This mode is distinguished by the oscillation of the cantilever in close proximity to the surface, while maintaining a non-contact configuration. It is roughly 10-20 nm directly above the surface and hence, the tip only interacts with Van der Walls forces. The cantilever can be related to a harmonic oscillator whose acceleration depends on the distance to the surface due to Van der Waals forces. These forces alter either the amplitude or the frequency of oscillations, and, since both depend on the distance to the surface, they can be utilized as feedback signals. Non-contact mode presents the advantage of damaging neither the tip nor the sample and is very popular to probe fragile materials. However, due to the low intensity of Van der Waals forces and their susceptibility to water adsorption on surfaces, it is recommended to utilize non-contact mode in ultra-high vacuum (UHV) for improved image quality. KPFM is an AFM electrical extension that uses non-contact mode.
After several years, tapping mode was introduced in 1993 [42]. Tapping mode can be defined as a semi-contact mode since as the tip oscillates, it makes short and intermittent contact with the sample surface during the upswing of its oscillation. As in the case of non-contact mode, the amplitude and the frequency of the signal can be utilized as feedback signals. Tapping mode has several advantages compered to contact and non-contact mode. For instance, it has the benefit of interacting with a strong contact force and

not being sensitive to water meniscus, and thus it can be convenient for ambient conditions measurements. Additionally, it has the benefit of being more stable on very textured surfaces and of lowering the friction force, consequently avoiding the degradation of the tip or the sample. Nevertheless, one drawback associated with tapping mode is the time to perform a measurement, which is larger compared to the other modes. Several AFM extensions can be coupled to AFM tapping mode such as KPFM, Electrostatic Force Microscopy (EFM) and Magnetic Force Microscopy (MFM).

## 1.3 Exploring the Invisible World: The Benefits of Scanning Probe Microscopy

In this section, we will delve into the principal characteristics of scanning probe microscopy with particular emphasis on KPFM and c-AFM techniques exploring why these methods are particularly suitable for solar cell analysis. Here, we will focus on the many benefits that make these methods valuable, including their non-intrusive nature, spatial resolution, low charging effects and sensitivity to illumination.

### 1.3.1 Spatial resolution

SPM techniques offer significant benefits in terms of spatial resolution, with KPFM being capable of achieving resolutions superior to 10 nm even in ambient conditions [43]. Additionally, UHV-KPFM can achieve higher resolution of the order of sub-nanometer, and it is worth noting that by functionalizing the tip with a CO molecule, atomic resolution can also be attained [44].

As already mentioned in paragraph 1.2.1, the lateral resolution significantly depends on the tip radius and shape. Various types of cantilevers and conductive coatings may be used in KPFM measurements. According to [43], heavily doped silicon cantilevers, Pt/Ir-coated silicon cantilevers, and Au or Cr coated silicon cantilevers are the most commonly used types of cantilevers. When conducting high-resolution imaging under UHV, heavily doped silicon cantilevers are frequently used. However, prior to analysis, the native oxide layer must be eliminated through methods such as heating, ion bombardment, or etching. This procedure is one of the reasons why conducting measurements under UHV is time-consuming.

Pt/Ir-coated silicon cantilevers do not necessitate considerable tip preparation but lead to lower spatial resolutions for KPFM. Eventually, Au or Cr coated silicon can be employed for high resolution imaging. The benefit is that materials as Cr are less responsive in air than silicon.

Generally, in ambient conditions analysis, c-AFM offers higher spatial resolution than KPFM because the tip is in direct contact with the surface, allowing for more precise measurements of surface features. In contrast, KPFM operates at a distance from the surface, limiting the spatial resolution that can be achieved.

For instance, high-resolution c-AFM images (below 10 nm) are obtained with bulk diamond probes (radius = 10 ± 5 nm) [45]. It has been demonstrated that for c-AFM scans at an interface, the resistance signal convolution is just contained by two tip radii distance from the interface [46]. Nevertheless, the limitations to smaller tip radius are the speed of erosion and the resistance signal which is higher for smaller tip radii.

Fundamentally, two strategies can be adopted to enhance the spatial resolution: using smaller radius tips, and measurements under UHV. Another approach consists of tilting the sample to improve the spatial resolution, as shown by Zhang et al. [47].

SPM possesses 2D scanning capabilities that can deliver exceptional nano-scale resolution. For instance, SPM enables the investigation of the cross-section of solar cells which represents a significant advancement, as traditional micro-scale characterization techniques were impractical due to the thickness of the layers in solar cells, which can vary from a few microns (e.g., epitaxial layers) to a few atoms (layers deposited by atomic layer deposition).
For instance, with nano-scale resolution techniques, the analysis of the properties of pn junctions on the cross-section of the solar cell is now achievable. Furthermore, pn junctions can be studied under operating conditions such as “under illumination” or under external applied bias [47]. Additionally, it is possible to investigate charge transport mechanisms and gain insight into the performance of the device. By mapping the potential variations at the interfaces with high spatial resolution, KPFM can reveal the location and extent of charge accumulation or depletion, which may be indicative of defects or impurities. Additionally, the technique can be used to identify the presence of interfacial dipoles or space charge regions, which can influence the overall performance of the solar cell.

### 1.3.2 Low charging effect

Low charging effect is a common feature of many SPM techniques which can make them particularly useful for studying materials that are prone to charge buildup. In SPM, the probe tip is brought into close proximity with the sample surface, creating an electric field that can cause charge accumulation or depletion in the sample. This can result in distortion of the measurement due to electrostatics screening or even damage to the sample. However, SPM techniques are designed to minimize this effect by controlling the charge buildup. This is typically achieved through a combination of measures such as using conductive probes, applying a bias voltage to the probe, or using an electrostatic force feedback mechanism. By doing so, the charge accumulation can be minimized, and high-quality measurements can be obtained without damaging the sample.
Specifically, KPFM exhibits low charging effects and does not damage the material during measurements making it a non-invasive technique. Furthermore, tip-induced oxidation may be limited by operating under a controlled atmosphere, resulting in easily reproducible KPFM images. This is a valuable benefit, as it allows for the examination of degradation phenomena over time or exploration of the influence of external parameters, such as light or electrical bias, by acquiring successive images of the same area under different conditions [48].

### 1.3.3 Sensitivity to illumination

The low charging effect described in the previous paragraph is particularly advantageous for investigating solar cells because it allows for a clear evaluation of the effect of illumination at the nano-scale. SPM is able to detect the variation of the surface potential caused by the photo-generated carriers that are produced when the solar cell is exposed to external illumination.
For instance, KPFM enables the evaluation of the surface photovoltage (SPV), which is defined as the light-induced change of the contact potential difference at the surface of a photoactive material [20]. As an example, by SPV measurements, it is possible to measure the lifetime of minority carriers by detecting the alteration in surface potential caused by the photo-generated carriers. Specifically, by examining the decay of the SPV signal, it becomes possible to estimate the lifetime of minority carriers [56]. Additionally,

*SPV* analysis can be used to measure the open-circuit voltage ($V_{OC}$) by analyzing the *SPV* signal under illumination. This technique provides a non-destructive and non-contact method for evaluating $V_{OC}$ of solar cells. For instance, this approach can be used as a monitoring strategy for solar cells during the several fabrications stages.
Surface defects can have a significant impact on the electronic properties of semiconductor materials and devices. *SPV* analysis can be used to detect the presence of surface defects by measuring changes in the *SPV* signal. Surface defects can alter the recombination rate of photo-generated carriers, resulting in a change in the *SPV* signal [49]. By analyzing the *SPV* signal, it is possible to identify and locate surface defects and gain insight into their impact on the device performance.
Finally, it is also possible to perform c-AFM measurements under illumination. In particular, this allows the estimation of the photogenerated current of a solar cells under operating conditions by comparison with current (or resistance) maps acquired in dark.

### 1.3.4 Direct electrical measurements

For solar cell characterization, the comparison between local analysis and macro characterization e.g., local *SPV* and overall $V_{OC}$ it is of primary interest [50]. By comparing macroscopic and local measurements, one can better understand how the device operates at different regions and how local variations of physical properties affect the overall performance. This approach can also help identify and address issues such as non-uniformity and degradation, leading to the development of more efficient and reliable solar cells.
KPFM and c-AFM techniques do not require an intermediate signal to detect the surface potential and current signals at the nanoscale, making easier to achieve quantitative measurements. C-AFM is particularly suitable for achieving quantitative nanoscale mapping of carrier concentrations [46].
In solar cells, series resistance is a common limiting factor, which can be extracted from the I-V curve. However, determining the cause of series resistance is not always straightforward, as it can result from problems with contacting or doping in the semiconductor. Since series resistance causes a potential drop at high currents, KPFM can locally detect its presence under forward voltage bias conditions. By using these techniques, it is possible to obtain a better understanding of the underlying causes of performance limitations in solar cells.

### 1.3.5 Adaptability

SPM techniques are widely recognized for their versatility, as they can be used under various conditions, including different pressures, temperatures, and environments [51]. These techniques can operate in ambient air, controlled atmospheres, ultra-high vacuum, and even in liquids [52]. While measurements conducted under UHV conditions may alleviate or eliminate some artifacts, measurements under ambient air or controlled atmosphere offer the benefit of being fast and allow for high-throughput analysis.
Performing high-resolution measurements in ambient air can be completed within less than one hour, while a single scan under UHV may take a day or more. One approach is to combine measurements in both environments. Experiments can be rapidly set up and external excitation sources such as illumination or electrical bias can be easily introduced in SPM setups under ambient conditions. Once the underlying

theory of a measurement is well established, the setup can be transferred to UHV to perform time-consuming but high-resolution scans.
Furthermore, SPM can be readily integrated into various other characterization setups. This includes a broad spectrum of optical microscopy techniques [53], such as ellipsometry and Raman spectroscopy. SPM can also be combined with electron microscopy setups, as well as time-of-flight mass spectrometer and X-Ray spectroscopy. The remarkable integration of SPM with other characterization techniques allows for the identification of artifacts in both methods and the analysis of various types on the same regions. Additionally, the integration of SPM with other techniques offers a broader range of possibilities. For example, mechanical information, such as friction, phase, and deflection, can be obtained in addition to topographical and electrical images. These supplementary signals can help to establish correlations and enhance interpretations.
SPM, particularly KPFM, is also suitable for in-situ monitoring of fabrication processes. Watanabe et al., [54] have used KPFM for in-situ analysis of nano-structuring in organic solar cells. The non-invasive nature of KPFM also makes it possible to investigate degradation phenomena, such as in-situ light-induced and potential-induced degradations. Additionally, SPM can probe a wide range of materials, including soft and fragile ones such as organic materials. The low material dependence of the electrical signals measured makes it possible to analyze the interfaces of solar devices effectively. Moreover, SPM can operate under ambient air, allowing for the investigation of hydrated samples that typically cannot be studied under UHV. Finally, SPM has relatively low acquisition and maintenance costs.

### 1.3.6 Acquisition time

SPM techniques offer a high temporal resolution (≈ ms), enabling the monitoring of electrical signal evolution over time. KPFM has been extensively used to investigate temporal properties with a reported temporal resolution of about 20 µs [55]. However, conventional KPFM is not sufficient to analyze solar devices with lifetimes below the millisecond range, such as perovskites (ns-µs).
In this regard, two possibilities can be considered. New KPFM setups without feedback can achieve precise surface potential measurements opening up to the possibility of performing time-resolved KPFM (tr-KPFM) measurements. Tr-KPFM is expected to have improved temporal resolution with the emergence of new modes such as G-mode KPFM, which simplifies signal detection, resolves frequency-shift artifacts, and captures the entire cantilever dynamics in the frequency domain. It may enable temporal resolution studies below the µs.
Another possibility for investigating temporal properties in KPFM is to use its time-averaging ability. In this method, the surface potential changes in response to an excitation source such as illumination or electrical bias. By modulating the intensity of the excitation at high frequency, KPFM can time-average the signal. Varying the frequency of the excitation can provide information on lifetime in the ns and µs range. KPFM measurements under modulated frequency illumination have been shown to be effective in investigating low lifetime solar cells at the nano-scale [56].

## 1.4 Looking beyond the surface: the challenges of scanning probe microscopy

In this section, the disadvantages of SPM approaches are explored, encompassing drawbacks such as artifacts, crosstalk, and limitations. Artifacts are modifications in the collected data that can be misleading and are caused by inadequacies in the equipment. These inaccuracies can have a significant impact on data interpretation and comprehension. Conversely, limitations are characterized by the lack of certain features that other competing techniques may offer. Although they do not affect data precision, they can restrict access to critical information. Integrating additional investigative methods like SEM and TEM with SPM analysis can provide substantial benefits, enhancing the overall value and comprehensiveness of the research.

### 1.4.1 Parasitic illumination

As previously described, AFM-based methods require a laser to track the movement of the cantilever. Nevertheless, this laser may also inadvertently illuminate the sample if its spot size exceeds that of the cantilever or if it is misaligned, as shown in Figure 14.

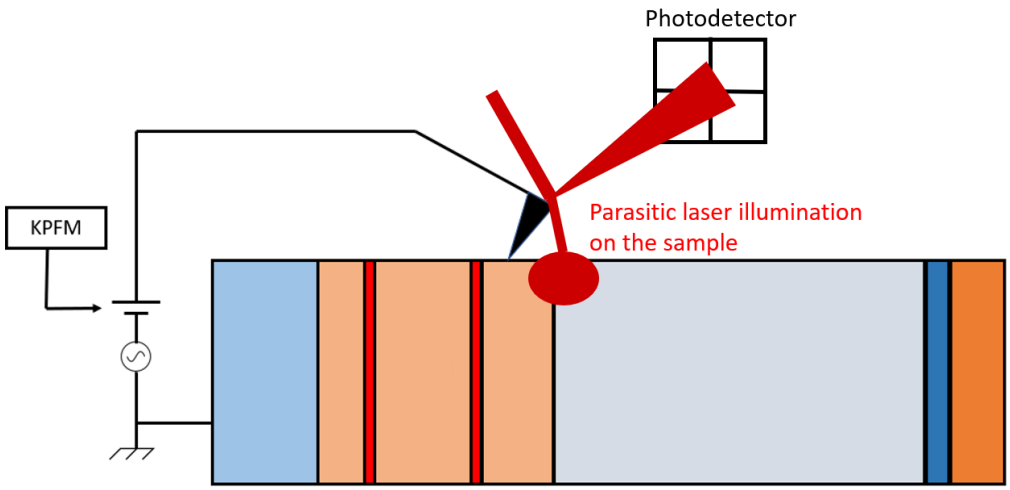


**Figure 14:** AFM laser spreading over the surface of the sample.

When characterizing solar cells, the light used can be considered as parasitic since measurements in true dark conditions are unattainable, which can cause offsets in the measured current or surface potential values. To minimize the interference of parasitic laser absorption in our AFM laser beam deflection system, we employ a laser with a wavelength of 1310 nm, which is significantly below the bandgap of the semiconductor samples investigated during the PhD. Alternatively, it is possible to use larger cantilevers than the laser spot size, or adopt techniques such as the AFM/KPFM method described by Takihara et al., that monitors cantilever motion using a piezoresistive sensor instead of an AFM laser [57]. To assess the effect of parasitic laser absorption, $V_{OC}$ generated solely by the AFM laser in the AFM or KPFM setup can be measured. If the effect is not negligible, it must be accounted for to correctly interpret the data.

## 1.4.2 Tip-induced surface degradation

When the tip comes into contact with the surface, it can create artifacts that may result from surface or tip degradation. Such artifacts can cause unreliable or misleading measurements. Tip-induced surface degradation may occur through three primary processes, which include tip-induced oxidation, nano-scratching, and tip-induced band bending.

### 1.4.2.1 Tip-induced oxidation

In c-AFM and KPFM a strong electrical confinement between the tip and the sample is present, since a small conducting tip with a high voltage bias scans the surface.

During measurements conducted in ambient conditions, water molecules present in humidity can be adsorbed on the surface of the sample as well as on the tip. The presence of a water layer can significantly impact measurements as even slight variations in its thickness can affect the data. Sugimura et al. have established a clear correlation between humidity levels and KPFM contrast [58]. Additionally, a water meniscus forms between the tip and sample, which can undergo a tip-induced electrochemical process if a negative bias is applied to the tip due to the high electric field. This results in the reaction of tip electrons, surface sample atoms, and water to produce oxide, dioxygen, etc.

The presence of tip-induced oxide layers can have a significant impact on c-AFM and KPFM measurements. In c-AFM, for instance, tunneling through the oxide layer can occur, leading to changes in the measured current [59]. Similarly, in KPFM, surface band-bending induced by the oxide layer can alter the surface potential, potentially resulting in artifacts. To mitigate the impact of tip-induced oxidation, measurements can be conducted under UHV conditions, where the sample is annealed beforehand to eliminate any remaining water films. However, various strategies can also be employed to minimize this phenomenon in ambient conditions. For example, a dry and controlled atmosphere can significantly reduce the rate of oxide growth and allow for numerous consecutive scans without concerns of surface oxidation. A nitrogen atmosphere, for instance, can be used to reduce oxidation.

### 1.4.2.2 Nano-scratching

C-AFM is performed in contact mode and a high force is required to enable a larger area of interaction and an increased current flow. However, this high force can also result in the tip scratching the surface of the sample, making it difficult to obtain accurate topography images and causing sample damage, making c-AFM a destructive technique under these conditions [50]. Therefore, a balance must be found between attaining a sufficient signal and minimizing surface degradation. Fine optimization of c-AFM parameters, such as tip force, voltage, and surface cleaning, may lead to non-destructive c-AFM measurements. Alternatively, c-AFM in tapping mode may be considered, but it can be time-consuming. Finally, optimizing c-AFM to detect lower currents would decrease nano-scratching since it would require a smaller contact area.

Conversely, KPFM measurements are performed in non-contact mode, eliminating the presence of nano-scratching artifacts.

### 1.4.2.3 Tip induced surface band-bending

During its approach to a semiconductor sample, the tip can generate band-bending on the surface due to a metal-insulator-semiconductor (MIS) effect. This is particularly true for KPFM measurements performed

in tapping mode. Here, the tip represents the metal, the air serves as the insulator, and the sample is the semiconductor. Tip-induced band-bending (TIBB) results from a Schottky effect caused by the difference in work functions between the tip and the semiconductor, and it is reversible when the tip moves away from the surface. This artifact is often considered negligible since the electrostatic force contribution of the tip-vacuum-sample is typically greater than the band-bending. However, TIBB can electrostatically screen defects under certain conditions, affecting electronic defect imaging resolution. Rosenwaks et al., [49] suggested a mitigation strategy involving the selection of a low AC voltage amplitude in KPFM measurement parameters, and TIBB can be almost entirely eliminated by using KPFM in UHV.

#### 1.4.2.4 Tip degradation during scans

The interaction between the tip and the sample may also contribute to the degradation of the tip, which in turn affects the accuracy of measurements. If a change in signal is observed during measurements, it is possible to differentiate between tip degradation artifacts and surface degradation artifacts by comparing two scans of the previously scanned and a new area. If the scans are similar, then the tip is likely degraded, whereas if they are different, the examined area is likely damaged. There are two types of tip degradation: tip coating degradation and tip contamination. The former is an irreversible artifact, while the latter can be reversed.

#### 1.4.2.5 Tip degradation coating

The application of strong forces in c-AFM can cause the tip to degrade. This deterioration is caused by the wearing down of the conductive coating on the tip during the scans, resulting in a decrease in current signal and potentially affecting measurement reproducibility. This is why c-AFM tips have a shorter lifespan compared to KPFM tips, which operate in non-contact or soft tapping mode and therefore degrade less quickly. To extend the lifespan of c-AFM probes, one possible solution is to use bulk conducting probes since they remain conductive for a much longer time. Additionally, bulk probes offer higher spatial resolution since they are sharper than coated probes, which have extra layers of coating at the tip edge. However, it should be noted that bulk diamond probes are significantly more expensive.

#### 1.4.2.6 Tip contamination

During tip scanning the particles adsorbed on the sample surface can stick to the tip, causing contamination that dominates the interaction between the tip and the sample and ultimately altering the experimental results. This phenomenon affects both KPFM and c-AFM, as adsorbed particles on the tip can alter the work function of the probe and corresponding contact potential difference ($V_{CPD}$) signal, making previous scans non-comparable to newer ones. This process occurs quickly due to fast adsorption of particles from the air and surface.

To prevent tip contamination, it is crucial to pay close attention to the cleaning and storage of samples and probes, using highly purified solvents and filtered dry nitrogen for cleaning and drying, and storing samples in sealed vials or nitrogen-filled containers. Additionally, utilizing low adhesion conducting materials for the coating of scanning probes is another option. However, the key to greatly reducing the risk of tip contamination is to operate under UHV conditions following thorough sample cleaning.

### 1.4.3 Convolution to topography

When analyzing a sample with a rough surface using SPM techniques, the topographical image may be imprinted onto the electrical or potential image due to the sensitivity of SPM to surface topography. This artifact can lead to misleading analysis as it is challenging to extract actual electrical or potential information from topographic alterations.

In c-AFM, the resistance detected is strongly dependent on the radius of contact between the tip and the sample, resulting in higher resistance in nano-valleys compared to nano-hills. This dependence is also highlighted by measurements on the sample cross-section. The use of logarithmic amplifiers in c-AFM increases errors associated with topography exponentially.

KPFM is also affected by the local features of the topography of the analyzed sample. Specifically, a topographical imprint on the experimental surface potential images can occur in the case of a rough and/or inhomogeneous topography. This effect is magnified by artifacts known as cross-talks which stem from the interaction between the applied AC voltage and the photodiode; however, it can be mitigated by selecting an appropriate AC voltage frequency. Additionally, KPFM measurements can be performed at different distances from the surface, and a new setup named heterodyne KPFM has shown promising results by reducing topographical coupling. Additionally, FM-KPFM can be used to reduce topography-related artifacts on the potential image. SPM is more suitable for investigating flat surfaces, and a polishing step may be necessary for very rough surfaces to attain suitably flat surfaces while paying attention not to degrade electrical properties.

Finally, KPFM is affected by the tip-averaging effect due to the long-range nature of the electrostatic force. Tip-averaging effect occurs when the analyzed sample has features that are smaller than the tip-apex radius. In this case, the tip cannot accurately resolve the features, and instead, it averages out the surface potential over a larger area, leading to a loss of lateral resolution.

Even at extremely short tip-sample distances (5 nm), the tip-averaging effect can lower the lateral resolution as well as the measured KPFM signal [60]. This is especially evident in ambient conditions KPFM where typical tip-surface distances are of the order of tens of nm due to the amplitude of the vibrating tip necessary to achieve an acceptable signal-to-noise ratio.

### 1.4.4 Stray capacitance

Stray capacitances can affect KPFM measurements due to the influence of topography which can cause artifacts, as Diesinger et al. [61] have explained. Although the capacitance between the tip-apex and the surface is the only significant factor, additional interactions between the other components of the probe and the sample can lead to inconsistencies in KPFM measurements due to the long-range of the electrostatic force. For instance, parasitic capacitances can affect the phase of the cantilever oscillation by causing undesired phase shifts in the cantilever oscillation.

In Figure 15 is shown the stray capacitances that are responsible for these discrepancies: the interaction between the tip sidewall and the sample and the interaction between the cantilever and the sample.

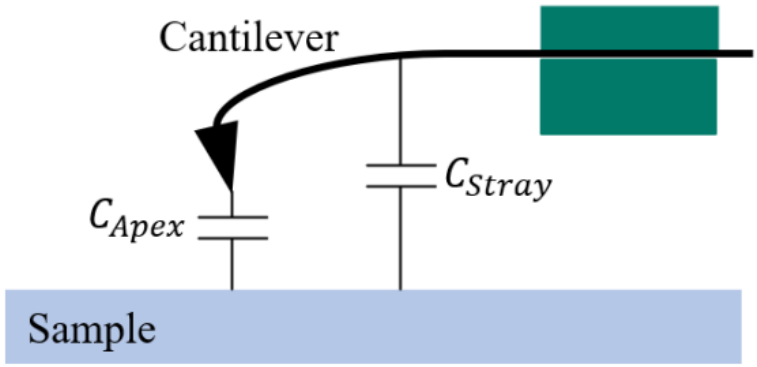


**Figure 15:** Schematic illustration of stray capacitance. Between the tip-apex and the sample are local capacitance contributions that are deliberately measured, while the tip cone and the macroscopic cantilever contribute to interfering stray capacitance.

Stray capacitances not only affect surface potential, but also its lateral resolution. The resulting surface potential is a combination of the interaction between the AFM tip apex/surface and stray capacitances. This explains why it is difficult to detect steep surface potential changes and why the lateral resolution of KPFM is limited to approximately 10 nm, which hinders our understanding of surface potential measurements at the interface of solar cells [62]. The impact of stray capacitances is more apparent in AM mode than in FM mode in KPFM, as the electrostatic force gradient decreases more quickly than the force, as it will be addressed in Chapter 2.
Measuring surface potential at different distances from the surface using two-pass KPFM can reveal the impact of stray capacitances. If surface potential values are dependent on the tip-sample distance, then it can be inferred that stray capacitances have a significant effect. To mitigate the impact of stray capacitances, KPFM software can employ internal parameters to correct the tip-sample distance. Additionally, using longer and thinner probes with a larger tip edge can positively impact stray capacitances. Furthermore, de-convolution techniques can be employed to recover surface potential without the effects of stray capacitances [63].

### 1.4.5 Thermal noise

Thermal fluctuations of the tip position are the primary source of noise in KPFM [60]. The minimum detectable difference ΔV is used to determine the sensitivity of the equipment in detecting the surface potential and it is defined as:

$$\Delta V = \frac{d}{\epsilon_0 V_{AC} R}\sqrt{\frac{2Bk_B Tk}{\pi^3 Q f_0}}, (7)$$

where $k_B$ is the Boltzmann constant, T is the temperature, k is the cantilever spring constant, B is the instrument bandwidth, Q is the cantilever quality factor, $f_0$ is the cantilever resonance frequency, d is the tip-to-sample distance, $\epsilon_0$ is the dielectric constant of the vacuum, R is the tip radius and $V_{AC}$ is the amplitude of the sinusoidal voltage applied to the tip. In ambient conditions, the quality factor Q is typically around 100, resulting in a minimum measurable variation between 10 and 50 mV. However, in ultrahigh

vacuum (UHV), Q can reach values over 1000, as the effect of air dampening is suppressed, resulting in ΔV values of couple of mVs.
To determine which signal fluctuations are detectable, it is essential to assess the noise level. For example, to achieve better contrasts in KPFM measurements of doping levels, some groups have successfully used buffer intrinsic layers between different doping steps. However, compared to c-AFM, KPFM is not the most effective tool for doping measurements, even under UHV conditions. Nonetheless, KPFM noise levels do not limit measurements on devices where illumination and electrical bias lead to surface potential changes between 100 mV and 1 V. In such cases, the signal-to-noise ratio ranges between 10 and 100, which is acceptable.
Thermal noise is the limiting factor in AM but not in FM, where the bandwidth has an offset from the first resonance frequency, and the cantilever deflection sensor is the dominant source of noise. One way to reduce the noise level on surface potential profiles is to average numerous consecutive lines, which works well when studying phenomena that occur along one scan line.
New KPFM techniques, such as G Mode KPFM, aim to eliminate noise during the acquisition process by using a low-pass filter with a high time constant. To suppress thermal noise, the best approach is to perform KPFM measurements under UHV at low temperatures. In this case, the thermal noise level reaches 1 mV and below and becomes negligible compared to other noise sources, such as electronics and the photodiode.

### 1.4.6 Limited scan speed, size, and height

SPM equipment has limitations in terms of scan size, scan height, and scan speed, which arise from the piezoelectric actuator capacities. SPM images are typically limited to an area of around 100x100 µm, and the scan height is usually restricted to about 20 µm [64]. Additionally, it generally takes approximately 20 minutes to acquire a high-resolution 5x5 $\mu m^2$ image with 512x512 pixels resolution. Scan speed is another limitation in SPM, as if it is too high, the tip cannot follow the topography, and the image quickly degrades. The degradation of the image is proportional to the increasing scan speed. Several studies in the literature focus on overcoming the scan speed limitation, primarily to achieve a video time resolution to monitor fast dynamic processes at the nanoscale, such as chemical reactions [65]. However, increasing the speed often comes at the expense of scan size due to the required increase in rigidity. Recently, some studies have demonstrated the possibility of achieving high-speed atomic force microscopy with large scan sizes in the future [66]. KPFM has also been developing toward high speed, with AM measurements achieving scan speeds of over 1 mm/s reported in the literature [67]. However, achieving high speed with UHV-KPFM is more challenging, but recent progress has shown fascinating prospects, such as heterodyne KPFM. Combining electron and scanning probe microscopy is one strategy to overcome the limitations of scan size and scan height. For instance, it is possible to conduct KPFM analysis on a smaller scan area by first identifying the areas of interest using SEM, as suggested in [68].

### 1.4.7 Effect of the surface

SPM is limited to gathering information solely from the surface of a sample. Nonetheless, surface characterization is beneficial in distinguishing surface phenomena from those in the bulk. For example, Rosen-

waks et al., [49] found that KPFM measurements under ambient conditions cannot identify defects beyond a depth of 2 nm from the surface. In contrast, KPFM under UHV can detect defects up to several tens of nanometers deep. One solution to this limitation is to perform measurements on the cross-section of the sample.
However, the strong dependence of KPFM on the surface can pose problems. Surface potential may differ from bulk potential due to surface states that affect electrostatic properties, resulting in surface band-bending (SBB) or Fermi level pinning. This effect is more pronounced in cross-sectional measurements of solar cells immediately after cleaving and can lead to signal contrast screening [69].
Dangling bonds at the top of the cross-section induce SBB, which causes the surface potential to differ from the bulk potential due to surface states affecting electrostatic properties. As a result, KPFM analysis is sensitive to how the cross-section is produced (cleaving process) and prepared (cleaning, passivation), as described in literature [62]. Humidity-induced water layer effects are known to intensify the band-bending and reduce measurement contrast. Additionally, surface potential contrast can degrade over time due to oxidation and other phenomena. Therefore, it is recommended to find a suitable surface passivation treatment that allows to obtained surface properties similar to the “bulk” ones and ideally perform measurements under UHV to reduce contamination and tip-induced oxidation over time.
Recently, a new method to prepare cross-sections in-situ using FIB milling has been proposed for KPFM analysis. This approach enables the acquisition of a 3D KPFM image by performing successive 2D images and digging into the material with FIB. However, it is assumed that FIB milling does not locally affect the electrical properties of the sample.

## 1.5 PhD Project Overview: Analyzing research achievements and insights

In this last paragraph of Chapter 1, an overview of the PhD project is presented. In particular, Kelvin probe force microscopy (KPFM) and conductive-AFM (c-AFM) techniques have been investigated for the characterization of PV materials and devices, with particular attention for cross-section analyses. In this thesis we present results on a variety of structures developed at IPVF and partner laboratories: III-V-based multilayer structures and finalized solar cells, half and fully processed perovskite solar cells, CZTGS and CIS solar cells and Silicon heterojunctions have been studied.
Among the existing PV technologies, III-V-based solar devices belong to the PV technology of thin and ultra-thin films in which layers with widths of the order of a few nm are often integrated for an optimal surface passivation or for better carrier extraction, considerably enhancing device efficiency. Consequently, the experimental demonstration of the sensitivity of the KPFM technique to the narrower layers can play a crucial role in the investigation and comprehension of the local surface properties and charge transport mechanisms at the interfaces. In particular, we have investigated an InP:S/InP:Fe and an InP:Zn/GaInAs(P):Zn multilayer structure with layers of different widths and doping concentrations. For this analysis we have set different objectives: the first objective was the evaluation of the spatial resolution of our KPFM setup in ambient conditions. The second objective was a full understanding of the contact potential difference ($V_{CPD}$) results combined with a description of the principal factors that affect KPFM measurements with the application of Kelvin Probe (KP) numerical modelling. A quantitative evaluation of the distribution of surface defects concentrations was proposed to explain the experimental $V_{CPD}$ results.

C-AFM and KPFM analysis was then continued on a p-AlGaAs:Be/n-GaInP:Si heterojunction multilayer structure and finalized solar cell. C-AFM analysis proved to be a reliable method for measuring the local resistance along a III-V based multilayer structure, enabling the identification of various layers and regions with different doping type. Nonetheless, a thorough analysis was performed to elucidate the true nature of the electrical contact between the AFM tip and the surface of the sample which resulted to be a Schottky contact. Therefore, a potential barrier will be always present at the tip/sample interface which can hinder (or facilitates) the collection of charges and in turn affect the local measured resistance.
Cross-sectional KPFM was also used to provide an explanation for the unsatisfactory PV performance of the CZTGS devices. In particular, KPFM revealed the presence of a bulky $MoS_2$ layer which acts as a barrier for an efficient collection of positive charge carriers. One issue in cross-sectional KPFM is the exact determination of the front surface of the solar cell structure, i.e. the real physical edge of the cross section. This was addressed through a study of a n-cSi/i-aSi:H/p-µc$SiO_x$ heterojunction structure where we show that a V-shape artifact can occur in the $V_{CPD}$ profile and how it can be avoided.
Finally, two further illustrations of the usefulness are given. The first one is the determination of the potential open-circuit voltage in a non-fully processed device. This has been addressed through the characterization of an unfinalized Mo-detached CIS solar cell. The second one is the tuning of work functions at interface layers for better selective charge carrier extraction. Thus, we showed how the work function of FTO can be modified by the additional $SnO_2$ and $SnO_2$/NaF layers, and also a thin layer of $Al_2O_3$ is capable of reducing the work function of the $SnO_2$ layer. This is of particular interest for improving electron collection in perovskite-based devices.

## Bibliography

[1] Parida, B.; Iniyan, S.; Goic, R. A Review of Solar Photovoltaic Technologies. *Renewable and Sustainable Energy Reviews* **2011**, *15* (3), 1625–1636. https://doi.org/10.1016/j.rser.2010.11.032
[2] Li, J.; Aierken, A.; Liu, Y.; Zhuang, Y.; Yang, X.; Mo, J. H.; Fan, R. K.; Chen, Q. Y.; Zhang, S. Y.; Huang, Y. M.; Zhang, Q. A Brief Review of High Efficiency III-V Solar Cells for Space Application. *Frontiers in Physics* **2021**, *8*. https://doi.org/10.3389/fphy.2020.631925
[3] Painter, D. S. Oil and Geopolitics: The Oil Crises of the 1970s and the Cold War. *Historical Social Research* **2014**, *39* (4), 186–208. https://doi.org/10.12759/hsr.39.2014.4.186-208
[4] Blakers, A. W.; Green M. A. *20% efficiency silicon solar cells: Applied Physics Letters **1986**, 48 (3)*. https://aip.scitation.org/doi/10.1063/1.96799
[5] El Chaar, L.; lamont, L. A.; El Zein, N. Review of Photovoltaic Technologies. *Renewable and Sustainable Energy Reviews* **2011**, *15* (5), 2165–2175. https://doi.org/10.1016/j.rser.2011.01.004
[6] Borduas, N.; Donahue, N. M. Chapter 3.1 - The Natural Atmosphere. In *Green Chemistry*; Török, B., Dransfield, T., Eds.; Elsevier, 2018; pp 131–150. https://doi.org/10.1016/B978-0-12-809270-5.00006-6
[7] Aguiar, F. C.; Bentz, J.; Silva, J. M. N.; Fonseca, A. L.; Swart, R.; Santos, F. D.; Penha-Lopes, G. Adaptation to Climate Change at Local Level in Europe: An Overview. *Environmental Science & Policy* **2018**, *86*, 38–63. https://doi.org/10.1016/j.envsci.2018.04.010
[8] Poulopoulos, S. G. Chapter 2 - Atmospheric Environment. In *Environment and Development*; Poulopoulos, S. G., Inglezakis, V. J., Eds.; Elsevier: Amsterdam, 2016; pp 45–136. https://doi.org/10.1016/B978-0-444-62733-9.00002-2
[9] Schleussner, C.-F.; Rogelj, J.; Schaeffer, M.; Lissner, T.; Licker, R.; Fischer, E. M.; Knutti, R.; Levermann, A.; Frieler, K.; Hare, W. Science and Policy Characteristics of the Paris Agreement Temperature Goal. *Nature Clim Change* **2016**, *6* (9), 827–835. https://doi.org/10.1038/nclimate3096
[10] Coburn, T. C.; Farhar, B. C. Public Reaction to Renewable Energy Sources and Systems. In *Encyclopedia of Energy*; Cleveland, C. J., Ed.; Elsevier: New York, 2004; pp 207–222. https://doi.org/10.1016/B0-12-176480-X/00462-9
[11] https://www.iea.org/data-and-statistics/charts/net-renewable-capacity-additions-by-technology-2017-2023
IntechOpen, 2020. https://doi.org/10.5772/intechopen.89494.
[12] Holechek, J. L.; Geli, H. M. E.; Sawalhah, M. N.; Valdez, R. A Global Assessment: Can Renewable Energy Replace Fossil Fuels by 2050? *Sustainability* **2022**, *14* (8), 4792. https://doi.org/10.3390/su14084792

[13] Branker, K.; Pathak, M. J. M.; Pearce, J. M. A Review of Solar Photovoltaic Levelized Cost of Electricity. *Renewable and Sustainable Energy Reviews* **2011**, *15* (9), 4470–4482. https://doi.org/10.1016/j.rser.2011.07.104
[14] Dubey, S.; Jadhav, N. Y.; Zakirova, B. Socio-Economic and Environmental Impacts of Silicon Based Photovoltaic (PV) Technologies. Energy Procedia **2013**, 33, 322–334. https://doi.org/10.1016/j.egypro.2013.05.073
[15] Kumar, M. *Social, Economic, and Environmental Impacts of Renewable Energy Resources*;
[16] Yang, Y.; Bremner, S.; Menictas, C.; Kay, M. Battery Energy Storage System Size Determination in Renewable Energy Systems: A Review. *Renewable and Sustainable Energy Reviews* **2018**, *91*, 109–125. https://doi.org/10.1016/j.rser.2018.03.047
[17] Sze, S.M. and Ng, K.K. (2006) Physics of Semiconductor Devices. 3rd Edition, John Wiley and Sons, Hoboken. https://doi.org/10.1002/0470068329
[18] Wurfel, P. and Wurfel, U. (2009) Physics of Solar Cells: From Basic Principles to Advanced Concepts. John Wiley & Sons, Hoboken
[19] Satpathy, R.; Pamuru, V. Chapter 4 - Making of Crystalline Silicon Solar Cells. In *Solar PV Power*; Satpathy, R., Pamuru, V., Eds.; Academic Press, 2021; pp 71–134. https://doi.org/10.1016/B978-0-12-817626-9.00004-6
[20] R. Kavanagh, S.; O. Scanlon, D.; Walsh, A.; Freysoldt, C. Impact of Metastable Defect Structures on Carrier Recombination in Solar Cells. *Faraday Discussions* **2022**, *239* (0), 339–356. https://doi.org/10.1039/D2FD00043A.
[21] Dev, S., Wang, Y., Kim, K. *et al.* Measurement of carrier lifetime in micron-scaled materials using resonant microwave circuits. *Nat Commun* **10**, 1625 (2019). https://doi.org/10.1038/s41467-019-09602-2
[22] Le, A.H.T., Bonilla, R.S., Black, L.E., Seif, J.P., Allen, T.G., Dumbrell, R., Samundsett, C. and Hameiri, Z. (2023), Recombination in Passivating Contacts: Investigation Into the Impact of the Contact Work Function on the Obtained Passivation. Sol. RRL, 7: 2201050. https://doi.org/10.1002/solr.202201050
[23] Du, B.; He, K.; Zhao, X.; Li, B. Defect Passivation Scheme toward High-Performance Halide Perovskite Solar Cells. *Polymers* **2023**, *15*, 2010. https://doi.org/10.3390/polym15092010
[24] McEvoy, A., Castaner, L. and Markvart, T. (2012) Solar Cells: Materials, Manufacture and Operation. 2nd Edition, Elsevier Ltd., Oxford, 3-25
[25] Cuevas, A. The Recombination Parameter J0. *Energy Procedia* **2014**, *55*, 53–62. https://doi.org/10.1016/j.egypro.2014.08.073
[26] Farah Khaleda, M. Z.; Vengadaesvaran, B.; Rahim, N. A. Chapter 18 - Spectral Response and Quantum Efficiency Evaluation of Solar Cells: A Review. In *Energy Materials*; Elsevier, 2021; pp 525–566. https://doi.org/10.1016/B978-0-12-823710-6.00014-5
[27] *https://www.pveducation.org/pvcdrom/solar-cell-operation/quantum-efficiency*
[28] Reich, N., Sark, W.V., Alsema, E.A., Kan, S.Y., Silvester, S., Heide, A., Lof, R.W., & Schropp, R.E. (2005). WEAK LIGHT PERFORMANCE AND SPECTRAL RESPONSE OF DIFFERENT SOLAR CELL TYPES.
[29] *Guide for the perplexed to the Shockley–Queisser model for solar cells | Nature Photonics*. https://www.nature.com/articles/s41566-019-0479-2
[30] S. Rühle (2016). "Tabulated values of the Shockley–Queisser limit for single junction solar cells". *Solar Energy*. **130**: 139–147.
[31] Ehrler, B.; Alarcón-Lladó, E.; Tabernig, S. W.; Veeken, T.; Garnett, E. C.; Polman, A. Photovoltaics Reaching for the Shockley–Queisser Limit. *ACS Energy Lett.* **2020**, *5* (9), 3029–3033. https://doi.org/10.1021/acsenergylett.0c01790].
[32] Bedair, S.M.; Lamorte, M.F.; Hauser, J.R. A two-junction cascade solar-cell structure. *Appl. Phys. Lett.* **1979**, *34*, 38–39.
[33] [Kant, N.; Singh, P. Review of next Generation Photovoltaic Solar Cell Technology and Comparative Materialistic Development. *Materials Today: Proceedings* **2022**, *56*, 3460–3470. https://doi.org/10.1016/j.matpr.2021.11.116.].
[34] [https://www.nrel.gov/pv/cell-efficiency.html].
[35] Anirban, A. 40 Years of Scanning Tunnelling Microscopy. *Nat Rev Phys* **2022**, *4* (5), 291–291. https://doi.org/10.1038/s42254-022-00462-2.
[36] Aabid, A.; Raheman, M. A.; Ibrahim, Y. E.; Anjum, A.; Hrairi, M.; Parveez, B.; Parveen, N.; Mohammed Zayan, J. A Systematic Review of Piezoelectric Materials and Energy Harvesters for Industrial Applications. *Sensors* **2021**, *21* (12), 4145. https://doi.org/10.3390/s21124145.
[37] Bazylewski, P.; Ezugwu, S.; Fanchini, G. A Review of Three-Dimensional Scanning Near-Field Optical Microscopy (3D-SNOM) and Its Applications in Nanoscale Light Management. *Applied Sciences* **2017**, *7* (10), 973. https://doi.org/10.3390/app7100973.
[38] Maghsoudy-Louyeh, S.; Kropf, M.; Tittmann, B. R. Review of Progress in Atomic Force Microscopy. *The Open Neuroimaging Journal* **2018**, *12* (1). https://doi.org/10.2174/1874440001812010086.
[39] Khatiwada, D.; Lamichhane, S. K. A Brief Overview of AFM Force Distance Spectroscopy. *Himalayan Physics* **2011**, *2*, 80–83. https://doi.org/10.3126/hj.v2i2.5222.
[40] Binnig, G.; Quate, C. F.; Gerber, Ch. Atomic Force Microscope. *Phys. Rev. Lett.* **1986**, *56* (9), 930–933. https://doi.org/10.1103/PhysRevLett.56.930.
[41] Martin, Y.; Williams, C. C.; Wickramasinghe, H. K. Atomic Force Microscope–Force Mapping and Profiling on a Sub 100-Å Scale. *Journal of Applied Physics* **1987**, *61* (10), 4723–4729. https://doi.org/10.1063/1.338807.
[42] Zhong, Q.; Inniss, D.; Kjoller, K.; Elings, V. B. Fractured Polymer/Silica Fiber Surface Studied by Tapping Mode Atomic Force Microscopy. *Surface Science* **1993**, *290* (1), L688–L692. https://doi.org/10.1016/0039-6028(93)90582-5.

[43] Melitz, W.; Shen, J.; Kummel, A. C.; Lee, S. Kelvin Probe Force Microscopy and Its Application. *Surface Science Reports* **2011**, *66* (1), 1–27. https://doi.org/10.1016/j.surfrep.2010.10.001.
[44] Kim, M.; Chelikowsky, J. R. CO Tip Functionalization in Subatomic Resolution Atomic Force Microscopy. *Appl. Phys. Lett.* **2015**, *107* (16), 163109. https://doi.org/10.1063/1.4934273.
[45] Hantschel, T.; Niedermann, P.; Trenkler, T.; Vandervorst, W. Highly Conductive Diamond Probes for Scanning Spreading Resistance Microscopy. *Applied Physics Letters* **2000**, *76* (12), 1603–1605. https://doi.org/10.1063/1.126109.
[46] P. De Wolf, R. Stephenson, T. Trenkler, T. Clarysse, T. Hantschel, W. Vandervorst; Status and review of two-dimensional carrier and dopant profiling using scanning probe microscopy. Journal of Vacuum Science & Technology **2000**, 18 (1): 361–368. https://doi.org/10.1116/1.591198
[47] Zhang, Z.; Hetterich, M.; Lemmer, U.; Powalla, M.; Hoelscher, H. Cross sections of operating Cu(In,Ga)Se2 thin-film solar cells under defined white light illumination analyzed by Kelvin probe force microscopy. *Applied physics letters* **2013**, *102* (2), 023903. https://doi.org/10.1063/1.4775679.
[48] Sengupta, E.; Domanski, A. L.; Weber, S. A. L.; Untch, M. B.; Butt, H.-J.; Sauermann, T.; Egelhaaf, H. J.; Berger, R. Photoinduced Degradation Studies of Organic Solar Cell Materials Using Kelvin Probe Force and Conductive Scanning Force Microscopy. *J. Phys. Chem. C* **2011**, *115* (40), 19994–20001. https://doi.org/10.1021/jp2048713.
[49] Rosenwaks, Y.; Shikler, R.; Glatzel, Th.; Sadewasser, S. Kelvin Probe Force Microscopy of Semiconductor Surface Defects. *Phys. Rev. B* **2004**, *70* (8), 085320. https://doi.org/10.1103/PhysRevB.70.085320.
[50] Narchi, P.; Alvarez, J.; Chrétien, P.; Picardi, G.; Cariou, R.; Foldyna, M.; Prod'homme, P.; Kleider, J.-P.; i Cabarrocas, P. R. Cross-Sectional Investigations on Epitaxial Silicon Solar Cells by Kelvin and Conducting Probe Atomic Force Microscopy: Effect of Illumination. *Nanoscale Res Lett* **2016**, *11*, 55. https://doi.org/10.1186/s11671-016-1268-1.
[51] Palermo, V.; Palma, M.; Samorì, P. Electronic Characterization of Organic Thin Films by Kelvin Probe Force Microscopy. *Advanced Materials* **2006**, *18* (2), 145–164. https://doi.org/10.1002/adma.200501394.
[52] Collins, L.; Jesse, S.; Kilpatrick, J. I.; Tselev, A.; Okatan, M. B.; Kalinin, S. V.; Rodriguez, B. J. Kelvin Probe Force Microscopy in Liquid Using Electrochemical Force Microscopy. *Beilstein J. Nanotechnol.* **2015**, *6* (1), 201–214. https://doi.org/10.3762/bjnano.6.19.
[53] Flores, S. M.; Toca-Herrera, J. L. The New Future of Scanning Probe Microscopy: Combining Atomic Force Microscopy with Other Surface-Sensitive Techniques, Optical Microscopy and Fluorescence Techniques. *Nanoscale* **2009**, *1* (1), 40–49. https://doi.org/10.1039/B9NR00156E.
[54] Watanabe, S.; Fukuchi, Y.; Fukasawa, M.; Sassa, T.; Kimoto, A.; Tajima, Y.; Uchiyama, M.; Yamashita, T.; Matsumoto, M.; Aoyama, T. In Situ KPFM Imaging of Local Photovoltaic Characteristics of Structured Organic Photovoltaic Devices. *ACS Appl Mater Interfaces* **2014**, *6* (3), 1481–1487. https://doi.org/10.1021/am4038992.
[55] Strelcov, E.; Yang, S. M.; Jesse, S.; Balke, N.; Vasudevan, R. K.; Kalinin, S. V. Solid-State Electrochemistry on the Nanometer and Atomic Scales: The Scanning Probe Microscopy Approach. *Nanoscale* **2016**, *8* (29), 13838–13858. https://doi.org/10.1039/C6NR01524G.
[56] Borowik, Ł.; Lepage, H.; Chevalier, N.; Mariolle, D.; Renault, O. Measuring the Lifetime of Silicon Nanocrystal Solar Cell Photo-Carriers by Using Kelvin Probe Force Microscopy and x-Ray Photoelectron Spectroscopy. *Nanotechnology* **2014**, *25* (26), 265703. https://doi.org/10.1088/0957-4484/25/26/265703.
[57] Masaki Takihara, Takuji Takahashi, Toru Ujihara; Minority carrier lifetime in polycrystalline silicon solar cells studied by photoassisted Kelvin probe force microscopy. *Appl. Phys. Lett.* 14 July 2008; 93 (2): 021902. https://doi.org/10.1063/1.2957468
[58] Sugimura, H.; Ishida, Y.; Hayashi, K.; Takai, O.; Nakagiri, N. Potential Shielding by the Surface Water Layer in Kelvin Probe Force Microscopy. *Applied Physics Letters* **2002**, *80* (8), 1459–1461. https://doi.org/10.1063/1.1455145.
[59] Houzé, F.; Meyer, R.; Schneegans, O.; Boyer, L. Imaging the Local Electrical Properties of Metal Surfaces by Atomic Force Microscopy with Conducting Probes. *Applied Physics Letters* **1996**, *69* (13), 1975–1977. https://doi.org/10.1063/1.117179.
[60] Kronik, L.; Shapira, Y. Surface Photovoltage Phenomena: Theory, Experiment, and Applications. *Surface Science Reports* **1999**, *37*, 1–206. https://doi.org/10.1016/S0167-5729(99)00002-3.
[61] H. Diesinger, D. Deresmes, and T. Mélin, "Capacitive Crosstalk in AM-Mode KPFM," Chapter 3 in Kelvin Probe Force Microscopy, S. Sadewasser and T. Glatzel, Eds. Springer Berlin Heidelberg, 2012, pp. 25–44.
[62] Glatzel, Th.; Steigert, H.; Sadewasser, S.; Klenk, R.; Lux-Steiner, M. Ch. Potential Distribution of Cu(In,Ga)(S,Se)2-Solar Cell Cross-Sections Measured by Kelvin Probe Force Microscopy. *Thin Solid Films* **2005**, *480–481*, 177–182. https://doi.org/10.1016/j.tsf.2004.11.065.
[63] Machleidt, T.; Sparrer, E.; Kapusi, D.; Franke, K.-H. Deconvolution of Kelvin Probe Force Microscopy Measurements—Methodology and Application. *Meas. Sci. Technol.* **2009**, *20* (8), 084017. https://doi.org/10.1088/0957-0233/20/8/084017.
[64] J. T. Heath, C. -S. Jiang and M. M. Al-Jassim, "Diffused junctions in multicrystalline silicon solar cells studied by complementary scanning probe microscopy and scanning electron microscopy techniques," *2010 35th IEEE Photovoltaic Specialists Conference*, Honolulu, HI, USA, 2010, pp. 000227-000232, https://doi.org/10.1109/PVSC.2010.5614484.
[65] Ando, T. High-Speed Atomic Force Microscopy Coming of Age. *Nanotechnology* **2012**, *23* (6), 062001. https://doi.org/10.1088/0957-4484/23/6/062001.
[66] Soltani Bozchalooi, I.; Careaga Houck, A.; AlGhamdi, J. M.; Youcef-Toumi, K. Design and Control of Multi-Actuated Atomic Force Microscope for Large-Range and High-Speed Imaging. *Ultramicroscopy* **2016**, *160*, 213–224. https://doi.org/10.1016/j.ultramic.2015.10.016.

[67] Sinensky, A. K.; Belcher, A. M. Label-Free and High-Resolution Protein/DNA Nanoarray Analysis Using Kelvin Probe Force Microscopy. *Nat Nanotechnol* **2007**, *2* (10), 653–659. https://doi.org/10.1038/nnano.2007.293.
[68] Anspach, N.; Hitzel, F.; Zhou, F.; Eyhusen, S. Hybrid SEM/AFM System from Carl Zeiss Revolutionizes Analysis of Functional Micro- and Nanostructured Specimen. *Microsc Microanal* **2014**, *20* (S3), 992–993. https://doi.org/10.1017/S1431927614006680.
[69] Kikukawa, A.; Hosaka, S.; Imura, R. Silicon Pn Junction Imaging and Characterizations Using Sensitivity Enhanced Kelvin Probe Force Microscopy. *Applied Physics Letters* **1995**, *66* (25), 3510–3512. https://doi.org/10.1063/1.113780.

# Chapter 2

# Methods

This chapter presents a thorough analysis of the underlying principles and experimental methodologies employed in the application of Kelvin Probe Force Microscopy (KPFM) and Conductive Atomic Force Microscopy (c-AFM) techniques throughout the course of the PhD thesis. The primary focus is to provide an in-depth understanding of these techniques, their underlying principles, and the step-by-step procedures implemented for data acquisition. Furthermore, a section will be devoted to describing the modeling tool utilized to assist in the interpretation of KPFM data.

## 2.1 Unveiling the essentials: an introduction to the principles of Kelvin Probe Force Microscopy

Kelvin probe force microscopy (KPFM) is an electrical extension of the AFM for the evaluation of surface potential with a nanometric resolution. KPFM is a valuable investigative approach for the study of work functions (WFs) via the measurement of the contact potential difference ($V_{CPD}$), i.e., the difference between the electrostatic potential at the surface of the investigated structure and that of the KPFM nano-sized probe.

In 1991, Nonnenmacher et al. [1] introduced the KPFM technique showing for the first-time measurements of $V_{CPD}$ between different materials using scanning force microscopy which built upon the principles of Kelvin Probe measurement established almost a century earlier by Lord Kelvin in 1898 [2].

Between these two milestones, in 1932, Zisman pioneered a novel approach to evaluate contact potential differences among different metallic materials, thus establishing a foundation for the contemporary KPFM technique, bridging the gap between the conceptualization of the Kelvin probe principle and the advent of the initial KPFM instrument [3]. The method was based on the response of the electrometer deflection as a function of the voltage applied to the tip ($V_{DC}$) to find the zero force on the tip, meaning that $V_{DC}$ equals the potential difference between the probe and the sample. Zisman used a vibrating metal plate to have continuous measurements of the potential difference. This technique enabled measurement with a resolution down to mm size.

The essence of the principles behind Kelvin probe measurement can be understood following the energy diagrams of the sample and the probe shown in Figure 1 [4].

The tip and the sample are characterized by work functions $\Phi_t$ and $\Phi_S$, respectively, which are defined as the difference between the vacuum level and the Fermi level. When the probe and the sample are far from each other and isolated, their Fermi levels are different, but the vacuum levels are the same.

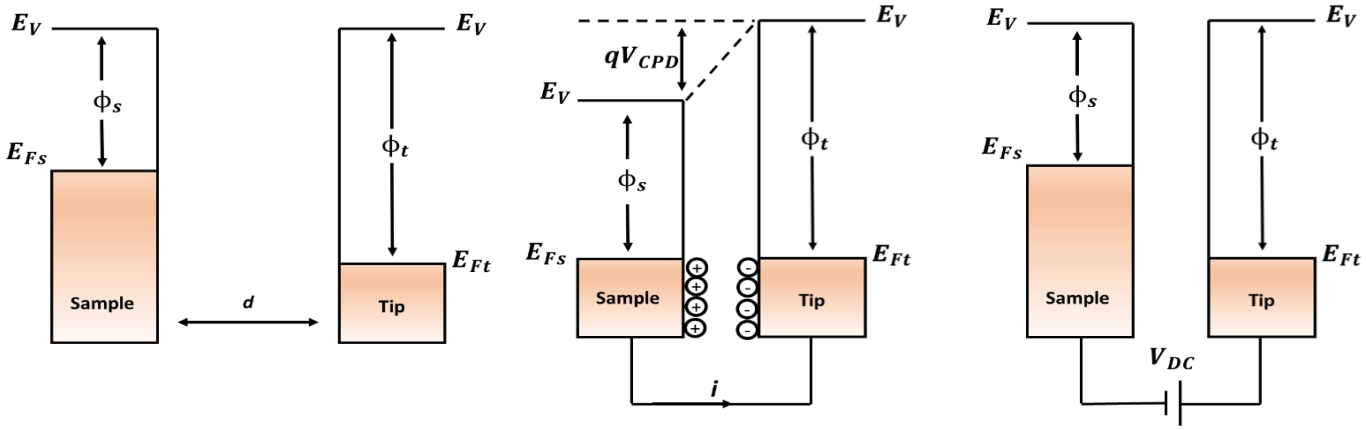


**Figure 1:** The electronic energy levels of an AFM tip and a sample can be analyzed in three different cases. In the first case, the tip and the sample are separated by a distance d without any electrical contact. In the second case, direct electrical contact is established. In the third case, an external bias ($V_{DC}$) is applied between the tip and sample to cancel out the contact potential difference ($V_{CPD}$) and nullify the tip-sample electrical force. The vacuum energy level is represented by $E_V$, while $E_{Fs}$ and $E_{Ft}$ denote the Fermi energy levels of the sample and the tip, respectively.

When the probe and the sample are connected, a current flow can establish between the sample and the tip to reach equilibrium. This aligns the Fermi levels and results in a distortion of the vacuum level reflecting the appearance of an electrostatic potential difference, called the contact potential difference at equilibrium, and denoted $V_{CPD,eq}$. At equilibrium, we thus have:

$$q(V_S - V_t)_{eq} = qV_{CPD,eq} = \phi_t - \phi_S, \quad (1)$$

with $q$ being the absolute value of the electron charge.
The electrostatic potential difference (vacuum level distortion) can be adjusted by applying an external electrical DC bias, that is by imposing an electrochemical potential difference $V_{DC} = (\phi_t - \phi_S)$ between the tip and the sample:

$$q(V_S - V_t) = (\phi_t - \phi_S) - q(\varphi_t - \varphi_S) = (\phi_t - \phi_S) - qV_{DC}, \quad (2)$$

until it is nullified, which thus leads to $V_{DC} = V_{CPD,eq}$. The WF difference is then directly obtained from this DC voltage.
In a traditional Kelvin probe, the tip oscillates, it generates a changing electric field that induces a displacement current between the tip and the sample that constitutes the monitoring signal. When the current is zero, it indicates that the vacuum levels are aligned, and that the applied electrical bias equals $V_{CPD,eq}$.
However, in KPFM the monitoring signal is either the amplitude modulation (AM mode) or the frequency modulation (FM mode).

## 2.1.1 Amplitude modulation KPFM (AM-KPFM)

KPFM measurements are generally performed in two-pass scanning mode in which topographical data are collected on the first pass whereas $V_{CPD}$ is evaluated during the second one. During the second pass, the tip is lifted above a predefined height (from a few nanometers to tens of nanometers) and a bias voltage is applied between the tip and the sample:

$$V_{bias} = V_{DC} + V_{AC}\ sin\ sin\ \omega_{el}t\ , (3)$$

$V_{AC}$ generates oscillating electrical forces between the AFM tip and sample surface, and $V_{DC}$ nullifies the oscillating electrical forces that originated from $V_{CPD}$ between tip and sample surface. Note that the response is tracked by a lock-in amplifier (see Figure 12 in Chapter 1). The frequency of the electrical excitation $\omega_{el}$ is usually matched to the eigenfrequency $\omega_0$ of the cantilever to achieve higher sensitivity.
When the tip is approached to the surface, an electrical force is generated between the tip and the sample and since in most cases at least the tip or the sample are conductive, a mirror charge with opposite sign builds up on either side.
Since the tip-sample system can be approximated to a capacitor, the electrical force ($F_{el}$) can be expressed as follows:

$$F_{el} = \frac{1}{2}\frac{\partial C}{\partial z}(\Delta V)^2, (4)$$

In a standard KPFM measurement, the sample is grounded and $\Delta V$, which is defined as:

$$\Delta V = (V_{DC} + V_{CPD}) + V_{AC}\ sin\ sin\ \omega_{el}t, (5)$$

is the potential difference between $V_{CPD}$ and the voltage applied to the AFM tip. Under these conditions, $F_{el}$ can be divided into three spectral components:

$$F_{DC} = \frac{1}{2}\frac{\partial C(z)}{\partial z}\left[(V_{DC} - V_{CPD})^2 + \frac{V_{AC}^2}{2}\right], (6)$$

$$F_{\omega_{el}} = \frac{\partial C(z)}{\partial z}(V_{DC} - V_{CPD})V_{AC}sin(\omega_{el}t), (7)$$

$$F_{2\omega_{el}} = -\frac{\partial C(z)}{\partial z}\frac{1}{4}V_{AC}^2\ cos\ cos\ (2\omega_{el}t), \quad (8)$$

The electrostatic force $F_{\omega_{el}}$ drives the cantilever into oscillation. In order to measure $V_{CPD}$ the Kelvin controller adjusts $V_{DC}$ until the electrostatic force $F_{\omega_{el}}$ is canceled out. This is achieved when $V_{DC} - V_{CPD} = 0$. According to Eq. (1), the local work function of the sample can be evaluated if the one of the tip is known. It is important to mention that for absolute work function measurements operation under UHV conditions is mandatory [5]. This is because ambient conditions promote the oxidation of the surface, the adsorption of water molecules on the surface coming from the humidity in air and the possible presence of nanoparticles of dust [6]. These aspects together may lead to surface inhomogeneities which locally affect $V_{CPD}$ and result in variations in otherwise constant surface physical properties.
Additionally, it is worth to mention that $F_{DC}$ (Eq. 6) results in a static deflection of the AFM tip and thus it contributes to the topography signal, and finally $F_{2\omega_{el}}$ (Eq. 8) can be used for capacitance microscopy.

The lift is an important parameter in AM-KPFM, as it determines the spatial resolution of the measurement and the sensitivity of the technique. In general, a smaller lift corresponds to a higher spatial resolution and a greater sensitivity to the surface properties, as the tip is able to probe the sample more closely. However, the lift also determines the range of electric potentials that can be measured, as the electric potential difference between the tip and the sample must be large enough to produce a measurable cantilever deflection.

AM-KPFM is generally likely to introduce artifacts into the measured $V_{CPD}$ maps [5]. One of the most studied and widely reported in literature artifacts in AM-KPFM is the presence of parasitic capacitances between the sample and the cantilever due to their conductive nature. Parasitic capacitances directly affect the estimation of the $V_{CPD}$ since, as expressed in Eq. 7, the amplitude of the electrostatic force is proportional to the capacitance gradient.

For many commercially available AFM tips, the large surface area of the tip body and the cantilever yields a significant contribution to the capacitance, even at relatively low tip/sample distance of a few nanometers. This capacitive artifact can affect the measured signal in several ways. For instance, as the cantilever oscillates, the parasitic capacitance will vary, leading to a modulation of the cantilever oscillation amplitude, (as it was described in paragraph 1.4.4).

One possible approach to reduce the effect of long-ranged electrostatic interactions between the sample and the cantilever is to use force gradient detection: FM-KPFM.

### 2.1.2 Frequency modulation KPFM (FM-KPFM)

FM-KPFM mode exploits the presence of a force field between the tip and the sample, $F_{ts}(z)$. This causes a shift in the angular resonance frequency $\omega_0$ of the cantilever which will cause the cantilever to oscillate to a new modified angular resonance frequency $\omega_0'$ which is proportional to the derivative of $F_{ts}(z)$ with respect to the z position. Therefore, instead of modulating the oscillation amplitude of the cantilever, FM-KPFM modulates the oscillation frequency of the cantilever.

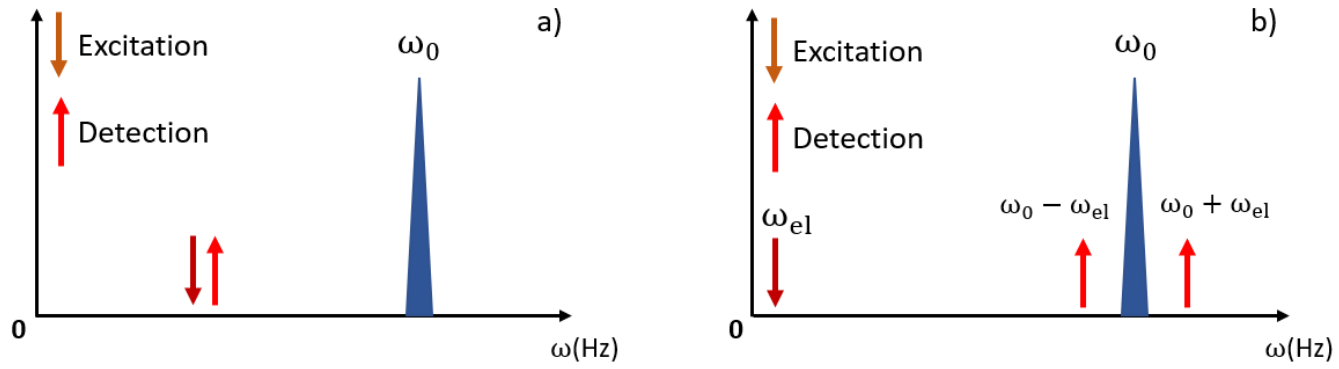


**Figure 2:** Frequency spectra for a) AM-KPFM and b) FM-KPFM.

In particular, for small oscillation amplitudes $\omega_0'$ can be described by an effective spring constant $k_{eff} = k - \frac{\partial F_{ts}}{\partial z}$ and thus $\omega_0' = \left[\frac{1}{2\left(k-\frac{\partial F_{ts}}{\partial z}\right)}\right]^{1/2}$. It follows that $V_{AC}$ is responsible of generating periodic fluctuations in $F_{el}$ (Eq. 7), and additionally in the frequency of resonance. The magnitude of this frequency modulation is proportional to the electrical force gradient $\nabla F_{el}$ and thus to the second derivative of the tip-sample

system capacitance $\frac{\partial^2 C}{\partial z^2}$. As a consequence of this frequency modulation, sidebands appear at $\omega_0 \pm \omega_{el}$ in the frequency spectrum of the cantilever deflection, as shown in Figure 2.
The application of a $V_{DC}$ value that matches with $V_{CPD}$ between the tip and the sample compensates for the electrostatic force and the sidebands disappear. Similarly to AM-KPFM, $V_{CPD}$ is measured by adjusting $V_{DC}$ to nullify $\nabla F_{el}$. It results that the FM mode is more sensitive to the electrostatic interaction between the apex of the tip and the sample surface mitigating the effect of cantilever parasitic capacitances.
FM-KPFM generally uses a two lock-in amplifier system. In particular, the first lock-in is used to mechanically excite the cantilever by the piezo, while the second lock-in generates the electrical excitation $V_{AC}$. The resulting modulation of the cantilever oscillation is detected on the first lock-in amplifier and the phase, or the resulting frequency shift, is demodulated on the second lock-in using a phase locked loop.
Borgani et al., [7] showed that the electrostatic frequency modulation can be detected by using a nonlinear frequency mixing with a mechanical cantilever oscillation at angular frequency $\omega_m$, e.g., the tapping oscillation used for the height feedback.
The capacitance gradient decreases monotonically with the distance of the tip from the surface, and it will also oscillate with frequency $\omega_m$. The capacitance gradient can be written as a Fourier series:

$$\frac{\partial C}{\partial z}(t) = \frac{a_0}{2} + \sum_{n=1}^{\infty} a_n cos(n\omega_m t)\,, (9)$$

and therefore, Eq. 4 can be expressed as:

$$F_{el} = \sum_{n=0}^{\infty} a_n\, cos(n\omega_m t)\{\left[\frac{(V_{DC}-V_{CPD})^2}{2} + \frac{V_{AC}^2}{2}\right] + [(V_{DC} - V_{CPD})V_{AC} sin(\omega_{el} t)] - \left[\frac{1}{4} V_{AC}^2\, cos(2\omega_{el} t)\right]\}, (10)$$

Considering Fourier coefficients just up $n = 1$, it is possible to separate the electrostatic force in its spectral components:

$$F_{\omega_{el}} = \frac{a_0}{2}(V_{DC} - V_{CPD})V_{AC} sin(\omega_{el} t), (11)$$

$$F_{2\omega_{el}} = \frac{a_0}{8} V_{AC}^2 cos(2\omega_{el} t), (12)$$

$$F_{\omega_m \pm \omega_{el}} = \frac{a_1}{2}(V_{DC} - V_{CPD})V_{AC}[sin((\omega_{el} - \omega_m)t) + sin\ sin\ ((\omega_{el} + \omega_m)t)], (13)$$

$$F_{\omega_m \pm 2\omega_{el}} = -\frac{a_1}{8} V_{AC}^2 [cos((2\omega_{el} - \omega_m)t) + sin\ sin\ ((2\omega_{el} + \omega_m)t)], (14)$$

Eqs. 11 and 12 are the FM equivalent to Eqs. 7 and 8 for AM-KPFM. Note that the Fourier coefficient $a_0$ can be correlated to the capacitance gradient as $a_0 = \frac{2\partial^2 C}{\partial z^2}$.
Eqs. 13 and 14 show that the electrostatic force signal can be detected at the sidebands. Eq. 13 is the fundamental equation that describes FM-KPFM since it contains $V_{DC} - V_{CPD}$ and it is the equivalent of Eq. 7 in analogy to Eq. 11.
FM-KPFM presents enhanced lateral resolution with respect to AM-KPFM since the $\frac{\partial^2 C}{\partial z^2}$ is more sensitive to local tip-apex/surface interactions.

However, the force signal (AM) is stronger than the force gradient signal and therefore higher $V_{AC}$ amplitudes are generally required, and this can introduce new artifacts, for instance local band-bending in case of semiconductor samples [8].
As already mentioned, one advantage of FM-KPFM over AM-KPFM is that it is less sensitive to artifacts due to parasitic capacitance between the sample and the cantilever.
In FM-KPFM, the parasitic capacitance does not significantly affect the oscillation frequency, so it does not introduce artifacts into the measured signal.
FM-KPFM has an additional benefit of being less susceptible to noise and errors arising from other sources. This is because the oscillation frequency is significantly higher than the amplitude of oscillation, leading to a more precise measurement of the electric potential.
A schematic of the scanning probe microscopy system from AIST-NT (TRIOS platform) used for KPFM analysis during the PhD is described in Figure 3.

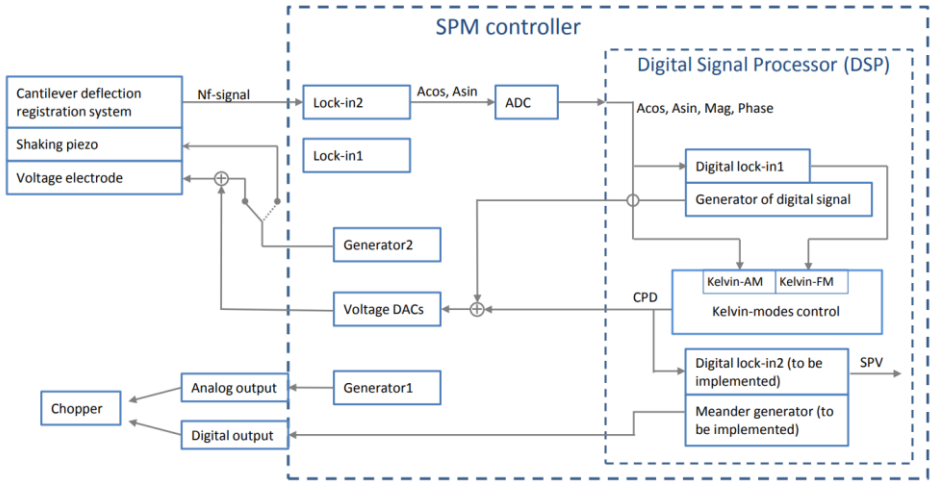


**Figure 3:** Scanning probe microscopy system from AIST-NT (TRIOS platform) which allows to perform KPFM analysis in AM and FM mode.

## 2.2 Setting the stage: the experimental setup of Kelvin Probe Force Microscopy

KPFM measurements were performed using a HORIBA/AIST-NT (TRIOS platform) scanning probe microscopy system. The TRIOS platform (Figure 4) combines AFM with a series of AFM electrical extensions to perform a range of different scanning probe characterizations, e.g., Magnetic Force Microscopy (MFM), Electric Force Microscopy (EFM), PiezoResponse Force Microscopy (PRFM), KPFM and c-AFM. The TRIOS platform works both in contact and non-contact mode based on the chosen technique. Prior to analysis, the AFM tip and the sample must be placed in the probe holder and sample stage, respectively. An image of the probe holder is reported in Figure 5.
The tip is kept in place by a metallic probe spring clip. The tip positioning is really important since in the case the tip resulted to be crooked, image artifacts may happen during analysis.

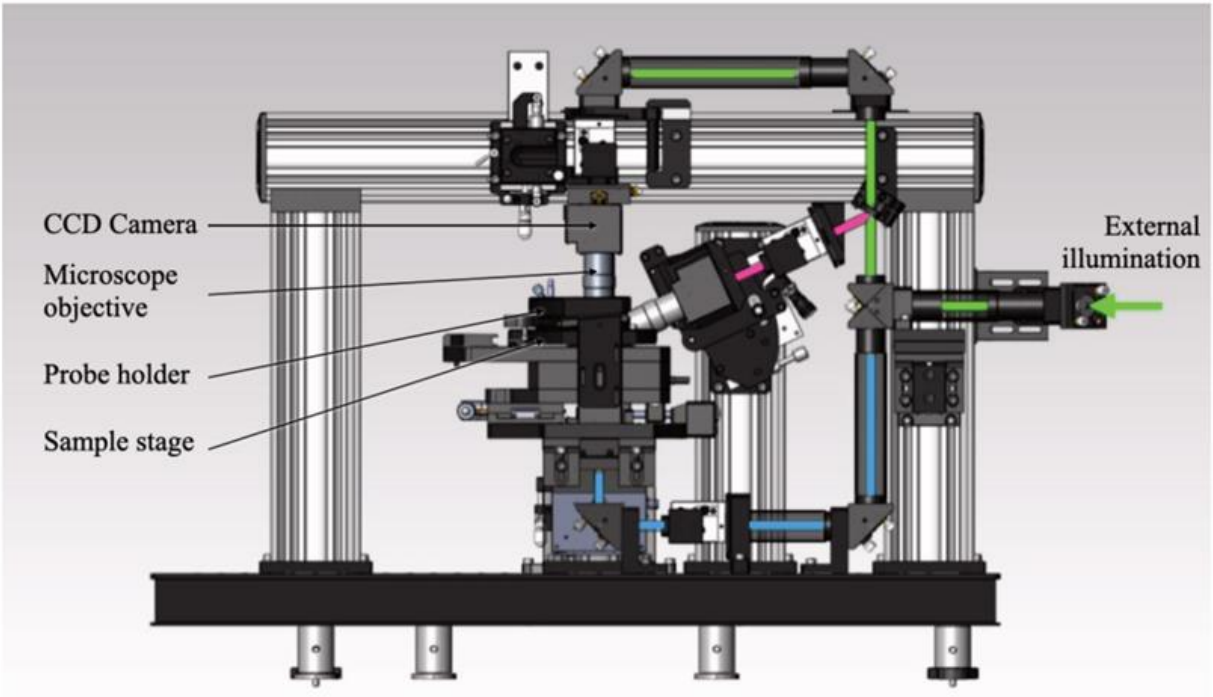


**Figure 4**: Schematic of the TRIOS platform.

In particular, for KPFM characterization, ARROW-EFM Pt/Ir coated high-doped n-type single crystal silicon tips were used. The tips are provided from NanoWorld and present a tip-apex radius below 25 nm, resonance frequency at 75 kHz, force constant of 2.8 N/m and the cantilever is 240 µm long.
In order to ease the sample position, the TRIOS platform is provided with a CCD camera which acts like an optical microscope. Based on necessity, it is possible to choose objectives with different magnification: x25, x50 and x100.
Once the sample and tip are properly placed, the tip is approached to the sample surface and the measurements can be performed.
As already mentioned in paragraph 1.4.1, the TRIOS platform allows to guarantee "dark" conditions during the measurements thanks to its peculiar laser-based cantilever deflection system that uses a 1310 nm photodiode minimizing parasitic absorption in the analyzed semiconductor samples that may occur with a laser at lower wavelengths. This is because the wavelength at 1310 nm is generally well below the bandgap of the semiconductor samples analyzed during the thesis and therefore the parasitic laser absorption, which may interfere with the KPFM measurement, is reduced to negligible levels [9]. Nonetheless, KPFM analysis under illumination represents an important experimental value since it allows to perform surface photovoltage analysis (as it will be defined in section 2.3.1) or studying a solar cell under operating conditions. For this reason, in the TRIOS platform, a system of mirrors is included in the setup enabling it to perform measurements under illumination through external lasers. The sample can be illuminated with one or two lasers at the same time. The illumination is provided by optical fibers, and it is possible to change the optical path to illuminate the sample from different directions: from the top (green), from the side (pink) and from the bottom (blue), as shown in Figure 4. The beam is then focused on the sample by an objective.

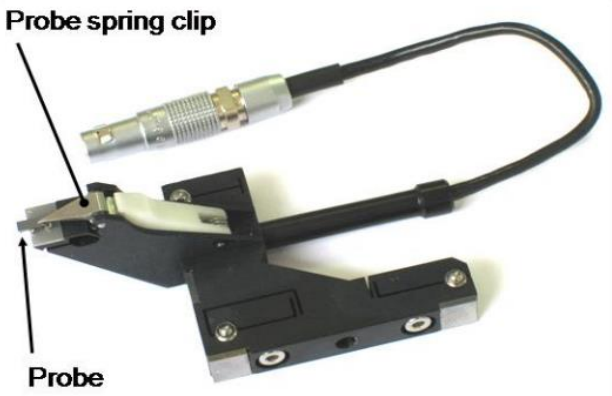


**Figure 5**: Image of the probe holder with a typical AFM probe placed in position.

It is important to note that the power of the laser reaching the sample is attenuated with respect to the value that is set directly on the source. This is directly related to the optical path between the laser source and the sample in addition to the CCD camera that behaves itself as a filter. For this reason, to evaluate the real power illumination reaching the sample, additional power measurements must be done by using a power meter. Several lasers from Oxxius with different wavelengths have been used during the realization of the PhD thesis based on the energy gap of the analyzed semiconductor sample, namely 980 nm, 785 nm, 532 nm, and 488 nm.

KPFM is an electrical measurement and thus it is important to properly ground the sample. This is generally achieved with a metallic clip which is connected to the KPFM ground. Generally, the ground is taken from a conductive layer in the sample that will represent the reference frame. For instance, consider a simple structure formed by a stack of an FTO layer and a $SnO_2$ layer deposited on a glass substrate, as in the study that will be shown in section 5.2. To investigate the impact of the $SnO_2$ layer on $V_{CPD}$ in comparison to the bare FTO, a two-step characterization is essential. Firstly, one needs to characterize a reference sample consisting solely of the bare FTO layer (Figure 6, left). Subsequently, the same analysis can be performed on the sample containing the $SnO_2$ layer while maintaining grounded the FTO layer (Figure 6, right). A schematic representation of this setup is provided in Figure 6 where the green rectangle represents the FTO and the orange one the $SnO_2$ layers, respectively.

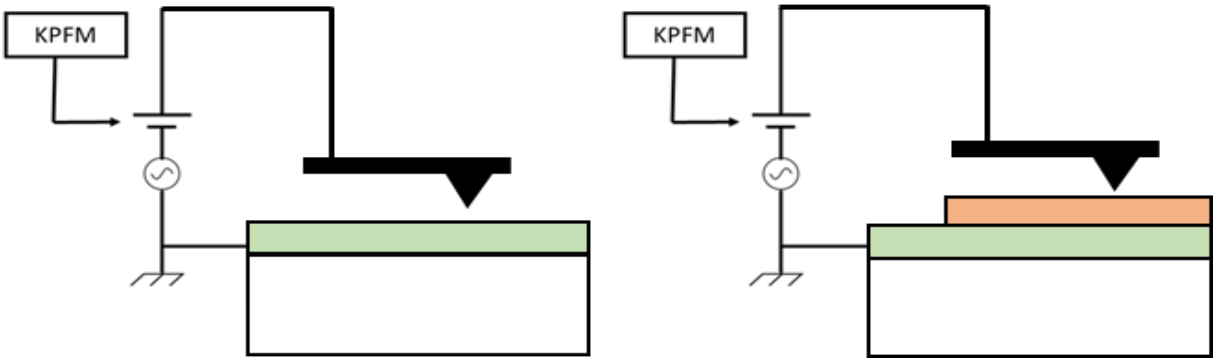


**Figure 6:** Schematic of the KPFM experimental setup and the role of the electrical ground. Specifically, the ground is taken from a conductive layer in the sample that will represent the reference frame. Here, the green rectangle represents the FTO and the orange one the $SnO_2$ layers, respectively. In the image on the right, the $V_{CPD}$ measured on the $SnO_2$ layer will be referenced to the FTO layer.

In the experimental configuration shown in Figure 6 (right), the $V_{CPD}$ measured on the $SnO_2$ layer will be referenced to the FTO layer.
Finally, when it comes to solar cell analysis, the ground is generally taken from the back contact. In order to provide operando analysis of the solar device, we generally also externally connect the back and front contact to a sourcemeter (Keithley 2400) which enable in situ monitoring of the solar cell through I-V analysis, as shown in Figure 7 which refers to the analysis of a n-cSi/i-aSi:H/p-µcSiO$_x$ heterojunction which will be described in section 4.3.

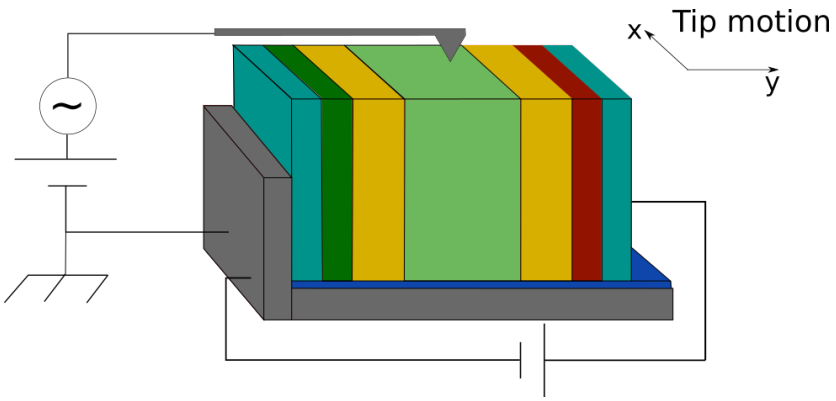


**Figure 7:** Schematic of the KPFM and sample setup for cross-sectional analysis. The light green, yellow and brown rectangles refer to the n-cSi/i-aSi:H/p-µcSiO$_x$ layers, respectively, whereas the light blue rectangles represents ITO.

If the experiment is set up correctly, it is also possible to apply an external bias evaluating the surface potential under real operating conditions in the form of external applied biases and illumination.

## 2.3 Methodical approaches: a close examination of the experimental procedure for KPFM

The following paragraphs outline the experimental procedures employed throughout the entirety of this PhD thesis, serving as a standardized approach applicable to both planar and cross-sectional measurements.

### 2.3.1 Kelvin Probe Force Microscopy standard characterization

KPFM is performed using the scanning probe microscopy system from AIST-NT (TRIOS platform) presented in the previous chapter. Our KPFM operates in ambient conditions, and it is generally used in frequency modulation (FM-KPFM) using a two-pass scanning mode where the second pass is preferably performed at a constant distance of 10 nm from the sample surface: topographical data are collected on the first pass whereas $V_{CPD}$ is evaluated during the second one. It is important to mention that the lift is a tunable parameter. A lift of 10 nm is generally used for samples that present a flat surface, otherwise, for samples that are characterized by rougher surface, a lift up to 30 nm can be selected.
In line with the specifications outlined in paragraph 2.2, the TRIOS system enables illumination from three distinct positions. Nonetheless, the primary emphasis was placed on utilizing top illumination as the main approach, while lateral illumination was additionally employed specifically for the analysis of finalized solar cells. The schematic of our KPFM setup is depicted in Figure 8.

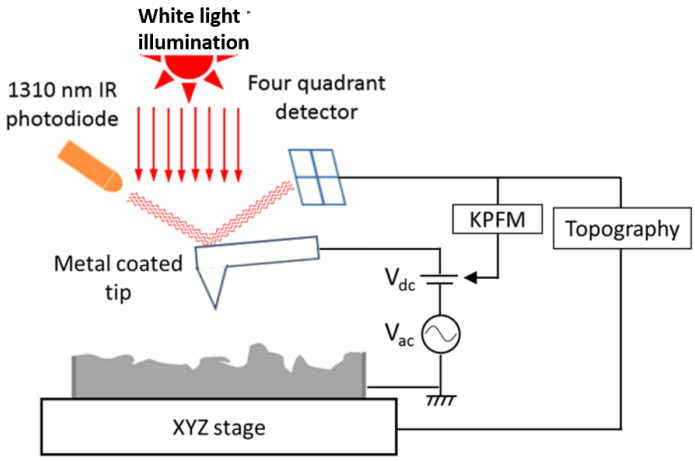


**Figure 8:** Schematic diagram of the KPFM system. While a $V_{AC}$ + $V_{DC}$ voltage is applied, the KPFM tip scans across a surface. The $V_{AC}$ signal is sinusoidal with a frequency that equals the mechanical resonance of the cantilever. The four-quadrant detector gives feedback in order to minimize cantilever oscillation modifying the $V_{DC}$ signal providing the sample surface potential relative to that of the tip.

We have generally always privileged FM-KPFM mode over the amplitude modulation mode (AM-KPFM) since, as already described, FM-KPFM is more sensitive to local tip apex/sample surface interactions and therefore the long-range electrostatic interactions of the cantilever are reduced as well as the effect of parasitic capacitances [5]. Additionally, in FM-KPFM surface potential measurements are less dependent on the lift-height tip/sample distance than in AM-KPFM since this mode results to be less sensitive to static offsets induced by capacitive coupling or crosstalk [10].
KPFM measurements have been performed in ambient conditions and thus the sensitivity of the measured $V_{CPD}$ is ± 20 mV. During ambient conditions KPFM measurements, tip contamination is likely to occur due to the pollutants which may be present on the sample surface causing a variation of $\phi_{tip}$ [11]. For this reason, it is a good practice to evaluate periodically $\phi_{tip}$ in the course of the analysis using Eq. 1 by measuring the $V_{CPD}$ value of a freshly exfoliated surface of highly ordered pyrolytic graphite (HOPG) [12]. In order to be able to compare KPFM data acquired scan after scan, it is important that the successively measured $\phi_{tip}$ values show negligible variations.
As a general rule, in order to perform successful KPFM measurements, a low surface roughness is essential to obtain high-quality images since surface inhomogeneities can cause a topographical image imprint on the potential image. Furthermore, other factors, including the presence of electrically active surface defects, the experimental measurement environment, and the AFM probe operating conditions, can affect KPFM measurements [9,13], as it will be explained in Chapter 3.
During the course of the PhD, KPFM measurements were performed in dark conditions and under illumination with the samples being in planar or cross-sectional configuration. The acquisition of the contact potential difference under illumination $V_{CPD/light}$, enables the evaluation of the surface photovoltage (SPV), which is defined as the light-induced change of the surface potential of a photoactive material [20]. Since the surface potential of the tip is assumed to be unaffected by illumination, the difference between $V_{CPD/light}$ and the $V_{CPD}$ value in the dark, $V_{CPD/dark}$, is equal to the change in surface potential of the sample between illumination and dark, so that the surface photovoltage is obtained from this difference:

$$SPV = V_{CPD/light} - V_{CPD/dark}, (15).$$

It is important to mention that although KPFM is primarily a surface technique, the SPV can be sensitive to the presence of buried interfaces and/or deep charge trap states that may be present far from the surface in the bulk of semiconductors. For this reason, we did not use only the laser illumination described in paragraph 2.2. In particular, the white light coming from the camera connected to the microscope has also been used for top illumination. This is because the white light wavelength range is between 400 nm and 700 nm and for these wavelengths, for instance, the penetration depth in III-V based materials generally ranges between 10 and 100 nm. This makes our measurements mainly sensitive to the surface states and surface band-bending. Additionally, a uniform illumination of the cross-section is achieved thanks to the wide light spot.

The power density of the white light at maximum power is 750 $Wm^{-2}$ as it was measured by a thermal power sensor S401C from Thorlabs which has a flat spectral response in the white light range of wavelengths. This relatively low power density allows to minimize the Dember effect since its contribution becomes significant only in high injection conditions [14]. This procedure was utilized for the characterization of III-V multilayer structures, which will be presented in Chapter 3.

### 2.3.2 Exploring surface potential variations across the interfaces with cross-sectional KPFM analysis

The cross-section of a device provides a 2D view of the layers and interfaces within the device, which cannot be obtained from top-view measurements alone. By analyzing the cross-section, it is possible to obtain detailed information about the electronic properties and device performance, including, for instance, charge carrier distribution, mobility, and recombination rates [15].

In particular, in a solar cell, cross-sectional analysis allows investigating the interface between the different layers of the device, such as pn junctions or absorber/charge transport layer. The efficiency of a solar cell is highly dependent on the properties of interfaces, including energy level alignment, charge carrier concentration, and recombination rate which are critical parameters that govern the device performance. Furthermore, the cross-section allows the investigation of the effect of surface defects and impurities within the device which can impact the efficiency and stability of the solar cell. Defects such as dislocations, grain boundaries, or vacancies can impact the charge carrier transport and recombination, and their location and concentration can be revealed [16].

Generally, the information accessible through cross-sectional analysis can be used to optimize the design and improve the efficiency and reliability of the device. However, in order to acquire meaningful data, cross-sectional KPFM requires a significant amount of effort, both in terms of experimental setup and data analysis, often requiring modeling for a thorough data comprehension. For instance, the experimental setup requires precise alignment of the device under the KPFM tip and under the external laser illumination as well as careful calibration of the KPFM instrument to ensure accurate measurements. Additionally, the samples need to be carefully prepared to obtain a clean and well-defined cross-section without introducing any damage or contamination to the device. This requires specialized sample preparation techniques and instrumentation, as well as significant attention to details.

In our studies, we focused on characterizing mainly the cross-section of III-V and silicon-based samples thanks to their stability in ambient conditions and ease of cleaving with respect to other PV materials. As

a general idea, KPFM was used to map the surface potential along the cross-section of devices and multi-layer structures under different illumination and bias conditions to obtain a comprehensive understanding of the surface potential.
In summary, our study aims to show the potentialities of KPFM characterization for understanding the electronic properties of solar cells at the cross-section level.

### 2.3.3 Cross-sectional KPFM setup for operando device characterization

The experiment setup required to perform satisfactory and meaningful cross-sectional KPFM analysis is nontrivial to configure, both in terms of sample preparation and positioning in the KPFM sample stage. Over time and through the acquisition of expertise, we have developed an experimental configuration that is both quick to assemble and relatively straightforward to operate which is shown in Figure 9.

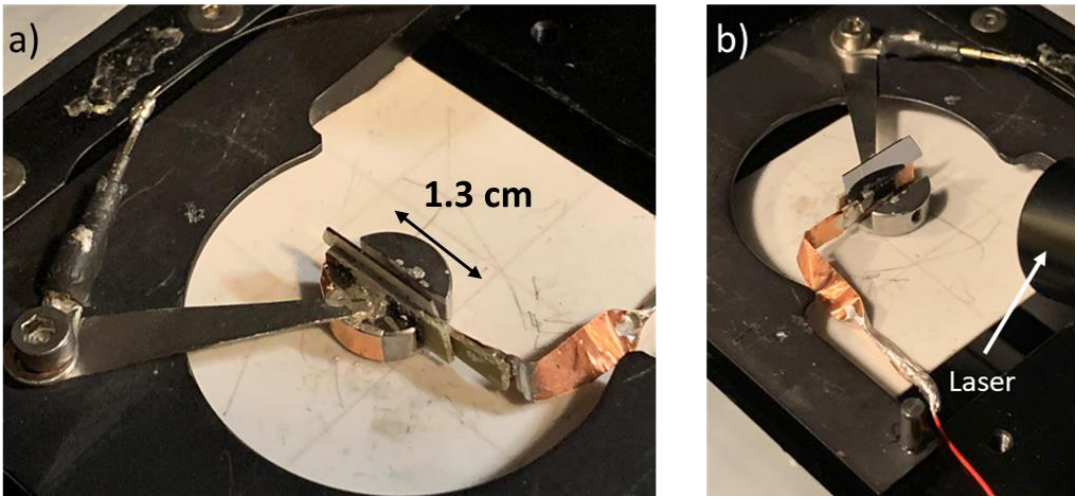


**Figure 9:** Experimental setup for cross-sectional KPFM analysis of a solar cell, a) back contact and b) front contact. The back contact is connected to the KPFM ground which is represented by the metallic clip. The back and front contacts are then connected to a Keithley 2400 with an extra wire (not shown) and copper tape + metallic wire, respectively. The diameter of the sample holder is 1.3 cm.

It is worth describing the steps necessary to achieve this experimental configuration. In order to perform cross-sectional analysis, the sample must be cleaved and must be placed upright in a metallic sample holder. The choice of the sample holder is imposed by the sample height which, generally, has to be illuminated from the side, e.g., the front surface of the solar cell.
Due to the metallic nature of the sample holder, the initial critical aspect consists in ensuring that the solar cell's back and front contacts are electrically isolated in order to avoid the short-circuit of the device. For this reason the first step consists of electrically insulating the base of the sample holder with an insulating layer.
Subsequently, a method must be identified to maintain the sample in an upright position while simultaneously enabling the connection of the front and back contacts of the solar cell. For this step, we use two insulating plastic plates which present a layer of copper on just one of the two sides. Using double-sided tape, the two plates are adhered together with one on the copper side and the other on the plastic side, resulting in electrical disconnection. It is important that the plates must be attached together slightly shifted to allow space for the sample.

The sample is then positioned in the space between the two plates. The back contact will be connected to the first copper layer while the front contact to the second one thanks to conductive silver paste (Figure 10). Since the samples are generally small and silver paste tends to spread, it is important to constantly check with a multimeter the electrical disconnection of the two plates until drying.

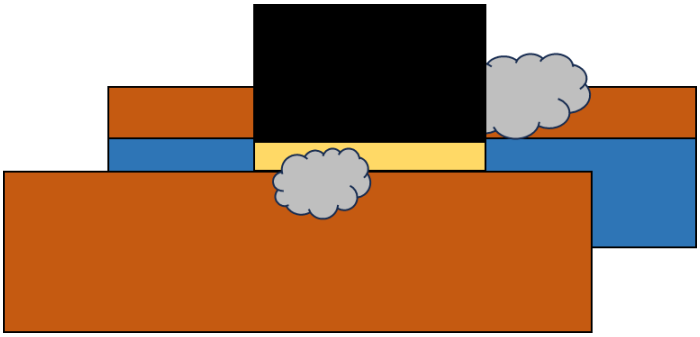

**Figure 10:** Schematic of the experimental configuration for cross-sectional KPFM analysis. The brown rectangles represent copper plates, and the blue rectangle is an insulating layer placed between the two plates. The gray clouds represent silver paste used to ensure a good electrical connection.

The sample setup is then placed in the KPFM equipment. There, through additional wires, the back and front contacts are connected to a sourcemeter. To test that the system is working properly, and the solar cell is not damaged after cleaving, I-V curves can be acquired directly with the Keithley 2400.
As a final step, it is important to place the sample perpendicular to the scanning direction of the tip and, additionally, in a position that maximizes $V_{OC}$ under the particular selected laser illumination.
By following this procedure, the experimental setup previously shown in Figure 9 is arranged and it is now possible to perform KPFM analysis.
During cross-sectional KPFM, rectangular scans are generally preferred in order to cover the whole length of the layers stuck along the y-axis, an example is reported in Figure 11 which shows the topography and $V_{CPD}$ images acquired on the cross-section n-cSi/i-aSi:H/p-µcSiO$_x$ heterojunction which will be described in section 4.3. Note that the origin (0;0) is identified as a point in the cross-section of the sample and moving along the positive direction of the y-axis, one will reach the end of the sample.

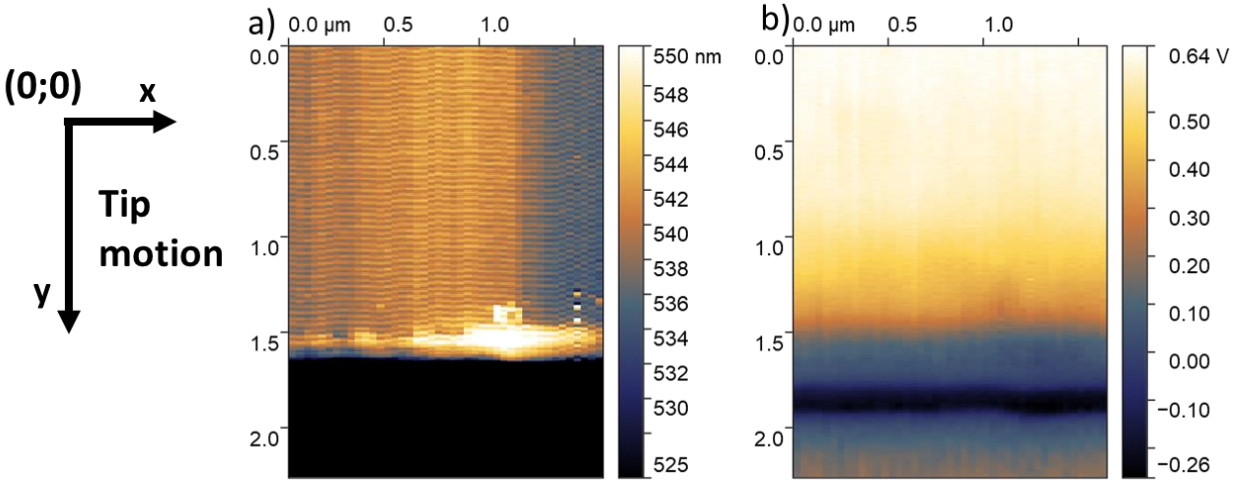


**Figure 11:** Example of a typical cross-sectional KPFM analysis in which the topography a) and $V_{CPD}$ map b) were acquired on the cross-section of the n-cSi/i-a-Si/p-µcSiO$_x$ sample.

Generally, it is a good practice to include part of the substrate in the scan using it as a reference frame for the identification of the other layers. One single scan can take from 20 to 40 minutes based on the image resolution, scanning rate and scan dimension. A good compromise was found performing scans with a resolution of 500x500 with a tip scan rate (the speed at which the AFM tip is moved across the surface) of 0.4 Hz. Specifically, it means that the entire image is composed of a grid or array of 500 data points along the horizontal (x-axis) direction and 500 data points along the vertical (y-axis) direction and each line that forms the final image takes approximately 2.5 seconds to be acquired.
However, when a good region is identified, long scans can be performed to obtain high-quality images, for instance 1024x1024 with a scan rate of 0.1 Hz.

## 2.4. Unraveling the complexities: exploring the problematics of cross-sectional KPFM

In this paragraph the challenges associated with the cross-sectional KPFM technique will be presented and described. Additionally, some cases of artifacts that may occur during cross-sectional analysis will be illustrated. Note that in order to provide experimental evidence of these problematics, KPFM data acquired on the cross-section of a GaAs solar cell will be used as illustrations.

### 2.4.1 Sample preparation

One of the biggest challenges in sample preparation for cross-sectional KPFM is ensuring that the cleaved surface is clean, smooth and in perfect conditions. For example, any contaminants on the surface can affect the local surface potential measurements. Additionally, any surface irregularities or roughness can also have an impact on the local surface potential, leading to inaccurate or unreliable results. The cleaving process is best performed with the utilization of suitable equipment, such as a focused ion beam (FIB) [17], which can be prohibitively expensive and may not be readily accessible. Furthermore, proper operation of such equipment necessitates adequate training. In my particular case, due to unavailability of the aforementioned equipment, I resorted to a method that involved indenting the sample with a diamond tip, followed by breaking the sample along the direction of the scratch.
Throughout the cleaving process, numerous challenges may arise. For instance, the sample could fracture or split during cleaving, rendering it unsuitable for subsequent analysis. Furthermore, cleaving may induce stress or damage to the material, thereby impacting the local surface potential measurements.
Figure 12 provides a top-view optical image of a real cross-section obtained after cleaving, highlighting the issues that may arise with such an elementary cleaving process. Specifically, after the cleaving process, the sample was placed in the sample holder and observed with the optical microscope integrated in the KPFM equipment. For this reason, the shadow visible at the bottom center of the optical image is related to the AFM probe and additionally, to guide the readers, a black arrow was added to show the location of the edge of the sample.
Note that the thickness of the cross-section is generally in the order of hundreds of micrometers whereas the layers of interest (e.g., pn junctions, buffer layers) are located in a few microns in a region very close to the edge of the sample.

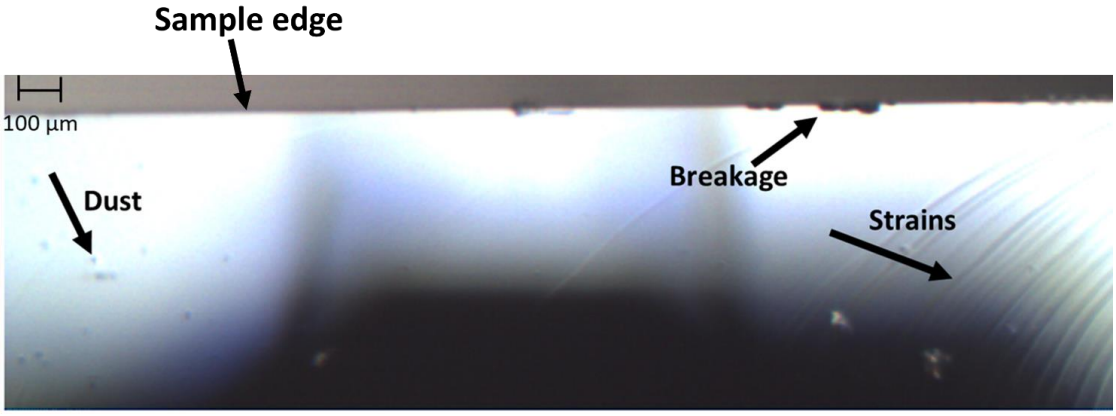


**Figure 12:** Top-view optical image of a real sample cross-section. Note that the shadow visible at the bottom center of the optical image is related to the AFM probe.

The cross-section displays holes and breaks at the edge where the layers of interest are located. Notably, the presence of breaking points can cause voltage losses across the semiconductor-based structure. Furthermore, the sample exhibits visible strains that stem from the stress that was induced during the cleaving process.
Identifying an optimal location for KPFM analysis is crucial to achieve meaningful results. It is noteworthy that, although it may be feasible to avoid macroscopic areas of damage, the surface could contain nano or micro damaged regions that may have a localized effect on surface potential but are undetectable through the TRIOS platform optical microscope. The same is valid for the presence of nano or micro dust particles on the surface. For these reasons, in cross-sectional KPFM analysis, reproducibility is crucial to ensure consistent and reliable results when repeating the experiment. However, the different factors involved in sample preparation, as previously discussed, can introduce variability and uncertainty into the local surface potential measurements, thereby reducing the reproducibility of results.

Another important aspect to consider is the oxidation process. When the cross-section is exposed, natural oxidation begins to occur, and since KPFM analysis can be time-consuming, the surface potential signal may change over time due to the formation of an oxide layer. In our case, as the equipment operates in ambient conditions and thus, this process is unavoidable.
Furthermore, the unsuitability of ambient conditions for materials prone to humidity-induced instability, such as perovskite-based materials, intensifies the urgency and time sensitivity of their characterization process.

### 2.4.2 Unwanted tip/sample contact

A commonly encountered issue in KPFM analysis is the inadvertent contact of the tip with the sample surface during scanning. This contact can cause a shift in the work function (WF) of the tip. Since $V_{CPD}$ directly depends on the WF of the tip, any change in it due to tip-sample contact will be reflected in the measured $V_{CPD}$. Regrettably, this phenomenon is uncontrollable and can manifest at any point during the KPFM analysis. Its most significant consequence is that the $V_{CPD}$ value changes, rendering previous measurements incomparable with new ones. This issue necessitates the repeated execution of the entire analysis from the start, adding a significant burden to the research process.

An instance of this phenomenon is demonstrated in Figure 13, where the white arrow highlights a point at approximately 0.5 um along the x-axis where the tip has inadvertently touched the sample surface. This contact caused an increase in the $V_{CPD}$ value in comparison to the previous measurements (Figure 13b), rendering the newly acquired $V_{CPD}$ values incomparable to those obtained earlier.

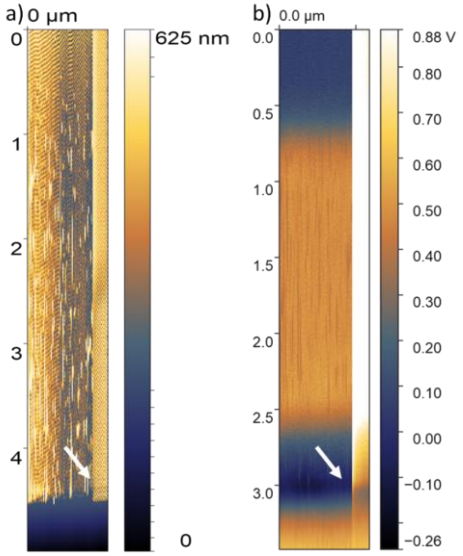


**Figure 13:** Example of the tip touching the surface of the sample. The point of contact is highlighted by the white arrow in both topography a) and $V_{CPD}$ b) images.

There are two potential solutions that can help to mitigate this issue. Ideally, the KPFM apparatus should be located in a room isolated from external sources of vibration which can trigger undesirable movements of the tip. Note that our KPFM setup is placed on an anti-vibrating table which can help to reduce the occurrence of these unwanted tip/sample contacts but not remove it completely.
Additionally, one can execute measurements with a relatively high tip lift from the surface, approximately 30/50 nm. However, a trade-off must be considered, as a higher lift corresponds to lower image resolution. Hence, it becomes imperative to reach a balance between the tip lift and image resolution in order to attain optimal outcomes.
This unwanted tip/surface interaction may appear in both cross-sectional and planar configurations, especially when the analyzed sample presents a rough and inhomogeneous topography.

### 2.4.3 Image deformation

Piezo actuators are a crucial component of AFM/KPFM systems, as they enable the precise and rapid scanning of the surface of a sample. These actuators control the piezoelectric effect, which generates mechanical stress in response to an electric field, to regulate the movement of the AFM/KPFM tip. Despite their exceptional precision and reliability, piezo actuators can introduce artifacts in the AFM/KPFM image [18].
Some of the common artifacts related to piezo actuators include:
Piezo hysteresis: All piezoelectric ceramics display hysteretic behavior, that is, if slowly scanned back and forth cyclically, to the same driving signal does not correspond to the same position in the two scanning directions. This effect can introduce artifacts in the image, particularly in regions where the surface is not uniform or where there are discontinuities in the sample.

Mechanical crosstalk: Piezo actuators can introduce mechanical crosstalk, where the movement of one actuator affects the position of adjacent actuators. This can lead to distortions in the AFM/KPFM image, particularly in regions where the surface is not flat or where there are significant topographical features.
Electrical noise: The use of piezo actuators can also introduce electrical noise into the AFM/KPFM measurement. This could happen if the voltage applied to the actuator is unstable or if there are electromagnetic interference sources in the environment. The electrical noise can affect the precision and accuracy of the AFM/KPFM measurement, leading to artifacts in the image.
Here, we present our observations on two frequently occurring problematics in cross-sectional KPFM that we believe may be linked to the use of piezo actuators.
In certain instances, the AFM/KPFM image may appear rotated even when the sample is positioned perpendicular to the direction of the scanning tip, as depicted in Figure 14. The primary issue associated with this problematic is that during the scanning process, a portion of the intended scanned area may result to be cut off from the final image.
In such cases, angular rotation correction may be required during data processing to obtain a straight image for comparison of different regions. Unfortunately, direct control over this occurrence is not possible, and consecutively acquired scans may appear horizontally or even rotated in the opposite direction.

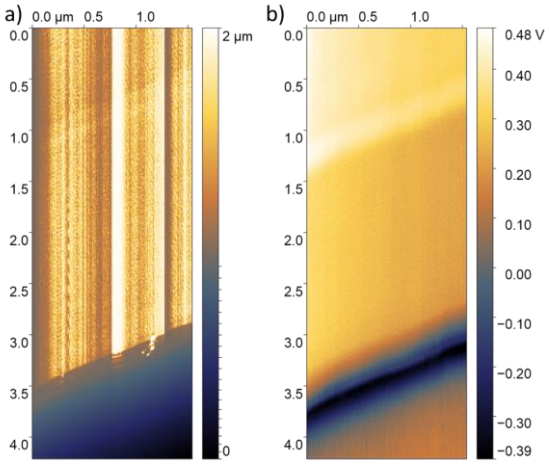


**Figure 14:** Topography a) and $V_{CPD}$ b) images of a KPFM scan which appears rotated with respect to the scanning direction.

In addition, the image may appear non-uniform, creating the illusion of a flexible and non-straight cross-section, as reported in the example of Figure 15. Even in this situation, direct control over this artifact is not possible. In fact, it is likely that the following scan may not exhibit this artifact.
It should be noted that the improper positioning of the tip in the probe spring clip (Figure 5) can also result in similar types of artifacts or increasing their occurrence. However, it is important to note that these types of image distortions are primarily encountered in cross-sectional analysis, whereas the planar configuration remains largely unaffected by these issues. Nonetheless, in the case their appearance persists, it is possible to make use of calibrated samples to check the quality of the AFM actuators. Specifically, calibrated samples serve as a valuable tool to assess the accuracy of the AFM actuator system. For instance, a silicon wafer etched with precise periodic patterns, like lines or grooves, of known dimensions, traceable to standards, can be used as a calibrated sample. By scanning this specially designed sample

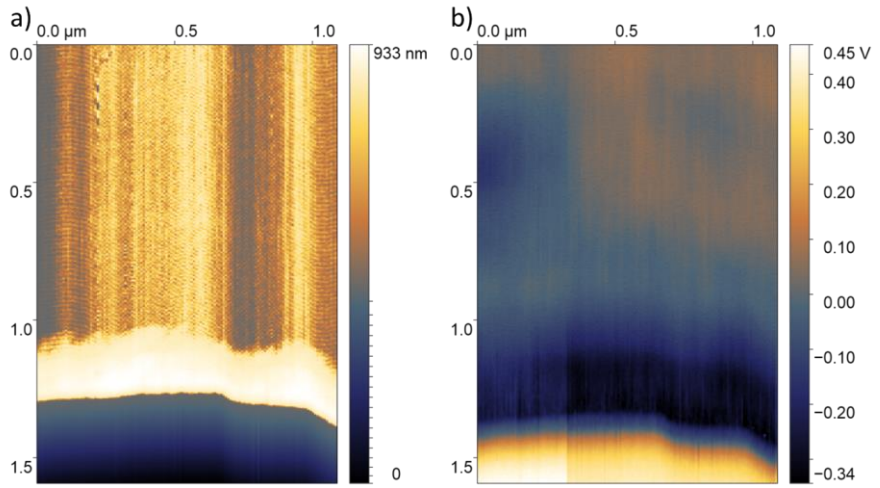


**Figure 15:** Topography a) and $V_{CPD}$ b) images of a KPFM scan in which the cross-section appears flexible and non-straight.

with known and precise features, one can verify that the actuator is functioning correctly, ensuring that the AFM delivers accurate and reliable measurements [30].

## 2.5 A modeling tool: KELSCAN

As KPFM is a surface-sensitive technique, the measured surface potential can be affected by the presence of surface defects, leading to variations in potential compared to the otherwise constant bulk potential. Consequently, understanding KPFM data can be challenging, and the use of a modeling tool is essential to enable a comprehensive analysis of experimental results.

The simulations were performed using in-house software KELSCAN developed at the IPVF institute, and which delivers a targeted KPFM modeling tool using SILVACO ATLAS software evaluating the contact potential and surface photovoltage as a function of position [19]. ATLAS solves the Poisson equation self-consistently coupled to carrier continuity and transport equations and includes standard radiative and nonradiative (Auger and Shockley-Read-Hall) recombination mechanisms in the well-known drift diffusion model, as detailed by Huang et al. [20].

The simulations always assume ohmic contacts and therefore Dirichlet boundary conditions fixing potential and carrier concentrations at the boundaries, as reported in section 3.5 of the SILVACO ATLAS manual. The ATLAS module solves semiconductor transport and continuity equations numerically in two dimensions (2D) and includes flexible descriptions of bulk and surface defect distributions.

KELSCAN simulates the experimental setup by sequentially moving the AFM tip across the surface of the sample, statically solving the semiconductor equations at each position, and then evaluating the contact potential at each position from the field distribution calculated by ATLAS and exported to KELSCAN.

The contact potential difference is modeled by physically defining a 2D probe of realistic dimensions with a variable WF and placing it at the experimental distance from the sample surface. An air ambient is defined between the sample and the tip as in the experimental setup. A numerical interpolation scheme in KELSCAN evaluates the zero-field condition by comparing fields with no bias applied between KPFM tip and sample contacts, and with non-zero bias estimated from the analytical value of $V_{CPD}$ which can be easily estimated from the tip and sample material work functions and the doping level.

KELSCAN allows two-dimensional definition of samples which provides a realistic representation of charge distribution within the volume of the device, particularly from the perspective of placement of electrodes on the sides of the samples (orthogonal to the KPFM tip) or at the lower surface of the sample (below the KPFM tip). This methodology furthermore allows the specification of arbitrary doping and composition profiles in the sample and enables the study of doping gradients and interfaces, and of pn junction devices in cross section. An illustration is reported in Figure 16 in which the structure of the p-AlGaAs:Be/n-GaInP:Si heterojunction solar cell that will be shown in section 4.1 is used as an instance.

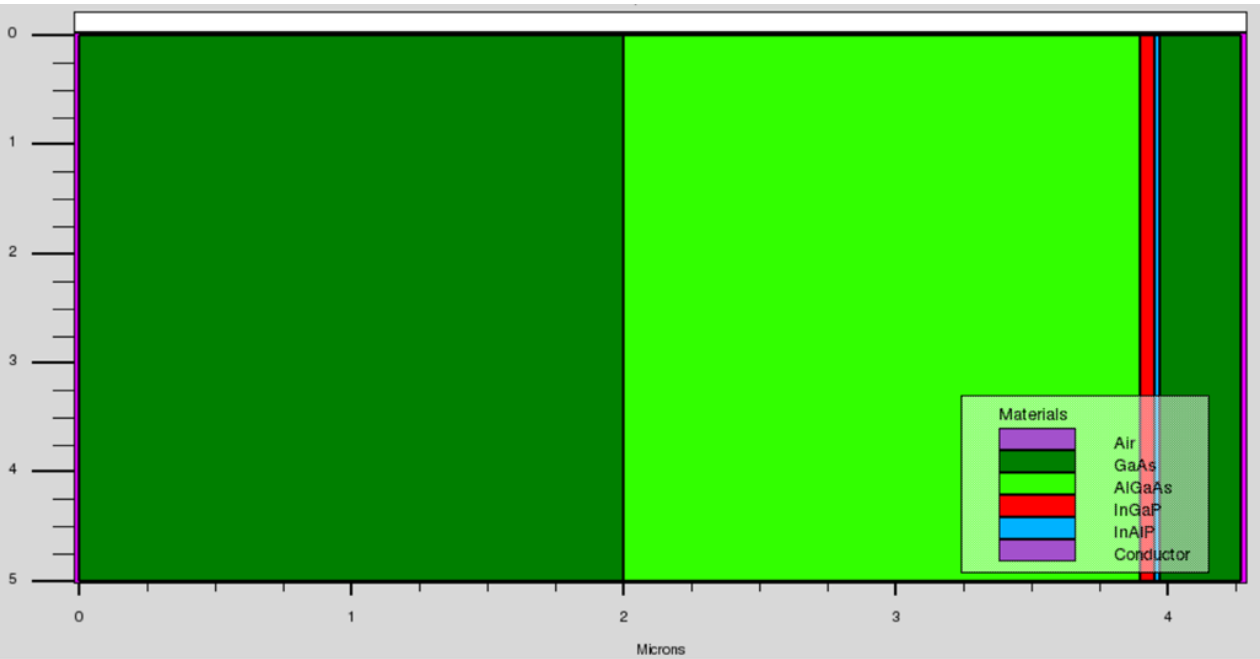


**Figure 16:** Two-dimensional representation of the cross-section of the p-AlGaAs:Be/n-GaInP:Si heterojunction solar cell that will be shown in section 4.1 obtained with the KELSCAN tool. An inset of the different layers that comprise the structure is also reported.

In this two-dimensional modeling, simulation of KPFM tip scanning across the surface is possible, and a more exact simulation of the consequences of tip geometry and sample contact placement is enabled.
In order to replicate the experimental conditions, the radius of the tip is set at 25 nm, and the other experimental parameters such as the tip/sample distance and the $\phi_{tip}$ values are set accordingly to the experimental conditions and tip characterization.
Note that KELSCAN allows to simulate $V_{CPD}$ measurements either in dark conditions or under illumination: in the case of "under illumination" simulations, it is possible to select a power density that matches the one used during the experiment.
In order to provide a quantitative analysis of the experimental results, and thus considering a real surface cross-section, the modeling allows the introduction of donor and acceptor type defects in a surface layer of arbitrary depth which are defined by a Gaussian defect distribution width, peak and energy position. The model of defects extending into the volume is physically more appropriate than a two-dimensional surface distribution [21]. The introduced defect volume density of states (DOS), $N(E)$ ($eV^{-1}cm^{-3}$), is assumed homogeneous throughout the thickness of the defective layer, $t_{DL}$, which we took equal to 1 nm. This can be translated into a surface density of states $N_{ss}(E)$ ($eV^{-1}cm^{-2}$): $N_{ss}(E) = N(E) \times t_{DL}$ with $t_{DL}=10^{-7}$ cm.

In addition, the DOS consists of the sum of two distributions of monovalent donor and acceptor states, $N_D(E)$ and $N_A(E)$, respectively: $N(E) = N_D(E) + N_A(E)$. These determine the charge neutrality level (CNL) of the surface defects. More precisely, when the Fermi level ($E_F$) at the surface coincides with the CNL there is no net charge coming from the surface defects, while when $E_F$ is above (below) the CNL surface defects are overall negatively (positively) charged.
An example is reported in Figure 17, for which a Gaussian distribution of acceptor-like surface defects with a maximum density of $10^{10}$ $eV^{-1}cm^{-2}$ and a width (σ) of 2 eV was modeled along the whole energy gap for the case of a Si sample.

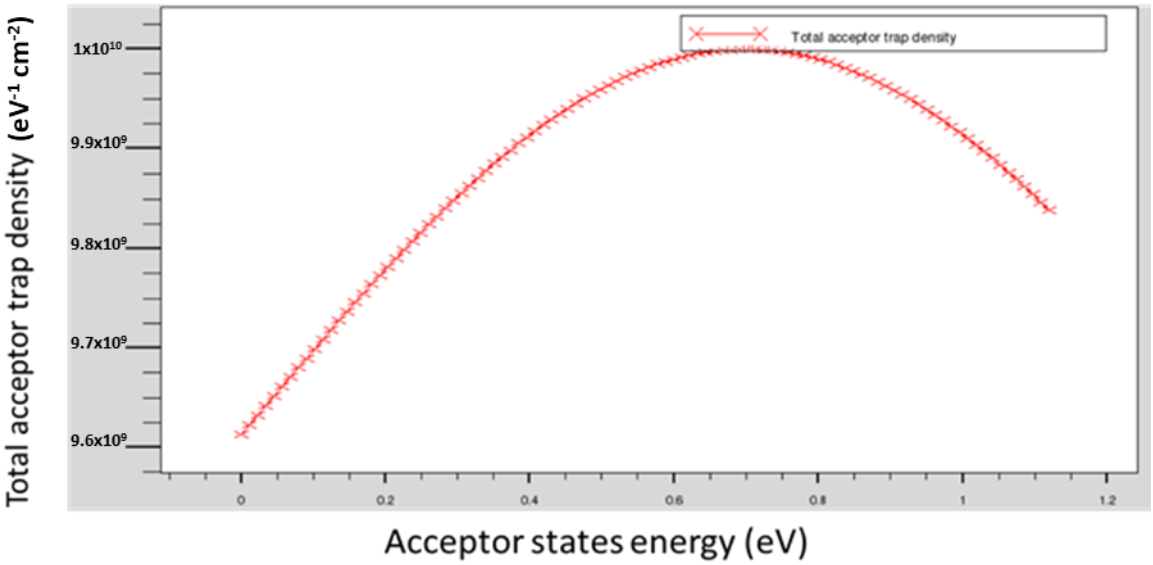


**Figure 17:** Example of a distribution of acceptor-like surface defects with a density of $10^{10}$ $eV^{-1}cm^{-2}$ introduced along the whole energy range of the energy gap for the case of a Si sample.

In the regard of this PhD thesis, the final objective is not to replicate the exact surface state densities for each semiconductor-based sample since there are numerous free parameters involved in selecting defect distributions [31]. Our goal is rather to analyze the influence of surface defects on the surface properties of a semiconductor material, with particular emphasis to extra surface charge provided by surface defects and its subsequent impact on surface band-bending, which ultimately determines $V_{CPD}$. We then compare these surface properties to the bulk properties in order to explain the experimental $V_{CPD}$ profiles.
For these reasons, to illustrate the impact of surface defects on the energy bands and surface potential of the analyzed structures, we will simplify and introduce surface defect distributions that can be approximated as a simple uniform DOS for both donor and acceptor states across the entire energy range within the energy gap. This is achieved by specifying a very large width of tens of eV for the Gaussian distribution. The CNL is thus easily deduced from the ratio of the constant donor and acceptor DOS. If they are chosen equal, the CNL is set at mid-gap whereas it is moved towards the valence (conduction) band if the ratio of acceptor to donor DOS is larger (smaller) than 1 [22].

## 2.6 Probing nanoscale conductivity: insights from Conductive Atomic Force Microscopy

During the late 1980s, several attempts were initiated to measure contact resistance at a local level in different applications [23,24], leading to the acquisition of the first experimental image demonstrating the surface local resistivity by employing a conductive AFM probe. This method is known as conductive AFM (c-AFM) and it enables the simultaneous generation of topography and resistance (or current) maps. In that period, Shafai et al., [25] proposed a technique that described semiconductor doping with a lateral resolution of less than 35 nm.

A major milestone in this field occurred in 1996 when a French team at Laboratoire de Génie Electrique de Paris (L.G.E.P), which is now known as laboratoire de Génie électrique et électronique de Paris (GeePs), proposed a highly promising method for measuring the electrical resistance at a local level using a conductive probe [26]. This technique is distinct in that it includes a logarithmic amplifier that allows resistance measurement over a vast range of ten orders of magnitude: from $10^2$ Ω to $10^{12}$ Ω. By the early 2000s, the commercialization of this AFM extension known as "Resiscope" allowed for local resistance measurements to be conducted using commercially available AFMs.

In c-AFM, the topography is measured in contact mode and at the same time, the current is measured while a DC bias is applied between the sample and the conductive AFM tip; in other words, during c-AFM the I/V ratio is measured. A sketch of an AFM with Resiscope system is given in Figure 18.

The tip and the cantilever are constituted either of a highly conducting material such as doped silicon and full diamond or of silicon nitride but coated with metal film for conduction. Pt/Ir and diamond are two instances of coating materials for conductive AFM tips. The sample and the cantilever holders are cautiously insulated from the apparatus structure.

The resistance measured using the Resiscope apparatus is determined by the cumulative effect of multiple resistances connected in series, including the resistance associated with the probe, the inherent resistance of the sample, the resistance at the interface between the sample and the sample holder, and the resistance arising from the contact between the tip and the sample. However, due to the extremely

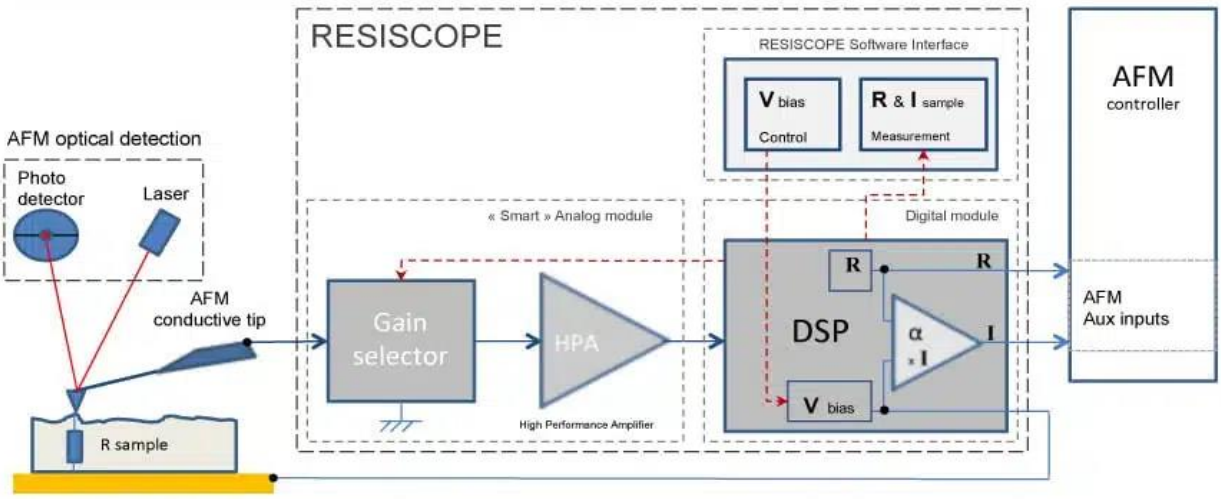


**Figure 18:** Schematic of the Resiscope setup. The AFM is in contact mode and the current flow through the tip and the sample is amplified and measured through a logarithmic amplifier.

small contact area between the tip and the sample at the nanoscale level, the resistance arising from the tip-sample interaction becomes the primary contributor compared to other sources of resistance. This resistance, commonly referred as *spreading resistance* or tip-sample resistance, plays a crucial role in achieving accurate and effective c-AFM analysis. It is important to ensure an ohmic contact between the sample and the tip for successful measurements. Conversely, if a Schottky contact is present, the tunneling effect will become the dominant factor in the resistance equation.

The examination of electrical contact resistance entails the categorization of physical mechanisms into three distinct regimes, primarily dictated by the relative dimensions of the contact compared to the electron mean free path within the materials involved. These regimes include the diffusive regime, the ballistic regime, and the intermediate regime, as outlined by reference [27]. In scenarios where the contact size substantially exceeds the electron mean free path, electron transport occurs across the interface through diffusive mechanisms.

The model that describes electrical contact resistance in the diffusive regime was derived by Maxwell from Ohm's law as:

$$R_{Maxwell} = \frac{\rho}{4a}, (16)$$

where $R_{Maxwell}$ is the electrical contact resistance in diffusive regime, $\rho$ is the electrical resistivity of the contact and a is the contact radius. As described by equation 16, the electrical contact resistance exhibits an inverse relationship with the contact radius in the diffusive regime. Conversely, when the size of the contact is considerably smaller than the mean free path of the electrons involved, ballistic transport phenomena come into play.

Electrical contact resistance in the ballistic regime is given by Sharvin's equation as:

$$R_{Sharvin} = \frac{4\rho\lambda}{3\pi a^2}, (17)$$

where $R_{Sharvin}$ is the electrical contact resistance in ballistic regime, and $\lambda$ is the electron mean free path. As indicated by equation 17, the electrical contact resistance displays an inverse correlation with the contact area in the ballistic regime. Furthermore, when the size of the contact approaches the magnitude of the electron mean free path, the electrical contact resistance switches into the intermediate regime. In this regime, Wexler introduced a model to describe the electrical contact resistance, which is given by:

$$R_{Wexler} = \Gamma\left(\frac{\lambda}{a}\right)\frac{\rho}{2a} + \frac{4\rho\lambda}{3\pi a^2}, (18)$$

where $\Gamma$ is a function of $\lambda/a$, which varies from 1 to 0.694 [28].

Hence, c-AFM has the capability to assess the local resistivity at the nanoscale level. This aspect holds significant relevance within the microelectronic and photovoltaic fields, as resistivity plays a pivotal role in determining the doping carrier density and doping levels, which, in turn, are intricately associated with the mobility of charge carriers.

### 2.6.1 Conductive AFM for solar cells characterization

Conductive AFM is performed in contact mode and thus, since a bias is applied between the tip and the sample, it allows the acquisition of local resistance maps along the cross-section and surface of a sample. For this reason, c-AFM represents an important investigative tool for solar cell characterization. This is

because in principle it is possible to acquire local resistance maps in dark and under illumination under different applied bias enabling the study of the current path under real device operando conditions.
During this PhD, c-AFM characterization was performed using a Resiscope directly coupled to the scanning probe microscopy system from AIST-NT (TRIOS platform) used for KPFM characterization. For c-AFM characterization, highly doped n-type single crystal silicon SPM-probes with conductive diamond coating with a force constant of 9.5 N/m were used.
Resiscope measurements can be performed under different experimental conditions. Specifically, the sample can be analyzed in open-circuit (contact taken only from one side) and short-circuit (contacts taken from both sides) conditions. Both configurations can provide valuable insights due to the different preferential electrical path of the collected charge carriers. A schematic of these two experimental configurations is shown in Figure 19.

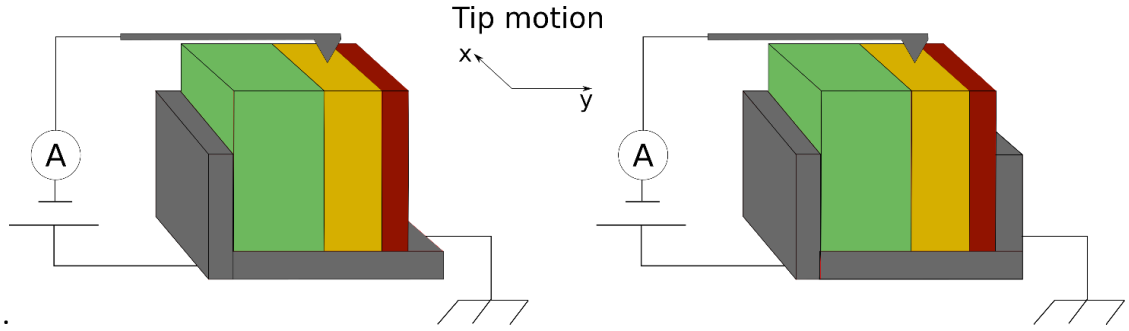


**Figure 19:** Schematic representation of a cross-sectional Resiscope measurement in open-circuit (left) and short-circuit (right). Silver paste is generally used to assure a reasonable electrical contact between the sample holder and the sample.

During Resiscope analysis, a voltage is applied between the sample and the AFM tip and the so-called Voltage maps can be acquired, an example is reported in Figure 20b. From the output voltage measured from the logarithmic amplification system of the setup shown in Figure 18, one can deduce the corresponding resistance value from:

$$R = 10^{(V+2)}, (19)$$

where the resistance is expressed in ohms and the measured output voltage in volts [26]. The voltage map can thus be converted into a resistance map, which can in turn be converted into a resistance profile.

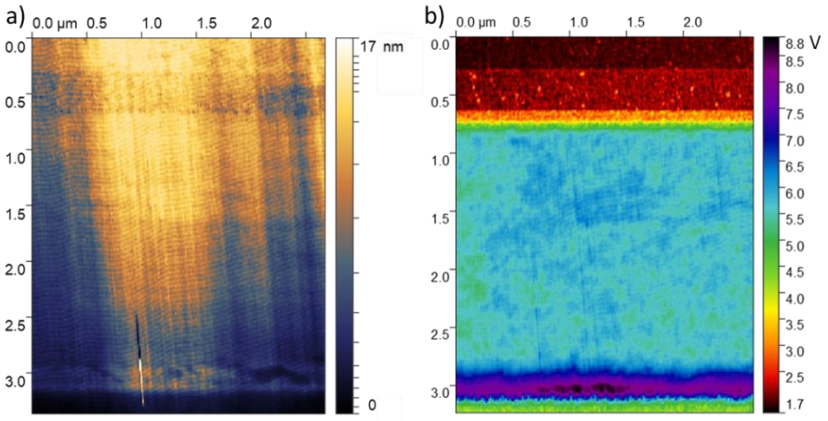


**Figure 20:** Examples of topography a) and voltage map b) acquired by Resiscope on the cross-section of the AlGaAs-based sample that will be presented in section 4.1.

## 2.7 Data analysis

A software called Gwyddion was employed for the analysis and processing of the collected data following KPFM and c-AFM analysis [29].

Gwyddion is a versatile software package widely used for analyzing surface microscopy data obtained from a variety of techniques, including AFM, STM, SEM, SNOM, and confocal microscopy.

This open-source program provides a user-friendly interface that allows easy access to and manipulation of microscopy data, supporting many different file formats. Gwyddion offers a wide range of tools for enhancing, analyzing, and visualizing microscopy data. These include contrast and brightness adjustment, filtering, and surface analysis tools such as roughness, height distribution, and curvature analysis. Additionally, Gwyddion offers data visualization tools for creating 2D and 3D visual representations of microscopy data and data processing tools such as image stitching, smoothing, and filtering to improve the accuracy and reliability of microscopy data.

Additionally, Gwyddion provides the capability to extract profiles from KPFM scans, which can be subsequently exported to Origin for additional processing and analysis.

In order to have an averaged profile along the x-axis of a scan, each point of the extracted profiles represents an average of 207 points over a width of 0.7 µm along the x-axis of the scan. An example is reported in Figure 21.

Throughout the manuscript, for the scans which refer to cross-sectional analysis, the origin (0;0) is identified as a point in the substrate and moving along the positive direction of the Y axis, one will reach the end of the sample (see Figure 20 for an example).

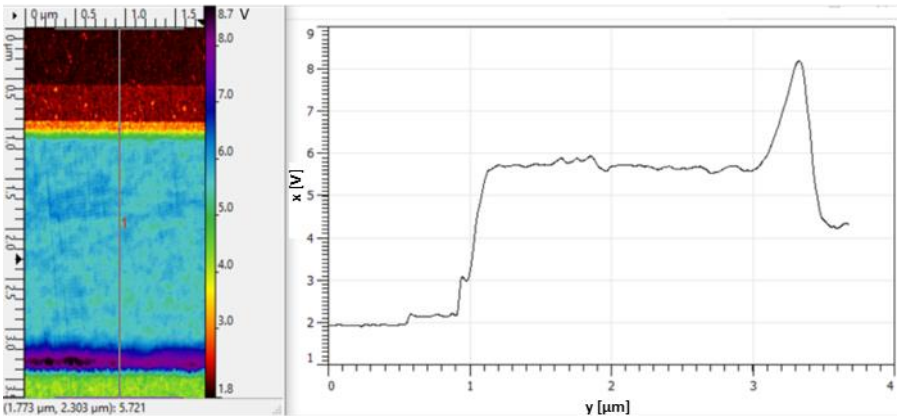


**Figure 21:** Extrapolation of profiles from the experimental AFM images. A profile represents an average of 207 points over a width of 0.7 µm along the x-axis of the scan.

## Bibliography

[1] Nonnenmacher, M.; O'Boyle, M. P.; Wickramasinghe, H. K. Kelvin Probe Force Microscopy. *Applied Physics Letters* **1991**, *58* (25), 2921–2923. https://doi.org/10.1063/1.105227.

[2] Lord Kelvin, "Contact electricity of metals," Philos. Mag. Ser. 5, vol. 46, no. 278, pp. 82–120, Jul. 1898

[3] W. A. Zisman, "A new method of measuring contact potential differences in metals.," Rev. Sci. Instrum., vol. 3, no. 7, pp. 367–370, Jul. 1932.

[4]Melitz, W.; Shen, J.; Kummel, A. C.; Lee, S. Kelvin Probe Force Microscopy and Its Application. *Surface Science Reports* **2011**, *66* (1), 1–27. https://doi.org/10.1016/j.surfrep.2010.10.001.

[5] Axt, A.; Hermes, I. M.; Bergmann, V. W.; Tausendpfund, N.; Weber, S. A. L. Know Your Full Potential: Quantitative Kelvin Probe Force Microscopy on Nanoscale Electrical Devices. *Beilstein J Nanotechnol* **2018**, *9*, 1809–1819. https://doi.org/10.3762/bjnano.9.172.

[6] Narchi, P.; Alvarez, J.; Chrétien, P.; Picardi, G.; Cariou, R.; Foldyna, M.; Prod'homme, P.; Kleider, J.-P.; i Cabarrocas, P. R. Cross-Sectional Investigations on Epitaxial Silicon Solar Cells by Kelvin and Conducting Probe Atomic Force Microscopy: Effect of Illumination. *Nanoscale Res Lett* **2016**, *11*, 55. https://doi.org/10.1186/s11671-016-1268-1.

[7] Borgani, R.; Forchheimer, D.; Bergqvist, J.; Thorén, P.-A.; Inganäs, O.; Haviland, D. B. Intermodulation Electrostatic Force Microscopy for Imaging Surface Photo-Voltage. *Applied Physics Letters* **2014**, *105* (14), 143113. https://doi.org/10.1063/1.4897966.

[8] Ma, Z.-M.; Mu, J.; Tang, J.; Xue, H.; Zhang, H.; Xue, C.; Liu, J.; Li, Y. Artifacts in KPFM in FM, AM and Heterodyne AM Modes. *Key Engineering Materials* **2014**, *609–610*, 1362–1368. https://doi.org/10.4028/www.scientific.net/KEM.609-610.1362.

[9] Marchat, C.; Connolly, J. P.; Kleider, J.-P.; Alvarez, J.; Koduvelikulathu, L. J.; Puel, J. B. KPFM Surface Photovoltage Measurement and Numerical Simulation. *EPJ Photovolt.* **2019**, *10*, 3. https://doi.org/10.1051/epjpv/2019002.

[10] Ziegler, D.; Stemmer, A. Force Gradient Sensitive Detection in Lift-Mode Kelvin Probe Force Microscopy. *Nanotechnology* **2011**, *22* (7), 075501. https://doi.org/10.1088/0957-4484/22/7/075501.

[11] Narchi, P. Investigation of Crystalline Silicon Solar Cells at the Nano-Scale Using Scanning Probe Microscopy Techniques. These de doctorat, Université Paris-Saclay (ComUE), **2016**.

[12] Garrillo, P. F.; Grevin, B.; Chevalier, N.; Borowik, Ł. Calibrated Work Function Mapping by Kelvin Probe Force Microscopy. *Review of Scientific Instruments* **2018**, *89* (4), 043702.https://doi.org/10.1063/1.5007619.

[13] da Lisca, M.; Connolly, J. P.; Alvarez, J.; Mekhazni, K.; Vaissiere, N.; Decobert, J.; Kleider, J.-P. Revealing of InP Multi-Layer Stacks from KPFM Measurements in the Dark and under Illumination. *EPJ Photovoltaics* **2022**, *13*, 19. https://doi.org/10.1051/epjpv/2022017.

[14] Kronik, L.; Shapira, Y. Surface Photovoltage Phenomena: Theory, Experiment, and Applications. *Surface Science Reports* **1999**, *37*, 1–206. https://doi.org/10.1016/S0167-5729(99)00002-3.

[15] Lan, F.; Jiang, M.; Tao, Q.; Li, G. Revealing the Working Mechanisms of Planar Perovskite Solar Cells with Cross-Sectional Surface Potential Profiling. *IEEE Journal of Photovoltaics* **2018**, *8* (1), 125–131. https://doi.org/10.1109/JPHOTOV.2017.2762525.

[16] Naumann, V.; Lausch, D.; Großer, S.; Werner, M.; Swatek, S.; Hagendorf, C.; Bagdahn, J. Microstructural Analysis of Crystal Defects Leading to Potential-Induced Degradation (PID) of Si Solar Cells. *Energy Procedia* **2013**, *33*, 76–83. https://doi.org/10.1016/j.egypro.2013.05.042.

[17] Ishitani, T.; Yaguchi, T. Cross-Sectional Sample Preparation by Focused Ion Beam: A Review of Ion-Sample Interaction. *Microscopy research and technique* **1996**, *35* (4). https://doi.org/10.1002/(SICI)1097-0029(19961101)35:4<320::AID-JEMT3>3.0.CO;2-Q.

[18] Ricci, D.; Braga, P. C. Recognizing and Avoiding Artifacts in AFM Imaging. In *Atomic Force Microscopy*; Humana Press: New Jersey, 2003; Vol. 242, pp 25–38. https://doi.org/10.1385/1-59259-647-9:25.

[19] SILVACO® ATLAS™ User's Manual **2016**.

[20] Huang, Y.; Gheno, A.; Rolland, A.; Pedesseau, L.; Vedraine, S.; Durand, O.; Bouclé, J.; Connolly, J.; Etgar, L.; Even, J. A New Approach to Modelling Kelvin Probe Force Microscopy of Hetero-Structures in the Dark and under Illumination. *Optical and Quantum Electronics* **2018**, *50*. https://doi.org/10.1007/s11082-017-1305-z.

[21] Rosenwaks, Y.; Shikler, R.; Glatzel, Th.; Sadewasser, S. Kelvin Probe Force Microscopy of Semiconductor Surface Defects. *Phys. Rev. B* **2004**, *70* (8), 085320. https://doi.org/10.1103/PhysRevB.70.085320.

[22] Tersoff, J.; Harrison, W. A. Transition-Metal Impurities in Semiconductors---Their Connection with Band Lineups and Schottky Barriers. *Phys. Rev. Lett.* **1987**, *58* (22), 2367–2370. https://doi.org/10.1103/PhysRevLett.58.2367.

[23] Morita, S.; Ishizaka, T.; Sugawara, Y.; Okada, T.; Mishima, S.; Imai, S.; Mikoshiba, N. Surface Conductance of Metal Surfaces in Air Studied with a Force Microscope. *Jpn. J. Appl. Phys.* **1989**, *28* (9A), L1634. https://doi.org/10.1143/JJAP.28.L1634.

[24] Salmeron, M.; Neubauer, G.; Folch, A.; Tomitori, M.; Ogletree, D. F.; Sautet, P. Viscoelastic and Electrical Properties of Self-Assembled Monolayers on Gold (111) Films. *Langmuir* **1993**, *9* (12), 3600–3611. https://doi.org/10.1021/la00036a041.

[25] Shafai, C.; Thomson, D. J.; Simard-Normandin, M.; Mattiussi, G.; Scanlon, P. J. Delineation of Semiconductor Doping by Scanning Resistance Microscopy. *Applied Physics Letters* **1994**, *64* (3), 342–344. https://doi.org/10.1063/1.111169.

[26] Houzé, F.; Meyer, R.; Schneegans, O.; Boyer, L. Imaging the Local Electrical Properties of Metal Surfaces by Atomic Force Microscopy with Conducting Probes. *Applied Physics Letters* **1996**, *69* (13), 1975–1977. https://doi.org/10.1063/1.117179.

[27] Slade, P. G. *Electrical Contacts: Principles and Applications, Second Edition*; CRC Press, **2017**.

[28] Wexler, G. The Size Effect and the Non-Local Boltzmann Transport Equation in Orifice and Disk Geometry. *Proc. Phys. Soc.* **1966**, *89* (4), 927. https://doi.org/10.1088/0370-1328/89/4/316.

[29] Nečas, D.; Klapetek, P. Gwyddion: An Open-Source Software for SPM Data Analysis. *Open Physics* **2012**, *10* (1), 181–188. https://doi.org/10.2478/s11534-011-0096-2.

[30] Leang, K.; Devasia, S. Feedback-Linearized Inverse Feedforward for Creep, Hysteresis, and Vibration Compensation in AFM Piezoactuators. *Control Systems Technology, IEEE Transactions on* **2007**, *15*, 927–935. https://doi.org/10.1109/TCST.2007.902956.

[31] E. H. Poindexter, G. J. Gerardi, M.-E. Rueckel, P. J. Caplan, N. M. Johnson, D. K. Biegelsen; Electronic traps and *Pb* centers at the $Si/SiO_2$ interface: Band-gap energy distribution. *J. Appl. Phys.* 15 November 1984; 56 (10): 2844–2849. https://doi.org/10.1063/1.333819

# Chapter 3

# Cross-sectional KPFM for the study of III-V multilayer stacks

As a first step in this PhD project, the capability of cross-sectional KPFM for the study of III-V multilayer stacks in ambient conditions was investigated.

Among the existing PV technologies, III-V-based solar devices belong to the PV technology of thin and ultra-thin films in which layers with widths of the order of a few nanometers are often integrated for an optimal surface passivation or for better carrier extraction, considerably enhancing device efficiency [1,2]. Consequently, the experimental demonstration of the sensitivity of the KPFM technique to the narrower layers can play a crucial role in the investigation and comprehension of the local surface properties and charge transport mechanisms at the interfaces.

In this chapter, cross-sectional KPFM analysis performed on two different III-V multilayer samples is presented. In particular, we have investigated an InP:S/InP:Fe and an InP:Zn/GaInAs(P):Zn multilayer structure with layers of different widths and doping concentrations. For this analysis we have set different objectives: the first objective is the evaluation of the spatial resolution of our KPFM setup in ambient conditions. The second objective is a full understanding of $V_{CPD}$ results combined with a description of the principal factors that affect KPFM measurements with the application of Kelvin Probe (KP) numerical modeling. This enables the interpretation of the KPFM data, specifically to investigate the effect of space charge regions, surface defects and illumination on $V_{CPD}$.

The measurements performed on the InP:S/InP:Fe and InP:Zn/GaInAs(P):Zn samples have been presented at two different conferences, JNPV 2021 and NC-AFM 2022, respectively. Two different papers were then published in the dedicated issue in EPJ photovoltaics [3] and Beilstein Journal of nanotechnology [4].

## 3.1 Revealing of InP multi-layer stacks from KPFM measurements in the dark and under illumination

As a first project we have investigated the potentiality of our KPFM setup for the analysis of the doping and in particular its sensitivity to local doping concentration variations. In semiconductor materials, the doping plays a key role since it can strongly impact the electrical, optical, and structural properties of a material and device performance. In this regard, a multitude of techniques can be applied for its characterization. Secondary-ion mass spectrometry (SIMS) and electron holography in transmission electron microscopy (TEM) can be used for this purpose with a resolution of the order of 10 nm [5]. Nevertheless, technical limitations can arise in detecting low doping concentrations ($10^{14}$ $cm^{-3}$) and thin layers (nm) as in the case of SIMS [6]. Challenging sample preparation is often required, making these methods time consuming and destructive.

Scanning probe microscopy (SPM) is another approach that allows the investigation of the doping thanks to the wide variety of AFM electrical extensions that have been developed to perform a broad range of characterizations at the nanoscale [6]. Specifically, scanning spreading resistance microscopy (SSRM) [7],

scanning capacitance microscopy (SCM) [8] and Kelvin probe force microscopy (KPFM) [9] are suitable for this purpose. SSRM and SCM measure the local resistivity and capacitance of a semiconductor material, respectively. Nonetheless, SSRM is classified as a destructive method since high normal forces are applied in order to penetrate the oxide layer and specially to keep a stable electrical contact, while SCM requires an oxide layer on the surface and modelling to obtain quantitative results [10]. Conversely, KPFM is a non-contact method which does not require specific sample preparation and has been used to detect and contrast doping concentrations in a range from $10^{14}$ to $10^{19}$ $cm^{-3}$ [6, 10-12].
For this reason, we have investigated an ambitious sample which consists of a repetition of 42 layers of InP:S and InP:Fe with different thickness.
It is worth mentioning that in order to perform the characterization of interfaces, thicker layers in the order of over 1 µm would be more suitable to better analyze the surface properties of the two semiconductors materials and the band-bending at the interfaces. Nonetheless, our focus lies specifically on materials designed for III-V solar cell applications, where the thickness of the layers that comprise a device typically ranges from less than a micron to tens or hundreds of nanometers.

### 3.1.1 InP:S/InP:Fe sample preparation

The InP stack was epitaxially grown using MOVPE process in an AIXTRON Close-Coupled Showerhead reactor (6 x 2") at a surface temperature of 580°C on a n-type
InP substrate from AXT whose doping is typically in the range of 3 to $5\times10^{18}$ $cm^{-3}$ with a thickness of 500 µm. The growth rate and the surface temperature of the InP layers are determined using an in-situ Laytec EpiCurve TT tool by employing a laser reflectometer with a laser wavelength of 980 nm.
Trimethylindium (TMIn) and phosphine ($PH_3$) are the source materials mixed to hydrogen ($H_2$) as a carrier gas. Hydrogen sulfide ($H_2S$) and ferrocene ($Cp_2Fe$) compounds are used respectively for n-type InP:S and semi-insulating InP:Fe layers. After the synthesis, the S and Fe concentrations were determined by secondary-ion mass spectrometry (SIMS) and found to be equal to $2\times10^{19}$ $cm^{-3}$ and $9\times10^{16}$ $cm^{-3}$ for the InP:S and InP:Fe layers, respectively. The Fe doping concentration is close to optimal since adding more Fe to the growth will only form FeP precipitates that degrade the crystalline quality without adding electrical benefits. The layers stack is enclosed by two 200 nm-thick non-intentionally doped InP layers called buffer and cap. Inside the stack and starting from the epitaxial interface toward the surface, two 200 nm-thick layers of InP:S/InP:Fe were grown plus four loops of five repetitions by varying the thickness of each layer as follows: 100/100, 50/50, 80/20 and 20/80 nm for InP:S/InP:Fe (see Figure 1 for a SEM image of the sample).
Impurities of S are known to form shallow donors in InP [13]. Moreover, they can efficiently reduce the dislocation density produced in the crystal during the growth process. Dislocation-free InP crystals can be used as substrates to fabricate devices such as lasers and photodiodes with high reliability and high performance [14]. InP:S-based solar devices have been also reported in the literature. In particular, Faur et al. [15] reported an $p^+n$ InP solar cells for space applications and a InP:S/AlInAs:C tunnel junction, presented

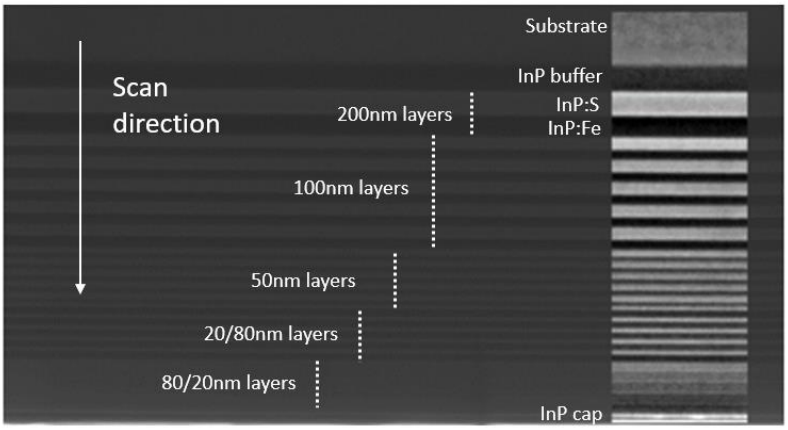


**Figure 1:** SEM image of the InP:S and InP:Fe sample surface. The image was edited to highlight with the gray and black color the InP:S and InP:Fe layers, respectively. The first two layers following the scan direction, represent the substrate and the nid buffer layer.

by the III-V Lab group [16], has been successfully produced and used to fabricate InP/InGaAs tandem solar cells [2].

Undoped InP crystals always contain unintentional impurities due to the growth process. In particular, the non-intentionally doped (nid) InP layers fabricated at III-V Lab usually present an intrinsic n-type doping in the order of $10^{15}$ $cm^{-3}$ that results in shallow donor energy levels within the energy gap.

Fe doping provides acceptor levels in the mid-gap region of InP which compensate shallow donors and thus produce a semi-insulating (SI) material [17]. InP:Fe is generally used as substrate for the growth of Si an InP with low dislocation density for III-V integration on Si [18]. Therefore, the investigation of the surface properties at the nano-scale of InP:S and InP:Fe is of great interest, as is the need of quantitative analysis of the experimental data.

KPFM is a surface investigation technique, and therefore, the presence of a native oxide surface layer on top can influence $V_{CPD}$ measurements and, in extreme case, hide the surface features of interest. Preliminary results confirmed the presence of an oxide layer which prevents the detection of the underlying surface potential of the InP:S and the InP:Fe layers. For this reason, prior to the KPFM analysis, a surface cleaning was carried out with the purpose of removing the expected oxide at the surface. In particular, a chemical treatment based on sequential ultrasonic baths of acetone, ethanol, and deionized water was used. The sample was then placed in 1% HF solution for 30 seconds to chemically etch the top oxide layer. This step was followed by a rinsing with deionized water and drying in air.

### 3.1.2 InP:S/InP:Fe KPFM experimental results

In these paragraphs the KPFM results acquired in dark conditions and under illumination on the cross-section of the sample will be presented along with a discussion on the principal factors which affect KPFM measurements in order to develop a methodology of analysis and apply it to the experimental results. Note that the discussion reported in paragraphs 3.1.2.2 and 3.1.2.5 also apply to the InP:Zn/GaInAs(P):Zn sample and it will not be reiterated in the corresponding section.

### 3.1.2.1 KPFM cross-sectional investigation in dark conditions

The experimental procedure followed for the characterization of the InP:S/InP:Fe multilayer structure has been already described in paragraph 2.3.1 and thus only the principal experimental parameters are repeated here. Specifically, KPFM was performed using a scanning probe microscopy system from AIST-NT (TRIOS platform) in ambient conditions, and operated in frequency-modulation KPFM (FM-KPFM) using a two-pass scanning mode where the second pass was performed at a constant distance of 10 nm from the sample surface. AFM tips $n^+$-Si ARROW EFM tips with a conductive Pt/Ir coating at a resonance frequency of 75 kHz were used.

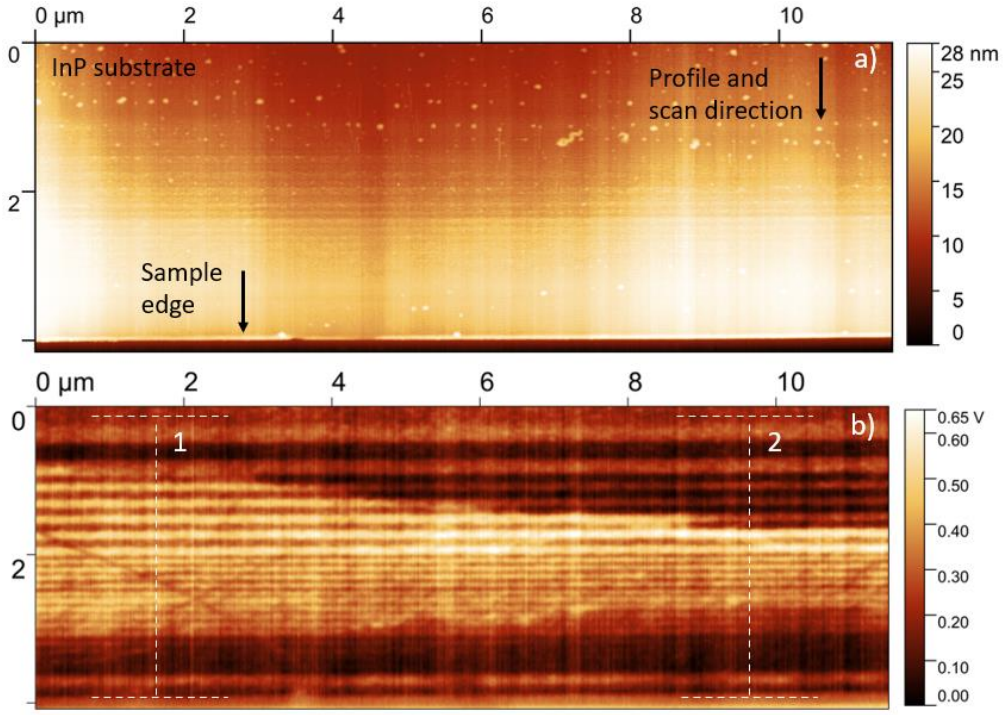


**Figure 2**. KPFM measurement in ambient conditions on the surface cross-section of the InP sample in dark conditions. a) Topography image of the cross-section of the InP sample after chemical removal of the oxide layer. b) The $V_{CPD}$ image measured during the second pass. Two regions with different behavior were detected and labelled with 1 and 2.

The topography and the $V_{CPD}$ images obtained from cross-sectional KPFM investigation in dark conditions after the chemical surface treatment are reported in Figure 2a and 2b, respectively.

According to Figure 1, the dark regions in the $V_{CPD}$ image (see Figure 2b) represent the InP:S layers while the InP:Fe ones are identified by the bright lines.

During the KPFM analysis, the tip scanned vertically the cross-section from the InP substrate to the sample edge which caused the imprint of vertical lines in the images, which is especially observed in Figure 2b. Note that the origin (0;0) is identified as a point in the InP substrate and moving along the positive direction of the y-axis, one will reach the end of the sample.

The topography image (Figure 2a) indicates that a smooth and homogeneous surface was provided by the HF treatment and a complete detection of the stack in the $V_{CPD}$ image was achieved. The topography revealed a dip in its middle (from 3 µm to 8 µm along the x-axis) of 10 nm which cause can be attributed to the cleaving process. Nonetheless, the topographic features are barely visible and thus the nature of the

physical contrast can be attributed to a pure dopant effect excluding any topography imprint on the $V_{CPD}$ map.

The $V_{CPD}$ profiles along region 1 and 2 identified in Figure 2b are reported in Figure 3. These two regions are compared in particular because they show different contrasts for the 100 nm thick layers. For this reason, several vertical profiles around regions 1 and 2 were extracted from the topography image and compared (not shown). All the profiles were comparable definitively excluding the presence of topographic artifacts imprinted on the $V_{CPD}$ image. Therefore, the reason for the discrepancy between these two regions is not of trivial comprehension but may be related either to the deoxidation treatment or to the cleaving process. For this reason, paragraph 3.1.2.2 will be devoted to the description of those factors which can influence $V_{CPD}$ both in terms of sample preparation and experimental conditions. Nonetheless, the examination of $V_{CPD}$ profiles allows a first qualitative analysis. The width of the peaks is comparable to the one of the layers presented in Figure 1. This represents consistent evidence of the great sensitivity of the KPFM technique to the local doping concentration, already reported in a number of publications [9,19].

The intensity of the peaks changes with the width of the layers. In particular, considering the profile extrapolated from region 1, the $\Delta V_{CPD}$ was calculated among adjacent InP:S and InP:Fe with same thickness. Note that in the case of the 100, 50 and, 20/80 regions, which comprise a repetition of 10 layers each, an averaged $\Delta V_{CPD}$ value is reported. In particular, the $\Delta V_{CPD}$ is 230 mV for the 200 nm wide layers, 185 mV for the 100 nm wide layers, 78 mV for the 50 nm wide layers and 52 mV for the 20/80 nm (InP:S/InP:Fe) wide layers, respectively. In the last region, the 80/20nm (InP:S/InP:Fe), the 20 nm wide InP:Fe layers are poorly detected and the evaluation of a clear $\Delta V_{CPD}$ is not achieved. The two uneven 20/80 and 80/20 InP:S/InP:Fe stacks near the cap layer present a different resolution in the detection of the 20 nm thick layers. In the 20/80 region, the InP:S layers are still reasonably well detected despite being only 20 nm thick, whereas the 20 nm InP:Fe layers in the 80/20 region are not well identified although they present the same thickness, this is especially evident in the profile along region 1. Therefore, the poor detection of the 20 nm thick InP:Fe layers cannot be only related to the limitations of resolution of ambient conditions KPFM. In particular, since KPFM demonstrated a strong dependence on the local doping concentration, in the 80/20 region, where the InP:S layers are four times the size of the InP:Fe ones, the contribution to the $V_{CPD}$ signal of the InP:S layers tends to dominate over the one from the InP:Fe due to the large difference in dimension and in the doping concentration between the two layers. As a matter of fact, the $V_{CPD}$ value in the 80/20 region is comparable to the one measured for the 200 nm InP:S thick layer. This is also consistent with the fact that the 20 nm thick InP:S layers in the 20/80 region are reasonably well-resolved. Nonetheless, from this first stage analysis, it is clear that an adequate detection of the narrower layers in the $V_{CPD}$ image becomes more challenging. This is related to the spatial limitations of the KPFM measurement setup. In fact, approaching the 20 nm wide layers, their dimension become comparable to that of the probe (below 25 nm).

Interestingly, InP:S and InP:Fe layers of different but similar thickness tend to show different $\Delta V_{CPD}$ despite, respectively, being of the same S or Fe doping. This suggests that minor changes in thickness can lead to more significant difference in $V_{CPD}$ than one might expect from the position of the bulk Fermi level. The principal reason for this behavior is the fact that successive InP:S and InP:Fe layers form homojunctions, and the extension of the space charge regions depends on the thickness of the layers. In particular, the

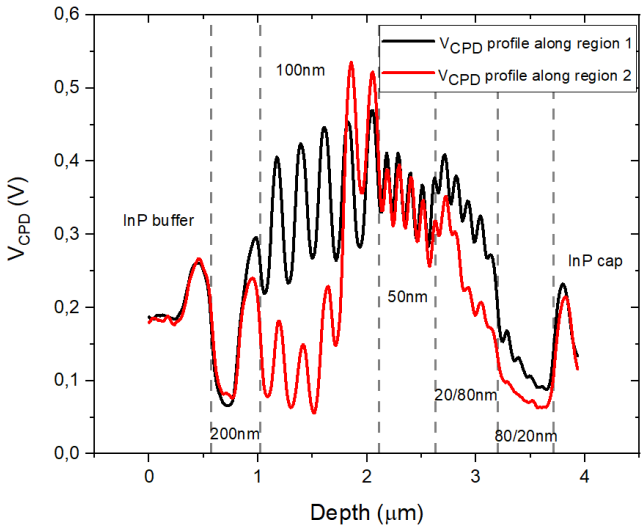


**Figure 3**: Vertical profiles of the two regions labeled with 1 and 2 identified in the $V_{CPD}$ map in Figure 3b. The profiles correspond to the regions identified by the two dotted white segments, and they were obtained by averaging over a width of 128 points.

effect of space charge on $V_{CPD}$ will be discussed in paragraph 3.1.2.3 with the help of energy bands modelling.

### 3.1.2.2 Sample preparation and KPFM experimental conditions

We have described in the previous paragraph that different $V_{CPD}$ values were detected for the two different regions identified in Figure 2b despite belonging to the same scan and being distant only a few micrometers. Several factors can influence KPFM measurements, namely the experimental conditions and the status of the sample surface and AFM tip, additionally the presence of surface nonidealities (e.g., surface defects) have an effect on the surface potential and thus on the measured $V_{CPD}$. All these aspects can lead to surface inhomogeneities which result in $V_{CPD}$ variations compared to the otherwise constant in bulk material.

A further aspect to consider concerns the experimental conditions. KPFM analysis was carried out in ambient conditions which result in surface oxidation and in the adsorption of water molecules on the sample surface due to the humidity present in air [20]. Furthermore, a non-optimal deoxidation procedure may result in an inhomogeneous removal of the surface oxide. Additionally, the condition of the tip during the numerous scans along the sample cross-section must also be considered. In particular, the contamination of the tip is likely to occur due to pollutants (e.g., nano and/or micron size dust grains) which may be present on the sample surface producing a variation of the tip surface potential. For these reasons, the reproduction of identical $V_{CPD}$ profiles along the structure analyzing different regions is a challenging task. Furthermore, we have pointed out how the lateral resolution of the KPFM technique decreases with the width of the layers. This phenomenon relates to the tip-averaging effect due to the long-range nature of the electrostatic force. Since the layers are particularly narrow and alternate, the KPFM tip, scanning at tip-surface distance of 10 nm, can sense multiple layers at the same time resulting in the detection of an averaged $V_{CPD}$. In our case, this effect is especially relevant since the dimension of the narrower layer (20 nm) is comparable to the radius of the tip. The tip-averaging effect largely affects the lateral resolution and the measured KPFM signal, even for very small tip-sample distance (5 nm) [21]. This is particularly

observed in ambient conditions KPFM measurements, where typical tip-surface distances are of the order of tens of nm due to the amplitude of the vibrating tip required to obtain a reasonable signal-to-noise ratio.

### 3.1.2.3 Effect of the space charge on the $V_{CPD}$

As mentioned in paragraph 3.1.2.1, successive layers of InP:S and InP:Fe form homojunctions with layer thicknesses ranging from 200 nm to 20 nm. Note that the width of the space charge is determined by the doping concentration, and thus an electron accumulation region is expected in the InP:Fe layers that have less Fe impurities as compared to the S concentration in the InP:S layers. Given the thicknesses of the fabricated layers, it can be expected that all InP:Fe layers are in accumulation and that "the end" of the space charge is never reached, hence limiting the $V_{CPD}$ contrast.

As anticipated in paragraph 3.1.1, Fe impurities introduce acceptor levels in the mid-gap region of InP that compensate residual shallow donors making the InP semi-insulating. The Fe doping thus is responsible for increasing the resistivity of the InP material. The literature reports that introducing a concentration of the order of $10^{16}$ $cm^{-3}$/$10^{17}$ $cm^{-3}$ of Fe impurities results in resistivities of InP reaching values of the order of $10^{7}$/$10^{8}$ Ωcm with an associated residual majority charge carrier density (electrons) of $10^{7}$/$10^{6}$ $cm^{-3}$ [22]. For this reason, in order to replicate the band profiles of the structure, we have used Silvaco software [23] to model a $n^{+}n$ homojunction specifying a doping concentration of $2\times10^{19}$ $cm^{-3}$ and $10^{6}$ $cm^{-3}$ for the InP:S and InP:Fe layers respectively. The energy variation of the valence and conduction bands along the structure is reported in Figure 4a along with the Fermi level ($E_F$). Note that the Fermi level is pushed within the conduction band (degenerate) due to the higher doping concentration of S with respect to the InP effective conduction band density of states ($5.7\text{x}10^{17}$ $cm^{-3}$).

As mentioned at the beginning of this section and shown in Figure 4a, the thickness of the layers has a direct impact on the width of the space charge region among the homojunctions. As comparison, the energy bands profile variation of a hypothetical 2 µm thick InP:S/InP:Fe structure constituted by only two layers was simulated maintaining the same parameters and reported in Figure 4b. In this case, InP:Fe bands finally reach the flat-band condition showing that the space charge region extends in the InP:Fe for around 1 µm.

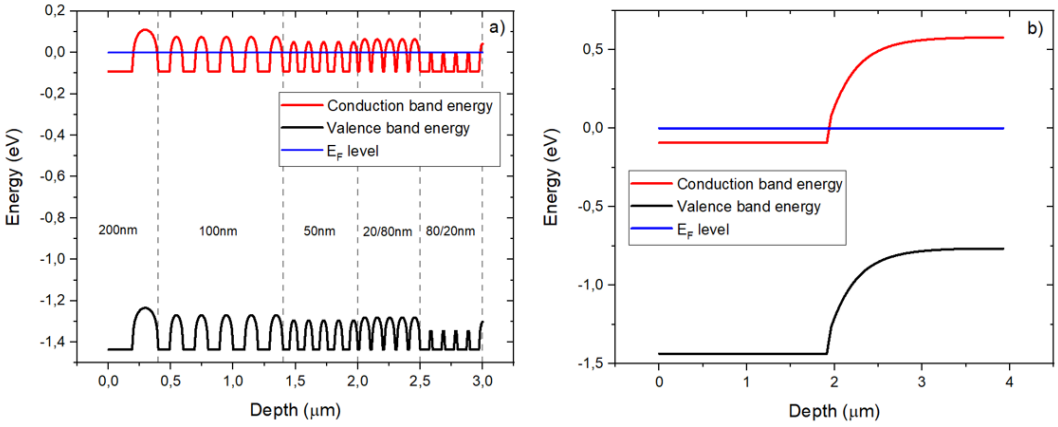


**Figure 4**: Valence and conduction band energy profiles a) along the InP:S/InP:Fe structure and b) along a hypothetical 2 µm thick InP:S/InP:Fe homojunction. The valence and conduction bands are represented by the black and red color, respectively. The Fermi level ($E_F$) level represents the reference frame, and it is reported in blue.

In the case of our sample, the space charge region covers the entire width of the InP:Fe layers. This has a direct effect on the $V_{CPD}$ values since the number of charges in the space charge region depends on the thickness of the layers, this reveals how decreasing the thickness of the layers decreases the corresponding potential variation and in turn $V_{CPD}$.
Moreover, the bands evolution of this simpler structure points out also that the space charge is present at both sides of the InP:Fe layers since each layer is in contact with two different InP:S layers. This is the reason why the InP:Fe bands in our sample structure are symmetric with respect to an axis passing through half of the thickness.

#### 3.1.2.4 KPFM under illumination: the effect of the light

As a final step of this characterization, the $V_{CPD}$ was also evaluated under top illumination using the white light coming from the CCD camera (see paragraph 2.3.1).
In order to evaluate the effect of the illumination on the sample, KPFM measurements were thus started in dark conditions (region 1) and completed under illumination (region 2); the corresponding $V_{CPD}$ map is reported in Figure 5.
Interestingly, the inhomogeneities described in section 3.1.2.2 are also visible in the dark $V_{CPD}$ profile reported in Figure 6a. Although it is not directly comparable with the two dark $V_{CPD}$ profiles in Figure 3, it is evident that it shows the same qualitative $V_{CPD}$ profile. A significant contrast improvement is observed along all the structure, as shown by the red profile in Figure 6a. The peaks related to the illuminated region are more pronounced with respect to ones extrapolated from $V_{CPD}$ values obtained in dark conditions. In particular, the 20 nm and 80 nm wide layers in the last two regions are only visible and well-distinguished after the application of the light, as highlighted by the more prominent red peaks in the zoomed vertical profiles reported in Figure 6b.

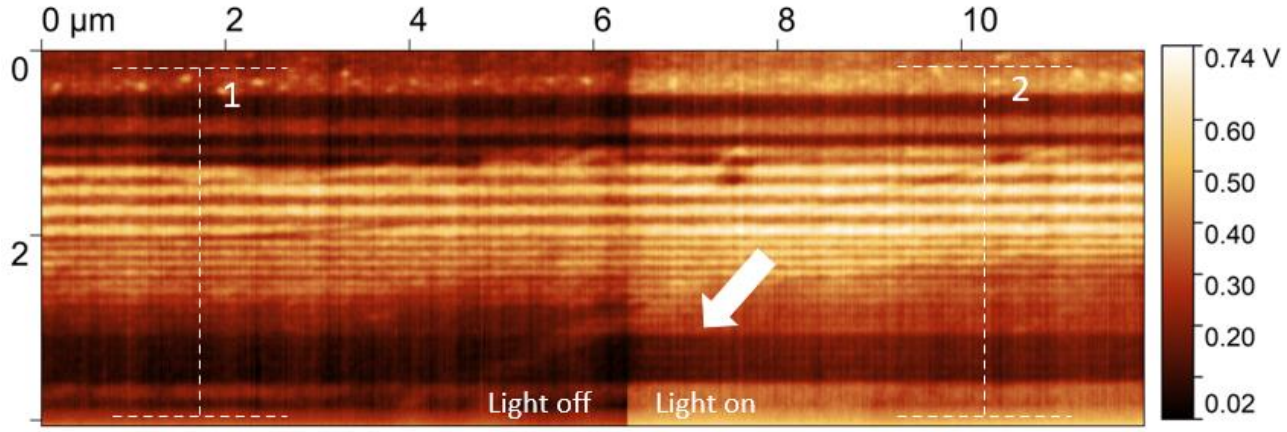


**Figure 5:** KPFM measurement in ambient conditions on the surface cross-section of the InP sample in dark conditions (left half) and under white light illumination (right half).

According to the definition of surface photovoltage ($SPV = V_{CPD(light)} - V_{CPD(dark)}$), from Figure 6a we observe that the *SPV* is positive all along the structure in the order of hundreds of mV for both the InP:S and InP:Fe layers, which is unexpected from the bulk properties of InP:S. In particular, for the highly-doped InP:S, we expect a positive *SPV* but close to 0 and probably below detection limits under the low light intensity illumination used in the experiment [24].

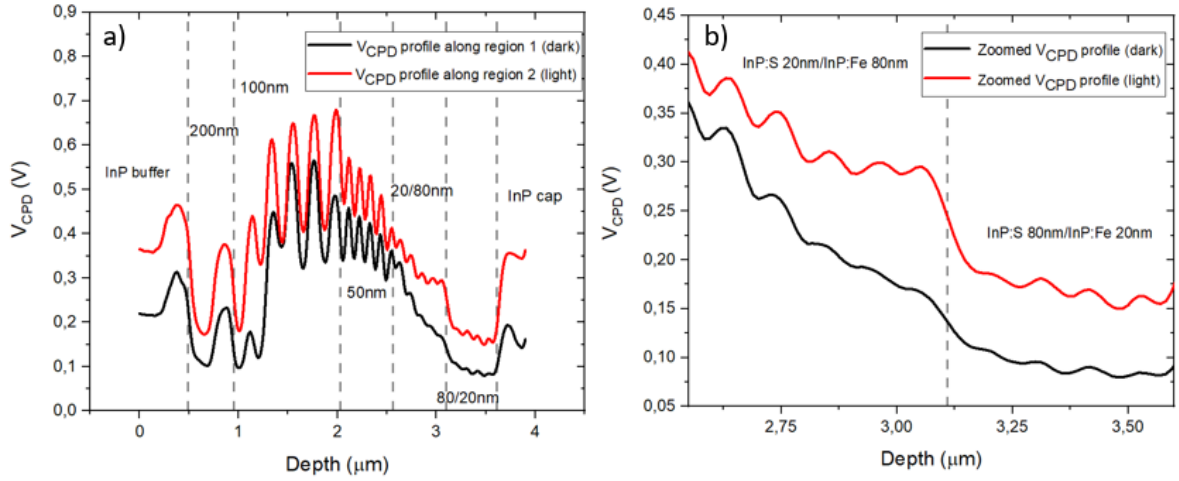


**Figure 6:** a) Vertical profiles extrapolated from the dark and illuminated region of Figure 5. b) Vertical profiles extrapolated from the dark and illuminated regions zoomed on the 20 and 80 nm layers. Note that the profiles correspond to the regions identified by the two dotted white segments in Figure 5.

### 3.1.2.5 Effect of the illumination on the surface band-bending

In the previous section, we have pointed out the enhancement of contrast in the $V_{CPD}$ image after white light illumination of the sample cross-section. In particular, since the bulk lattice periodicity is interrupted at the surface of a cleaved semiconductor, surface reconstruction and formation of dangling bonds of surface atoms may occur creating surface states within the energy bandgap. For instance, these surface states can pin the Fermi level and cause downward (upward) band-bending from the bulk to the surface in a p-type (n-type) semiconductor in the case of the formation of a depletion (or inversion) space charge layer imposed by the charge neutrality condition [25,26].

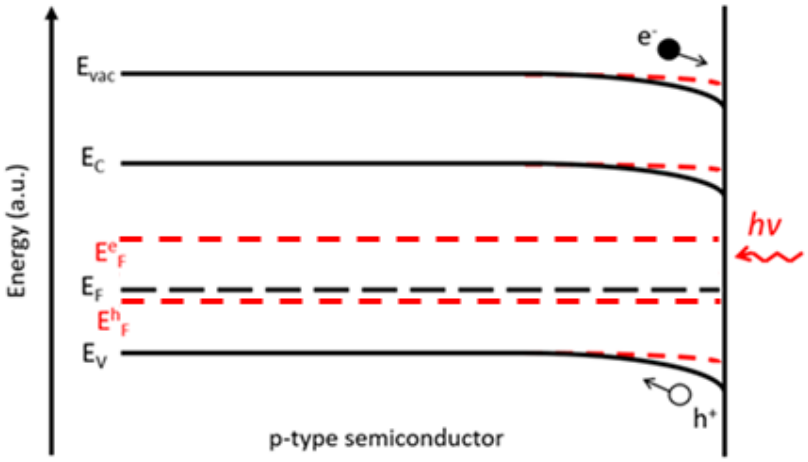


**Figure 7:** Representation of the energy bands profile in a p-type semiconductor in dark conditions and under illumination depicted by black solid lines and red dashed lines, respectively. $E^e_F$ and $E^h_F$ represent possible profiles for the quasi-Fermi levels for electron and holes, respectively.

By illuminating the sample, a *SPV* is generated by the drift and diffusion of photo-generated carriers towards the surface which counteracts the defect-induced band-bending energy variations [24].

As illustrated in Figure 7, in the case of downward surface band-bending in an p-type semiconductor, photogenerated holes are repelled from the surface, while photogenerated electrons flow in the direction of the surface, balancing the positive charges corresponding to empty donor-type surface states. This results in a reduction of surface band-bending and a decrease of surface potential, i.e., a negative *SPV*.
Conversely, in the case of upward surface band-bending in an n-type semiconductor, photogenerated electrons are repelled from the surface, while photogenerated holes flow towards the surface, balancing the negative charges corresponding to ionized occupied acceptor-type surface states, i.e., a positive *SPV*. However, in case of pn junctions, the *SPV* can also include the contribution of an open-circuit voltage due to the splitting of the quasi-Fermi levels of electrons and holes [27]. Moreover, experiments performed on silicon wafers with varying doping densities have shown that, overall, the *SPV* signal tends to be larger for low doping densities [27].
From Figure 8 we observe that the *SPV* is positive all along the structure in the order of hundreds of mV for both the InP:S and InP:Fe layers with variations in the order of tens of mV and it can be noticed that the *SPV* is indeed larger in the InP:Fe layers.
The *SPV* sign is in good agreement with what is expected for the InP:S and InP:Fe layers. However, in terms of *SPV* intensity, a significant positive *SPV* is detected in the highly doped n-type InP:S layers which is surprising considering the low light intensity illumination since in the absence of surface states a very low *SPV* signal is expected after the illumination by a low light intensity [24]. Nonetheless, as it will be shown in section 3.2.3, this can be explained by the presence of a large surface states density caused by surface defects inducing significant upward band-bending even in highly doped layers [19,24] and thus the light-induced surface band-bending reduction explains the significant contrast improvement in the $V_{CPD}$ image reported in Figure 5 and described in section 3.1.2.4.

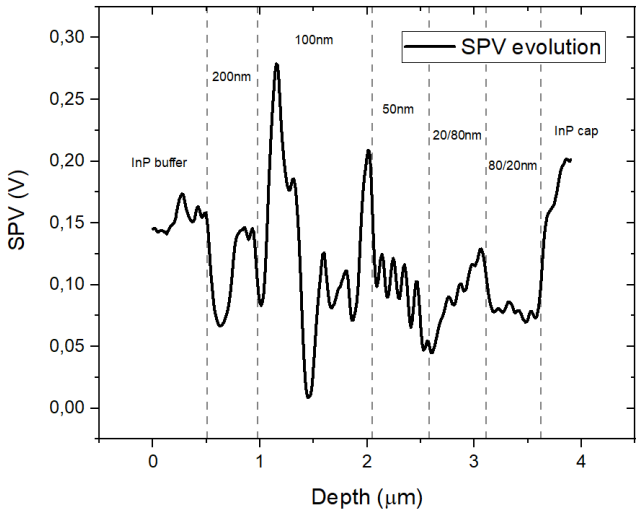


**Figure 8:** *SPV* profile along the structure calculated from the dark and light profiles showed in Figure 6a.

## 3.2 Cross-sectional Kelvin Probe Force Microscopy on III-V epitaxial multilayer stack: challenges and perspectives

For this second work we have selected a sample whose structure reflects more the one of a III-V solar cell. In this work we have strongly implemented KP modelling in order to provide a quantitative explanation of the effect of surface defects on the experimental $V_{CPD}$.

### 3.2.1 InP:Zn/GaInAs(P):Zn sample preparation

The structure of the studied sample is summarized in Table 1. This multilayer stack structure was epitaxially grown using a MOVPE process in an AIXTRON Close-Coupled Showerhead reactor (6 x 2") at three different surface temperatures (640/600/580°C). The n-type AXT substrate doping was typically in the range of 3 to $5x10^{18}$ $cm^{-3}$ with a thickness of 500 µm. Trimethylindium (TMIn), trimethylgallium (TMGa), phosphine ($PH_3$) and arsine ($AsH_3$) were the source materials, with hydrogen ($H_2$) as a carrier gas. Diethylzinc (DEZn) compound was used as a source of Zn for p-type doping for InP:Zn, phosphorus-based quaternary (GaInAsP:Zn) and GaInAs:Zn layers by varying the precursor flow in order to cover a doping level range from $1x10^{18}$ $cm^{-3}$ to $2.5x10^{19}$ $cm^{-3}$. The first part of the structure was used to measure the growth rate of the non-intentionally doped InP layers (InP:nid) at surface temperatures of 640 and 600°C. The reflectance signal, monitored with an in-situ Laytec EpiCurve TT tool, did not show any difference between the growth rates at the two surface temperatures, which were around 2.13 µm/h. The second part of the structure corresponds to the Zn calibration stack used for the p-type cladding of multi quantum wells (MQWs) based structure. The doping concentration of the InP:Zn layers was made varying from $2x10^{18}$ $cm^{-3}$ to $1x10^{18}$ $cm^{-3}$. Here, the three Zn doping levels of InP layers were purposely inverted along the growth direction to facilitate electrochemical capacitance-voltage (ECV) characterization due to the strong Zn diffusion. The InP:Zn and the GaInAsP:Zn layers were epitaxied at a surface temperature of 600°C. Note that the GaInAsP:Zn is an intermediate layer with a doping concentration of $6x10^{18}$ $cm^{-3}$ with the purpose to smooth the InP:Zn/GaInAs:Zn transition bandgap and reduce contact resistances. Finally, a GaInAs:Zn contact layer was made at a lower temperature of 580°C in order to reach a higher doping level around $2.5x10^{19}$ $cm^{-3}$.

| Layer | Material | Doping concentration ($cm^{-3}$) | Thickness (nm) |
|---|---|---|---|
| Substrate | InP:S | $3\text{-}5x10^{18}$ | 500µm |
| Buffer | InP | nid | 100 |
| Interlayer | GaInAs | nid | 5 |
| Buffer | InP | nid | 300 |
| Interlayer | GaInAs | nid | 5 |
| Buffer | InP | nid | 250 |
| Cladding | InP:Zn | $2x10^{18}$ | 500 |
| Cladding | InP:Zn | $1.50x10^{18}$ | 750 |
| Cladding | InP:Zn | $1x10^{18}$ | 500 |
| Transition | GaInAsP:Zn | $6x10^{18}$ | 20 |
| Contact | GaInAs:Zn | $2.50x10^{19}$ | 200 |

**Table 1:** Full structure of the investigated multilayer stack sample.

Before starting the KPFM analysis, the sample was cleaved, and a surface cleaning was carried out to expose a clean cross-section. We performed a chemical treatment based on sequential ultrasonic baths of acetone, ethanol, and deionized water. The sample was then placed in 1% HF solution for 30 seconds to etch the top oxide layer. This step is followed by a rinsing with deionized water and drying in air. This

procedure was necessary for an optimal KPFM analysis since the presence of a native oxide surface layer on top can influence the $V_{CPD}$ measurements [19].

## 3.2.2 Cross-sectional KPFM results on InP:Zn/GaInAs(P):Zn

The forthcoming section will present the obtained KPFM results on the cross section of the InP:Zn/GaInAs(P):Zn sample, both in the absence of light and under illumination. To ensure the originality of our study with respect to the InP:S/InP:Fe sample analyzed in the previous section, we have extensively incorporated KP modeling to offer a comprehensive and quantitative analysis of the experimental findings.

### 3.2.2.1 KPFM cross-sectional investigation in dark conditions

The cross-section of the sample was first investigated by KPFM in dark conditions, immediately after the chemical cleaning step. The topography and the associated $V_{CPD}$ image are reported in Figure 9a and 9b, respectively. Note that the origin (0;0) is identified as a point in the InP substrate and moving along the positive direction of the y-axis, one will reach the end of the sample that is the surface of the 2D wafer (e.g., around 3.09 µm in Figure 9a). In order to achieve a successful KPFM analysis, a low surface roughness is essential to obtain high-quality images since surface inhomogeneities can cause a topographical image imprint on the surface potential image. With sufficiently low surface roughness, the topographic influence on the measurement is minor, and the observed contrast of the $V_{CPD}$ map is dominated by the surface potential such that topographic artefacts can be neglected.

A first look at the $V_{CPD}$ image and the extrapolated profile (Figure 9c) allows a qualitative analysis. KPFM successfully detects the n-InP substrate (from 0 µm to 0.46 µm), the InP:nid/GaInAs:nid region (from 0.46 µm to 1.12 µm), the InP:Zn region (from 1.12 µm to 2.87 µm), and the GaInAsP:Zn/GaInAs:Zn region (from 2.87 µm to 3.09 µm).

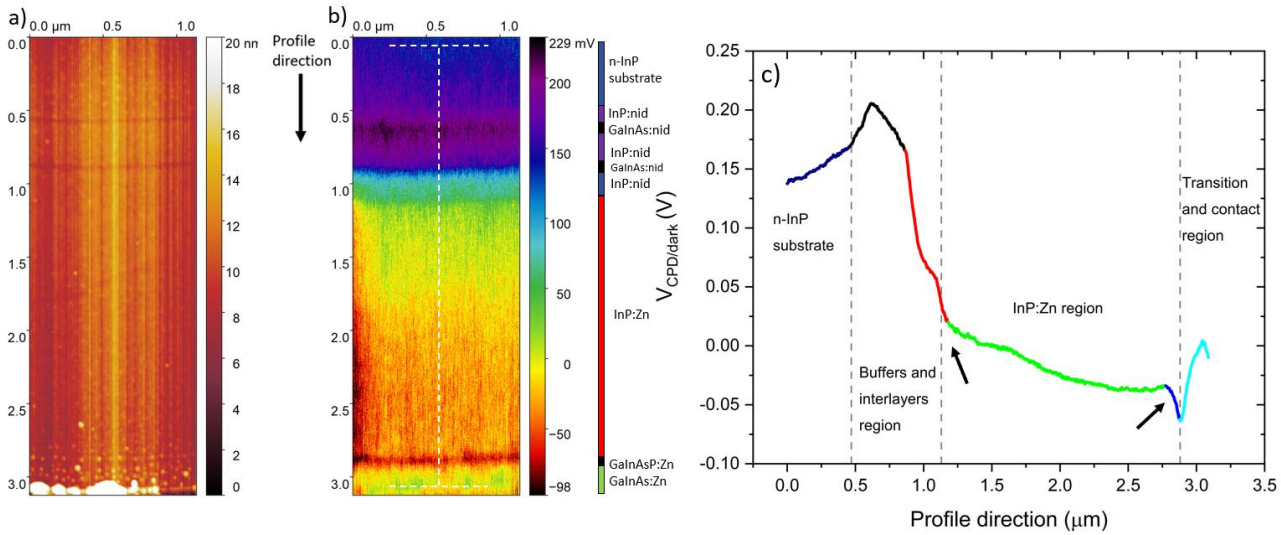


**Figure 9:** KPFM measurement in ambient conditions on the surface cross-section of the sample in dark conditions: (a) topography and (b) $V_{CPD}$ image. A vertical-coloured bar was included to ease the identification of the different layers. The profile in (c) corresponds to the region identified by the dotted white segments in b), each point of the profile (vertical) direction being an average of 207 points over a width of 0.7 µm along the x-axis. Several regions along the structure have been highlighted using different colours (see text). Two black arrows were included to indicate the space charge regions at the interfaces of the InP:Zn region.

KPFM demonstrated a strong sensitivity on the local doping concentration as reported in a number of publications [3,6]. However, a clear identification of the 5 nm GaInAs:nid interlayers among the InP:nid buffer layers is not achieved in the $V_{CPD}$ image. Nevertheless, their presence was still detected and represented in the $V_{CPD}$ image by the dark and blue lines at 0.61 µm and 0.91 µm, respectively. The low resolution of the interlayers can be attributed either to their narrowness and/or to the experimental conditions since the two GaInAs:nid layers are well-resolved in the topography image. Certainly, the width of these layers is narrower than the radius of the tip (below 25 nm) and the operating conditions, namely the tip-surface distance and ambient measurements, negatively affect the resolution of KPFM measurements [30]. In particular, KPFM in ambient conditions is affected by the tip-averaging effect due to the long-range nature of the electrostatic force: the tip can sense multiple layers with different properties simultaneously, resulting in the detection of an averaged $V_{CPD}$ at the interfaces [31].

During KPFM measurements, the tip scans the cross-section from the n-InP substrate to the end of the sample and consequently it will sense the surface potential variation along the structure. The progression of the $V_{CPD}$ profile shows that four different slopes are present considering the region from the last InP:nid buffer layer to the GaInAs:Zn contact layer (from 0.86 µm to 3.09 µm). In particular, the first is located between the last InP:nid buffer layer and the first InP:Zn layer (from 0.86 µm to 1.17 µm), the second in the InP:Zn region (from 1.17 µm to 2.76 µm), the third between the last InP:Zn layer and the GaInAsP:Zn transition layer (from 2.76 µm to 2.87 µm), and the fourth between the GaInAsP:Zn transition layer and the GaInAs:Zn contact layer (from 2.87 µm to 3.09 µm). These regions have been identified with the colours red, green, blue, and light blue in the $V_{CPD}$ profile, respectively.

The green profile represents the InP:Zn region and, due to the comparable doping concentration of the three InP:Zn layers, a small variation of $V_{CPD}$ of the order of 20 mV is expected to be measured along this region. However, the experimental $V_{CPD}$ profile presents a $V_{CPD}$ variation of the order of 50 mV along the InP:Zn region (from 1.13 µm to 2.87 µm). Several factors can influence KPFM measurements leading to this experimental evidence namely the sample preparation, the experimental conditions, and the presence of surface defects. All these aspects have an impact on the surface potential, as already described in paragraph 3.1.2.2.

For what concerns the other slopes pointed out above, their detection is attributable to the formation of space charge regions among the different layers along the structure [28]. Specifically, the $V_{CPD}$ profile reflects the band-bending present in the presence of depletion and accumulation regions.

In particular, undoped InP crystals always contain different unintentional impurities due to the growth processes. The InP:nid layers fabricated at III-V Lab usually present an intrinsic n-type doping of the order of $10^{15}$ $cm^{-3}$ which results in shallow donor energy levels within the energy gap. Since the intentional Zn p-type doping concentration is much greater than this residual n-type doping present in the InP:nid buffer, the space charge region is expected to be located almost exclusively in the buffer layer.

Similarly, two Zn doping concentration gradients are present from the last InP:Zn layer to the GaInAsP:Zn transition layer (from $1x10^{18}$ $cm^{-3}$ to $6x10^{18}$ $cm^{-3}$) and from the GaInAsP:Zn transition layer to the GaInAs:Zn contact layer (from $6x10^{18}$ $cm^{-3}$ to $2x10^{19}$ $cm^{-3}$), respectively. This results in two space charge regions situated almost completely in the InP:Zn layer and in the GaInAsP:Zn transition layer, respectively.

It is worth to mention that the band-bending induced by the different space charge regions along the structure depends on the doping concentration (e.g., number of involved charge carriers) and on the width of the layers and consequently the corresponding $V_{CPD}$ variation will depend on the same parameters [3].

In order to investigate the effect of the space charge on the measured $V_{CPD}$ we have implemented theoretical modelling to this work. As a first step, we have simulated through ATLAS/Silvaco software [23] the energy bands profile of the analysed structure in the ideal case in which no surface defects are considered, qualitatively reproducing the expected energy bands profile in our sample. The widths and doping concentrations of the layers were chosen as reported in Table 1, whereas the other physical parameters (e.g., energy gaps) are present in the Silvaco database [23]. Note that in order to simulate the InP:Zn region we have specified just one Zn doping concentration of $1.5 \times 10^{18}$ $cm^{-3}$. Furthermore, in order to replicate the experiment, we have included a metal layer on the left of the n-type InP substrate. Under these conditions, the metal layer represents the contact between the sample-holder and the n-type InP substrate. Finally, the WF of the metal is set to be equal to that of the substrate to guarantee an ohmic contact.
The simulated energy bands profile confirmed our hypothesis showing the induced band-bending along three space charge regions at the InP:nid/InP:Zn, the InP:Zn/GaInAsP:Zn and the GaInAsP:Zn/GaInAs:Zn interfaces, as shown in Figure 10a.
In particular, due to the low doping concentration of the InP:nid layer compared to the adjacent n-InP substrate and InP:Zn region, a space charge extends over its complete width. The $V_{CPD}$ profile across the InP:Zn/GaInAsP:Zn/GaInAs:Zn interfaces results from the different work functions. The work function of GaInAsP:Zn is slightly larger (by 0.04 eV) than that of InP:Zn, but it is 0.32 eV smaller than that of the GaInAs:Zn contact layer, which leads to a decrease and an increase of potential, respectively. It is important to note that due to the narrowness of the GaInAsP:Zn transition layer (20 nm), the space charges at the two neighbor heterojunctions overlap in this layer, leading to an asymmetric U shape of the $V_{CPD}$ profile. The asymmetric U shape is also present in the experimental profile in Figure 9c (dark blue and light blue parts emphasizing the decrease and increase in potential, respectively).

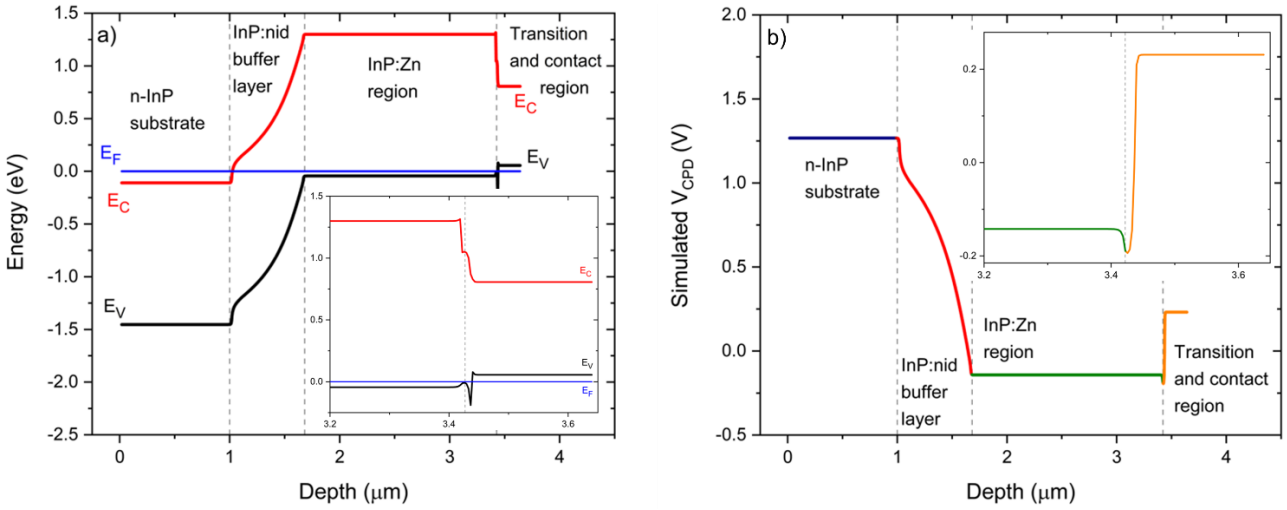


**Figure 10**: a) Cross-sectional profile at equilibrium of the surface band energies (black: valence band maximum, $E_V$, and red: conduction band minimum, $E_C$) along the structure assumed free of any surface defects. The constant Fermi level, $E_F$, is taken as the energy reference (blue horizontal line). b) $V_{CPD}$ profile along the same simulated structure obtained by KP modelling. Note that both figures present an inset detailing the InP:Zn/GaInAsP:Zn/GaInAs:Zn interfaces close to the external surface of the sample.

The mismatches at the conduction and valence bands between these materials then leads to the peculiar band energy diagram. Insets have been added to Figures 10a and 10b to zoom in this region. Additionally,

KP modelling [32] was used to simulate the $V_{CPD}$ profile along the same structure assumed free of any surface defects for a quantitative evaluation of the effect of space charge on the surface potential (see Figure 10b). On this point it is reminded that $V_{CPD}$ is proportional to the difference between the vacuum level and $E_F$ and therefore the changes in the energy bands profile will be reflected in the simulated $V_{CPD}$ profile.

The simulated $V_{CPD}$ profile shows the same qualitative progression as the experimental profile reported in Figure 9c. However, several important differences can be noted by the comparison between the experimental and simulated $V_{CPD}$. In particular, the experimental $V_{CPD}$ profile (Figure 9c) seems to show that part of the first space charge extends in the first InP:Zn layer (from 1.12 µm to 1.20 µm) and similarly, the second space charge seems to extend more in the last InP:Zn layer than the modelling predicts (from 2.76 µm to 2.87 µm), these two regions are indicated by the two black arrows in Figure 9c. Additionally, the simulated $V_{CPD}$ shows a flat profile after few nanometers inside the GaInAs:Zn contact layer whereas experimentally, a flat surface potential is not reached. In other words, experimentally surface potential variations occur over distances larger than that one may expect solely from the extrinsic Debye lengths calculated from the nominal doping densities which are only a few nanometers [33]. As a consequence, the lack of a sharp transition among the interfaces can cause difficulties in identification of the position of the metallurgical junctions in the $V_{CPD}$ image [34]. In particular, one reason can be found in the aforementioned tip-averaging effect: the tip still senses part of the space charge in the InP:nid buffer layer and in the GaInAsP:Zn transition layer although being already on the first InP:Zn layer and on the GaInAs:Zn contact layer, respectively. Similarly, the tip starts to sense prematurely part of the space charge inside the last InP:Zn layer. Furthermore, non-ideal abrupt junctions may contribute to this effect for instance due to dopants interdiffusion, as will be described in section 3.2.2.2.

Finally, the simulated $V_{CPD}$ progression predicts an overall surface potential change of the order of around 1.34 V from the n-type InP substrate to the InP:Zn region. Conversely, this $V_{CPD}$ variation in our experimental results is of the order of around 0.18 V. This represents a first indication that the experimental surface potential is modified by the presence surface states induced by surface defects, since we know that KPFM is a surface technique, and that the simulated $V_{CPD}$ variation at this stage is based solely on bulk material properties and are not affected by any surface defects. Therefore, the experimental surface potential results to be less pronounced than in the «gedanken profile» that occurs far from the surface; this part will be fully addressed in section 3.3.2.3.

#### 3.2.2.2 KPFM cross-sectional investigation under illumination

In order to study the effect of the illumination on the sample cross-section, we have performed KPFM measurement under white light illumination. The topography and the associated $V_{CPD}$ image are reported in Figure 11a and 11b, respectively.

The $V_{CPD/light}$ image of Figure 11b shows a significant contrast enhancement due to the interaction with the light compared to $V_{CPD/dark}$ of Figure 9b. As a consequence, $V_{CPD/light}$ results to be more homogenous all along the cross-section with respect to the $V_{CPD/dark}$, as shown in the corresponding $V_{CPD/light}$ profile reported in Figure 11c. Moreover, the improvement of contrast also facilitates the identification of the narrower interlayers and of the position of the metallurgical junctions at the InP:nid/InP:Zn and the InP:Zn/GaInAsP:Zn interfaces being previously more undefined in the $V_{CPD/dark}$ image. Overall, the $V_{CPD/light}$ profile follows the same evolution as the $V_{CPD/dark}$ one and even in this case four different $V_{CPD}$ slopes are

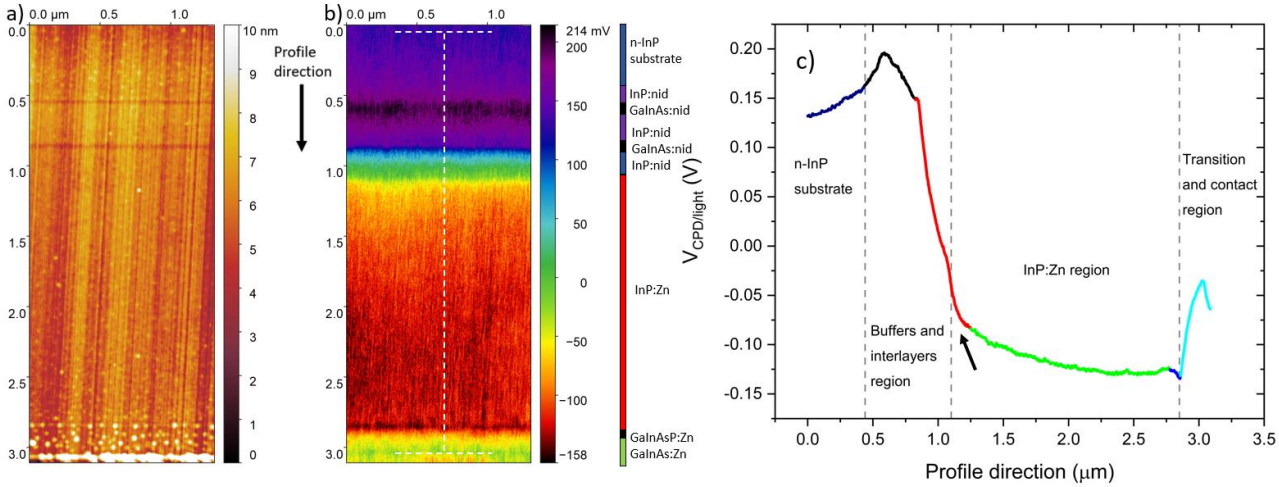


**Figure 11:** KPFM measurement in ambient conditions on the surface cross-section of the sample under illumination: (a) topography and (b) $V_{CPD}$ image. A vertical-coloured bar was included to ease the identification of the different layers. The profile in (c) corresponds to the region identified by the dotted white segments in b), each point of the profile (vertical) direction being an average of 207 points over a width of 0.7 µm along the x-axis. Several regions along the structure have been highlighted using different colours (see text). A black arrow was included to indicate the space charge region at the InP:nid InP:Zn interface.

present in the profile. In particular, the first is located between the last InP:nid buffer layer and the first InP:Zn layer (from 0.83 µm to 1.25 µm), the second in the InP:Zn region (from 1.25 µm to 2.78 µm), the third between the last InP:Zn layer and the GaInAsP:Zn transition layer (from 2.78 µm to 2.85 µm), and the fourth between the GaInAsP:Zn transition layer and the GaInAs:Zn contact layer (from 2.85 µm to 3.07 µm). These regions have again been identified with the colours red, green, blue, and light blue in the $V_{CPD}$ profile, respectively.Notably, the $V_{CPD/light}$ profile along the InP:Zn region between 1.25 µm and 2.78 µm is flatter compared to that of $V_{CPD/dark}$. This $V_{CPD/light}$ profile is more consistent with what the modelling predicts for such small variations in the Zn doping concentration along the InP:Zn region. Conversely, at the beginning of the InP:Zn layer, from 1.10 µm to 1.25 µm (indicated by the black arrow), the $V_{CPD}$ profile presents a steeper slope suggesting that the tip is still sensing the band-bending induced by the space charge between the last InP:nid and the first InP:Zn layer. However, the tip-averaging effect alone cannot explain the detection of a space charge that extends for around 0.16 µm inside the first InP:Zn region. As a matter of fact, the diffusion of Zn impurities is likely to happen due to the high temperatures required for the growth of the material and the high diffusion coefficient of Zn in InP [35]. Therefore, the true spatial extent of the space charge region is not trivial to determine and may differ from what would be expected given the nominal structure of the sample. Conversely, the width of space charge region between the last InP:Zn layer and the GaInAsP:Zn transition layer is reduced and closer to the modelled one. Additionally, the detected surface potential change related to the space charge region at the GaInAsP:Zn/GaInAs:Zn interface is higher and closer to the simulation.

The *SPV* along the structure is reported in Figure 12. The *SPV* progression along the structure shows an overall negative *SPV*. For highly doped semiconductors in the absence of surface states (or for surface state densities small enough so that they cannot introduce significant surface band-bending) a *SPV* signal close to 0 is expected to be measured [24]. We therefore expect a vanishing *SPV* signal in the highly doped n-type InP substrate which is degenerately doped at $5x10^{18}$ $cm^{-3}$ with respect to the InP effective conduction

band density of states ($5.7x10^{17}$ $cm^{-3}$ [36]). Experimentally the uncertainty on extracted *SPV* values can be evaluated at ± 20mV, so the obtained value of around -10mV in the highly doped n-type InP substrate is in good agreement with the theoretical expectation of vanishing *SPV*.

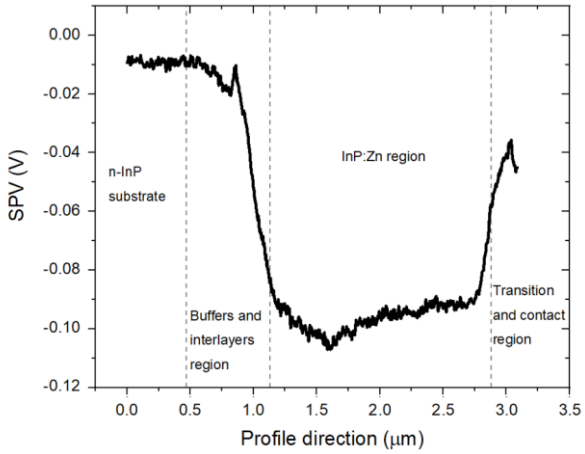


**Figure 12:** *SPV* profile along the structure calculated from the $V_{CPD/dark}$ and $V_{CPD/light}$ values showed in the profiles of Figure 9c and Figure 11c, respectively.

Furthermore, a negative *SPV* of around -95 mV is estimated for the InP:Zn region, which is consistent with the fact that a negative *SPV* is expected for a p-type semiconductor due to surface band-bending caused by surface states produced by surface defects. In particular, the detection of a negative *SPV* implies that a downward band-bending is present in the vicinity of the surface [25], this aspect will be fully addressed in section 3.2.3.1. Finally, it is worth mentioning that after illumination the initial conditions are restored, which excludes the presence of long-lived charge accumulation along the different junctions.

## 3.2.3 Surface defects

It is evident from the KPFM results shown on these two III-V based multilayer structures that the surface defects plays a central role on the experimental value of $V_{CPD}$, and their comprehension is crucial for a quantitative understanding of the experimental data. For this reason, before presenting the modeling results (paragraphs 3.2.4.1 and 3.2.4.2) used to provide a quantitative interpretation of the $V_{CPD}$ profiles shown in Figure 9c and 11c, it is important to dedicate a section to the description of surface defects and their impact on the surface band-bending with particular attention to the surface space charge and Fermi level pinning. For this reason, the subsequent sections (3.2.3.1 and 3.2.3.2) present a concise version of the theory concerning surface defects of semiconductor surfaces, derived from extensive analysis of three distinct sources [26,28,29]. Additionally, original modeling was added to analyze the effect of the Fermi level pinning in terms of surface defects-induced surface band-bending in function of variable doping concentrations.

### 3.2.3.1 Space-charge layers at semiconductors surfaces

A semiconductor surface is generally characterized by the presence of electronic surface states which represent a perturbation to the local charge balance. In particular, depending on the type of surface states

and on the position of the Fermi level at the surface, surface states may be charged. This surface charge is screened by an opposite charge inside the semiconductor material. It is worth to mention that, in semiconductors the free-carrier concentration is of the order of $10^{17}$ $cm^{-3}$ and as a consequence the typical screening lengths are of the order of hundreds of ångströms.

According to the theory it is possible to define two different kind of surface states based on their energy position relatively to the bulk conduction and valence band. In particular, surface states with high energy are derived from the conduction band and are called acceptor-type surface states. Similarly, surface states with lower energy are derived from the valence band and are called donor-type surface states (Figure 13). Acceptor-type and donor-type surface states show a different charging character. Specifically, the former is negatively charged when occupied and neutral when empty; conversely, the latter is neutral when occupied and positively charged when empty.

To summarize, donors and acceptors can carry a positive and a negative charge respectively, depending on the position of the Fermi level ($E_F$) at the surface.

The position of the Fermi level at the surface is determined by the condition of charge neutrality:

$$Q_{SS} = -Q_{SC}, (1)$$

where $Q_{SS}$ and $Q_{SC}$ represent the charge of the surface states and the compensating opposite charge inside the semiconductor respectively ($Q_{SC}$ is also called space charge). $Q_{SS}$ and $Q_{SC}$ are generally expressed in density per unit area ($cm^{-2}$).

In other terms, Eq. 1 says that due to $Q_{SS}$ carried by the surface states, an opposite $Q_{SC}$ must be originated from the semiconductor bulk to screen the surface charge in order to guarantee the charge neutrality, e.g., equilibrium.

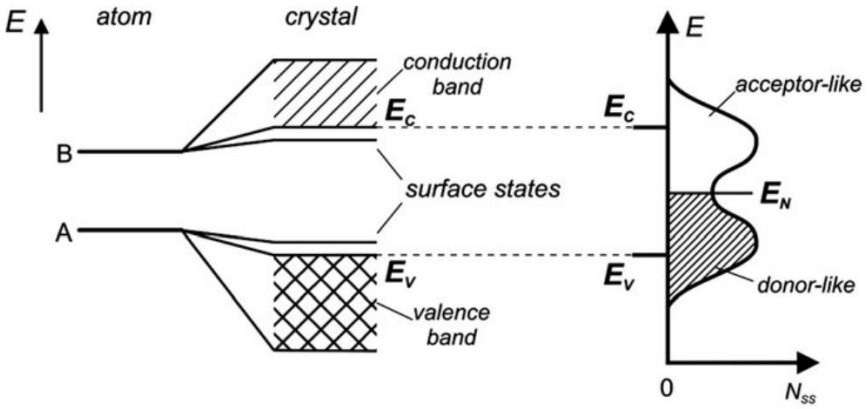


**Figure 13:** The presence of surface atoms leads to the generation of electronic energy levels that are close to those of free atoms, resulting in the separation of surface state levels from the bulk bands. The charging character of these states, whether acceptor-like or donor-like, depends on their specific origin. Figure 13 was reproduced from [26].

As an example, a n-type semiconductor with acceptor-type surface defects near mid-gap is reported in Figure 14. In this situation, a space charge layer will be formed by the ionized bulk donors in order to compensate the negative charge density of occupied acceptor-type surface states (e.g., charge neutrality). The formation of a space charge layer causes a bend of the energy bands in proximity of the surface. Naturally, the higher is the surface charge ($Q_{SS}$) to compensate the stronger is the band-bending ($Q_{SC}$) which can extend for hundreds of nanometers inside the bulk. It is worth to mention that $Q_{SC}$ extends

within a certain depth inside the semiconductor and the space charge distribution is related to band-bending by the Poisson's equation.

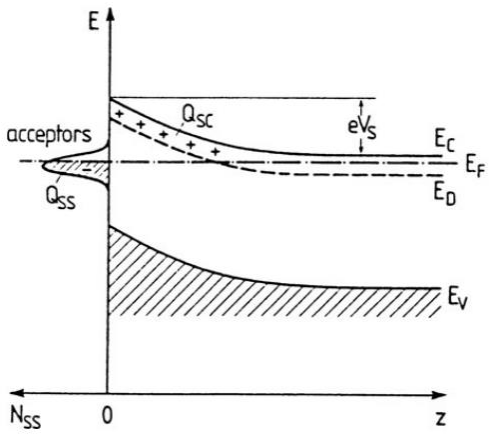


**Figure 14:** Qualitative energy bands representation of a n-type semiconductor with depletion space-charge layer originated by acceptors-type surface states**.** The terms $eV_S$ and $E_D$ represent the surface band-bending and the energy of bulk donors, respectively. Figure 14 was reproduced from [26].

Note that for the vast majority of semiconductors, the presence of surface states is intrinsically related to the existence of the surface itself (dangling bonds, surface reconstruction, external impurities…). The energy position of acceptor-type surface states with respect to the conduction band (or valence band in case of donor-type surface states) is fixed and defined by interatomic potentials.

Generally, in bulk semiconductors, the $E_F$ position with respect to the bulk conduction band minimum is defined solely by the bulk doping level and the energy bands are flat. However, considering Figure 14, if flat bands were present up to the very semiconductor surface, the $E_F$ position would have been located above the acceptor-type surface states distribution and all surface states would be charged and a negatively uncompensated surface charged would be present.

As a consequence, to ensure the charge neutrality, band-bending occurs. In this specific case, an upward-band-bending appears which allows the $E_F$ to cross the surface states energy distribution decreasing the negative surface charge ($Q_{SS}$). Additionally, bulk donors states are raised above the $E_F$ by the same magnitude and are emptied of electrons. Therefore, a positive space charge ($Q_{SC}$) is formed by the immobile ionized donors atoms. When the situation described above occurs the charge neutrality condition is fulfilled: $Q_{SS}$=-$Q_{SC}$.

The presented example showed a specific case called *depletion layer* since due to the band-bending, free conduction band electrons are driven away from the surface and therefore their density at the surface is lowered with respect to the electron bulk density ($n_b$). As a consequence, the electrical conductivity (σ) at the surface is decreased.

It is possible to define two further space charge layers: *inversion layer* and *accumulation layer*. In n-type semiconductors, an inversion layer is created when high densities ($N_{SS}$) of acceptor-type surface states are present even at lower energies along the band-gap. In this case, the excess of negative surface charges induces a stronger upward band-bending due to the higher amount of $Q_{SC}$ (ionized bulk donors) required to guarantee charge neutrality. In this situation, the band-bending is so strong that the intrinsic energy ($E_i$) crosses the $E_F$ near the surface.

According to the classical theory of physics of semiconductors, $E_i$ is defined as:

$$E_i = \frac{1}{2}(E_C + E_V) - \frac{1}{2}kTln\left(\frac{N_{eff}^C}{N_{eff}^V}\right), (2)$$

where $N_{eff}^C$ and $N_{eff}^V$ are the effective conduction and valence band density of states respectively.

The semiconductor character can be distinguish based on the $E_F$ energy value with respect to $E_i$. In particular, if $E_F$=$E_i$ the semiconductor is intrinsic, if $E_F$<$E_i$ the semiconductor is p-type and if $E_F$>$E_i$ the semiconductor is n-type.

In an inversion layer, since $E_i$ crosses $E_F$ near the surface, the n-type semiconductor becomes p-type near the surface. In particular, near the surface, the free-electron density (*n*) decreases to minor values than the intrinsic value $n_i$ whereas the hole concentration (*p*) exceeds $n_i$.

It is worth to mention that in the intersection point between n and p, the electrical conductivity reaches the lowest value (intrinsic behavior). However, in the inversion layer, the conductivity increases again thanks to the large density of free holes.

The excess of hole density near the surface contributes to the charge neutrality condition in addition to the concentration of ionized donors $N_D^+$.

Conversely, in order to form an accumulation layer in an n-type semiconductor, the presence of donor-type surface states with energies comparable and/or higher than the conduction band is required. If this condition is fulfilled, part of these surface states will be partially or completely empty and therefore they will carry a positive surface charge. As in the previous cases, this excess surface charge must be compensated by an equivalent amount of negative space charge arising from the semiconductor bulk. As a result, free electrons accumulate in the proximity of the surface causing downward band-bending.

It is worth to mention that in strong accumulation regime, the conduction band minimum can cross the $E_F$ making the semiconductor degenerate in the proximity of the surface.

As mentioned before, the accumulation layer is induced by free electrons (and not from fixed ionized ions as in the depletion and inversion space charge). Due to this different nature of this space charge, accumulation layers are generally narrower than depletion and inversions layers.

Finally, thanks to the higher density of free electrons at the surface, accumulation layers are characterized by a higher conductivity with respect to the bulk.

In the case of p-type semiconductors the situations described above are reversed and therefore their description is not treated in details for brevity.

In a p-type semiconductor, the formation of a depletion (or inversion, $N_{SS}$>>) layer requires partially (fully) empty donor-type surface states which carry a positive surface charge, as shown in Figure 15. For the charge neutrality condition, a negative space charge must arise from the semiconductor bulk in order to compensate the positive surface charge. This negative charge is carried by the occupied bulk acceptors ions which are pushed below the $E_F$ and therefore the equilibrium requires downward band-bending in the proximity of the surface.

Conversely, in a p-type semiconductor, an accumulation layer is formed due to the presence of partially filled acceptor-type surface states carrying a negative charge. Again, to assure charge neutrality, an equivalent amount of positive space charge arising from the semiconductor bulk causing an upward band-bending.

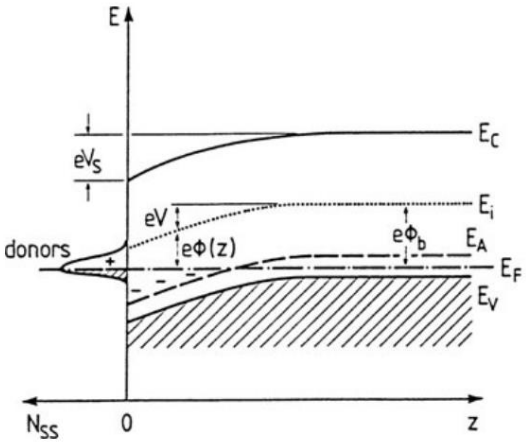


**Figure 15:** Qualitative energy bands representation of a p-type semiconductor with depletion space-charge layer originated by donors-type surface states**.** Note that eV the local band bending, $e\phi(z)$ the local potential, $e\phi_b$ the potential in the bulk, $E_i$ is the intrinsic energy and $E_A$ the energy of bulk acceptors. Figure 15 was reproduced from [26].

Further development of the physics of space charge regions can be found in Appendix A where some theoretical cases in which is possible to obtain approximate analytic solutions of the Poisson's equation are presented.

### 3.2.3.2 Fermi level pinning

In order to elucidate some other concepts that will be useful to understand the modeling results that will be presented in paragraph 3.2.4.1, we have used modeling to study the effect of surface defects on the surface band-bending in function of variable doping concentrations. The sample chosen for modeling consists of a n-type Si sample that comprise of six different regions with different doping concentrations: from $10^{15}$ $cm^{-3}$ to $10^{20}$ $cm^{-3}$. Each region is formed by a rectangle of area 3 x 3 $\mu m^2$ and the whole structure is represented in Figure 16.

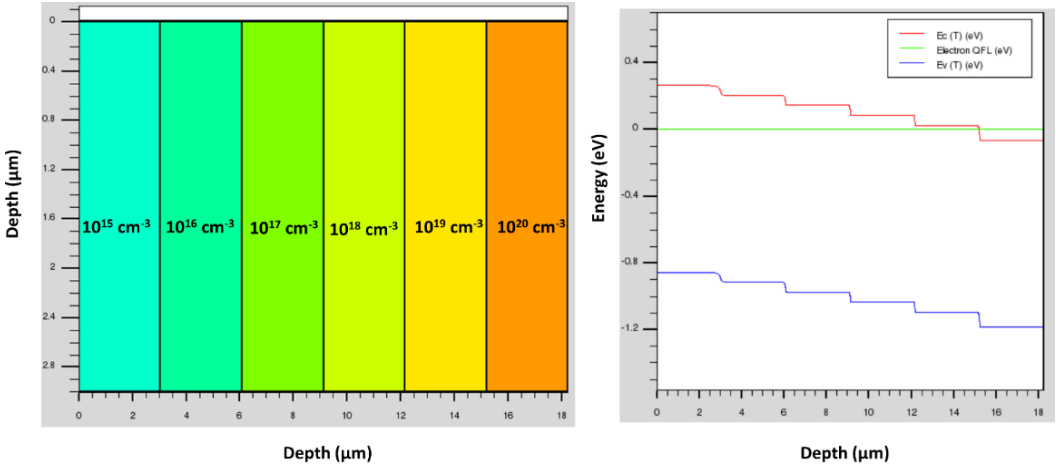


**Figure 16:** a) 2D representation of the n-Si staircase modeled structure. Each region is formed by a rectangle of area 3 x 3 $\mu m^2$ and the doping concentrations range from $10^{15}$ $cm^{-3}$ to $10^{20}$ $cm^{-3}$. b) Bands energy representation along the x-axis, the Fermi level is taken as reference frame.

Note that, as shown in the corresponding energy band-diagram of the structure (Figure 16 right), the n-Si layer with a doping concentration of $10^{20}$ $cm^{-3}$ results to be degenerate.
As described in section 2.5 of Chapter 2, we then introduce a defective layer of thickness equal to 1 nm ($t_{DL}$) in which the density of states (DOS), $N(E)$ ($eV^{-1}cm^{-3}$), is assumed homogeneous throughout its thickness. This can be translated into a surface density of states $N_{ss}(E)$ ($eV^{-1}cm^{-2}$): $N_{ss}(E) = N(E) \times t_{DL}$ with $t_{DL}$= $10^{-7}$ cm. In addition, the DOS consists of the sum of two constant distributions of monovalent donor and acceptor states, $N_D(E)$ and $N_A(E)$, respectively: $N(E) = N_D(E) + N_A(E)$.
In order to show the effect of surface defects up to the degenerated n-Si layer, the total surface density of states $N_{ss}(E)$ was chosen to range from $2x10^{7}$ $eV^{-1}cm^{-2}$ to $2x10^{13}$ $eV^{-1}cm^{-2}$. The results obtained from modeling are shown in Figure 17 in which the absolute band-bending variation induced by surface defects is plotted against the density of surface states.
As described in paragraph 3.2.3.1, surface defects will cause an upward band-bending due to the formation of a depletion region at the surface of the n-type silicon sample. Figure 17 offers the opportunity to explore several considerations, beginning with the case of n-Si with a doping concentration of $10^{15}$ $cm^{-3}$. From Figure 17 (black profile), it is clear that the band-bending is quite small up to a surface-state density of $2x10^{9}$ $eV^{-1}cm^{-2}$. However, for a DOS of $2x10^{10}$ $eV^{-1}cm^{-2}$, the band-bending sharply increases compared to the previous value of DOS. Finally, starting from $2x10^{11}$ $eV^{-1}cm^{-2}$, the band-bending reaches a saturation value that does not change even with DOS with 4 or 5 order of magnitude higher. This is because the surface states are now energetically located near the Fermi level $E_F$ and to an increase of their density $N_{SS}$ corresponds only an infinitesimal increase in band-bending and a concurrent discharging of states, to which corresponds a stabilization of the $E_F$. This effect is called *pinning* of the Fermi level.

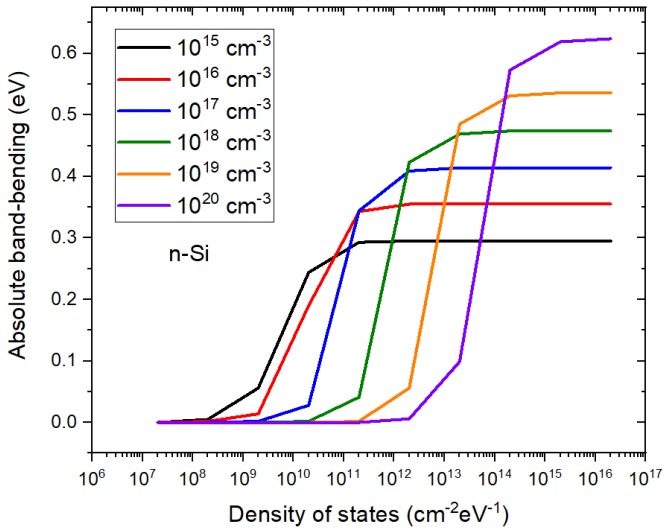


**Figure 17:** Absolute band-bending variation induced by surface defects Vs the density of surface states with reference to the nSi-based structure presented in Figure 16.

In other words, Figure 17 shows the amount of band-bending necessary for the valence and conduction bands to become symmetric with respect to the Fermi level which is now pinned at mid-gap. Note that the final saturation band-bending value depends on the position of $N_{ss}(E)$ and thus on the position of the

charge neutrality level (CNL). Since we have chosen equal acceptor-like and donor-like constant surface defect distributions, the CNL is set at the mid-gap of the Si-based structure (0.55 eV).
In order to delve further into point, the energy bands at the surface of the modeled n-Si structure for the case of a total DOS of $2x10^{12}$ $eV^{-1}cm^{-2}$ is shown in Figure 18.

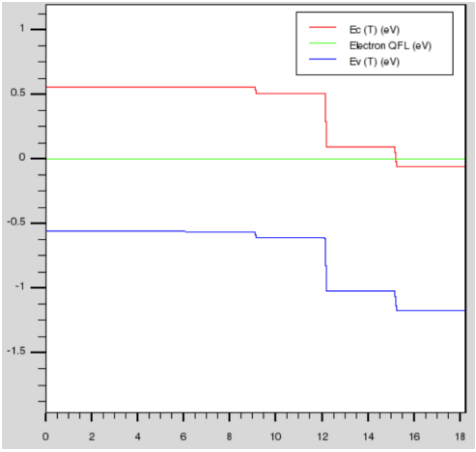


**Figure 18:** Energy bands at the surface of the modeled n-Si structure for the case of a total DOS of $2x10^{12}$ $eV^{-1}cm^{-2}$, the Fermi level is taken as reference frame.

Figure 18 shows that for a DOS equal to $2x10^{12}$ $eV^{-1}cm^{-2}$, the $E_F$ for the n-Si regions with a doping concentration up to $10^{17}$ $cm^{-3}$ is already pinned at mid-gap, whereas, for the higher doped regions ($10^{19}$ $cm^{-3}$ and $10^{20}$ $cm^{-3}$), the impact of surface defects it still negligible. As a matter of fact, the higher is the doping concentration, the higher is the number of free charge carriers that the surface defects must compensate to induce surface band-bending. In other words, only surface defects DOS higher than the bulk doping concentration can indeed induce a charge imbalance at the surface higher enough to induce a compensating severe surface band-bending.
Moreover, Figure 17 illustrates that the absolute amount of band-bending required to pin the Fermi level at the mid-gap point increases as the doping concentration rises. This phenomenon occurs because increasing the doping concentration moves the Fermi level closer to the conduction band and even within it, in the case of the degenerate n-Si region. Consequently, a greater band-bending is necessary to attain the mid-gap position at the surface.
Note that similar absolute band-bending values are obtained in the case of a p-type silicon sample which are not shown for brevity. This is because, considering a material with same doping concentration but opposite type, there are only negligible changes in the relative Fermi level offset due to non-equal effective densities of states in the conduction and valence band. Nonetheless, in the case of a p-type sample, one must consider a downward band-bending (see Figure 15) instead of an upward one as in the presented case.
Finally, it is important to mention that the modeling results presented in Figure 17 were shown in order to better explain the physics related to the surface defects. In the reality, typical surface defects DOS for silicon are in the order of $10^{13}$ $eV^{-1}cm^{-2}$ [39], which is a value well-below the $2x10^{16}$ $eV^{-1}cm^{-2}$ that we showed to be necessary to cause the Fermi level pinning in the degenerate n-Si region.

Further description of the Fermi level pinning can be found in Appendix A.

## 3.2.4. InP:Zn/GaInAs(P):Zn sample: discussion on surface defects

It is evident from the previous discussion that surface defects play a fundamental role in determining the experimental $V_{CPD}$. Therefore, to accurately interpret the experimental outcomes obtained from the InP:Zn/GaInAs(P):Zn sample, we have extensively employed modeling techniques with the objective to provide a quantitative explanation of the experimental surface potential data. The modeling procedure is outlined in detail in paragraph 2.5.

### 3.2.4.1 Surface defects modeling and their impact on the surface potential

It is well-documented in the literature [24] that the cleavage procedure produces surface defects which strongly impact the $V_{CPD}$. In particular, in order to study the effects of surface defects on the $V_{CPD}$ we have extended the energy bands simulations to a non-ideal case in which constant distributions of acceptor-like and donor-like defects have been introduced at the surface. In order to clarify the analysis and focus on essentials, we have simulated a simpler structure with respect to the analyzed multilayer sample in which we did not include the 5 nm InGaAs:nid interlayers and the final InGaAs(P):Zn transition and contact layers. Specifically, we have compared the ideal structure free of surface defects to three different cases in which identical acceptor-like and donor-like surface defects densities of $10^{12}$ $eV^{-1}cm^{-2}$, $10^{13}$ $eV^{-1}cm^{-2}$ and $5x10^{13}$ $eV^{-1}cm^{-2}$ (taken to be constant throughout the bandgap) were introduced at the surface. Results are reported in Figure 19a, 19b, 19c, 19d respectively. In this specific case, the charge neutrality level of surface defects is set at mid-gap. Thus, increasing the surface defect densities will produce a pinning of the Fermi level at the neutrality level of the surface states and the valence and conduction bands energy will appear symmetric with respect to mid-gap position [37]. In particular, it is possible to observe this trend even at relatively low surface defects densities ($2x10^{12}$ $eV^{-1}cm^{-2}$, see Figure 20b) in the InP:nid layer due to low doping concentration ($10^{15}$ $cm^{-3}$) compared to the other two layers. Conversely, in the n-InP substrate and in the InP:Zn layer, this is only well-evidenced when high surface defects densities (>$10^{13}$ $eV^{-1}cm^{-2}$) are introduced at the sample surface; the trend is already visible for $2x10^{13}$ $eV^{-1}cm^{-2}$ and really clear for $10^{14}$ $eV^{-1}cm^{-2}$ in Figure 19c and 19d, respectively. Increasing the surface defect densities leads to an increase of the valence and conduction band energies within the n-InP substrate, and to a decrease in the InP:Zn layer, so that the overall potential drop across the junctions is significantly reduced, from 1.42 V in a) to 0.15 V in c). Specifically, to an increase of energy corresponds a decrease of surface potential which reflects the upward band-bending induced by the presence of surface defects. Conversely, a decrease of energy corresponds to an increase of surface potential which reflects the downward band-bending induced by the presence of surface defects.

We conclude that the presence of surface defects can explain the overall experimental $V_{CPD}$ variation along the structure that is less pronounced than in the simulated ideal case of a free defects surface, as described in section 3.2.2.1. This conclusion on the overall mitigation of the $V_{CPD}$ variation is not changed if we choose other surface defect density distributions (not constant vs energy) that produce different charge neutrality levels in the energy gap (which is not presented here for brevity). However, large surface defect densities not only mitigate the overall change in $V_{CPD}$, but they are also responsible for strong changes in the shape of the surface potential. For instance, in Figure 19d the surface potential appears flat along the simulated structure with the exception of very narrow transition regions at the two layers interfaces.

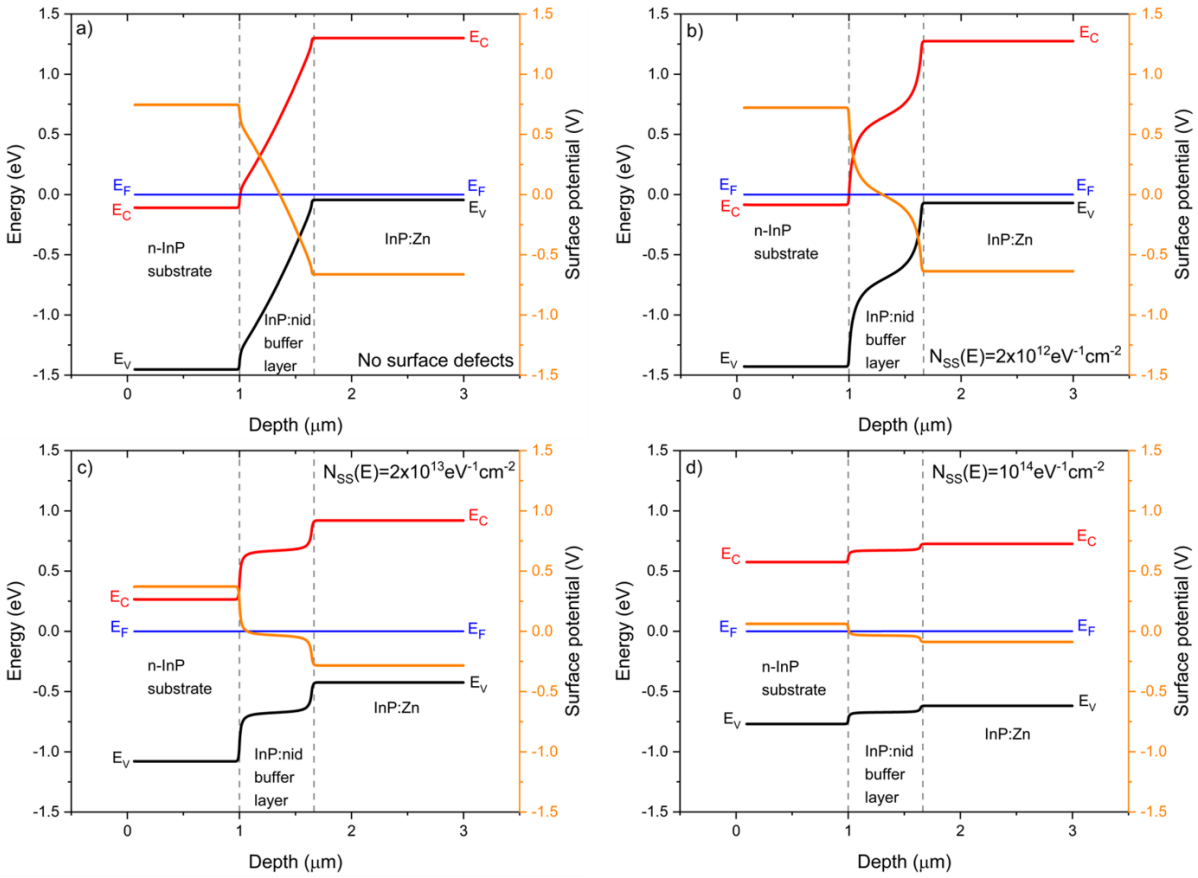


**Figure 19:** Cross-sectional profile at equilibrium of the surface band energies (black: valence band maximum, $E_V$, and red: conduction band minimum, $E_C$) along a simulated n-InP/InP:nid/InP:Zn structure considering surface defects densities made of the sum of constant and identical acceptor and defect distributions (in $eV^{-1}cm^{-2}$): a) 0; b) $2x10^{12}$; c) $2x10^{13}$ and d) $10^4$. The energy reference is taken at the constant Fermi level, $E_F$ (blue horizontal line). The profile of the surface potential is also shown in orange (right y-axis of the graphs).

In other words, large surface defect densities also decrease the effective screening lengths compared to the ones calculated exclusively from the nominal doping densities, due to the extra charges directly provided by the surface states. The essentially constant flat profile in the InP:nid buffer layer strongly departs from the progressively decreasing profile observed experimentally in Figure 9c. In order to provide an explanation for the observed experimental profile that is both mitigated and progressively decreased in this buffer layer, it is necessary to decrease the surface defect density in the buffer layer, while keeping a very large value in the external n-InP substrate and p-InP:Zn layer. Therefore, the n-InP substrate and p-InP:Zn layer require a high value of $N_{SS}=10^{14}$ $eV^{-1}cm^{-2}$, whereas the InP:nid layer requires a lower $N_{SS}=2x10^{12}$ $eV^{-1}cm^{-2}$. Furthermore, in order to provide a more quantitative explanation of the experimental profile of Figure 16c, the GaInAsP:Zn transition and GaInAs:Zn contact layers have been included again in the simulated structure ($N_{SS}=10^{14}$ $eV^{-1}cm^{-2}$). The energy bands and surface potential profiles simulated with these parameters are shown in Figure 20.

The surface potential shown in Figure 20 is in good agreement with the experimental profile of Figure 9c. In particular, the potential drop from the n-InP substrate to the InP:Zn layer is comparable to the 0.18 V obtained experimentally and additionally the shape of the surface potential in the InP:nid layer shows a progressive change extending all over the InP:nid buffer layer. Finally, the GaInAsP:Zn transition and

GaInAs:Zn contact layers are again consistent with the higher $N_{SS}=10^{14}$ $eV^{-1}cm^{-2}$. In particular, the potential difference between the InP:Zn and the GaInAs:Zn contact layers results also to be attenuated with respect to the ideal case shown in Figure 10b as in the experimental $V_{CPD}$ profile of Figure 9c. Overall, this approach demonstrates that surface defect densities variations provide good agreement with the experimental surface potential profile of Figure 9c.

In conclusion, a quantitative description of the accurate surface defects distributions that characterize the surface of semiconductors materials is a complex task, as it is not always certain that surface defects are homogeneously distributed across the entire cross-section. This is particularly true in our case since the several layers present different physical properties due to varying doping type and concentrations [37].

In order to overcome these challenges related to the operating conditions and to the cleaving process presented in this paragraph, KPFM measurements can be performed under ultra-high vacuum (UHV) at an optimal surface-tip distance of the order of a few nm [38] with particular attention to the sample preparation either in the deoxidation and cleaving process.

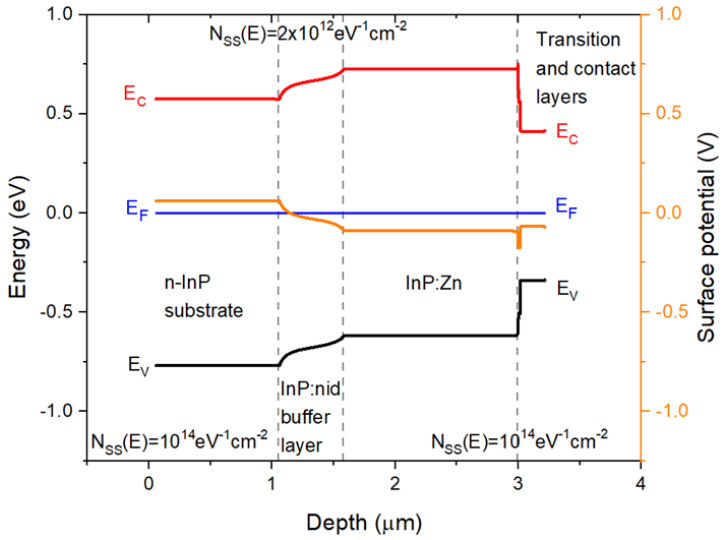


**Figure 20:** Cross-sectional profile at equilibrium of the surface band energies (black: valence band maximum, $E_V$, and red: conduction band minimum, $E_C$) along a simulated n-InP/InP:nid/InP:Zn/GaInAsP:Zn/GaInAs:Zn structure considering different surface defects densities in the various layers. For the n-InP substrate, InP:Zn, GaInAsP:Zn and GaInAs:Zn layers a total surface defect density (made of the sum of constant and identical acceptor and defect distributions) of $10^{14}$ $eV^{-1}cm^{-2}$ was considered whereas for the InP:nid layer a total surface defects density of $2x10^{12}$ $eV^{-1}cm^{-2}$ was introduced. The energy reference is taken at the constant Fermi level, $E_F$ (blue line). The profile of the surface potential is also shown in orange (right y-axis).

### 3.2.4.2 Effect of the illumination on the $V_{CPD}$: surface defects and $V_{OC}$

As shown in Figure 12, an overall negative *SPV* was calculated along the structure and a *SPV* of -95 mV was obtained in the InP:Zn region which seems in good agreement with the expected trend in a p-type layer with surface defects. However, in case of *pn* junctions, the *SPV* can also include the contribution of the open-circuit voltage ($V_{OC}$) of the pn junction due to the splitting of the quasi-Fermi levels of electrons and holes and related charge separation at the junction. In our case, due to the n-type side of the junction

(substrate) being grounded, we expect a positive *SPV* contribution from $V_{OC}$ of the pn junction at the surface of the p-layer outside the space charge region of the pn junction.
Therefore, the *SPV* measured in the InP:Zn region should be a trade-off between the negative contribution due to the flattening of surface-
defects related band-bending and the positive contribution of $V_{OC}$. As a consequence, the slightly negative *SPV* value of -95 mV measured in the InP:Zn region indicates a weaker contribution of the pn junction ($V_{OC}$) compared to the change in surface band-bending related to surface defects.
In order to provide a quantitative analysis of this experimental evidence, we have calculated the conduction and valence band energy shift induced by the illumination simulating two simple structures: the first one is metal/n-InP/air, the n-type InP simulates our n-type substrate with a doping concentration of $5x10^{18}$ $cm^{-3}$, and the second one is metal/InP:Zn/air, with InP:Zn having a p-type doping concentration of $1.5x10^{18}$ $cm^{-3}$, similarly to the p-doped layer in our sample. In these simulations, the back metal/InP contact was assumed to be ohmic in both structures. We introduced uneven donor-like and acceptor-like surface defect densities. Specifically, the donor-like defect density was chosen equal to $10^{13}$ $eV^{-1}cm^{-2}$, and the acceptor-like one 20 times lower, $5x10^{11}$ $eV^{-1}cm^{-2}$, resulting in a charge neutrality level very close to the conduction band of InP.
Under these conditions, a *SPV* close to 0 and a negative *SPV* are expected for the n-type InP substrate and for the InP:Zn layer, respectively. The simulated results gave a *SPV* close to 0 (very slightly positive) and a negative *SPV* of -356 mV for the n-type InP substrate and for the InP:Zn layer, respectively.
In this specific case, a $V_{OC}$ of 261 mV would have been produced across the pn junction considering the experimental *SPV* resultant of -95 mV. This surprisingly low $V_{OC}$ value could be explained either by a poor-quality material of the sample in which a high density of bulk defects is responsible of reducing the carrier lifetime or by the lack of a true ohmic contact between the sample-holder and the n-type InP substrate during the KPFM measurement. In the second case, a potential barrier would be present at the metal contact/n-InP substrate interface which could reduce the overall $V_{OC}$.

## 3.3 CONCLUSION

In Chapter 3, we have shown that KPFM is a valuable technique to investigate a InP:S and InP:Fe multilayer stack with high spatial resolution in ambient conditions. In particular, KPFM provided the detection of the entire stack after a surface deoxidation by an HF based chemical treatment. KPFM revealed a strong dependence on the local doping concentration providing a complete detection of the InP:S and InP:Fe layers which exhibited different color contrast in the $V_{CPD}$ image. Moreover, we showed that the $V_{CPD}$ contrast between the InP:S and InP:Fe layers could even be significantly improved when KPFM measurements were performed under illumination. The analysis of $V_{CPD}$ profiles shows that InP:S and InP:Fe layers of different but similar thickness tend to show different $V_{CPD}$, which can be attributed to the band-bending induced by the space charge due to the different doping densities of the InP:S and InP:Fe layers, as shown in the simulated energy bands profile. The $V_{CPD}$ profiles extrapolated from different regions of the same scan showed the same $V_{CPD}$ qualitative progression but presented minor variations. For this reason, a thorough analysis and description of the many factors that influence KPFM measurements was proposed in order to investigate these differences. Finally, the analysis of *SPV* along the structure pointed out that a positive SPV in the order of hundreds of mV was detected even for the InP:S layers, which is surprising considering the bulk properties of this material. Nonetheless, this can be justified by a large surface state defect density responsible of producing significant upward band bending.

Additionally, we have investigated a InP:Zn/GaInAs(P):Zn multilayer structure revealing a high spatial resolution of down to 20 nm of our KPFM setup. The verified sensitivity of our KPFM setup to the narrower layers will be crucial for the study of the cross sections of operating solar device in future works. The analysis of the surface potential profile identified the presence of space charge regions and, thus, the formation of several junctions along the stack. The complexity of the analyzed structure combined with the ambient operating conditions caused challenges in the identification of the real position of the junctions in the $V_{CPD}$ image. KPFM measurements are significantly affected by surface defects and other surface inhomogeneities. In particular, numerical modelling and analysis indicated that surface defects are responsible for a significant departure of the magnitude of the surface potential from the value in the bulk material. Also, we showed that the observed potential profile along the cleaved surface of the n-InP/InP:nid/p-InP:Zn heterojunction stack can be explained by large surface defect densities in the highly doped n-InP and p-InP:Zn layers, with a much lower defect density in the InP:nid buffer layer. With further characterization and analysis, we have shown that white-light illumination reduces the surface band bending induced by surface defects, providing an enhancement of the contrast in the $V_{CPD}$ image. The analysis of the *SPV* variation along the structure cross-section further suggests that either bulk defects or a non-ohmic contact between the metallic sample holder and the n-type InP substrate may exist. For future work, it will be necessary to assure a good ohmic contact between the sample holder and the sample and to carry out complementary characterization of the optoelectronic properties of the layers to refine the analysis of the results.

# Bibliography

[1] Li, J.; Aierken, A.; Liu, Y.; Zhuang, Y.; Yang, X.; Mo, J. H.; Fan, R. K.; Chen, Q. Y.; Zhang, S. Y.; Huang, Y. M.; Zhang, Q. A Brief Review of High Efficiency III-V Solar Cells for Space Application. *Frontiers in Physics* **2021**, *8*. https://doi.org/10.3389/fphy.2020.631925

[2] Soresi, S.; da Lisca, M.; Besancon, C.; Vaissiere, N.; Larrue, A.; Calo, C.; Alvarez, J.; Longeaud, C.; Largeau, L.; Linares, P. G.; Tournié, E.; Kleider, J.-P.; Decobert, J. Epitaxy and Characterization of InP/InGaAs Tandem Solar Cells Grown by MOVPE on InP and Si Substrates. *EPJ Photovolt.* **2023**, *14*, 1. https://doi.org/10.1051/epjpv/2022027.

[3] da Lisca, M.; Connolly, J. P.; Alvarez, J.; Mekhazni, K.; Vaissiere, N.; Decobert, J.; Kleider, J.-P. Revealing of InP Multi-Layer Stacks from KPFM Measurements in the Dark and under Illumination. *EPJ Photovoltaics* **2022**, *13*, 19. https://doi.org/10.1051/epjpv/2022017.

[4] da Lisca, M.; Alvarez, J.; Connolly, J. P.; Vaissiere, N.; Mekhazni, K.; Decobert, J.; Kleider, J.-P. Cross-Sectional Kelvin Probe Force Microscopy on III–V Epitaxial Multilayer Stacks: Challenges and Perspectives. *Beilstein J. Nanotechnol.* **2023**, *14* (1), 725–737. https://doi.org/10.3762/bjnano.14.59.

[5] Tsurumi, D.; Hamada, K.; Kawasaki, Y. Energy-Filtered Secondary-Electron Imaging for Nanoscale Dopant Mapping by Applying a Reverse Bias Voltage. *Jpn. J. Appl. Phys.* **2012**, *51* (10R), 106503. https://doi.org/10.1143/JJAP.51.106503.

[6] Gysin, U.; Meyer, E.; Glatzel, Th.; Günzburger, G.; Rossmann, H. R.; Jung, T. A.; Reshanov, S.; Schöner, A.; Bartolf, H. Dopant Imaging of Power Semiconductor Device Cross Sections. *Microelectronic Engineering* **2016**, *160*, 18–21. https://doi.org/10.1016/j.mee.2016.02.056.

[7] Eyben, P., Xu, M.W., Duhayon, N., Clarysse, T., Callewaert, S., & Vandervorst, W. Scanning spreading resistance microscopy and spectroscopy for routine and quantitative two-dimensional carrier profiling. *Journal of Vacuum Science & Technology B,* **2002**. *20*. https://doi.org/10.1116/1.1424280

[8] Kimura, K.; Kobayashi, K.; Yamada, H.; Matsushige, K. Two-Dimensional Dopant Profiling by Scanning Capacitance Force Microscopy. *Applied Surface Science* **2003**, *210* (1), 93–98. https://doi.org/10.1016/S0169-4332(02)01486-1.

[9] Melitz, W.; Shen, J.; Kummel, A. C.; Lee, S. Kelvin Probe Force Microscopy and Its Application. *Surface Science Reports* **2011**, *66* (1), 1–27. https://doi.org/10.1016/j.surfrep.2010.10.001.
[10] P. De Wolf; R. Stephenson; T. Trenkler; T. Clarysse; T. Hantschel; W. Vandervorst. Status and Review of Two-Dimensional Carrier and Dopant Profiling Using Scanning Probe Microscopy. *Journal of Vacuum Science & Technology. B. Microelectronics and Nanometer Structures* **2000**, *18* (1), 361–368. https://doi.org/10.1116/1.591198
[11] Shin, H.; Lee, B.; Kim, C.; Park, H.; Min, D.-K.; Jung, J.; Hong, S.; Kim, S. Measurement and Visualization of Doping Profile in Silicon Using Kelvin Probe Force Microscopy (KPFM). *Electronic Materials Letters* **2009**, *3* (5), 127–133. https://doi.org/10.3365/eml.2009.09.127.
[12] Henning, A.K., Hochwitz, T., Slinkman, J.A., Never, J.M., Hoffmann, S., Kaszuba, P., & Daghlian, C.P. Two-dimensional surface dopant profiling in silicon using scanning Kelvin probe microscopy. *Journal of Applied Physics* **1995,** *77*, 1888-1896. https://doi.org/10.1063/1.358819
[13] El-Nahass, M. M.; Youssef, S. B.; Ali, H. A. M. Optical Properties of Sulfur Doped InP Single Crystals. *Physica A: Statistical Mechanics and its Applications* **2014**, *402*, 216–223. https://doi.org/10.1016/j.physa.2014.01.069.
[14] Zafar, F.; Iqbal, A. Indium Phosphide Nanowires and Their Applications in Optoelectronic Devices. *Proc Math Phys Eng Sci* **2016**, *472* (2187), 20150804. https://doi.org/10.1098/rspa.2015.0804.
[15] Faur, M.; Faur, M.; Flood, D. J.; Goradia, C.; Brinker, D. J.; Goradia, M.; Moulot, J.; Bailey, S.; Fatemi, N. S.; Jenkins, P. P.; Wilt, D. M. Status of Diffused Junction p/Sup +/n InP Solar Cells for Space Power Applications. In *Proceedings of 1994 IEEE 1st World Conference on Photovoltaic Energy Conversion - WCPEC (A Joint Conference of PVSC, PVSEC and PSEC)*; 1994; Vol. 2, pp 2211–2216 vol.2. https://doi.org/10.1109/WCPEC.1994.521663.
[16] Soresi, S., Hamon, G., Larrue, A., Alvarez, J., Pires, M.P. and Decobert, J. InP:S/AlInAs:C Tunnel Junction Grown by MOVPE for Photovoltaic Applications. Phys. Status Solidi A. **2018** 215: 1700427. https://doi.org/10.1002/pssa.201700427
[17] Alyabyeva, L.N., Zhukova, E.S., Belkin, M.A. *et al.* Dielectric properties of semi-insulating Fe-doped InP in the terahertz spectral region. *Sci Rep.* **2017,** 7, 7360. https://doi.org/10.1038/s41598-017-07164-1
[18] Metaferia, W.; Kataria, H.; Sun, Y.-T.; Lourdudoss, S. Growth of InP Directly on Si by Corrugated Epitaxial Lateral Overgrowth. *J. Phys. D: Appl. Phys.* **2015**, *48* (4), 045102. https://doi.org/10.1088/0022-3727/48/4/045102.
[19] Glatzel, Th.; Sadewasser, S.; Shikler, R.; Rosenwaks, Y.; Lux-Steiner, M. Ch. Kelvin Probe Force Microscopy on III–V Semiconductors: The Effect of Surface Defects on the Local Work Function. *Materials Science and Engineering: B* **2003**, *102* (1), 138–142. https://doi.org/10.1016/S0921-5107(03)00020-5.
[20] Narchi, P.; Alvarez, J.; Chrétien, P.; Picardi, G.; Cariou, R.; Foldyna, M.; Prod'homme, P.; Kleider, J.-P.; i Cabarrocas, P. R. Cross-Sectional Investigations on Epitaxial Silicon Solar Cells by Kelvin and Conducting Probe Atomic Force Microscopy: Effect of Illumination. *Nanoscale Res Lett* **2016**, *11*, 55. https://doi.org/10.1186/s11671-016-1268-1.
[21] Jacobs, H. O.; Leuchtmann, P.; Homan, O. J.; Stemmer, A. *Resolution and contrast in Kelvin probe force microscopy.* **1998***, 84(3), 1168–0.* https://doi.org/10.1063/1.368181
[22] O. Ostinelli, A. R. Alt, R. Lövblom, C. R. Bolognesi; Growth and characterization of iron-doped semi-insulating InP buffer layers for Al-free GaInP/GaInAs high electron mobility transistors. *Journal of Applied Physics.* **2010**, 108 (11): 114502. https://doi.org/10.1063/1.3516490
[23] SILVACO® ATLAS™ User's Manual (2016)
[24] Kronik, L.; Shapira, Y. Surface Photovoltage Phenomena: Theory, Experiment, and Applications. *Surface Science Reports* **1999**, *37* (1), 1–206. https://doi.org/10.1016/S0167-5729(99)00002-3.
[25] Sun, X.; Wang, X.; Wang, P.; Sheng, B.; Li, M.; Su, J.; Zhang, J.; Liu, F.; Rong, X.; Xu, F.; Yang, X.; Qin, Z.; Ge, W.; Shen, B. Identifying a Doping Type of Semiconductor Nanowires by Photoassisted Kelvin Probe Force Microscopy as Exemplified for GaN Nanowires. *Opt. Mater. Express, OME* **2017**, *7* (3), 904–912. https://doi.org/10.1364/OME.7.000904.

[26] Lüth, H. *Solid Surfaces, Interfaces and Thin Films*; Graduate Texts in Physics; Springer: Berlin, Heidelberg, 2010. https://doi.org/10.1007/978-3-642-13592-7.
[27] Marchat, C. Caractérisation Électrique et Optoélectronique de Nouveaux Matériaux et Composants Photovoltaïques à Partir de Techniques AFM. These de doctorat, université Paris-Saclay, 2020. https://www.theses.fr/2020UPASS094
[28] Wandelt, K. *Surface and Interface Science*; Wiley VCH: Weinheim, 2005.
[29] Ibach, H. *Physics of Surfaces and Interfaces*; Springer Berlin Heidelberg, 2006. https://doi.org/10.1007/3-540-34710-0.
[30] Li, G.; Mao, B.; Lan, F.; Liu, L. Practical Aspects of Single-Pass Scan Kelvin Probe Force Microscopy. *Review of Scientific Instruments* **2012**, *83* (11), 113701. https://doi.org/10.1063/1.4761922.
[31] Baier, R.; Leendertz, C.; Lux-Steiner, M. Ch.; Sadewasser, S. Toward Quantitative Kelvin Probe Force Microscopy of Nanoscale Potential Distributions. *Phys. Rev. B* **2012**, *85* (16), 165436. https://doi.org/10.1103/PhysRevB.85.165436.
[32] Marchat, C.; Connolly, J. P.; Kleider, J.-P.; Alvarez, J.; Koduvelikulathu, L. J.; Puel, J. B. KPFM Surface Photovoltage Measurement and Numerical Simulation. *EPJ Photovolt.* **2019**, *10*, 3. https://doi.org/10.1051/epjpv/2019002.
[33] Shohet, J. L. Plasma Science and Engineering. In *Encyclopedia of Physical Science and Technology (Third Edition)*; Meyers, R. A., Ed.; Academic Press: New York, **2003**; pp 401–423. https://doi.org/10.1016/B0-12-227410-5/00584-6.
[34] Baumgart, C.; Helm, M.; Schmidt, H. Quantitative Dopant Profiling in Semiconductors: A Kelvin Probe Force Microscopy Model. *Phys. Rev. B* **2009**, *80* (8), 085305. https://doi.org/10.1103/PhysRevB.80.085305.
[35] Schubert, E.; Pinzone, C.; Geva, M. Phenomenology of Zn Diffusion and Incorporation in InP Grown by Organometallic Vapor-Phase Epitaxy (OMVPE). *Applied Physics Letters - APPL PHYS LETT* **1995**, *67*, 700–702. https://doi.org/10.1063/1.115279.
[36] Levinshtein, M.; Rumyantsev, S.; Shur, M. *Handbook Series on Semiconductor Parameters Volume 1, Si, Ge, C (Diamond), GaAs, GaP, GaSb, InAs, InP, InSb*; World Scientific: Singapore, 1996.
[37] Tersoff, J.; Harrison, W. A. Transition-Metal Impurities in Semiconductors---Their Connection with Band Lineups and Schottky Barriers. *Phys. Rev. Lett.* **1987**, *58* (22), 2367–2370. https://doi.org/10.1103/PhysRevLett.58.2367.
[38] Sadewasser, S.; Glatzel, Th.; Shikler, R.; Rosenwaks, Y.; Lux-Steiner, M. Ch. Resolution of Kelvin Probe Force Microscopy in Ultrahigh Vacuum: Comparison of Experiment and Simulation. *Applied Surface Science* **2003**, *210* (1), 32–36. https://doi.org/10.1016/S0169-4332(02)01475-7.
[39] E. H. Poindexter, G. J. Gerardi, M.-E. Rueckel, P. J. Caplan, N. M. Johnson, D. K. Biegelsen; Electronic traps and *Pb* centers at the $Si/SiO_2$ interface: Band-gap energy distribution. *J. Appl. Phys.* 15 November 1984; 56 (10): 2844–2849. https://doi.org/10.1063/1.333819

# Chapter 4

# Cross-sectional KPFM and c-AFM for the study of solar cells

In Chapter 4 the local probe characterization is extended to finalized solar cells. This chapter delves into the core of our research, presenting and analyzing the outcomes of KPFM and c-AFM measurements conducted on the cross-section of diverse photovoltaic technologies, along with the challenges associated with such characterizations.
Specifically, we present the characterizations carried out on AlGaAs, CZTGS, and silicon heterojunction solar cells. The AlGaAs and Silicon solar cells were made available through internal collaboration within IPVF, while the CZTGS solar cells were provided by the University of Milano-Bicocca.
In the context of this latter collaboration, the KPFM characterization was included in [1] to complement their findings, offering experimental evidence of the unsatisfactory PV performance of the CZTGS device under illumination. Additionally, the analysis performed on the AlGaAs solar cell was presented at the JNPV 2022.

## 4.1 p-AlGaAs:Be/n-GaInP:Si heterojunction solar cell

The AlGaAs-based samples used in this study were directly provided by two IPVF colleagues, Oleksander Bilousov and Amadéo Michaud who were involved in developing a III-V-based multijunction solar cell in the frame of IPVF programme III led by Stéphane Collin. As a matter of fact, this solar cell uses as absorber a p-AlGaAs:Be layer with a high energy gap of 1.73 eV, making it suitable as a top solar cell in a tandem configuration. To analyze the samples, KPFM and c-AFM techniques were employed in both planar (see paragraph 2.3.1) and cross-sectional (see paragraph 2.3.2) configurations.

### 4.1.1 p-AlGaAs:Be/n-GaInP:Si samples characteristics and preparation

In the context of this analysis, I studied two different samples. The first one consists simply in the unprocessed multilayer stack, similar to the samples presented in Chapter 3, whereas the second one is the finalized solar cell.
The comprehensive deposition and fabrication procedure of this solar cell can be accessed in reference [2]. Here we describe only the intricate structure, as it is very important for understanding the KPFM and c-AFM results which will be presented in the following sections.

| Detailed structure | Thickness (nm) | Doping concentration ($cm^{-3}$) |
|---|---|---|
| p-GaAs:Zn | / | $10^{19}$ |
| p-GaAs:Be | 300 | $10^{19}$ |
| p-$Al_{0.51}Ga_{0.49}As$:Be | 50 | $5x10^{18}$ |
| Gr: Al from 51% to 25% | 100 | |
| p-$Al_{0.25}Ga_{0.75}As$:Be | 1900 | $2x10^{16}$ |
| Gr: Al from 25% to 30% | 100 | |
| GaInP:Si | 50 | $5x10^{17}$ |
| AlInP:Si | 20 | $3.9x10^{18}$ |
| n-GaAs:Si | 300 | $10^{19}$ |

**Table 1:** Full structure of the investigated p-AlGaAs:Be/n-GaInP:Si HJ multilayer stack and solar cell. Note that, the abbreviation Gr stands for gradient and indicates additional transitional layers to regions with different Al concentration. Additionally, typical thicknesses of p-GaAs:Zn substrates are of the order of hundreds of microns.

As shown in Table 1, the solar cell is a pn heterojunction (HJ) formed by a p-AlGaAs:Be absorber and a n-GaInP:Si emitter. Additional layers are included in the structure for an optimal surface passivation, carriers extraction and to smoothen the transition between materials with very different band-gaps [2]. Note that, due to the greater thickness of the absorber layer (1.9 µm), it can serve as a reference frame to facilitate the identification of the position of the remaining layers in $V_{CPD}$ (KPFM) or voltage images (Resiscope).

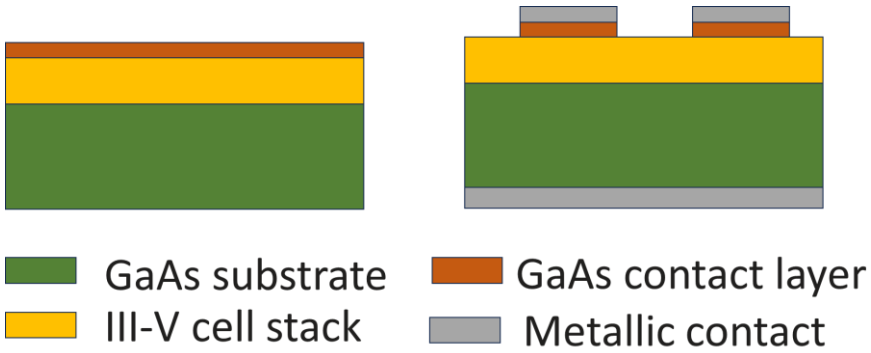


**Figure 1:** Schematic of the differences between the multilayer stack (left) and the finalized solar cell (right).

It is worth emphasizing that the completion of the device requires the process of etching the n-GaAs:Si contact layer within the multilayer stack. Once the n-GaAs:Si contact is etched, metallic contacts are subsequently deposited on both the top and bottom sides of the device [2], as illustrated in Figure 1.
Finally, prior to KPFM and c-AFM analysis, a simple surface cleaning was carried out with the purpose of removing possible surface contamination (e.g., dust particles) with acetone and drying in air.

### 4.1.2 p-AlGaAs:Be/n-GaInP:Si energy band profile

Before presenting the Resiscope experimental results performed on the cross-section of the multilayer sample (Figure 1, left), the calculated energy band profile of the structure, together with the potential, is shown in Figure 2 in which the Fermi level is used as the reference for the energies. For the purpose of

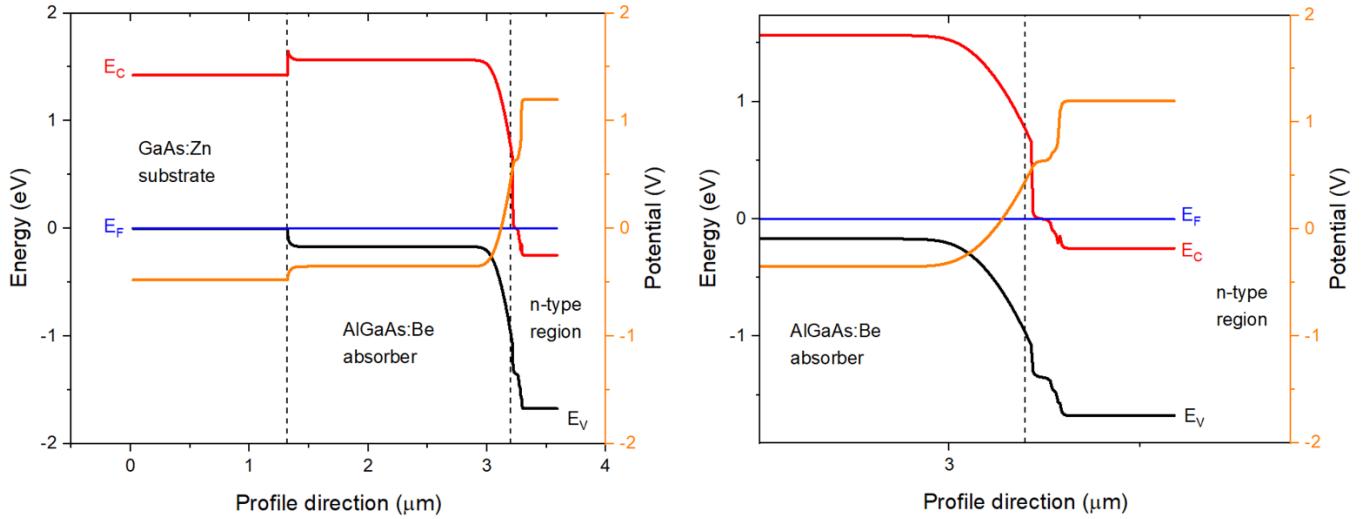


**Figure 2:** Energy band profile ($E_C$ in red, $E_V$ in black) across the layer stack reported in Table 1 represented together with Fermi level (energy reference, in blue) and the potential (which will be useful for the following section). Vertical reference lines have been included in order to divide the different regions of the structure. The Figure on the right represents a zoom at the p-AlGaAs:Be/n-GaInP:Si heterojunction. The profile was calculated assuming no surface states and with the material parameters given in [3].

replicating the analyzed structure in this study, the same layers and doping concentrations, as presented in Table 1, were utilized with the exception of the 50 nm p-$Al_{0.51}Ga_{0.49}As$:Be layer and the two 100 nm Gr transitional layers which were not included and a width of 1 µm was assigned to the GaAs:Zn substrate.
Notably, the KELSCAN tool (see paragraph 2.5) does not permit the specification of the dopant, only the type and concentration are allowed. Consequently, in the script, no distinction is made between the GaAs:Zn substrate and the GaAs:Be layer, as both are treated as p-type layers with a doping concentration of $10^{19}$ $cm^{-3}$. Nevertheless, this approximation is considered reasonable since the relative position of the valence band in relation to the Fermi level is expected to have minimal impact in either case.
As depicted in Figure 2, an upward shift in potential becomes evident at 1.3 µm near the GaAs:Be/AlGaAs:Be interface, progressing towards the absorber. This shift can be attributed to the creation of a narrow space charge, induced by the difference in work functions arising from the offset in energy band gaps between the GaAs:Be ($E_g$=1.42 eV) and $Al_{0.25}$GaAs:Be ($E_g$=1.73 eV) layers.
Additionally, considering the p-AlGaAs:Be/n-GaInP:Si heterojunction, due to the different doping concentrations, the space charge region is mostly located in the AlGaAs:Be absorber layer and it extends for around 280 nm (from 2.94 to 3.22 µm), as well-evidenced by the zoom of Figure 2 (right). Note that in reference [4] additional information regarding the band alignment diagram at the n-GaInP:Si/n-AlInP:Si interface can be accessed.
Furthermore, the Silvaco software enables the visualization of the free charge carriers profiles along the structure derived from the energy band profile, as shown in Figure 3a. Note that the dopants are assumed to be fully ionized at room temperature [5].
The free carriers concentrations can be in turn utilized for the estimation of the resistivity ($\rho$) profile. Specifically, the resistivity is defined as:

$$\rho = {}^{1}/_{q(n\mu_n + p\mu_p)}, (1)$$

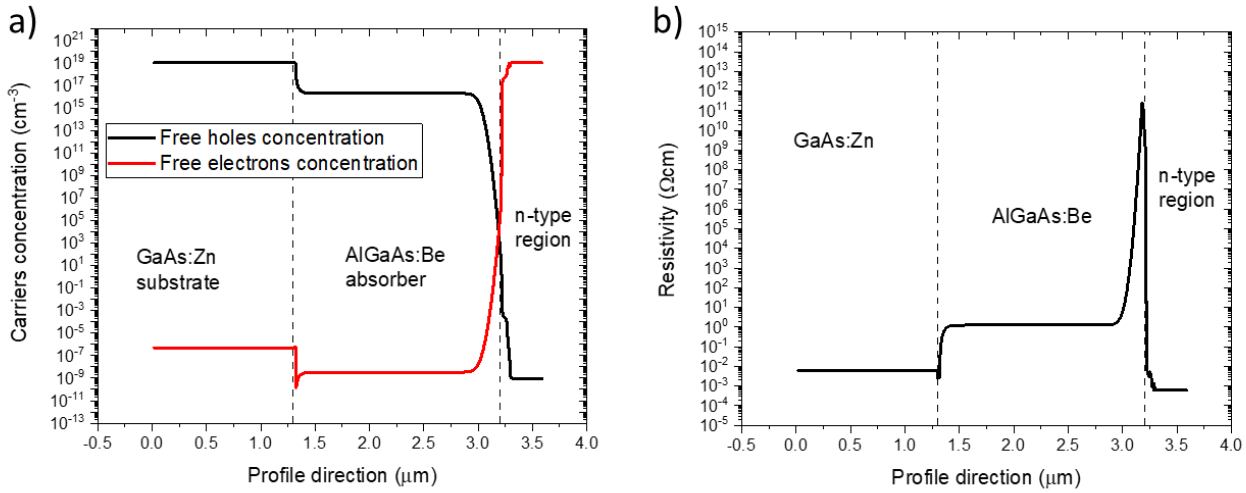


**Figure 3:** a) Free electrons and holes carrier concentrations profiles along the simulated structure shown in Figure 2. Note that the dopants are considered to be fully ionized at room temperature. b) Corresponding resistivity profile calculated applying Eq.1 with *n* and *p* being the values reported in a) and $\mu_n$ and $\mu_p$ being the values reported in [5] for GaAs.

where *n* and *p* are the carrier concentrations for holes and electrons, respectively, and $\mu_n$ and $\mu_p$ are the corresponding carrier mobilities. In the case of n-type materials, $n\mu_n$ is the only contributing factor to the resistivity since $n\mu_n >> p\mu_p$. For a p-type material, the situation is reversed since $p\mu_p >> n\mu_n$.

However, considering the carriers profile along the p-AlGaAs:Be layer, one can notice that along the space charge, $p$ becomes more and more comparable to $n$ and thus, both $n\mu_n$ and $p\mu_p$ must be considered in the evaluation of the resistivity (Eq. 1). Specifically, since the holes carrier concentration is decreasing, an increase in resistivity is expected along the space charge region. Finally, once crossed the space charge, the electrons carrier concentration (*n*) contribution will be predominant, and the resistivity will decrease accordingly. This a particularly valuable information since, from Resiscope analysis, one can expect to see an increase of the local resistance approaching the end of the p-AlGaAs:Be absorber layer which extends for around 400 nm (considering the 100 nm Gr AlGaAs transition layer that was not included in the modeling) due to the formation of the space charge (e.g., depletion region) [5], as shown in the resistivity profile reported in Figure 3b. The mobility values used in the calculation are reported in Appendix B.

However, it is important to recall that the band structure of Figure 2 represents the "bulk" properties and thus the likely presence of surface states is not considered. As widely illustrated in Chapter 3, surface states have a strong influence on the energy bands [6] and additionally they can also influence the measured local resistance (or current) [7,8]. In particular, surface states may act as traps for charge carriers, affecting their mobility and enhancing recombination. For this reason, in Figure 4, the "bulk" resistivity profile is compared to the resistivity profile obtained by introducing a total constant density of surface states $N_{ss}(E)=10^{13}$ $eV^{-1}cm^{-2}$ ($5x10^{12}$ $eV^{-1}cm^{-2}$ acceptor-type + $5x10^{12}$ $eV^{-1}cm^{-2}$ donor-type); see paragraph 2.5: A modeling tool: KELSCAN.

Specifically, owing to the high doping concentrations of the p-GaAs:Zn and the n-GaAs:Si layers, surface defects of this level have only little influence on the resistivity. However, surface defects have a significant impact on the p-AlGaAs:Be absorber due to its lower doping concentration ($N_A=10^{16}$ $cm^{-3}$).

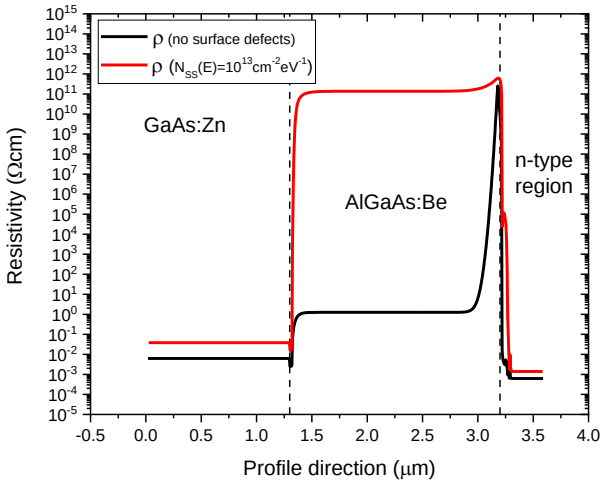


**Figure 4:** "Bulk" resistivity profile compared to the one obtained by introducing a total density of surface states $N_{ss}(E)=10^{13}$ $eV^{-1}cm^{-2}$.

In fact, resistivity within the absorber layer presents a dramatic increase, reaching values of the order of $10^{11}$ Ωcm, given the specific density of surface states chosen. Additionally, the space charge appears as only a small increase in resistivity, less than a single order of magnitude. In contrast, the "bulk" resistivity profile exhibits a change in resistivity of up to eleven orders of magnitude at its maximum.
To conclude this introductive paragraph, it is worth recalling (see paragraph 2.6) that the electrical contact resistance is given by:

$$R = {\rho}/{4a}, (2)$$

where $a$ is the radius of the point contact between the surface of the sample and the AFM tip. Therefore, local variations in topography, such as dips and valleys, can increase the value of $a$ giving rise to local resistance decreases due to higher collected current through the AFM tip. This effect can be especially noticeable in cross-sectional analysis because of the rough and non-uniform surface created following the cleavage process, particularly near the edge.

### 4.1.3 Cross-sectional c-AFM on the p-AlGaAs:Be/n-GaInP:Si multilayer stack: a first approach

As a first attempt to acquire expertise with the c-AFM technique, the characterization of the multilayer stack (Figure 1 left) was initially performed. The c-AFM analysis was made possible by implementing a Resiscope [9] directly connected to the TRIOS platform, as already detailed in paragraph 2.6.1. For this first stage analysis, the p-GaAs:Zn substrate was electrically connected to the metallic sample holder using silver paste. A schematic of the experimental setup is shown in Figure 5 in which the light green rectangle represents the GaAs:Zn substrate. Note that the base was not electrically isolated from the sample holder, however, when the electrodes of a multimeter were positioned, with one terminal connected to the sample holder and the other to the front n-GaAs:Si layer, a valid open-circuit voltage ($V_{OC}$) reading was obtained on the multimeter, confirming that the sample was indeed in an open-circuit condition.

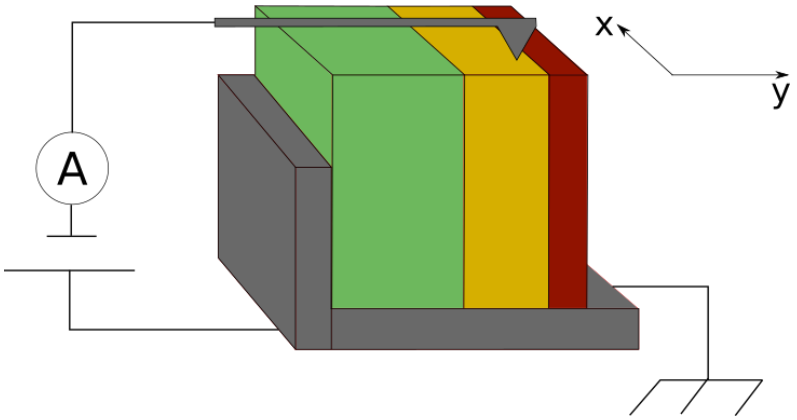


**Figure 5:** Schematic representation of a cross-sectional Resiscope measurement. Silver paste is generally used to ensure a reasonable electrical contact between the sample holder and the GaAs:Zn substrate. The same colors have been chosen as in Figure 2 to illustrate the different regions of the multilayer structure.

Finally, the measurements were performed in dark conditions applying a bias of +1 V between the sample and the AFM tip (highly doped diamond coated $n^+$-Si) with the contact interaction forces being in the range of 100-1000 nN. Note that a wide range of applied forces is reported because we generally start the measurement applying relative low forces, then we carefully increase the setpoint until reaching a reasonable signal-to-noise ratio and electrical contact between the AFM tip and the sample. It is thus important to mention that the following resistance profiles reported in sections 4.1 and 4.2 refer to a force range spanning from 700 nN to 1000 nN.

In Figure 6a and 6b, the topography image and the voltage map of the cross-section of the multilayer stack are shown, respectively. From the output voltage measured from the logarithmic amplification system of the setup [9], one can deduce the corresponding resistance value from: $R = 10^{(V+2)}$, where the resistance is expressed in ohms and the measured output voltage in volts. The voltage map can thus be converted into a resistance map, which can in turn be converted into a resistance profile along the cross-section as illustrated in Figure 6c. To this purpose, each point of the resistance profile represents an average of 207 points over a width of 0.7 µm along the x axis. Note that the origin (0;0) is identified as a point in the GaAs:Zn substrate and moving along the positive direction of the Y axis, one will reach the end of the sample.

A first look at the resistance profile allows a qualitative analysis. The Resiscope detected the different regions of the structure (between 0 and 3.63 µm). In particular, the measured resistance in the substrate (GaAs:Zn) is comparable to the one measured for the 300 nm GaAs:Be layer (between 0 and 0.85 µm), which is reasonable due to the identical p-type doping concentration ($10^{19}$ $cm^{-3}$). Nonetheless, the slight resistance step from $10^4$ to about $1.5x10^4$ Ω and the ≈ 300 nm plateau at $1.5x10^4$ Ω suggests that the conductivity of the GaAs:Zn substrate is slightly higher than the one of the GaAs:Be layer. Nonetheless, this small increase in resistance can be also related to a local different surface states density distribution that in turn induce a different local surface band-bending.

As the transition region to the AlGaAs:Be absorber is approached (from 0.85 µm), there is a notable rise in resistance, which eventually stabilizes at $5x10^7$ Ω across the absorber layer (≈ 2.9 µm). In the "transition to the absorber" region identified in Figure 6c, a narrow peak at ≈ $10^5$ Ω is present and it can be associated to the 50 nm p-$Al_{0.51}Ga_{0.49}As$:Be layer. A general increase in resistance is expected compared to the substrate (or to the 300 nm GaAs:Be layer) due to the lower doping concentration present in the absorber. It is noteworthy to highlight that the transition to the AlGaAs:Be absorber is not entirely abrupt (between 1

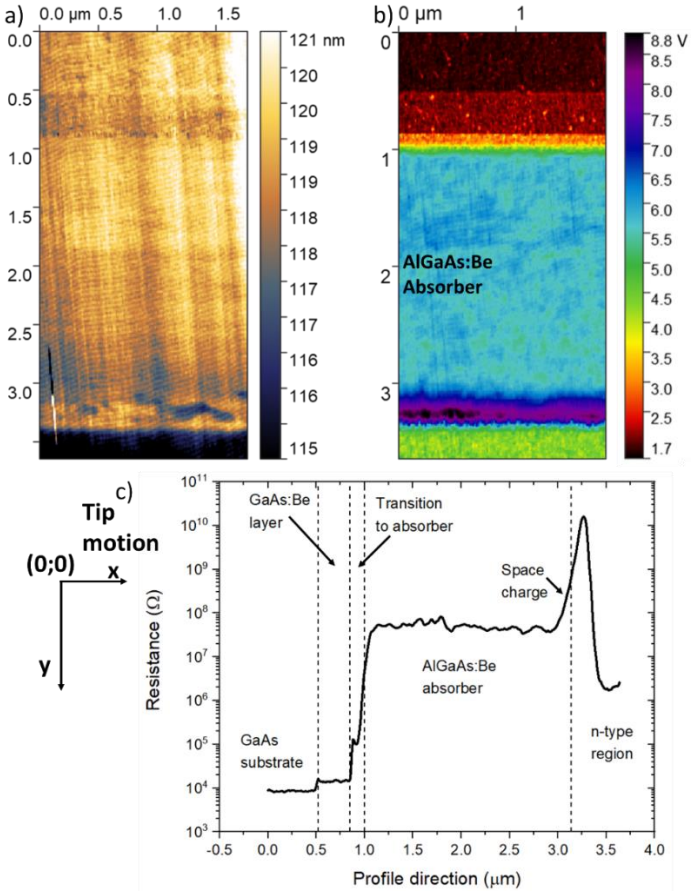


**Figure 6:** Topography image a) and voltage map b) acquired on the cross-section of the multilayer stack applying +1 V between the sample and the tip in dark conditions; c) corresponding resistance profile along the Y axis calculated from b) applying $R=10^{(V+2)}$. The profile data are an average of 207 points corresponding to 0.7 µm scan in the X direction.

and 1.14 µm), which can be attributed to either a slight space charge layer in the absorber and/or the convolution of the signal at the interface caused by the physical dimensions of the AFM tip radius (≈ 100 nm). Moreover, a rise in resistance is detected around 2.88 µm, from $5x10^7$ Ω to $10^{10}$ Ω and it extends up to 3.27 µm to which corresponds the maximum of the measured local resistance. The extent of this resistance increase (0.39 µm) is comparable to the space charge width calculated by modelling (0.28 µm), also considering the 100 nm Gr AlGaAs transition layer that was not included in the energy bands simulation. However, according to the thickness of the layers reported in table 1, the resistance increase extends well beyond the expected beginning of n-type part of the structure (at 3.14 µm). As already described, the tip radius is ≈ 100 nm and thus the signals associated to the Gr AlGaAs (100 nm), GaInP:Si (50 nm) and AlInP:Si (20 nm) layers are likely to be "hidden" (or at least, not well-resolved) between the final part of the AlGaAs:Be absorber layer and the beginning of the n-GaAs:Si layer.

After crossing the resistance maximum, a decrease in resistance is measured which eventually stabilizes (≈$10^6$ Ω) along the n-GaAs:Si contact layer. Although both n-GaAs:Si and p-GaAs:Zn layers have identical dopant concentrations, their local resistance values differ. Notably, despite the fact that hole mobility is greater than electron mobility [5], the p-GaAs:Zn layer exhibits lower resistance compared to the n-GaAs:Si

layer. This unique experimental observation will be further examined and discussed in light of new Resiscope measurements in paragraph 4.1.4.
Finally, the discussion concerning the extent of the space charge will be also resumed in paragraph 4.1.5.

To continue our discussion, it is important to mention that multiple voltage maps were collected during the analysis at different places of the cross-section, and the outcomes demonstrated reproducibility of the results shown in Figure 6, one example is reported in Figure 7. The resistance profile in Figure 7c closely resembles the one in Figure 6c, indicating a consistent increase of resistance as the tip approaches the end of the AlGaAs:Be layer towards the n-type region.

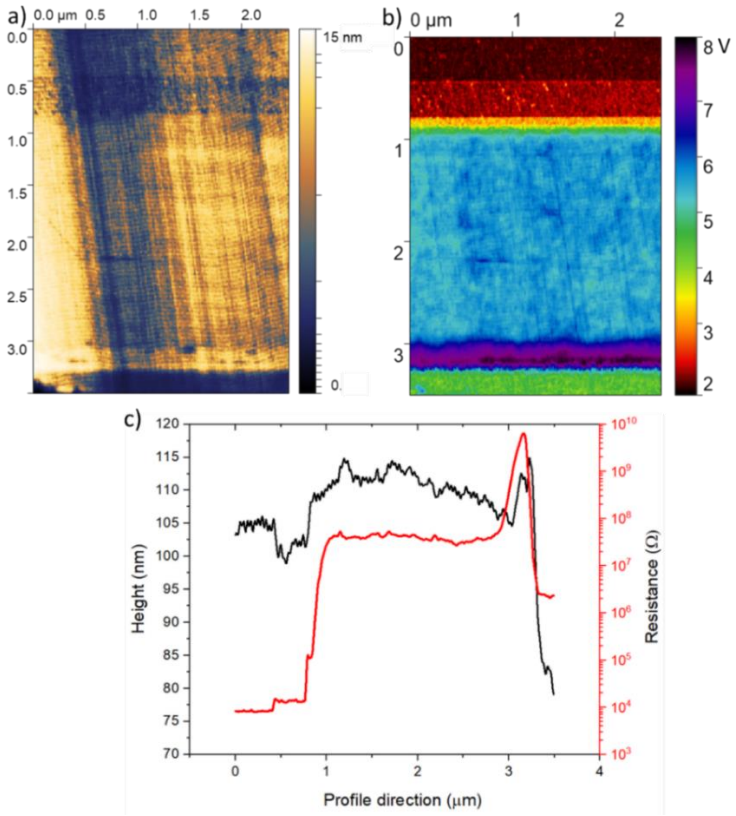


**Figure 7:** Topography a) and voltage map b) acquired on the cross-section (on a different region with respect to Figure 3) of the multilayer stack applying +1 V between the sample and the tip in dark conditions; c) corresponding height and resistance profiles extrapolated from a) and calculated from b) applying $R=10^{(V+2)}$, respectively.

Additionally, Figure 7c includes the topography height profile, which offers new insights for further discussion. In particular, accurately determining the true "end" of the cross-sectional area in the topography image proves to be a challenging task. The difficulty arises from the fact that the height profile shows only a minor decrease of a few tens of nanometers at approximately 3.3 µm, despite the expectation of a more substantial height decrease (around a few micrometers). Specifically, during c-AFM analysis, a relatively high force (up to 1000 nN) is applied by the AFM tip to ensure a reasonable electrical contact with the sample. Therefore, since the tip continues to exert a force even after its apex has passed beyond the sample edge, the tip body can still interact with the sample producing “parasitic” electrical signals. A schematic of this occurrence is shown in Figure 8.

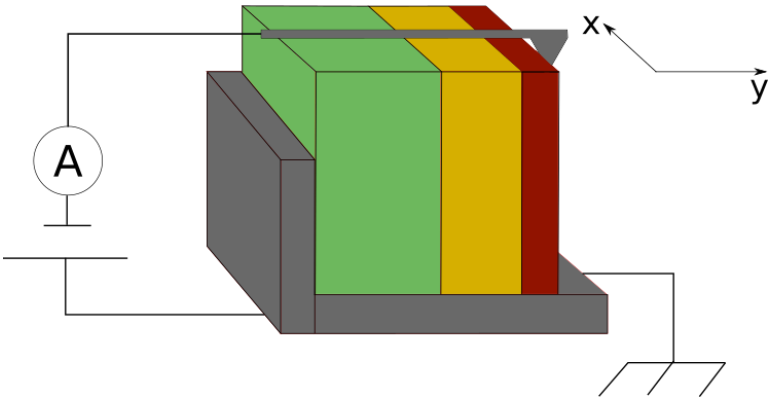


**Figure 8:** Schematic representation of the undesired interactions between the body of the tip and the edge of the sample. The increased contact area can give rise to a lower local resistance along with a decrease of lateral resolution.

Under these circumstances, a higher electrical contact radius (see Eq. 2) is established causing the collection of a higher current through the AFM tip and a consequent decrease of the measured local resistance, along with a decrease of lateral resolution [8]. In our case, the $\approx 10^6$ Ω resistance plateau value measured for the n-GaAs contact layer could be due to a signal convolution between AFM tip apex and body deriving from the interaction with the cross-section edge. Further details will be given in paragraph 4.1.4.
Nevertheless, a possible solution might involve conducting extended scans along the y-axis until a sharp reduction in topographical features is detected. Subsequently, by making comparisons with the physical dimensions of the layers that comprise the analyzed sample, it would be possible to localize with more precision the edge of the cross-section.

### 4.1.4 Evaluating the true nature of AFM tip/surface contact

In order to further discuss the experimental results presented in the previous paragraphs, let us focus on some of the physical aspects related to the c-AFM technique, elucidating some concepts concerning the nature of the electrical contact between the AFM tip and the surface of a semiconductor.
In paragraph 4.1.2, the electrical contact resistance and the resistivity were described and defined in equation 2 and equation 1, respectively. During c-AFM analysis, a bias voltage is applied between the conductive AFM tip and the sample (see paragraph 2.6). The variation in current, as the tip is scanned, should then be inversely proportional to the electrical contact resistance (Eq. 2) in the vicinity of the AFM tip, assuming an ohmic contact between the tip and the semiconductor. Additionally, according to the very definition of the resistivity (Eq. 1), for the same doping concentrations but different type, the only factor that can cause differences in the resistivity and in turn in the electrical contact resistance is the mobility (assuming that all introduced impurities act as dopants and are ionized). According to [5], the ratio between electron mobility and hole mobility in GaAs is in the order of a factor of 20 (see Appendix B $\mu_n$ and $\mu_p$ Vs doping concentration in GaAs). As a consequence, one can expect the electrical contact resistance (Eq. 2) to be about 20 times lower in n-GaAs compared to p-GaAs with the same doping concentration. However, experimentally (see Figure 6c), the local resistance measured in the p-GaAs:Zn substrate is more than two orders of magnitude lower than the one measured in the n-GaAs:Si contact layer.

In light of this experimental evidence further Resiscope analysis was performed. Specifically, we have investigated two different simple samples that were available at GeePs: a n-GaAs:Si ($N_D=10^{19}$ $cm^{-3}$) and a p-GaAs:Zn ($N_A=10^{18}$ $cm^{-3}$) bare substrate. Note that a p-GaAs:Zn substrate with a doping concentration of $10^{18}$ $cm^{-3}$ was analyzed since a sample with a doping concentration of $10^{19}$ $cm^{-3}$, as the p-GaAs:Zn substrate in the multilayer structure, was not available.
Resiscope measurements were performed in planar configuration and the samples were electrically connected to a metal plate through a silver paste layer from the back side whereas the tip scanned the polished front surface. A schematic of the experimental setup is shown in Figure 9a. Note that the same experimental conditions described in paragraph 4.1.2 were replicated and thus they will not be repeated here.

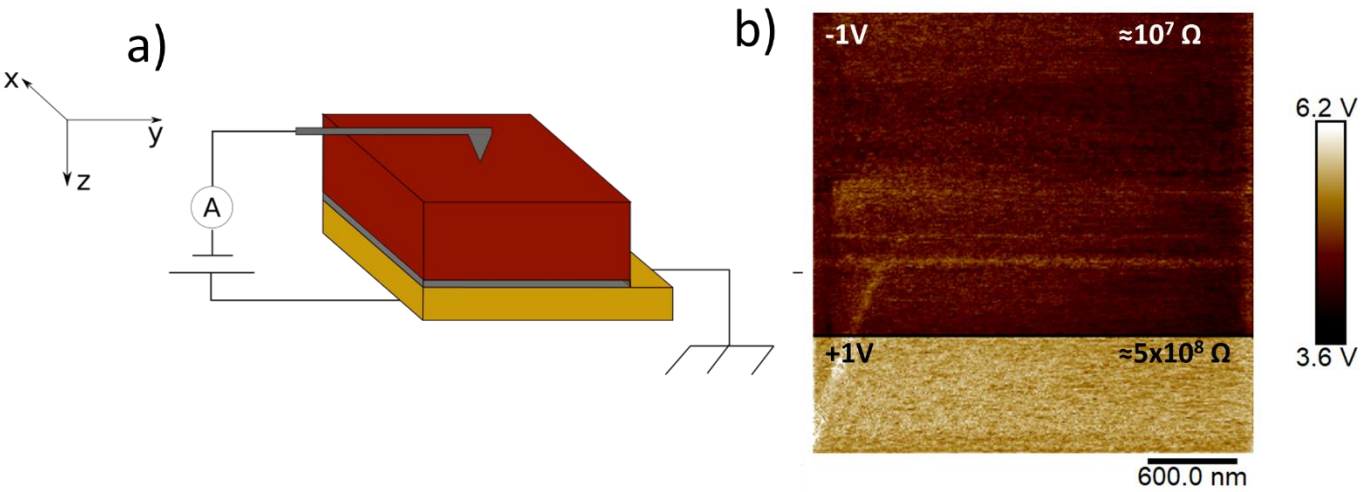


**Figure 9:** a) schematic of the experimental Resiscope setup used for the characterization of simple n-GaAs and p-GaAs samples. b) Resiscope results obtained on the front surface of a bare n-GaAs:Si substrate ($N_D=10^{19}$ $cm^{-3}$) for -1 V (top) and +1 V (bottom) bias applied between the sample and the tip.

As a first step, the n-GaAs sample was analyzed by applying +1 V and -1 V between the sample and the AFM tip; the corresponding voltage map is reported in Figure 9b. Note that the top part and bottom part of the voltage map correspond to the -1 V and +1 V polarization, respectively.
Averaged resistance values of the order of $10^7$ Ω and $5x10^8$ Ω are obtained for the -1 V and +1 V polarities, respectively. Interestingly, in the case in which the electrical contact between the AFM tip and the sample was an ohmic contact, the same resistance values would be expected to be found for opposite polarities. However, the experimental findings depicted in Figure 9b demonstrate that identical resistance values are not observed for the chosen opposite polarities. This indicates the presence of a rectifying behavior based on the applied polarity, suggesting that the actual nature of the electrical connection between the AFM tip and the semiconductor surface may be Schottky-type, rather than ohmic-type.
In order to provide further discussion, under the same experimental conditions depicted in Figure 9, local *I-V* curves have been acquired on both the bare n-GaAs and p-GaAs substrates samples directly using the Resiscope setup [10]. The applied voltage ranged between -1 V to +1 V and the results are shown in Figure 10.

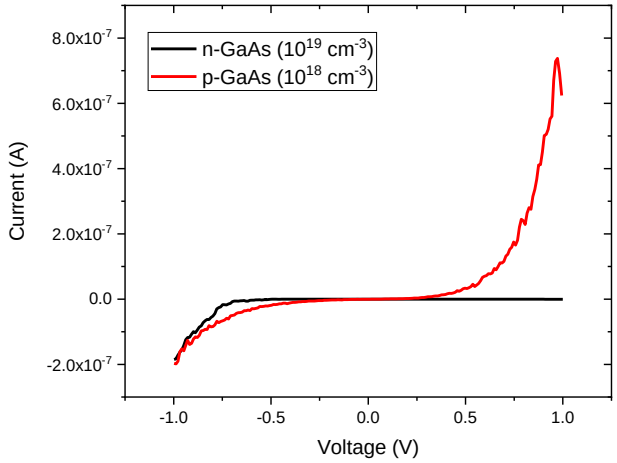


**Figure 10:** Local I-V curves obtained on the bare n-GaAs and p-GaAs substrates samples.

The local I-V curves show a diode-like behavior both for the n-GaAs and p-GaAs samples, confirming the Schottky nature of the electrical contact between the AFM tip and the surface of a semiconductor.

Consider Figure 11, in which a Schottky diode formed by a metal and a n-type semiconductor is shown. The metal is characterized by its work function ($\Phi_M$) and the semiconductor by its work function ($\Phi_{SC}$) and its electron affinity ($\chi_{SC}$). If the metal and semiconductor are brought into contact the Fermi levels will equilibrate. In the absence of interface defects, for the case of an n-type semiconductor for which $\Phi_{SC} < \Phi_M$, electrons will flow from the semiconductor to the metal, forming a negative surface charge in the metal that compensates the positive charge in the semiconductor in the vicinity of the surface due to the depletion of electrons (or even accumulation of holes). A Schottky barrier of height $F_{Bn} = \Phi_M - \chi_{SC}$ forms for electrons at the interface and an upward band bending takes place in the n-type semiconductor. Conversely, in a Schottky diode formed between a metal and a p-type semiconductor, if $\Phi_{SC} > \Phi_M$ a downward band-bending forms in the semiconductor due to the depletion of holes (or even accumulation of electrons) while a positive surface charge builds in the metal, and the Schottky barrier for holes is given by $F_{Bp} = E_g - (\Phi_M - \chi_{SC})$, $E_g$ being the band gap energy of the semiconductor [5].
Changing the electrochemical potential difference between the metal and the semiconductor by application of an external bias, $\varphi_M - \varphi_{SC} = V_{applied}$, is able to change the electrostatic potential barrier in the semiconductor ($V_{bi} = V_{bi} - V_{applied}$) facilitating (forward bias, positive $V_{applied}$) or hindering (reverse bias, negative $V_{applied}$) electron emission from the semiconductor to the metal through the potential barrier.
The current is thus expected to be larger for positive $\varphi_M - \varphi_{SC}$ compared to negative $\varphi_M - \varphi_{SC}$. Considering that, in resiscope measurements the bias is applied between the sample and the AFM tip, the shape of the current and its larger value observed for the n-type GaAs sample in Figure 10 at -1V compared to the one obtained at +1V is in line with the tip/n-GaAs interface acting as a metal/n-type semiconductor interface as described in Figure 11. In the same way, the shape of the current vs voltage curve and the larger current at +1V compared to the one at -1V observed for the p-type GaAs sample in Figure 10 is in line with the tip/p-GaAs interface acting as a metal/p-type semiconductor interface, having opposite (downward) band bending at the GaAs surface.

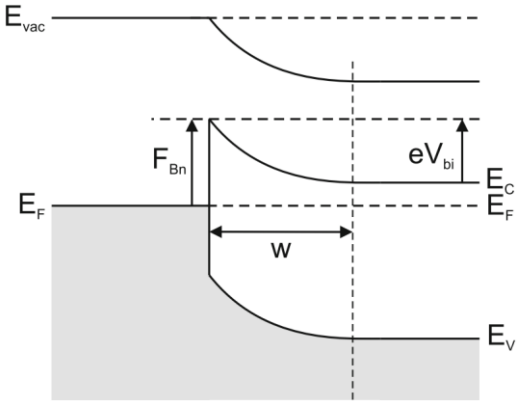


**Figure 11:** Energy band diagram of a metal/semiconductor junction for an n-type semiconductor having lower work function than the metal in the absence of surface states.

In section 4.1.3, we left as an open question the reason why the p-GaAs:Zn substrate exhibited lower resistance compared to the n-GaAs:Si layer in the multilayer structure despite having the same doping concentration and especially considering that the electron mobility is higher than the hole mobility in GaAs. Specifically, in Figure 10 it is shown that for an applied bias of +1 V, the current flowing through the AFM tip is almost zero ($10^{-12}$ A, e.g., lower Resiscope sensitivity limit) for the n-GaAs while it is $6x10^{-7}$ A for the p-GaAs samples. If we now move to the cross-sectional analysis (Figure 6), this corresponds to a higher local resistance in the n-type region with respect to the p-type region. Furthermore, the unexpectedly low current measured under +1 V polarity conditions in Figure 10 aligns with the possibility that the ≈ $10^6$ Ω plateau observed in the n-GaAs:Si contact layer (see Figure 6c) could potentially result from an increased point contact radius (*a*), caused by undesired interactions between the body of the tip and the edge of the sample.

In conclusion, our experimental data demonstrate that it is not possible to consider the contact between the AFM tip and the sample as an ohmic contact but it must be considered as a Schottky contact. In other terms, an electrostatic potential barrier will always form at the semiconductor surface due to the contact with the AFM tip. For this reason, the polarity applied during c-AFM analysis becomes a significant parameter since it can modulate the potential barrier in the semiconductor hindering or facilitating the collection of charges which in turn determines the local measured resistance.
However, the Schottky characteristics of the electrical contact introduce substantial complications to the acquisition of quantitative results and data interpretation. Indeed, the description of a Schottky barrier given in Figure 11 was drawn assuming that there was no surface dependent effect. As a matter of fact, the electrostatic potential barrier in the semiconductor depends on a multitude of different parameters that comprise not only the physical properties of the materials, such as doping concentration of the semiconductor, electron affinity and metal work function but also on possible surface dipole effects and surface defects distributions. This implies that the outcome of experimental results will consistently rely on the preparation of the cross-section, including cleaving and surface treatments.

Moreover, one has to consider another experimental condition specific to the c-AFM measurements, namely the applied forces, that also modifies the interface condition. This is why we provide an analysis

of how the applied force by the AFM tip on the surface of the sample affect the electrical signal. To investigate this, we have acquired different local I-V curves at varying applied forces on the simple n-GaAs sample which are shown in Figure 12.

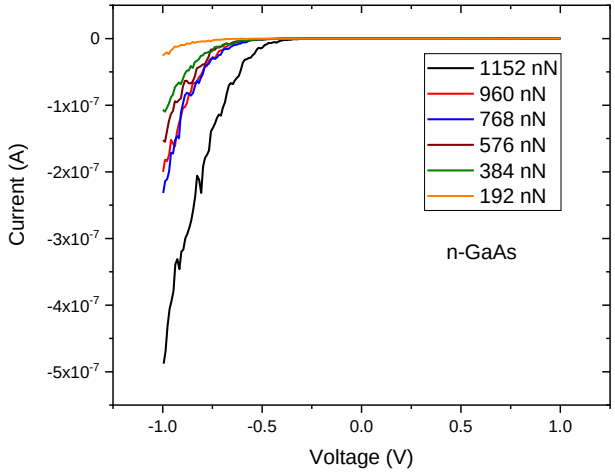


**Figure 12:** Local I-V curves obtained at varying applied forces on the simple n-GaAs sample.

Figure 12 clearly shows that the amount of current collected by the tip depends on the applied force. More precisely, when an applied force of 192 nN is selected, the current levels are very low, even at negative biases. However, within the range of applied forces spanning from 384 nN to 960 nN, it is noticeable that the current passing through the AFM tip steadily rises until it reaches values around $-2x10^{-7}$ A. Notably, the relatively higher current level observed at 1152 nN compared to the range from 384 nN to 960 nN suggests the presence of a potential threshold value beyond which a more consistent current level is achieved. This clearly illustrates that the electrical signal derived from c-AFM analysis depends on the applied force. Consequently, for the attainment of a satisfactory signal-to-noise ratio, the selection of the applied force is crucial. Nevertheless, to ensure the durability of the AFM tip and prevent rapid damage, a balance must be found between electrical signal resolution and the applied force. Furthermore, the influence of applied force on the electrical signal adds an additional variable to c-AFM characterization, further complicating the acquisition of precise quantitative and comparable local resistance profiles.

### 4.1.5 Cross-sectional c-AFM on the p-AlGaAs:Be/n-GaInP:Si multilayer stack: New measurements

In light of the experimental results and discussion reported in paragraph 4.1.4, we have decided to perform new Resiscope measurements on the cross-section of the multilayer stack replicating the experimental setup shown in Figure 5. Note that the resistance profiles to be presented in Figure 13 should not be quantitatively compared to those shown in Figure 6. The reason for this is that these measurements were conducted nearly a year later than the ones in Figure 6. Consequently, a different area of the cross-section has been analyzed, a new “fresh” AFM tip was used, and even though the contact forces employed fall within the same range, variations might be present. Nonetheless, the new measurements can bring additional value to the discussion since the resistance profile was also evaluated for an applied bias of -1 V between the sample and the AFM tip.

In Figure 13a and 13b, the topography image and the voltage map acquired on the cross-section of the multilayer stack are shown, respectively. Additionally, the corresponding resistance profiles are shown in Figure 13c.

Firstly, let us consider the resistance profile acquired for +1 V. The same qualitative behavior and profile is once again found as in the resistance profile shown in Figure 6c. Therefore, the same considerations described in section 4.1.2 will not be repeated here for brevity.

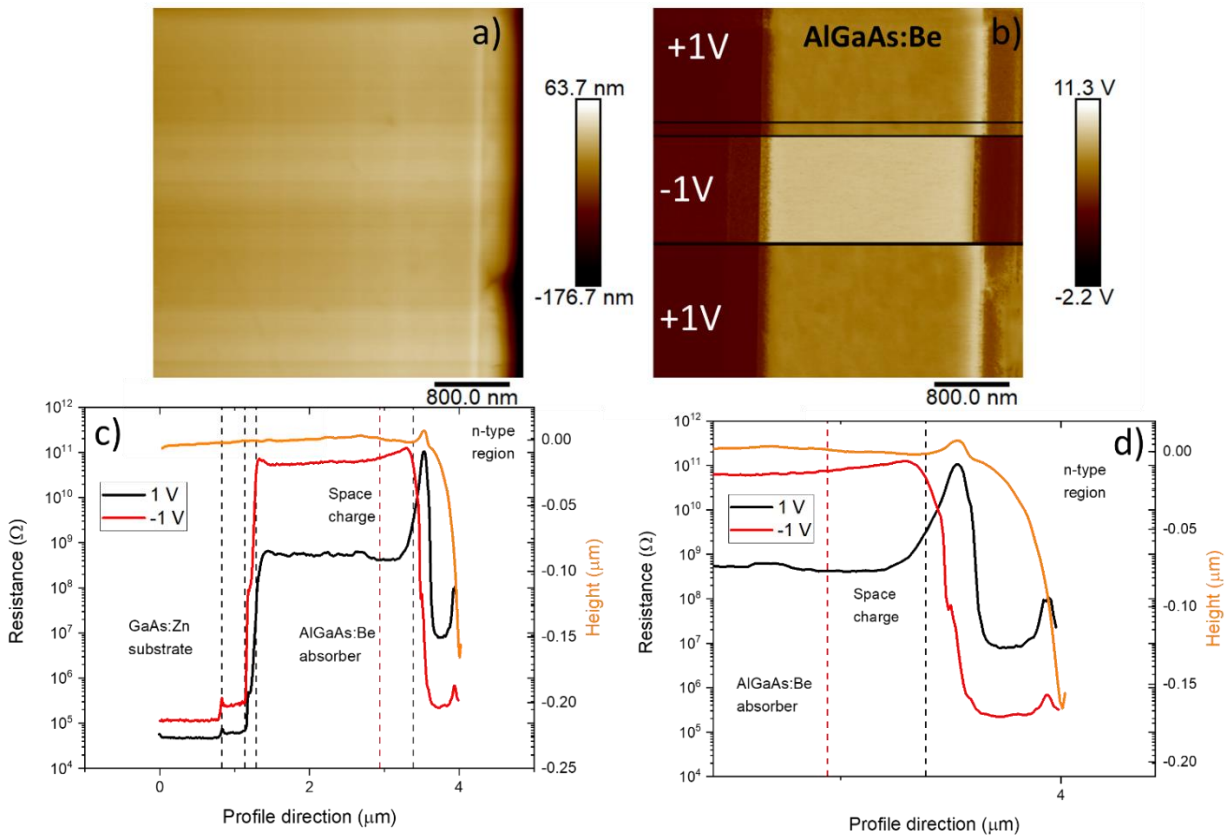


**Figure 13:** Topography a) and Voltage map b) acquired on the cross-section of the multilayer stack applying +1 V and -1 V between the sample and the tip in dark conditions; c) corresponding resistance profiles calculated from b) applying $R=10^{(V+2)}$. The profile is shown in log scale. The height profile is also shown. d) Zoom of Figure 13c between 2.5 μm and 4 μm.

The resistance profile acquired for -1 V provides a basis for further discussion. Specifically, the p-region of the structure appears to be more resistive compared to the corresponding +1 V case. As a matter of fact, as shown in the local I-V curves of Figure 10 for the p-GaAs sample, a lower current was measured for negative applied voltages. Conversely, the n-type region results to be less resistive for the -1 V polarity with respect to the corresponding + 1 V case, as again expected considering Figure 10. Specifically, as the AFM tip approaches the n-type region, a huge decrease in resistance is measured which stabilizes at ≈$5x10^5$ Ω once reached the n-GaAs contact layer.

However, the most valuable difference lies in the identification of the space charge region at the n/p front interface, which for the -1 V profile appears as a small increase in resistance between 2.94 μm (reference red dashed line in Figure 13c) and 3.32 μm. The spatial extension of the space charge, around 380 nm, is

in line with the theoretical value calculated from the modelling reported in Figure 2. Specifically, the resistance decrease at 3.30 µm (right after the small resistance increase related to the space charge) extends for around 100 nm before the intersection point between the two resistance profiles at 3.41 µm and thus it can be associated to the 100 nm Gr transition layer between the absorber and the beginning of the n-type region. Therefore, as a further point for discussion, one might speculate whether the point of intersection between the two distinct resistance profiles acquired at opposite polarities could represent the boundary of the pn junction (within the lateral limits set by the radius of the tip). This could potentially indicate the transition from a p-type to an n-type region.
Furthermore, as emphasized by the zoom of Figure 13c between 2.5 µm and 4 µm (Figure 13d), there is a narrow resistance discontinuity observed between 3.48 µm 3.50 µm. Given the limited extent of this specific feature, it is plausible to associate this step with GaInP:Si/AlInP:Si interface. However, in this particular region a bump is present in the height profile, signifying that a modification in the radius of the point contact (*a*) may also have occurred.
Furthermore, Lu et al. [11] report on cross-sectional Scanning Spreading Resistance Microscopy (SSRM) [12] performed on a GaAs-based device. It is described that only one polarity allowed to resolve the expected resistance profile and correctly visualize the space charge region at a GaAs $p^+n$ junction. Therefore, based on our experimental results, it appears that the -1 V polarity provides a clearer visualization of the actual extent of the space charge. In contrast, the +1 V polarity yields more intricate results due to the convolution of the space charge signal (resistance increase) with the sharper rise in resistance associated with the n-type region.

In conclusion, Resiscope analysis proved to be a valuable method for measuring the resistance along a III-V based multilayer structure, enabling the identification of the various layers and regions with different doping type. Nonetheless, the problematic and difficulties related to this investigative technique were also discussed with particular emphasis on the true nature of electrical contact between the AFM tip and surface of the sample which resulted to be Schottky-type. Finally, the recent experimental findings underscore the significance of comprehensive characterization including opposite polarities. This approach is critical for revealing subtle distinctions that could otherwise be disregarded when focusing solely on a single polarity.
Finally, it is important to recall that, as indicated earlier in this section within Figure 4, we presented the expected resistivity profiles based on "bulk" properties and after the introduction of a density of surface states. Our experimental findings unequivocally confirm the presence of surface states, which actively influence the determination of local resistance and its deviation from the “bulk” ideal case. Consequently, through comprehensive modeling, it becomes possible to utilize the resistance profile for the determination of the quantitative distribution of the surface states that characterize a given cross-section.

In appendix C, some of the experimental results presented in Lu et al. [11] will be shown and used to provide comparison and further discussion with our experimental result.

## 4.2 KPFM and c-AFM for the characterization of p-AlGaAs:Be/n-GaInP:Si finalized solar cell

Once familiarized with the c-AFM technique, I expanded the characterization to include the completed solar cell (Figure 1b). Following the cleaving process, the cross-section was subjected to analysis using KPFM and c-AFM under dark and laser-illuminated conditions. For the KPFM measurements, the device was connected to a sourcemeter (Keithley 2400), with the back contact serving as the positive terminal and the front contact as the negative terminal, enabling the application of an external bias to the device. Note that this terminal configuration gives a positive $V_{OC}$ value displayed on the sourcemeter under illumination. Conversely, for Resiscope analysis, the same configuration described in the previous paragraph was replicated. For comparison, a schematic of the experimental configurations used for cross-sectional Resiscope and KPFM analysis are compared in Figure 14. Note that in the KPFM setup, an insulating layer (blue layer) was also placed at the basis of the sample in order to avoid the short-circuit between the sample holder and the new added electrode.

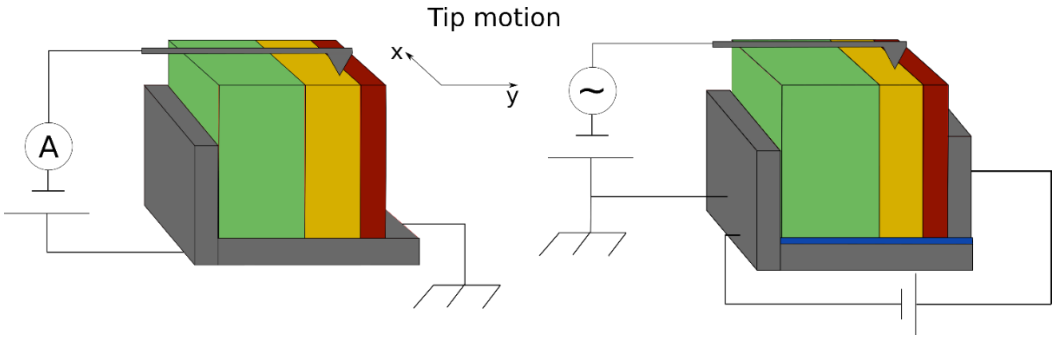


**Figure 14:** Schematic representation of the experimental setup for cross-sectional Resiscope (left) and KPFM (right) analysis. Note that in the KPFM setup, an insulating layer (blue layer at the basis of the sample) was added in order to avoid the short-circuit between the sample holder and the new added electrode.

The I-V curve under 1-Sun illumination (1 kW/m²) and the normalized EQE acquired for the solar cell before cleaving at IPVF are reported in Figure 15a and 15b, respectively. In the analysis of the I-V characteristics under illumination, the values of $I_{SC}$ (short-circuit current), $V_{OC}$ (open-circuit voltage), and FF (fill factor) were determined to be 3.32 mA, 1.16 V, and 77.9%, respectively, leading to an overall power conversion efficiency of 12 %.

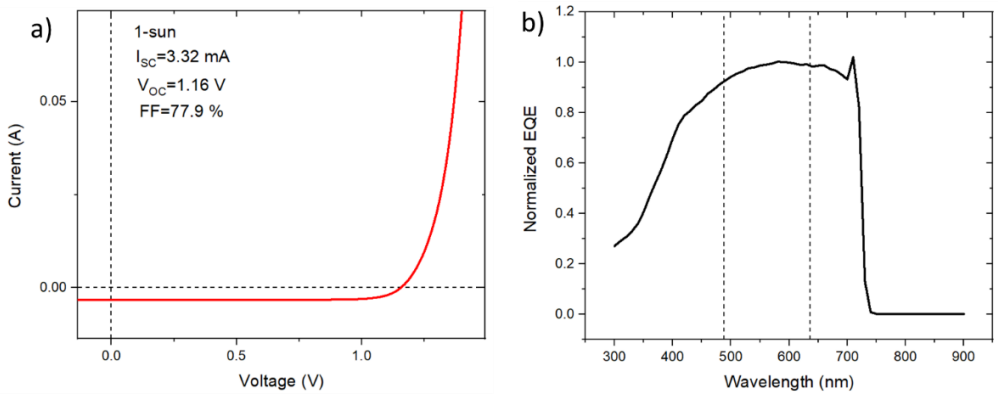


**Figure 15:** a) I-V curve of the p-AlGaAs:Be/n-GaInP:Si solar cell under 1-sun illumination and b) normalized EQE curve. The two vertical reference lines plotted at 488 nm and 636 nm in b) represent the wavelengths of the lasers used for Resiscope and KPFM measurements, respectively.

The EQE curve shows that the solar cell starts to efficiently absorb the incident light at around 720 nm which is in line with the expected energy gap value of 1.73 eV. In [2], it is argued that the steep decrease at short wavelengths is attributed to DX-centers related to the Si doping. They result in a high density of deep defects, which act as nonradiative recombination centers and reduce the minority carrier lifetime.
It is important to mention that the sample was subjected to two different cleaving procedures. In particular, the first characterization that was performed was cross-sectional Resiscope and thus a cleaving direction parallel to the macro metallic contact was chosen to expose the cross-section (Figure 16 left). After Resiscope characterization, the sample was cleaved along the perpendicular direction with respect to the first cleaving direction in order to expose a new fresh cross-section. This choice was a consequence imposed by constraints due to the physical dimensions of the GaAs wafer allowing to avoid macro damages to the solar cell.

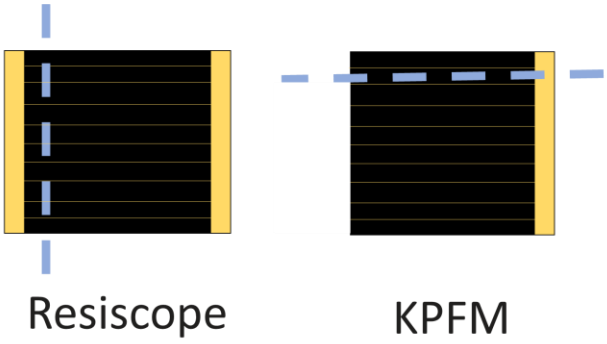


**Figure 16:** Schematic of the cleaving direction used for Resiscope (left) and KPFM (right) analysis. After the cleaving to perform Resiscope analysis, the same sample was cleaved along the perpendicular direction of the first cleaving in order to have a freshly exposed cross-section. Note that without considering the thin metal grids, the solar cell area is 0.5 x 0.5 $cm^2$.

Please note that in the “Resiscope cleaving direction”, it is conceivable to locate areas where both the GaAs:Si contact layer and the metallic contact coexist. However, it is highly probable that the metallic contact might undergo damages as a result of a non-optimal cleaving process. Conversely, when cleaving along the “KPFM direction”, the cleaving process either occurs along a metallic finger or the GaAs:Si contact layer is not accessible due to the etching procedure (see Figure 1).
Subsequent to the cleaving process, I-V measurements still displayed consistent diode behavior, indicating although cleaving might have induced surface states and potential shunts, it had not been destroyed the device that still acted as a solar cell.

### 4.2.1 Cross-sectional Resiscope analysis on the p-AlGaAs:Be/n-GaInP:Si solar cell

To continue the discussion presented in the previous section, Resiscope measurements have been performed on the finalized AlGaAs solar cell in the same experimental configuration reported in Figure 14 (left). During this analysis, two voltage maps have been acquired in dark conditions and under front illumination of the whole area of the solar cell with a 488 nm laser at a power density of 3 mW $cm^{-2}$. These were acquired for both + 1 V and -1 V polarities applied between the solar cell and the AFM tip, as done for Figure 13. In order to show the effect of the illumination, the voltage maps (Figure 18 and 20 for +1 V and -1 V, respectively) have been acquired half in dark and half under illumination. The initial emphasis of

our discussion will be directed towards the resistance profiles (Figure 17) acquired in dark conditions for +1 V and -1 V applied polarities.

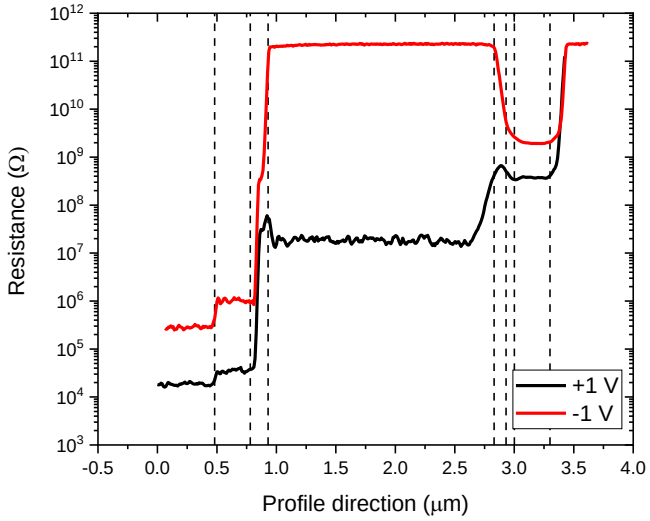


**Figure 17:** Resistance profiles acquired on the cross-section of the solar cell in dark conditions. The profiles were extracted and calculated from the "dark" part of the voltage maps reported in Figure 18 and 20 for +1 V and -1V applied polarities, respectively.

For what concerns the highly doped p-type region (GaAs:Zn substrate and GaAs:Be layer), the resistance values are in good agreement with the ones reported in Figure 13c showing once again a higher resistance for the -1 V polarity with respect to the +1 V polarity (due to some rectification effect of the tip/surface contact). Additionally, a small resistance increase is again found at the GaAs:Zn/GaAs:Be interface confirming the slightly higher resistivity of the GaAs:Be layer with respect to the GaAs:Zn substrate. A resistance increase is once again present as the AFM tip approaches the 150 nm transition layers moving toward the p-AlGaAs:Be absorber.

Considering the AlGaAs:Be absorber, for the +1 V case, the measured resistance value is comparable to the ones reported in Figure 6c and 7c. However, in this region, for the -1 V case, the resistance profile appears completely flat (even small resistance fluctuations are not present). This indicates that the actual resistance value is here higher than the upper measurement limit of the Resiscope equipment ($3x10^{11}$ Ω). As a consequence, the information related to the space charge region cannot be visualized since it would present even higher resistance values, as shown in Figure 13c in the case of the multilayer structure for -1 V applied bias. Several reasons can be related to this experimental evidence. For instance, a slightly different surface defects distribution density may be present that causes the AlGaAs:Be absorber to be more resistive or even the tip-induced oxidation phenomenon [13], already described in paragraph 1.4.2.1, can have had an effect.

Interestingly, for the +1 V case, we observe a resistance increase between 2.62 µm and 2.83 µm which can be associated to the space charge caused by the p-AlGaAs:Be/n-GaInP:Si heterojunction. Note that the resistance increase was also present in the multilayer sample (Figure 6c); however, in this case, the increase in resistance begins to occur at a point that is considered to be within the absorber layer, as predicted by the simulated energy bands shown in Figure 2. The Gr AlGaAs transition layer is placed between 2.83 µm to 2.93 µm and it appears as a small resistance peak. Finally, the n-region extends from 2.93 µm

to 3.30 µm. Interestingly, after crossing the GaInP:Si/AlInP:Si layers (70 nm), the resistance value reaches a plateau, that extends for approximately 300 nm before a huge increase in resistance reaching the detectable resistance limit, e.g., the end of the sample. Conversely, for the -1 V case, a resistance decrease is detected once crossed the end of the absorber layer, as obtained for the multilayer structure (Figure 13c). Specifically, the region from 2.83 µm to 3 µm can be identified as the Gr AlGaAs transition layer together with the two n-GaInP:Si/AlInP:Si layers. Finally, a resistance plateau is found as in the case of +1 V that can be associated to the n-GaAs:Si layer.

Nonetheless, the "solar cell" resistance profiles in the n-type region result to be generally different with respect to the "multilayer" profiles. Specifically, the "rectification ratio", i.e. the ratio of the measured resistance at -1V to that measured at +1 V is smaller with respect to the multilayer case and additionally, it is the opposite of that observed for the multilayer structure: the n-type region appears more resistive even at -1 V polarity. One reason can be related to the different condition of cross-section. Specifically, a more homogenous cross-section, especially near the edge, could have been obtained after cleaving for the solar cell with respect to the multilayer structure allowing a better visualization of the n-GaAs:Si layer; even a different surface defect density and distribution can be also present being responsible of the aforementioned differences.

Finally, the lack of a massive decrease of resistance associated to the AFM tip scanning on the metallic finger suggests that the metallic contact was damaged during the cleaving process.

Figure 18a shows the voltage map that was acquired under +1 V bias applied between the sample and the tip. Figure 18b shows the resistance profiles extrapolated from the dark (already shown in Figure 17) and the "under illumination" regions of Figure 18a, in black and red, respectively.

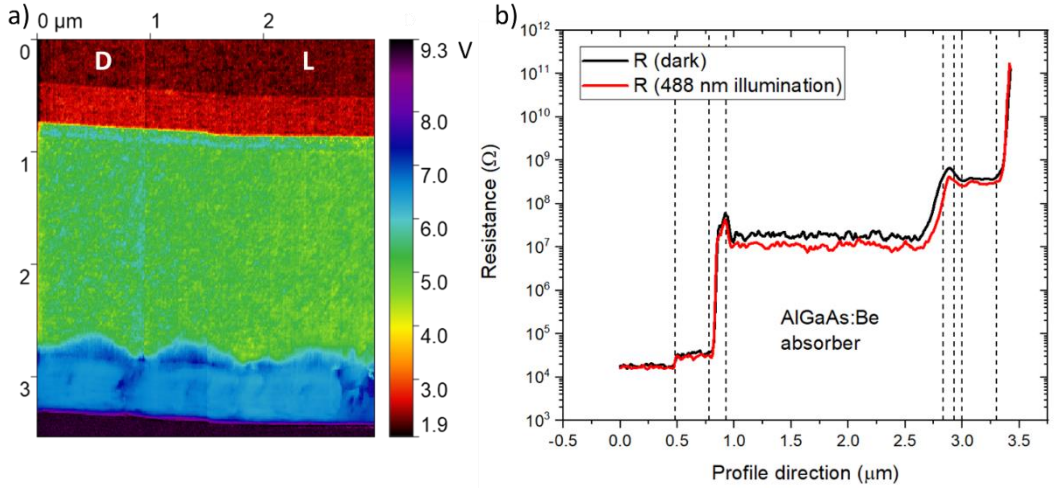


**Figure 18:** Voltage map a) acquired on the cross-section of the solar cell applying +1 V between the sample and the tip in dark conditions; b) corresponding resistance profile calculated from a) applying $R=10^{(V+2)}$. The profile in dark refers to dark conditions whereas the profile in red is obtained under 488 nm laser illumination.

Since the AFM tip scans the cross-section of the solar cell, as it reaches the n-GaAs:Si layer, the electrical circuit is closed, and charge carriers can flow. However, due to the high doping concentration of the layers in the structure, photogeneration mainly takes place in the AlGaAs:Be absorber. As a matter of fact, the illumination causes a slight decrease in resistance along the AlGaAs:Be absorber layer and a negligible effect along the rest of the structure. As a matter of fact, as can be seen in Figure 19 showing the I-V curves

of the device that were acquired just before cleaving, the current values at +1 V are almost the same in the dark and under the 488 nm laser illumination.

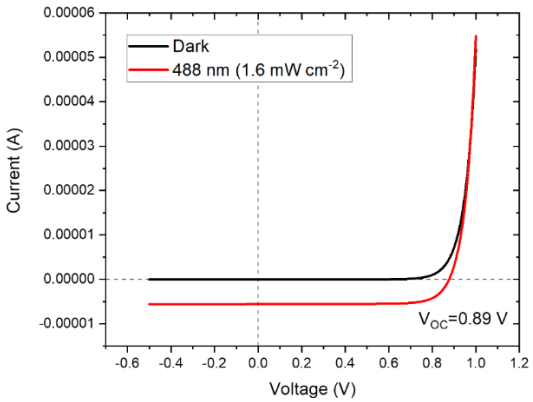


**Figure 19:** I-V characteristic in dark and under 488 nm laser illumination acquired on the same sample prior to the cleaving process.

Figure 20a shows the voltage map that was acquired under -1 V bias applied between the sample and the tip. Figure 20b shows the resistance profiles extrapolated from the dark (already shown in Figure 17) and the "under illumination" regions of Figure 18a, in black and red, respectively. Note that the voltage map obtained in the highly doped p-type region shows fluctuating resistances values under light and in the dark, suggesting a problem with the AFM tip contact. For this reason, in Figure 20b, a shaded rectangle was added to cover the resistance signal associated with the p-GaAs:Zn substrate and p-GaAs:Be layer. Additionally, in Appendix D it is possible to find horizontal profiles acquired along the p-GaAs:Zn substrate and the p-GaAs:Be layer showing that the application of the illumination is not responsible of a general decrease in the local resistance value of the highly doped p-type region.

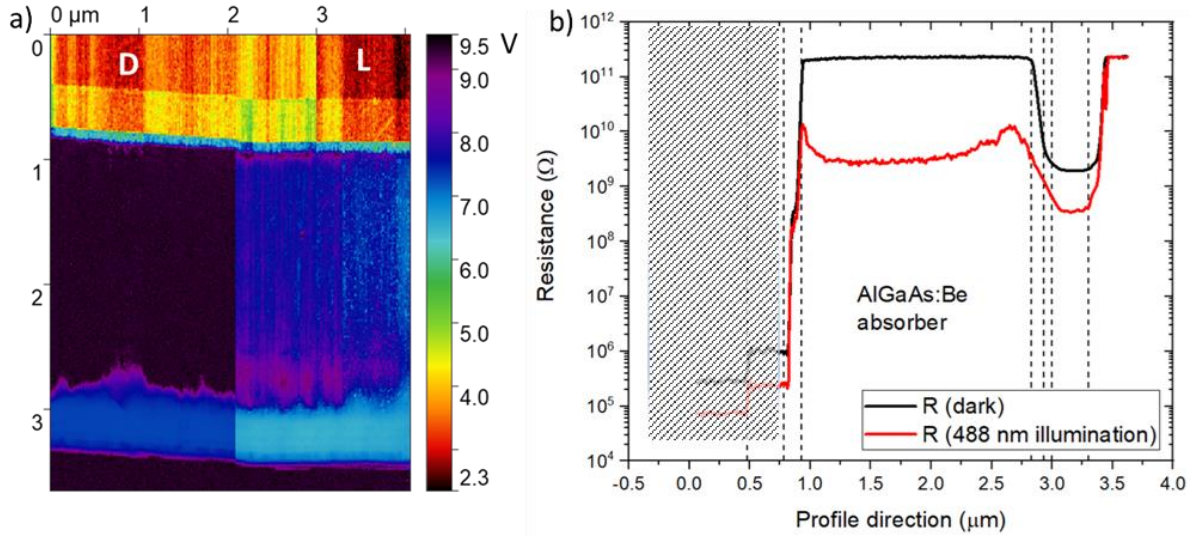


**Figure 20:** Voltage map a) acquired on the cross-section of the solar cell applying -1 V between the sample and the tip in dark conditions; b) corresponding resistance profile calculated from a) applying $R=10^{(V+2)}$. The profile in dark refers to dark conditions whereas the profile in red is obtained under 488 nm laser illumination.

When the solar cell is illuminated, the generated photocurrent appears to produce a signal higher than the lower limit of the Resiscope sensitivity. Intriguingly, focusing on the absorber layer (from 0.93 µm to 2.83 µm), at the beginning is present a resistance peak that can support the possibility of the presence of a space charge region at Gr AlGaAs/absorber interface which may act as a barrier for carriers. Additionally, approaching the end of the absorber layer, the increase of resistance related to p-AlGaAs:Be/n-GaInP:Si space charge is now resolved.
Interestingly, the application of the laser illumination caused a decrease of resistance along the whole analyzed structure (with the exception of the highly p-doped layers as already described). A decrease of resistance measured in the n-type region under illumination is reasonable. In fact, even though charge carriers photogeneration is expected to occur only in the absorber layer, the photogenerated carriers can diffuse and drift to the n-type region due to the presence of the electric field in the space charge region. The AFM tip, when in contact with the sample, can interact with these photogenerated carriers since as the AFM tip reaches the n-GaAs:Si layer, the electrical circuit is closed, and charge carriers can be collected. The AFM tip is sensitive to local variations in conductivity and charge distribution resulting in the detection of a lower local resistance in the n-type region compared to the "dark" case. Finally, GaAs is characterized by a relatively high diffusion lengths of electrons and holes which can range from 1 µm to 10 µm based on the doping concentration [14].

In summary, the c-AFM approach for the study of solar cells on the cross-section is not a very conventional approach but has been widely used for the study of other devices [9,11,15]. We show here that the analysis of the results is not straightforward since several parameters must be considered both during the analysis (such as the applied polarity, pressing force and oxidation state of the surface) and for data interpretation (mainly surface defects density distribution). This wide range of parameters shows the complexity of this approach. In fact, precautions must be taken both in terms of cleaving process and surface passivation treatments in order to acquire quantitative and reproducible data. Nevertheless, if we can succeed in controlling all these parameters, then c-AFM analysis should allow the identification of the different doped regions illustrating the junctions and the photocurrent.

### 4.2.2 Cross-sectional KPFM on the p-AlGaAs:Be/n-GaInP:Si solar cell

As described in section 4.2, after the Resiscope characterization, the solar cell was again cleaved in order to expose a fresh cross-section for KPFM analysis. The experimental procedure for KPFM used in this characterization has been previously detailed in paragraphs 2.3.1 and 2.3.3 and a schematic of the experimental setup is reported in Figure 14 (right). Cross-sectional KPFM analysis was performed with the TRIOS platform presented in paragraph 2.2. ARROW-EFM $n^+$-Si Pt/Ir coated AFM tips were used, with a resonance frequency at 75 kHz. FM-KPFM mode was selected with a lift (tip/surface distance) of 25 nm.
To start the discussion, KPFM results obtained on the cross-section of the device in dark and short-circuit condition are presented in Figure 21. Specifically, Figure 21a illustrates the topographical image, Figure 21b displays the $V_{CPD}$ map, and finally, Figure 21c exhibits the profiles extracted from Figure 21a and 21b. Again, each point of the $V_{CPD}$ profile represents an average of 207 points over a width of 0.7 µm along the x axis. Note that the origin (0;0) is identified as a point in the GaAs:Zn substrate and moving along the positive direction of the Y axis, one will reach the end of the sample.

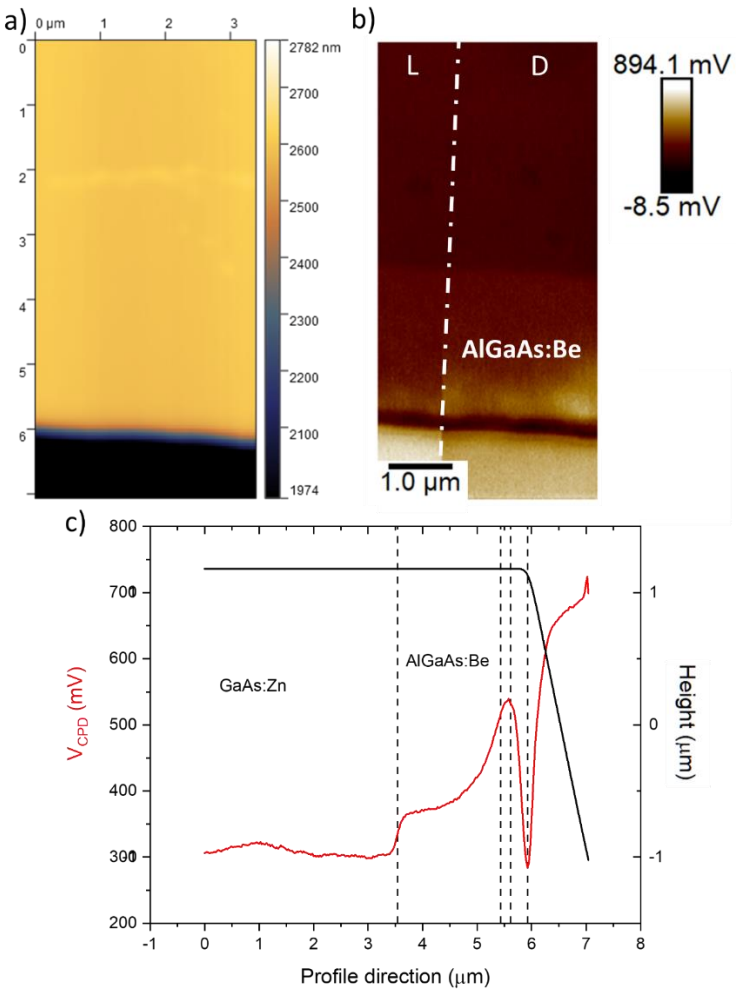


**Figure 21:** Topography a) and $V_{CPD}$ map b) acquired on the cross-section of the solar cell in dark conditions and under 636 nm laser illumination. The part of the image in dark and under illumination are indicated with "D" and "L", respectively. Corresponding height and $V_{CPD}$ profiles of the region in dark c); with reference to the main text, four reference lines were included at 3.53 µm, 5.41 µm, 5.58 µm and 5.95 µm in order to evidence the different regions of the analyzed structure. Specifically, the AlGaAs:Be absorber is located between 3.53 µm and 5.41 µm and the Gr transition layer together with the n-type region is located between 5.41 µm, and 5.58 µm. Note that the edge of the cross-section is found at 5.58 µm.

Upon initial examination of the "dark" $V_{CPD}$ profile, a qualitative analysis can be performed. Notably, a constant $V_{CPD}$ profile ranging from 0 µm to 3.52 µm, approximately at 300 mV, corresponds to the GaAs:Zn substrate. Additionally, a discernible increase in $V_{CPD}$ is observed at 3.52 µm, from 300 mV to 367 mV. This $V_{CPD}$ increase can be associated to the 150 nm Gr AlGaAs transition layer and the beginning of the AlGaAs:Be absorber layer. However, the $V_{CPD}$ profile observed at the interface does not demonstrate abrupt behavior, a characteristic that can be attributed to the averaging effect caused by the AFM tip, as discussed in paragraph 3.1.2.2. Notably, the $V_{CPD}$ begins to increase at 3.38 µm, and considering the additional 150 nm of the transition layers, it becomes evident that the signal associated with the absorber initiates at 3.53 µm, where it has not yet reached a flat profile.

Upon scanning the AFM tip over the AlGaAs:Be absorber, an initially flat profile is observed, which subsequently exhibits an increase at approximately 4.50 µm. By considering the point at 3.53 µm that was

identifyed as the beginning of the AlGaAs:Be absorber layer and adding its length (1.9 µm), a $\Delta V_{CPD}$ equal to 157 mV is present (considering 5.41 µm as ending point). This rise in $V_{CPD}$ can be associated with the presence of the space charge region, attributable to the AlGaAs:Be/GaInP:Si heterojunction. However, the $V_{CPD}$ variation associated with the space charge region appears to be attenuated compared to the predictions based on the bulk energy bands depicted in Figure 2. This observation can be related to the presence of surface states, as thoroughly explained in paragraph 3.3.2.3. Additionally, the extent of the space charge results to be wider with respect to the ≈ 400 nm obtained from the bulk energy bands shown in Figure 4, which could be attributed to the tip-averaging effect already described in paragarph 3.1.2.2. Moreover, the region from 5.41 µm to 5.58 µm (local $V_{CPD}$ maximum) can be identified as the Gr AlGaAs transition layer (100 nm) together with the n-GaInP:Si and n-AlInP:Si layers (50 nm and 20 nm, respectively).

Finally, a $V_{CPD}$ decrease is measured between 5.58 µm and 5.95 µm. However, it is important to note that such a decrease in $V_{CPD}$ is not compatible with a highly doped n-GaAs:Si, as depicted in the energy band profile presented in Figure 2: the energy bands continue to decrease, resulting in an increase in the surface potential. Drawing from the insights presented in Chapter 3, it becomes apparent that the observed decrease in surface potential within an highly doped n-type layer can only be explained by the presence of strong inversion at the surface, indicative of p-type behavior. Therefore, in order to further address this issue, the surface potential along the analyzed structure, as presented in Figure 2, was re-evaluated through modeling. In this simulation, we have incorporated a constant distribution of acceptor-like surface states with a density of states of $10^{22}$ $cm^{-3}eV^{-1}$ within a 1 nm thick surface layer (corresponding to a surface defect density of $N_{SS}=10^{15}$ $cm^{-2}eV^{-1}$, see paragraph 2.5), and the results were compared to the bulk surface potential and reported in Figure 22. Note that, due to the presence of only acceptor-like surface defects, the charge neutrality point will be set close to the valence band (at 0.2 eV from the valence band) and thus the p-type region of the structure will not be affacted. The existence of acceptor-like surface states leads to a less pronounced variation in $V_{CPD}$ across the pn junction. However, their effect is still not sufficient to induce an inversion layer at the GaAs:Si contact layer due to its high n-type doping concentration.

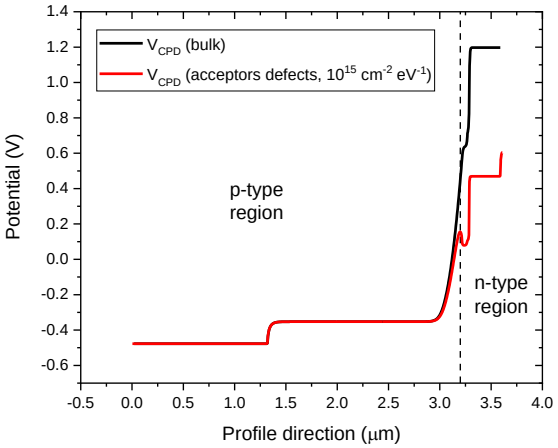


**Figure 22:** Simulated potential profiles along the analyzed structure for two different conditions, with no surface defects, denoted as "bulk" and reported in black; and with acceptor-like surface defects ($N_{SS}=10^{15}$ $cm^{-2}$ $eV^{-1}$) shown in red.

Therefore, in light of the simulations reported in Figure 22, we suggest that during cross-sectional KPFM analysis, a region without the GaAs:Si layer was probed due to the etching process required to obtain the finalized solar cell. Nonetheless, this was expected due to the cleaving direction used for KPFM analysis (see Figure 16, right). As a consequence, the real edge of the cross-section is located at 5.58 µm at the $V_{CPD}$ local maximum which is associated to the very last AlInP:Si layer.

However, it is noteworthy that this distinctive V-shaped potential pattern observed when the AFM tip crosses the edge of the sample has been encountered in other analyzed samples during cross-sectional analysis. This issue will be revisited in section 4.3.2, where a proposed solution will be presented to mitigate it.

Moreover, as mentioned in the introduction of paragraph 4.2, KPFM was also performed under illumination by illuminating the whole front surface with a 636 nm laser at a power density of 3 mW $cm^{-2}$. In Figure 23, the *I-V* curve of the cleaved solar cell under such illumination is reported, revealing a $V_{OC}$ of 0.93 V.

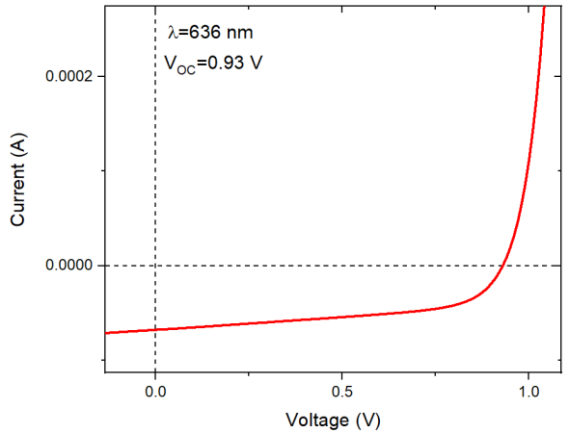


**Figure 23:** I-V curves under 636 nm laser illumination of the cleaved solar cell for KPFM measurements.

The $V_{CPD}$ profiles acquired in dark conditions and under illumination with the sample in short circuit (SC) and open circuit (OC) are reported in Figure 24a and 24b, respectively. Note that a shaded rectangle will be added to all the following $V_{CPD}$ profiles to cover the region that has been determined to be located already "outside" the cross-section area. The $V_{CPD}$ dark profiles under SC and OC conditions are very comparable, with only slight differences that are within the ± 20 mV error associated with ambient conditions KPFM measurements.

Interestingly, the $V_{CPD}$ profiles under illumination present substantial differences. Specifically, when a pn junction (i.e., a solar cell) is exposed to light, it undergoes significant changes in carrier dynamics. The absorption of photons generates electron-hole pairs, increasing the concentration of minority carriers. Consequently, the quasi-Fermi levels for these minority carriers shift towards their corresponding band.

In open-circuit (OC) condition, there is no external circuit to enable carrier flow, resulting in carriers segregating and accumulating near the junction. The quasi-Fermi levels for electrons and holes become highly separated, producing the open circuit voltage and a flattening of the energy bands (and in turn of the potential) within the illuminated region [5].

A qualitative schematic of the energy bands and splitting of the quasi-Fermi level of a generic pn junction under illumination in short circuit a) and open circuit b) conditions is shown in Figure 25 to highlight the difference in the quasi-Fermi level splitting in these two different configurations.

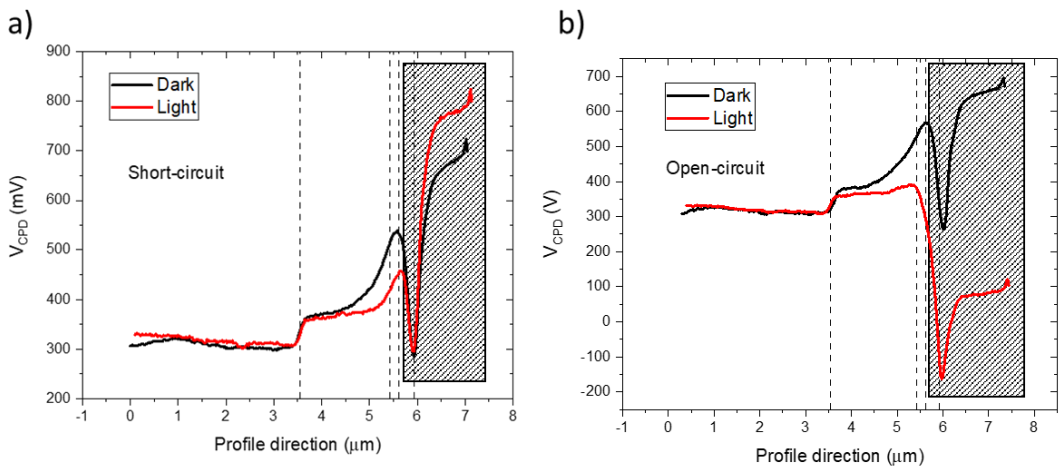


**Figure 24:** $V_{CPD}$ profiles acquired in dark and under 636 nm laser illumination in short circuit a) and open circuit b) conditions, respectively. Note that the same reference lines as in Figure 21c were added. The shaded rectangles illustrate the part of the profile suspected to correspond to a region where the tip has already passed the physical limit of the cross section of the sample.

The $V_{CPD}$ profiles obtained under illumination align with the theoretical pn junction illustrated in Figure 25. Specifically, considering Figure 24a, in SC condition, the $V_{CPD}$ profile in the absorber layer appears flatter compared to the corresponding "dark" SC $V_{CPD}$ profile. Nevertheless, it is still discernible the potential increase associated with the space charge at ≈5.15 µm. In contrast, in OC condition (Figure 24b), the "under illumination" $V_{CPD}$ profile in the absorber becomes almost entirely flat until the end of the absorber layer (5.41 µm) due to the splitting of the quasi-Fermi levels and additionally, it slightly decreases in the Gr AlGaAs layer/n-type region.
Interestingly, $V_{OC}$ measured on the Keithley 2400 instrument was found to be equal to 0.93 V (Figure 23). Upon calculating *SPV* from Figure 24b, using $V_{CPD/dark}$ (565 mV) and $V_{CPD/light}$ (291 mV) values at 5.58 µm (i.e., AlInP:Si layer end), a *SPV* value of only |274| mV is obtained. Note that in paragraph 5.1, we will illustrate that the *SPV* can be related to $V_{OC}$ of a solar cell. However, *SPV* signal is not only determined by $V_{OC,}$ but it also depends on the contribution caused by the light-induced change in surface band-bending. In the case of an n-type semiconductor, an upward band-bending is expected at the surface, therefore under illumination, a positive *SPV* contribution is expected from the surface band-bending which counteracts the open-circuit voltage. Additionally, it is worth to mention that charge carriers generation is only related to the physical properties of a semiconductor material or device and thus, surface defects have no impact on it. Nonetheless, surface defects have an active role on enhancing recombination phenomena. Since the semiconductor must equilibrate the generation and recombination of charge carriers, less photogenerated free carriers will be present in a semiconductor with surface defects with respect to another one without surface defects (bulk). This is especially true in the case of a bipolar device (e.g., pn junction) since the concentration of majority carriers is only altered under high-injection conditions.

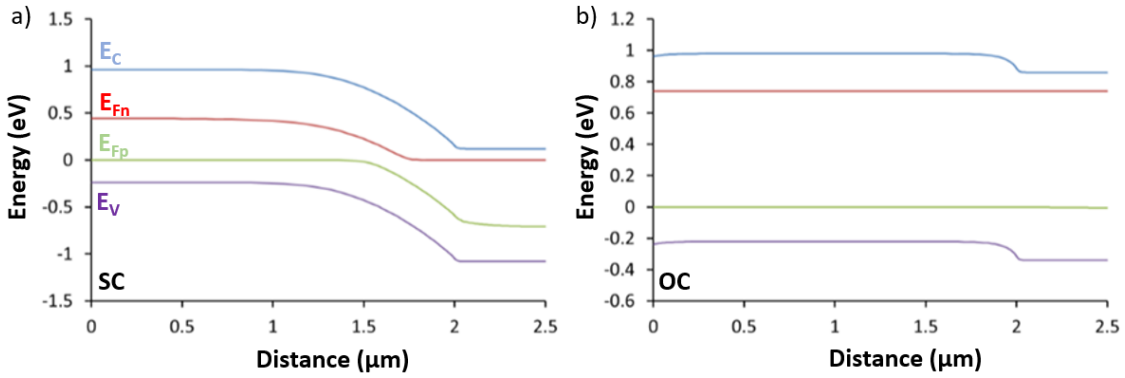


**Figure 25:** Band diagram of an illuminated pn junction under short circuit (SC) a) and open circuit (OC) b) conditions, respectively.

Finally, in order to complete section 4.2, the obtained $V_{CPD}$ profiles under dark conditions with different applied bias are discussed. Figure 26 presents the $V_{CPD}$ profiles obtained under forward applied bias (0.25 V, 0.5 V and 1 V) and under reverse bias (-0.25 V, -0.5 V and -1 V). The $V_{CPD}$ profile obtained in SC condition and previously shown in Figure 21 is also reported for comparison. Note that the $V_{CPD}$ profiles obtained under different applied bias were shifted in order to match the SC $V_{CPD}$ profile with respect to the first $V_{CPD}$ increase present at the Gr AlGaAs transition layer/AlGaAs:Be absorber interface (3.53 µm).

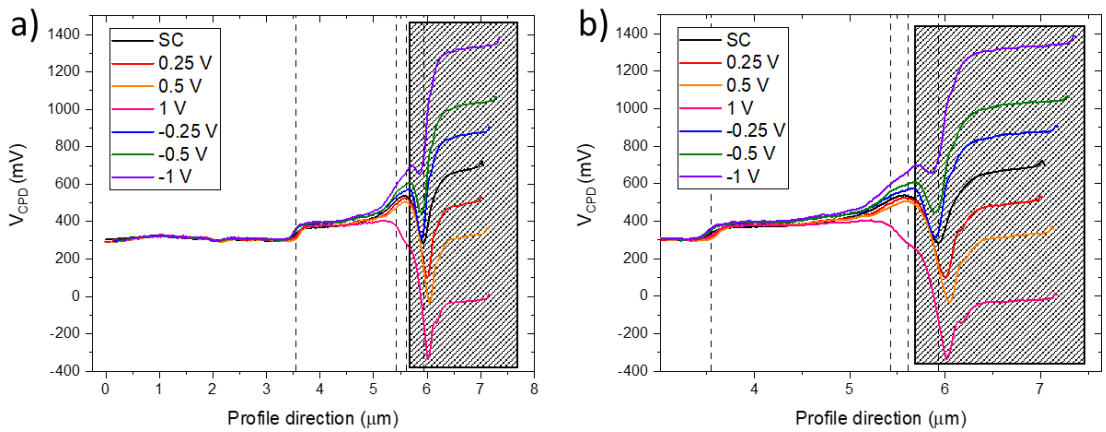


**Figure 26:** a) $V_{CPD}$ profiles obtained under forward and bias and reverse bias; the range of applied biases spanned from -1 V to +1 V. b) Zoom of a) between 3 µm and 7 µm. Note that the same reference lines as in Figure 21c were added.

Generally, the theory predicts that under forward bias, the pn junction's built-in potential decreases, allowing easy electron and hole movement and facilitating current flow. In reverse bias, the built-in potential increases, widening the depletion zone, restricting current flow, and preventing conduction except at breakdown voltages (e.g., rectifying behavior) [5].

This pattern is also evident in Figure 26, where the application of a forward bias results in a reduction of space charge compared to the SC case. Nevertheless, according to fundamental semiconductor physics, the built-in potential should decrease by an equal amount as the forward bias applied. Remarkably, experimental observations reveal that only when a +1 V bias is applied, a noticeable difference is observed, yet the exact voltage value is not retrieved from the $V_{CPD}$ profile. Similarly, under negative applied biases, it is

observed that the space charge increases, but once more, not by the exact amount of the reverse applied bias.

This discrepancy in the quantitative values has previously been encountered in studies on device cross-sections [16-18] and has become a major obstacle in analyzing device performance using the cross-sectional KPFM potentiometry. Specifically, in Chen et al., [19], it is described that this asymmetry between the applied voltage and $V_{CPD}$ profiles originate from systematic artefacts in KPFM including the finite-size tip convolution effect and the cantilever beam crosstalk. Nonetheless, we believe that surface states can also contribute to this experimental evidence. Therefore, in order to provide further discussion, I have employed a modeling approach using a simpler structure consisting of a pn junction comprised of a p-type and a n-type Si layers with a doping concentration of $10^{17}$ $cm^{-3}$; a schematic of the modeled structure is reported in Figure 27a. Figure 27b depicts the potential distribution along this structure under two conditions: 0 V and 0.5 V forward bias (with the p-type layer grounded). By calculating the potential difference between the values obtained in the n-type layer, the applied bias of 0.5 V is indeed found. Conversely, Figure 27c presents the same model, but this time, a constant surface defect distribution was introduced at the surface corresponding to a total surface defect concentration of $10^{11}$ $cm^{-2}$ $eV^{-1}$ ($5x10^{10}$ $cm^{-2}$ $cm^{-2}$ $eV^{-1}$ of acceptors and $5x10^{10}$ $cm^{-2}$ $cm^{-2}$ $eV^{-1}$ of donors, see paragraph 2.5). As experimentally obtained in Figure 26, in this scenario, the 0.5 V applied voltage is no longer found and the potential difference is only around 0.16 V.

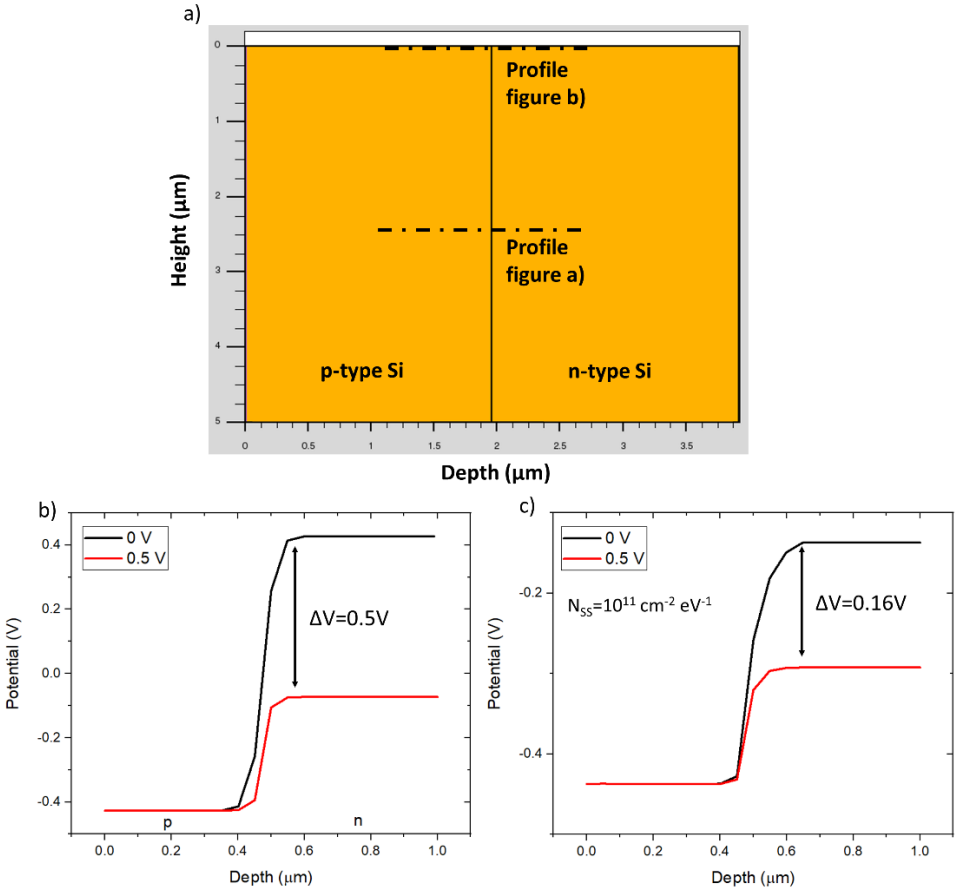


**Figure 27:** a) schematic of the simulated Si pn junction, metal contacts are present at the two sides of the structure. Potential variation across a Si pn junction at 0 and 0.5 applied bias: a) bulk b) with surface defects. The potential profiles shown in a) represents a profile obtained far from the 1 nm defective layer introduces at the surface whereas b) represents a profile obtained at the surface of the sample.

Surface defects can alter the dynamics of the junction in various ways. One key effect is the trapping of charges, creating local imbalances in charge distribution near the surface. As a result, when an external bias is applied, part of the voltage can be absorbed by these trapped charges instead of contributing to the built-in potential. Moreover, surface defects can introduce leakage currents, providing unintended paths for charge carriers to flow. These currents can divert some of the applied voltage away from the junction, effectively reducing the voltage that is available to influence the built-in potential. Additionally, these defects can modify the fundamental properties of the pn junction, including the built-in potential of the depletion region [20].

Finally, as a last point of reflection it is important to highlight that the $V_{CPD}$ profiles acquired in open-circuit conditions under illumination and under +1 V forward bias result to be comparable. These two $V_{CPD}$ profiles are compared in Figure 28, together with the $V_{CPD}$ profile obtained at 0.5 V.

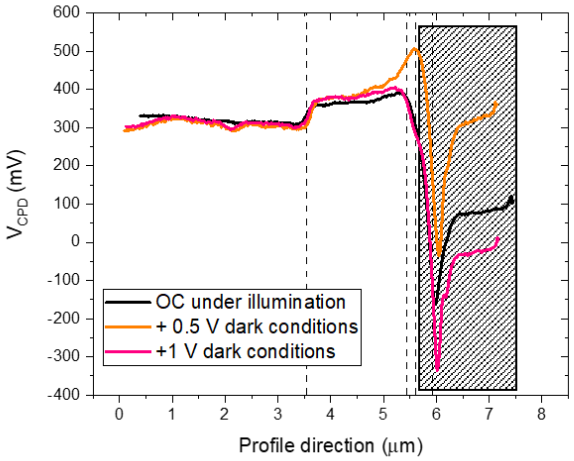


**Figure 28:** Comparison of the $V_{CPD}$ profiles obtained in open-circuit conditions under illumination and under +1 V forward bias. The $V_{CPD}$ profile obtained at 0.5 V is also reported for comparison.

In Figure 23, we have shown that under the selected laser illumination the measured macro-$V_{OC}$ of the solar cell was equal to 0.93 V. It is not a simple coincidence that a bias voltage similar to $V_{OC}$ is required to overlay the $V_{CPD}$ profiles in the dark to that under illumination. Indeed, when a forward bias is applied, the electron and hole concentrations deviate from their equilibrium values, and a splitting of quasi-Fermi levels occurs [5]. Therefore, the application of an external bias which is comparable to $V_{OC}$ of the solar cell is able to induce a quasi-Fermi levels splitting that is in turn comparable to the one caused by the illumination. Consequently, cross-sectional KPFM analysis can yield quantitative information in spite of the presence of severe tip/cantilever convolution effect [19] and the presence of surface defects. The application of an external bias between the metallic contacts of the device plays an important role in this process and can be further exploited for the quantitative measurements of other energy-level offsets in device depth profiles.

In order to provide further discussion, new modeling was performed. Specifically, we have simulated the same structure as reported in Figure 2 under 1-Sun illumination which is reported in Figure 29a. From this simulation we have calculated the open-circuit voltage produced in the structure which was equal to 1.2 V. Then, we have replicated the simulation under applied forward bias of 1.2 V (Figure 29b) in order to match the produced $V_{OC}$ under illumination. Note that, in light of the discussion reported in this section,

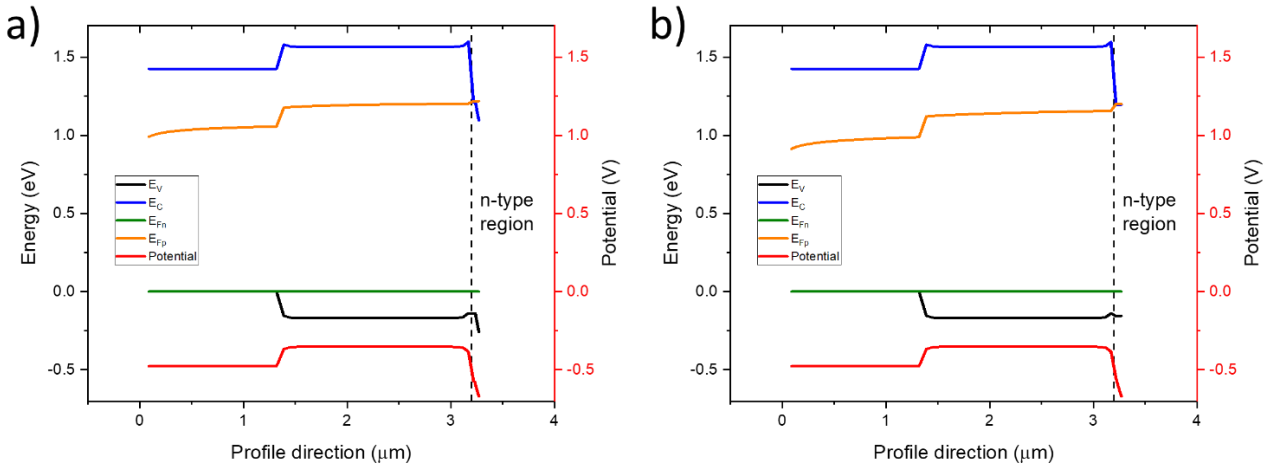


**Figure 29:** Energy bands and potential simulation of the analyzed solar cell reported in Table 1, under 1-sun illumination a) and under a forward applied bias of 1.2 V b). Note that, in light of the discussion reported in this section, the n-GaAs:Si layer was not included in the simulation.

the n-GaAs:Si layer was not included in the simulation, therefore in the script one electrode is placed in contact with the GaAs:Zn substrate and the other one directly in contact with the 20 nm AlInP:Si layer. As expected, the application of an external bias equal to the open-circuit voltage is able to produce a quasi-Fermi level splitting that is comparable to the one induced as a consequence of the illumination.

In conclusion, section 4.1 and 4.2 have demonstrated the capabilities and challenges associated with KPFM and c-AFM techniques in characterizing a III-V-based solar cell. These methods prove to be valuable tools for conducting thorough investigations under real operating conditions of the device. However, the acquisition of quantitative results is a challenging task due to the number of different parameters to be considered during both c-AFM and KPFM cross-sectional analysis. Additionally, as already described in Chapter 3, it is worth emphasizing again the central role that surface defects have in the determination of the surface properties of a sample. Surface defects can change the physical and electrical properties of a surface compared to the "bulk" which in turn affect and determine the experimental results. Nonetheless, we have tested several experimental conditions analyzing the cross-section under external applied bias and under illumination supporting the experimental data with modeling. Interestingly, we were able to point out that the application of an external bias equal to the open-circuit voltage is able to produce a quasi-Fermi level splitting that is comparable to the one induced as a consequence of the illumination- This opens up to quantitative measurements of other energy-level offsets in device depth profiles

## 4.3 Understanding of the V-shaped potential the cross-section edge

In Section 4.2.2, a V-shaped potential was identified when the AFM tip approached the edge of the sample and extended beyond it. Modelling was used to prove that this peculiar V-shaped was incompatible with the highly doped n-GaAs:Si layer (see Figure 22). Therefore, we believe that this peculiar signal could arise from interactions between the body of the tip and/or the cantilever and the sample surface.
It is noteworthy that this distinctive V-shaped potential pattern observed when the AFM tip reaches the edge of the cross-section has been encountered in other analyzed samples during cross-sectional analysis.

Since this V-shaped potential adds additional burden to data interpretation due to the consequent difficulties that arise in the identification of the real edge of the cross-section, in this new section of Chapter 4, we will delve further into this experimental phenomenon and present potential solutions aimed at facilitating data interpretation. In order to perform this analysis, the KPFM results acquired on the cross-section of a n-cSi/i-aSi:H/p-µcSiO$_x$ heterojunction will be used.

### 4.3.1 n-cSi/i-a-Si:H/p-µcSiO$_x$ sample and KPFM experimental configuration

The sample under investigation was provided by Pere Roca i Cabarrocas and his research team as part of a collaborative investigation within the IPVF framework. The analyzed structure is illustrated in Figure 30.

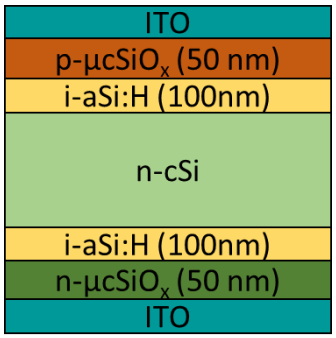


**Figure 30:** Sketch of the analyzed n-cSi/i-a-Si:H/p-µcSiO$_x$ heterojunction.

The sample consists of a Si heterojunction formed by a n-type crystalline silicon absorber ($N_D$=$10^{15}$ cm$^{-3}$), an intrinsic amorphous silicon (i-a-Si:H) passivation layer and a p-type micro-crystalline silicon oxide (p-µcSiO$_x$) emitter ($N_A$=5x$10^{16}$ cm$^{-3}$). On top of the p-µcSiO$_x$ an ITO layer was deposited to ease charge carriers extraction.

Additionally, a 1 nm thick a-SiO$_x$ tunnel junction is incorporated at the n-cSi/i-a-Si:H interface to facilitate the growth of a suitable amorphous layer, as the crystalline orientation of n-cSi may impede the growth of the amorphous layer.

It is important to mention that the thickness of the i-a-Si:H (100 nm) and p-µcSiO$_x$ (50 nm) layers were intentionally increased with respect to that of a typical Si HIT solar cell [21] in order to enhance their visibility and enable better analysis during cross-sectional KPFM analysis and subsequent data analysis.

Prior to the cleaving process, the solar cell was characterized using dark *I-V* measurements to ensure the proper functioning of the device. The I-V curve is shown in Figure 31.

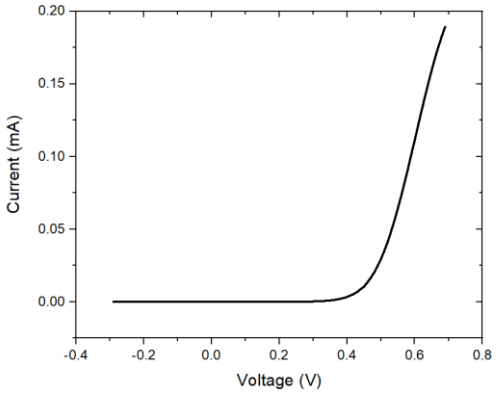


**Figure 31:** I-V characteristics in the dark of the n-cSi/p-µcSiOx heterojunction sketched in Fig. 30, before cleaving.

It is worth to mention that under illumination the performance of the device was limited by a low shunt resistance. Subsequent to the cleaving process, new I-V curves were acquired to assess any potential damages to the solar cell and similar *I-V* characteristic were once again observed. KPFM analysis was conducted immediately following the cleaving process, mitagating the need for additional surface cleaning treatments. The schematic description of the sample during the analysis is presented in Figure 32.

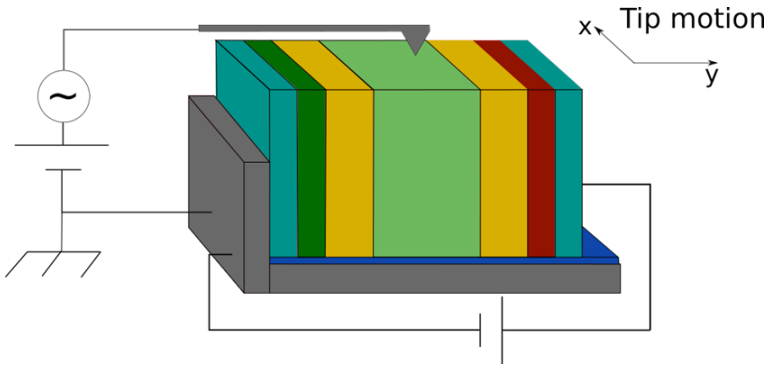


**Figure 32:** Schematic of the KPFM and sample setup for cross-sectional analysis. Note that the same pattern of colors is replicated following Figure 30.

In this setup, the back contact of the sample is connected to the KPFM mass and to the negative terminal of the sourcemeter (Keithley 2400), while the front contact is connected to the positive terminal. This specific configuration enables measurements to be conducted in SC, OC, and under applied bias conditions. The experimental procedure described in paragraph 2.3.3 was replicated in the FM-KPFM mode and a tip (Pt/Ir coated Si) lift of 25 nm was chosen.

### 4.3.2 Si HIT cross-sectional KPFM analysis: results and discussion

The KPFM results obtained in the dark with the sample in short-circuit conditions are reported in Figure 33. Specifically, Figure 33a shows the topography, Figure 33b shows the $V_{CPD}$ image and finally Figure 33c shows the corresponding profiles. Each point of the $V_{CPD}$ profile represents an average of 207 points over a width of 0.7 µm along the x axis. Note that the origin (0;0) is identified as a point in the n-cSi absorber and moving along the positive direction of the Y axis, one will reach the end of the sample. According to the nominal doping concentrations of the absorber and emitter reported in the previous paragraph, the expected space charge width is of the order of 1 µm [5], and due to the higher doping concentration (and also higher expected defect concentration) of the p-µcSiO$_x$ emitter, it is expected to be mostly located in the c-Si absorber.

For these reasons, the beginning of the space charge region is identified at around 0.75 µm where the $V_{CPD}$ variation becomes steeper with respect to n-cSi absorber $V_{CPD}$ values. In the short-circuit $V_{CPD}$ profile a decrease in surface potential is observed as the tip is moving in the space charge region towards the interface. This is in accordance with the expected behavior since the tip is evaluating the $V_{CPD}$ variation transitioning from an n-type region to a p-type region.

Nonetheless, approaching the cross-section edge a V-shaped potential is again present complicating the identification of the different layers and in turn of the real end of the sample. It is important to mention that, conversely to the $V_{CPD}$ profile shown in Figure 21c for the AlGaAs solar cell, the V-shaped potential appears in a region that already corresponds to a height decrease in the topography profile.

Moreover, the height profiles shows some inhomogeneities between 1.47 µm and 1.62 µm that may be related to consequences due to a non-optimal cleaving process and/or dust accumulation that can cause local $V_{CPD}$ variations as described in paragraph 3.1.2.2.

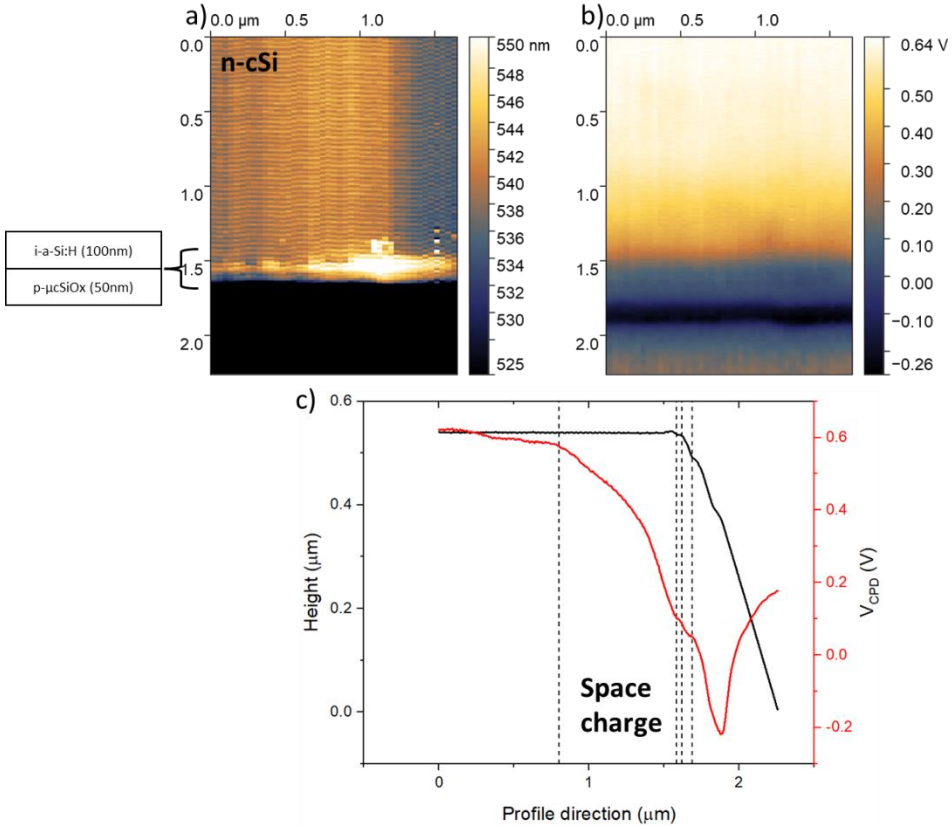


**Figure 33:** Topography a) and $V_{CPD}$ map b) acquired on the cross-section of the n-cSi/i-a-Si/p-µcSiO$_x$ cross-section in SC and dark conditions; c) corresponding topography and $V_{CPD}$ profiles. Four reference lines were added to highlight the beginning of the space charge region (0.75 µm) and three possible "ends of the cross-section".

At this stage, with the use of the only topography profile, it is possible to hypothesize that the edge of the sample is located between 1.58 µm and 1.68 µm to which correspond $\Delta V_{CPD}$ values in the range between 0.47 V and 0.52 V for the built-in potential at the surface considering as starting point of the space charge the $V_{CPD}$ value measured at 0.75 µm.

All these calculated values are reasonable since, as widely described in paragraph 3.2.4.1, the presence of surface defects are responsible of mitigating the expected potential variation across the pn junction (typical $V_{Built\text{-}in}$ is expected to be here larger than 0.7 V [22]). Additionally, the precise surface defects distribution is not known a priori since it depends on many factors as, for instance, the cleaving process and physical properties of the different layers, and thus it requires a complex modelling work to correctly estimate it (see 3.2.4.1). For this reason, the identification of the real edge of the sample becomes even more valuable in order to estimate the true $\Delta V_{CPD}$ related to the space charge which in turn can be used to estimate qualitatively (or quantitatively) the surface defects distribution.

It is worth to investigate the fundamental physical explanation for the occurrence of the V-shaped potential as the AFM tip approaches the edge of the sample.

As explained in paragraph 1.4.4, the capacitance between the tip-apex and the investigated surface is the only significant factor for $V_{CPD}$ evaluation, nonetheless, additional interactions between the other components of the probe and the sample can lead to inconsistencies in KPFM measurements due to the long-range of the electrostatic force, as shown in Figure 34.

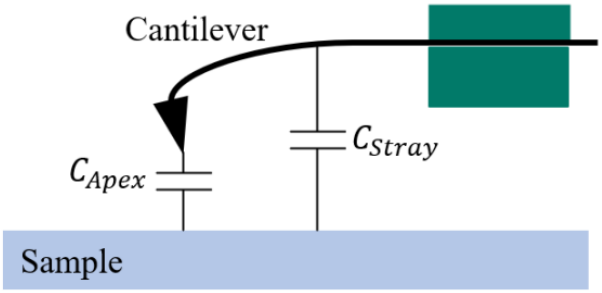


**Figure 34:** Schematic illustration of stray capacitance. Between the tip-apex and the sample are local capacitance contributions that are deliberately measured, while the tip cone and the macroscopic cantilever contribute to interfering stray capacitance.

In cross-sectional non-contact AFM, when the tip is scanning the edge of the sample, several interesting phenomena come into play. For instance, it is a good practice to include in the area of the scan a part that extends beyond the physical cross-section of the sample in order to be sure to have really reached the edge (e.g., steep decrease in the topography profile). During the tip scanning, even if the tip motion extends beyond the edge of the sample, the tip can still interact with the sample and surrounding environment, giving rise to unique challenges and $V_{CPD}$ signals that may affect the accuracy of measurements (e.g., V-shaped potential).

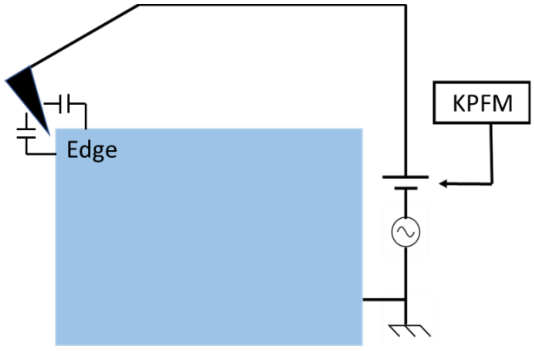


**Figure 35:** Schematic of the additional parasitic capacitance that can arise from the interaction between the body of the tip and the cross-section of the investigated sample.

As shown in the schematic in Figure 35, one key consideration is the interaction between the body of the tip and the edge of the sample, and not just the tip apex. The geometry of the tip body can influence the signal obtained during the scan. For instance, as the tip apex is approaching the edge of the sample, the body of the tip may interact with the layers previously measured by the tip apex and at the same time it can interact with the upmost layer (front surface) of the sample when crossed the edge. These parasitic interactions can introduce additional signals and affect the acquired data complicating the precise determination of the real end of the cross-section.

This is the so-called tip-averaging effect already widely described in paragraph 3.1.2.2. Nonetheless, in cross-sectional analysis configuration, not only the tip-averaging effect is responsible to negatively affect the lateral resolution of the KPFM technique, but it may lead to unexpected experimental $V_{CPD}$ profiles evolution resulting from the interaction of the tip with different layers with different physical properties and even the front surface.
Additionally, even the cantilever itself can also contribute to parasitic interactions when the tip has already crossed the edge of the sample, for the same principle of KPFM measurements in planar configuration.
Another important consideration lies in the condition of the edge of the sample. After the cleaving process, it is not evident to obtain an ideal abrupt cross-section, but it is more likely to obtain an inhomogeneous cross-section that presents local topography variation that can affect the local $V_{CPD}$ values.
From what we described so far; it is suggested that the V-shaped potential is a direct consequence of unwanted tip apex/tip body/cantilever interactions with the edge/front surface of the investigated sample. For this reason, the same characterization was performed by changing the experimental conditions. Specifically, the sample was rotated 180° relatively to the configuration used to acquire the data shown in Figure 33. A schematic of this new configuration is reported in Figure 36 where it is also compared to the previous one.

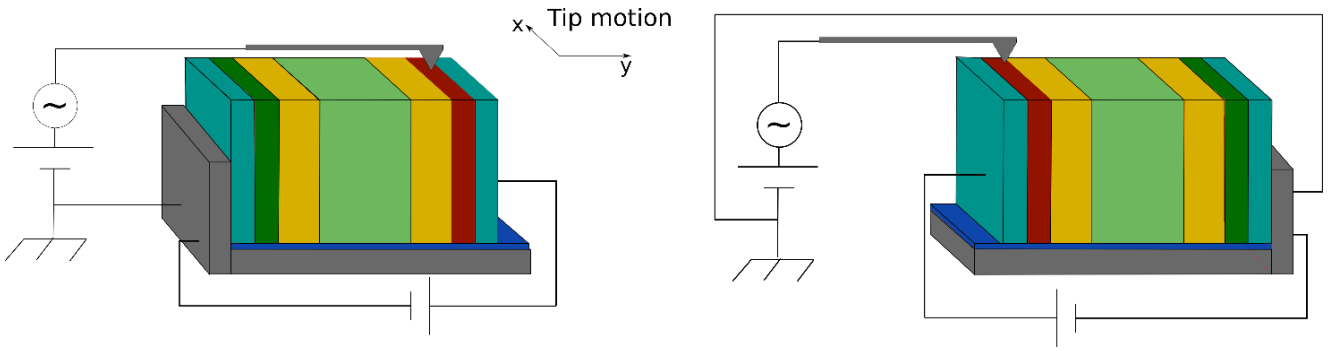


**Figure 36:** Schematic of the cross-sectional KPFM experimental conditions used for the acquisition of the data reported in Figure 33 a) and in Figure 37 b), respectively. Note that the same pattern of colors is replicated following Figure 30.

In this configuration the whole cantilever is located outside the sample thus reducing parasitic interaction. An example of $V_{CPD}$ profile acquired in this configuration is reported in Figure 37. In this experimental setup, the V-shaped potential is entirely eliminated, and it becomes evident that the precise positioning of the real end of the sample is more straightforward. As the topography signal decreases, the $V_{CPD}$ signal becomes here flatter, indicating that the tip/sample interaction is becoming weaker.
As a matter of fact, this configuration reduces parasitic interactions which arise from the cantilever, but it may also have a beneficial impact mitigating additional parasitic signals.
In this case, considering a space charge region that extends from around 1.4 µm to 2.43 µm, a $\Delta V_{CPD}$ of 0.55 V is estimated. This value is comparable with the $\Delta V_{CPD}$ located at 0.75 µm and 1.68 µm in the $V_{CPD}$ profile in Figure 33c making this as the most suitable value for $V_{built\text{-}in}$ at the surface of that particular region.
Despite the apparent simplicity of this proposed solution, a compromise is necessary due to the illumination configuration of the TRIOS system, as depicted in Figure 2 in Chapter 2.

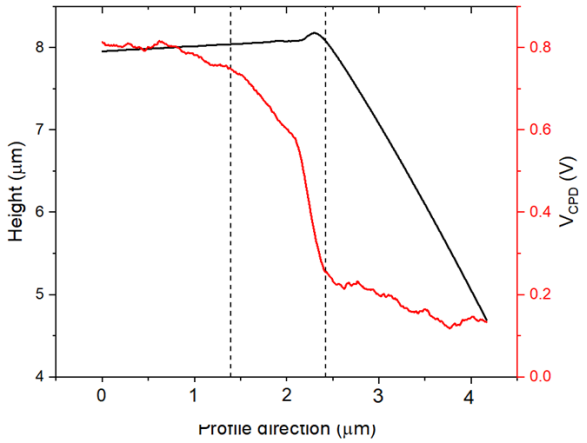


**Figure 37:** Topography and $V_{CPD}$ acquired in a sample configuration that allowed to minimize cantilever and tip body parasitic interactions with the sample surface and edge.

The purpose of this last study was to better understand the measurement of $V_{CPD}$ on the cross-section and notably when a V-shaped potential is highlighted. An important point to keep in mind is that by identifying the physical boundaries of the sample it is possible to exploit surface potential measurements even when the potential profile shows a V-shape. The following Figure shows examples of potential profiles obtained on this sample under different conditions. Specifically, Figure 38 shows the profile when the sample is short-circuited (SC) and open-circuited (OC) under dark conditions. It also shows the OC potential profile under illumination with a measured $V_{OC}$ of 0.47 V. For comparison, we illustrate the profile when a voltage of +0.5 V is applied to the device. The potential values indicated are taken at the physical edge of the sample defined by the dashed line.

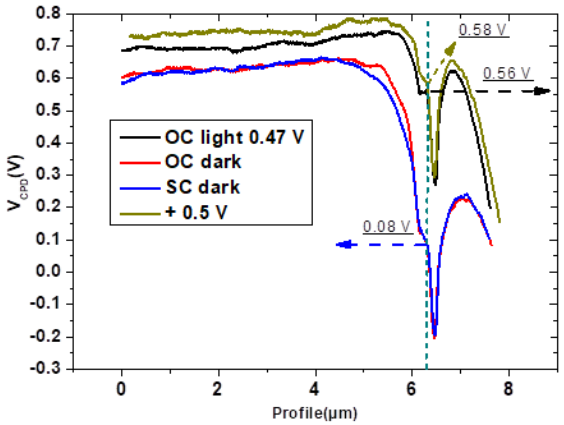


**Figure 38:** $V_{CPD}$ profiles obtained with the sample in the experimental configuration reported in Figure 36 left. The $V_{CPD}$ profiles acquired in dark conditions with the sample in SC and OC are reported together with the one acquired under applied forward bias of 0.5 V. Finally, the "under illumination" profile with the sample in OC conditions is also reported. Note that the x-axis is now wider since it shows a higher portion of the $V_{CPD}$ signal in the n-cSi absorber. Nonetheless, the dashed-line represents the estimated end of the cross-section and corresponds to the 1.68 µm point of Figure 33c.

As shown in Figure 24 for the AlGaAs solar cell, the $V_{CPD}$ profiles acquired in SC and OC in dark conditions result to be comparable. Additionally, as shown in Figure 28, the $V_{CPD}$ profile acquired under illumination

with the sample in OC condition results to be comparable to the one obtained under applied forward bias of 0.5 V, i.e., an applied bias similar to the expected $V_{OC}$.
Furthermore, we have already mentioned several times along the manuscript that *SPV* can be related to macro-$V_{OC}$ of a solar cell (see paragraph 5.1). Interestingly, with reference to the profiles "OC dark" and "OC light" reported in Figure 38, a *SPV* value equal to 0.49 V is calculated considering the corresponding $V_{CPD}$ values at the estimated "end" of the cross-section (dashed line in Figure 38). As previously mentioned, the macro-$V_{OC}$ of the analyzed solar cell was measured to be equal to 0.47 V thanks to the sourcemeter directly connected to the TRIOS platform which agrees with calculated local *SPV*. This experimental evidence, together with a quite consistent $\Delta V_{CPD}$ associated with the space charge region (0.52 – 0.55 V), suggests that the cross-section of the analyzed Si solar cell results to be less affected by surface defects than the AlGaAs solar cell. As a matter of fact, in the case of the III-V based device, the calculated experimental *SPV* demonstrated to be much smaller than $V_{OC}$ displayed on the sourcementer and additionally $\Delta V_{CPD}$ associated to the space charge was attenuated with respect to the corresponding "bulk" case.

In conclusion, an alternative approach that can be considered consists of initially conducting cross-sectional analysis in dark conditions using this second new configuration, which minimizes parasitic interactions and eliminates the issue of the V-shaped potential. Once the precise edge of the sample is well-identified, the sample can then be positioned in the first configuration for conducting measurements under front illumination.
Since the localization of the physical limits of the sample is an issue when analyzing KPFM measurements performed on the cross-section, we develop in the following section that one can also take benefit of the Phase and Magnitude signals in addition to the topography and $V_{CPD}$ signals to ease the localization of the edge of the cross-section.

### 4.3.3 Additional signals during KPFM analysis

In order to facilitate the identification of the real cross-section edge, during KPFM analysis it is possible to activate the acquisition of additional signals beyond the $V_{CPD}$. Specifically, the Mag (magnitude), Phase, and Dmag (differential magnitude) signals can be used together with the topography signal for this purpose [23].
In this final paragraph of section 4.3, the Mag (Figure 39), Phase (Figure 40), and Dmag (Figure 41) signals will be described using the experimental data obtained through the configuration used for the acquisition of the $V_{CPD}$ shown in Figure 33.
The Mag signal in KPFM is a crucial measurement that represents the magnitude or amplitude of the oscillation of the tip when subjected to an alternating voltage ($V_{AC}$). It serves as a sensitive indicator of the electrostatic forces between the sharp conductive tip and the surface of the sample. Essentially, the Mag signal quantifies how strongly the tip is interacting with the local surface potential of the sample at a specific point. This interaction arises from the redistribution of charges and the resultant electrostatic attraction or repulsion between the tip and the sample.
The Phase signal in KPFM is another critical component of the technique. It measures the phase shift between the applied $V_{AC}$ signal and the oscillation of the tip. This phase shift provides information about the temporal relationship between the motion of the tip and the voltage that drives it.

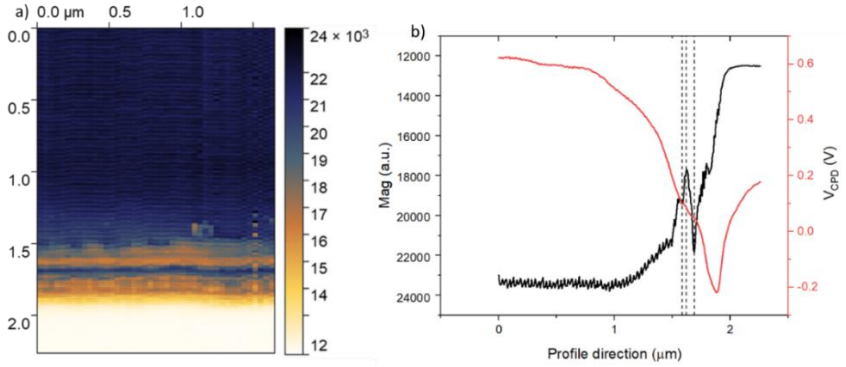


**Figure 39:** Corresponding Mag image of the topography shown in Figure 22 a), Mag and $V_{CPD}$ profiles b).

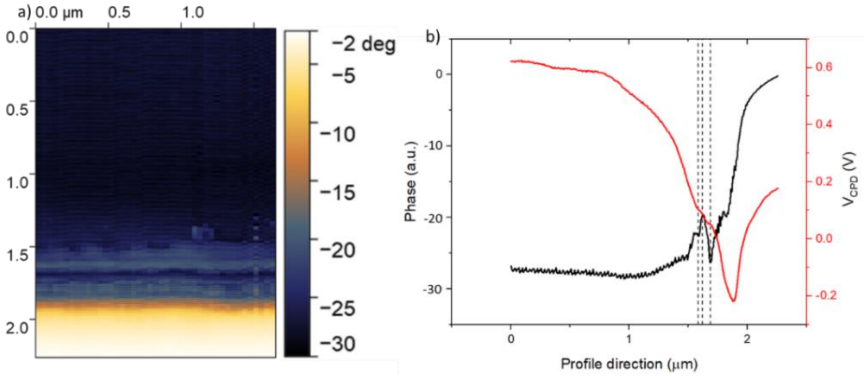


**Figure 40:** Corresponding Phase image of the topography shown in Figure 22 a), Phase and $V_{CPD}$ profiles b).

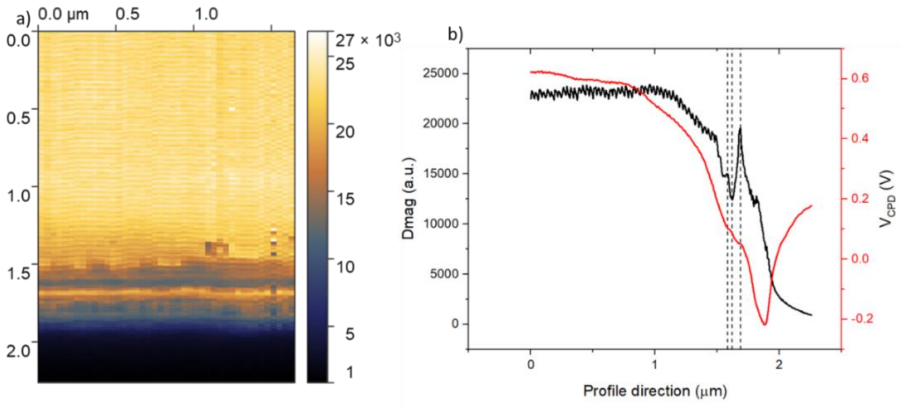


**Figure 41:** Corresponding Mag image of the topography shown in Figure 22 a), Dmag and $V_{CPD}$ profiles b).

Finally, the Dmag signal in KPFM is a differential measurement designed to highlight variations in local surface potential caused by the application of a $V_{DC}$. It quantifies the change in the Mag signal when the $V_{DC}$ is added to the system. Essentially, Dmag represents the difference in the oscillation of the tip amplitude with and without the $V_{DC}$ bias. By comparing these two conditions, the Dmag signal provides a direct indication of how the surface potential changes in response to the applied $V_{DC}$.

The Dmag signal, in other terms, reflects the variations in capacitance caused by changes in the local surface potential. As the surface potential changes, the capacitance changes accordingly, leading to variations in the electrostatic forces and, consequently, the Dmag signal.

In the reported Figures 39, 40 and 41, the point at 1.68 µm, that was previously identified as the edge of the sample, corresponds to local minima for the Mag and Phase signal while it corresponds to a local maximum for the Dmag signal.
In light of the profile depicted in Figure 41b, following its passage beyond the 1.68 µm threshold, the Dmag signal experiences a gradual decline, eventually converging to a nearly negligible value. This observation may be interpreted as a distinct manifestation of the tip's progressive distancing from the sample's edge, leading to an attenuation of the interaction to the extent that the signal tends toward zero.

In summary, the Mag, Phase, and Dmag signals in KPFM are fundamental measurements that collectively provide detailed information about the surface potential, electrostatic forces, and electronic properties of materials at the nanoscale. Gaining proficiency in acquiring and comprehending these signals can enhance the interpretation of experimental data, thereby adding further value to the only $V_{CPD}$ profile and helping in the precise identification of the real edge.

## 4.4 Cross-sectional KPFM for the characterization of a CZTGS solar cell

As part of a collaborative effort with the University of Milano-Bicocca, I have engaged in a side project involving the characterization of a CZTGS solar cell using cross-sectional KPFM offering experimental evidence of the unsatisfactory PV performance of the CZTGS device under illumination [1].

### 4.4.1 High band gap CZTGS solar cell: context

Prior to delving into the KPFM characterization, it is essential to provide contextual background regarding the research conducted at Milano-Bicocca University.
In the regard of sustainable energy sources, thin-film solar cell technologies have gained substantial attention for their potential cost-effectiveness, efficiency, and eco-friendliness. Among these, Copper Zinc Tin Sulfide (CZTS) solar cells have emerged as a standout candidate. An example of the structure of a CZTS-based solar cell is reported in Figure 42.

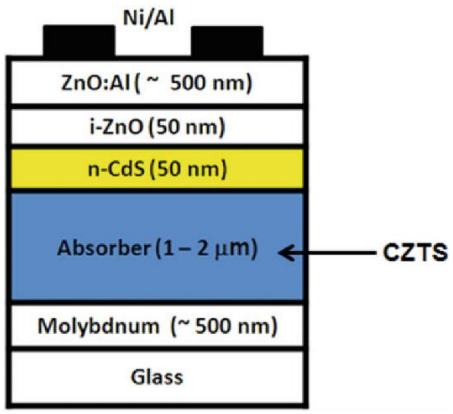


**Figure 42:** Schematic representation of a typical CZTS-bases solar cell.

CZTS, composed of abundant and non-toxic elements, offers the advantage of collecting sunlight efficiently. In contrast to Copper Indium Gallium Selenide (CIGS) solar cells, which incorporate rare and potentially problematic materials, CZTS presents a more environmentally friendly alternative, making it a promising player in the quest for sustainable energy solutions [1].

The research conducted in Milano-Bicocca focused on investigating the impact of substituting tin with varying amounts of germanium (Ge) in CZTS-based solar cells, which were fabricated using a sol-gel process. In the published study by Tseberlidis et al., ([24]), the research highlighted the ability to finely adjust the band gap of the absorber material and modify its chemical and physical properties through this approach.

The fundamental concept driving this research involves the creation of a diverse set of CZTGS samples with varying tin-germanium compositions. This approach aims to finely adjust the band gap of the material in order to fulfill the requirements of future tandem device applications. The motivation behind this pursuit stems from the growing demand to advance PV technology towards tandem solar-cell architectures. The purpose is to surpass the limitations of the Shockley limit for single junction solar cells and enhance the performance of cost-effective solar devices, such as silicon-based ones. Within this framework, there is a pressing need to develop high-bandgap materials that can serve as top cells in tandem architectures [25].

Detailed information regarding the findings can be found in [1]. However, a noteworthy discovery from their research is highlighted here. Among the various samples investigated, the composition containing 70% germanium ($Cu_2ZnSn_{0.3}Ge_{0.7}S_4$) stood out due to its favorable band gap of 1.77 eV. Consequently, this particular composition has been identified as the optimal absorber candidate for the top cell in a four-terminal tandem device architecture, where crystalline silicon (c-Si) serves as the bottom cell. Notably, it has been reported that a band gap ranging from 1.7 to 1.8 eV is desirable for the top cell in this specific tandem architecture [26]. Consequently, a single-junction CZTGS solar cell was fabricated, utilizing the absorber material with the most optimal band gap. The performance of the device was evaluated through J-V measurements conducted under both dark and light conditions (1-sun illumination), along with EQE measurements. The obtained results are presented in Figure 43a for J-V characteristics and in Figure 43b for EQE measurements.

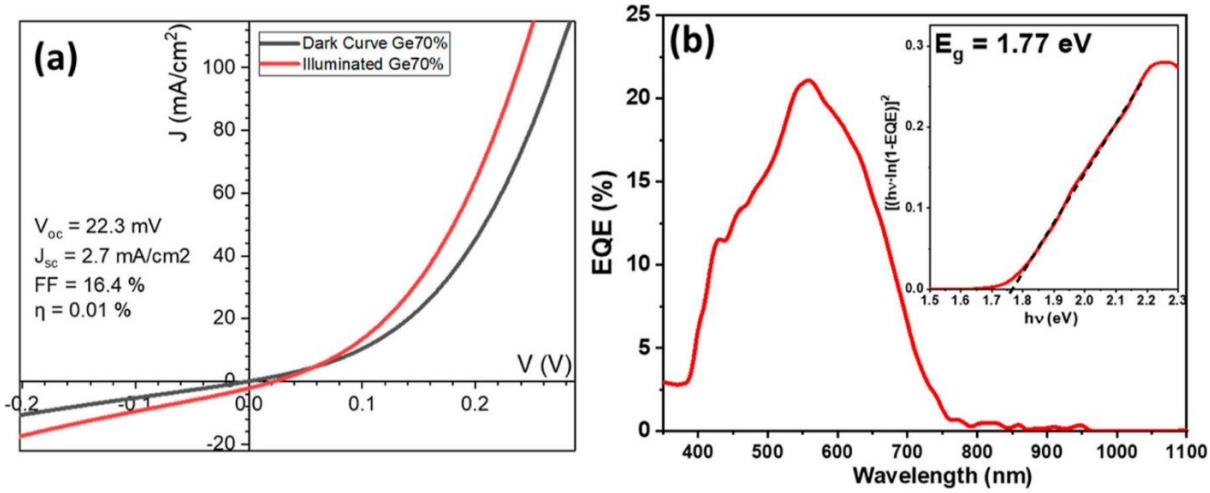


**Figure 43:** (a) JV curve of the $Cu_2ZnSn_{0.3}Ge_{0.7}S_4$ sample in the dark and illuminated mode showing poor charge extraction and (b) EQE curve of the $Cu_2ZnSn_{0.3}Ge_{0.7}S_4$ sample showing good shape.

The dark and illuminated J-V curves of our representative CZTGS solar cell exhibit strong deficiencies in charge generation and/or extraction, as evidenced by the cell parameters: $V_{OC}$ of 22.3 mV, $J_{sc}$ of 2.7 mA/cm2, FF of 16.4%, and η of 0.01%. Further investigation revealed that the resistivity of the sulfurized back contact, determined

through four-wire technique measurements, ranged from 90 to 120 kΩ. This high resistivity is likely attributed to the extensive sulfurization of the molybdenum layer, which occurred during annealing at elevated temperatures.

The EQE curve in the 300−550 nm region shows loss due to the parasitic absorption from the buffer layer (CdS absorption is around 530 nm) and from the window layers (i-ZnO/AZO layers cut the wavelengths shorter than 380 nm). The low response in the 400−600 nm range is attributed to the charge recombination related to trap states located at the interfaces and to the nonideal band alignment of a wide-band-gap absorber with the CdS buffer layer. The integrated $J_{SC}$ is approximately 3 mA/cm2, aligning well with the current density calculated from the measured J-V curve under AM1.5 illumination conditions.

Overall, the EQE measurements (Figure 43b) provide valuable insights into the characteristics of the high-band-gap absorber material. This suggests that the relatively low efficiency is primarily attributed to recombination processes that likely take place at the interfaces. Notably, this issue is linked to the presence of bulky $MoS_2$ in the back contact, as previously described in other studies [24].

### 4.4.2. Cross-sectional KPFM analysis on high band gap CZTGS solar cell

To provide direct evidence of the detrimental impact caused by the presence of a bulky $MoS_2$ layer, the sample was cleaved, and the resulting exposed cross-section was subjected to KPFM analysis.

The KPFM measurements were conducted under ambient conditions using the AIST-NT TRIOS platform previously described in paragraph 2.3.1. The measurements were performed in a two-pass scanning mode, where the second pass involved maintaining a constant distance of 30 nm from the surface of the sample. A lift of 30 nm was chosen in order to minimize likely inadvertent tip/sample interaction due to the granular nature of the CZTGS material. The exposed Mo back contact was connected to the KPFM ground and thus the solar cell was kept in open circuit during the whole analysis. Finally, to evaluate the surface potential, ARROW EFM conductive tips with a Pt/Ir coating operating at a resonance frequency of 75 kHz were employed.

Achieving a smooth topography is crucial for conducting accurate KPFM measurements. However, the initial analysis revealed that the cross-section under examination lacked homogeneity and exhibited significant roughness. This was attributed to suboptimal procedures employed during the cross-sectional preparation as well as the deposition process itself. As a result, to overcome the challenges posed by surface roughness and inhomogeneities, the analysis was carried out using frequency modulation KPFM (FM-KPFM) with a low scanning rate of 0.1 Hz. Specifically, FM-KPFM was chosen to minimize topographical imprint on the $V_{CPD}$ image and the low scanning rate for the same reason of the aforementioned likely tip/sample interaction that can change the WF of the tip and in turn $V_{CPD}$. The resulting topography and the corresponding $V_{CPD}$ image are presented in Figure 44a and 44b, respectively. The topography map depicts the solar cell structure, revealing the layers up to the CZTGS active layer. However, the remaining layers that comprise the device are not clearly discernible due to the limitations of the nonoptimized cross-sectional process. It is worth noting that the utilization of FM-KPFM successfully mitigated any topographical imprint on the $V_{CPD}$ image, as evidenced by the profiles shown in Figure 44c and 44d.

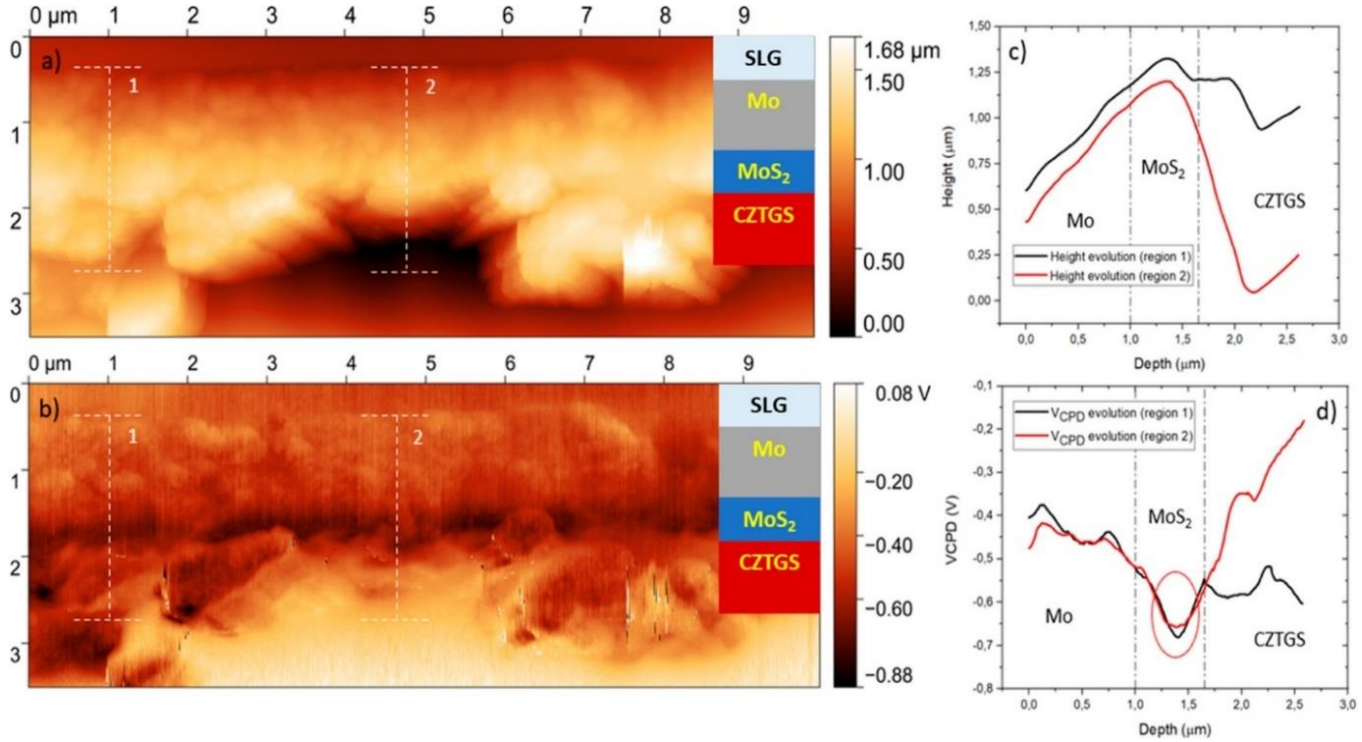


**Figure 44:** FM-KPFM measurement of the surface cross-section of the CZTGS device. The topography (a) and the $V_{CPD}$ image (b). The profiles in (c,d) show an average value of the data along with the topography and $V_{CPD}$ image, respectively. The profiles correspond to the two regions identified by the dotted white segment.

The obtained $V_{CPD}$ image provides valuable insights. In particular, moving from the CZTSG region to the Mo region, a minimum in $V_{CPD}$ is registered at 1.4 um which is highlighted by a red circle in the extracted profile, as depicted in Figure 44d. The observed peak in $V_{CPD}$ corresponds to the interface between the Mo layer and the CZTGS absorber, indicating the extensive formation of $MoS_2$ during the annealing process. The presence of a bulky $MoS_2$ layer was already pointed out in [1] through the acquisition of cross-sectional SEM images.

In kesterite-based solar cells, the Mo acts as a back contact and thus it is the collecting electrode for positive charge carriers. As a matter of fact, the holes move towards higher energy, e.g., lower potential. The increase of potential registered from the $MoS_2$ towards the Mo acts as barrier for the collection of holes and additionally it may also induce electron accumulation at the Mo/$MoS_2$ interface promoting recombination phenomena.

These results provide compelling evidence of the previously hypothesized charge extraction issues discussed in this study. Therefore, despite successfully achieving a pure-phase absorber with desired optical and morphological properties, the presence of an insulating $MoS_2$ layer, resulting from the extensive sulfurization of the back contact, hindering an efficient charge extraction from the device.

In conclusion, our research highlights that Kelvin Probe Force Microscopy serves as a valuable tool for advanced characterization, presenting experimental evidence of the underlying factors responsible for the unsatisfactory I-V characteristics observed in the solar cell under investigation. Specifically, an extensive sulfurization of the back contact caused the formation of a thick $MoS_2$ layer. Cross-sectional KPFM revealed that the “bulky” $MoS_2$ layer acts as a potential barrier for the collection of holes at the back contact (Mo).

## 4.5 Conclusions

In Chapter 4 the local probe characterization was extended to finalized solar cells. Specifically, we have presented the experimental outcomes of cross-sectional KPFM and c-AFM measurements conducted on diverse PV technologies: AlGaAs, CZTGS, and silicon heterojunction solar cells.

In section 4.1, cross-sectional Resiscope analysis was performed on the AlGaAs multilayer structure. In particular, Resiscope measurements allowed the identification of the several layers along the structure. Nonetheless, we have shown that the contact between the AFM tip and the surface of the semiconductor is of Schottky type. The Schottky characteristics of the electrical contact introduces substantial complications to the acquisition of quantitative results and data interpretation. The electrostatic potential barrier in the semiconductor depends on a multitude of different parameters that comprise the physical properties of the material, such as doping concentration but also surface defects distributions which determine the surface band-bending. Additionally, even the experimental conditions play an active role in the form of the applied polarity, applied forces and work function of the AFM tip.

In section 4.2, cross-sectional KPFM and c-AFM analysis was extended to the finalized AlGaAs solar cell; notably the $V_{CPD}$ and resistance profiles were also evaluated under illumination. In the case of Resiscope analysis, we have demonstrated that the AFM tip is sensitive to the photogenerated carriers along the structure, detecting a general decrease of the measured resistance under illumination. On the other hand, cross-sectional KPFM analysis revealed once again the strong impact of surface defects on the physical properties of the surface with respect to the "bulk". As a matter of fact, surface defects were responsible of a great departure of the surface potential variation along the depletion region. Interestingly, we have also shown that the application of a forward bias similar to the expected $V_{OC}$ of the solar cell is able to reproduce the $V_{CPD}$ profile that was acquired under illumination under open-circuit conditions.

In section 4.3, through cross-sectional KPFM analysis performed on a n-cSi/i-a-Si:H/p-µcSiO$_x$ heterojunction, we have explained in more detail the peculiar V-shaped potential artifact that is generally encountered during cross-sectional analysis, which complicates the identification of the "real" edge of the cross-section. The principal reason was related to the presence of parasitic interaction between the body of the AFM tip and the front surface of the sample under investigation. Nonetheless, a solution to remove this problematic was proposed in terms of a different experimental configuration. Moreover, we show that the acquisition of additional signals during analysis, such as Mag, phase and Dmag can also aid in a more precise identification of the real edge of the cross-section.

Finally, in section 4.4 we have demonstrated that KPFM can serve as a valuable tool for advanced characterization, presenting experimental evidence of the underlying factors responsible for the unsatisfactory *I-V* characteristics observed in the CZTGS solar cell under investigation. Specifically, thanks to the cross-sectional KPFM analysis, we could reveal a peculiar potential profile at the back Mo contact and suggest that the extensive sulfurization of this back contact causing the formation of a thick $MoS_2$ layer forms a potential barrier for the collection of holes.

## Bibliography

[1] Tseberlidis, G.; Trifiletti, V.; Vitiello, E.; Husien, A. H.; Frioni, L.; Da Lisca, M.; Alvarez, J.; Acciarri, M.; Binetti, S. O. Band-Gap Tuning Induced by Germanium Introduction in Solution-Processed Kesterite Thin Films. *ACS Omega* **2022**, *7* (27), 23445–23456. https://doi.org/10.1021/acsomega.2c01786.

[2] Ben Slimane, A.; Michaud, A.; Mauguin, O.; Lafosse, X.; Bercegol, A.; Lombez, L.; Harmand, J.-C.; Collin, S. 1.73 EV AlGaAs/InGaP Heterojunction Solar Cell Grown by MBE with 18.7% Efficiency. *Progress in Photovoltaics: Research and Applications* **2020**, *28* (5), 393–402. https://doi.org/10.1002/pip.3249

[3] SILVACO® ATLAS™ User's Manual **2016**.

[4] Zare Pour, M. A.; Romanyuk, O.; Moritz, D. C.; Paszuk, A.; Maheu, C.; Shekarabi, S.; Hanke, K. D.; Ostheimer, D.; Mayer, T.; Hofmann, J. P.; Jaegermann, W.; Hannappel, T. Band Energy Diagrams of N-GaInP/n-AlInP(100) Surfaces and Heterointerfaces Studied by X-Ray Photoelectron Spectroscopy. *Surfaces and Interfaces* **2022**, *34*, 102384. https://doi.org/10.1016/j.surfin.2022.102384.

[5] Sze, S.M. and Ng, K.K. Physics of Semiconductor Devices. 3rd Edition, John Wiley and Sons, Hoboken **2006**. https://doi.org/10.1002/0470068329

[6] da Lisca, M.; Alvarez, J.; Connolly, J. P.; Vaissiere, N.; Mekhazni, K.; Decobert, J.; Kleider, J.-P. Cross-Sectional Kelvin Probe Force Microscopy on III–V Epitaxial Multilayer Stacks: Challenges and Perspectives. *Beilstein J. Nanotechnol.* **2023**, *14* (1), 725–737. https://doi.org/10.3762/bjnano.14.59.

[7] Giannazzo, F.; Schilirò, E.; Greco, G.; Roccaforte, F. Conductive Atomic Force Microscopy of Semiconducting Transition Metal Dichalcogenides and Heterostructures. *Nanomaterials (Basel)* **2020**, *10* (4), 803. https://doi.org/10.3390/nano10040803.

[8] Jiang, L.; Weber, J.; Puglisi, F. M.; Pavan, P.; Larcher, L.; Frammelsberger, W.; Benstetter, G.; Lanza, M. Understanding Current Instabilities in Conductive Atomic Force Microscopy. *Materials (Basel)* **2019**, *12* (3), 459. https://doi.org/10.3390/ma12030459.

[9] Houzé, F.; Meyer, R.; Schneegans, O.; Boyer, L. Imaging the Local Electrical Properties of Metal Surfaces by Atomic Force Microscopy with Conducting Probes. *Applied Physics Letters* **1996**, *69* (13), 1975–1977. https://doi.org/10.1063/1.117179.

[10] Marchat, C., Dai, L., Alvarez, J., Le Gall, S., Kleider, J. P., Misra, S., & Roca I Cabarrocas, P. Local $V_{OC}$ Measurements by Kelvin Probe Force Microscopy Applied on P-I-N Radial Junction Si Nanowires. *Nanoscale research letters* **2019**, *14*(1), 398. https://doi.org/10.1186/s11671-019-3230-5

[11] R. P. Lu, K. L. Kavanagh, St. J. Dixon-Warren, A. Kuhl, A. J. SpringThorpe, E. Griswold, G. Hillier, I. Calder, R. Arés, R. Streater; Calibrated scanning spreading resistance microscopy profiling of carriers in III–V structures. *J. Vac. Sci. Technol. B* **2001**; 19 (4): 1662–1670. https://doi.org/10.1116/1.1387458

[12] P. Eyben, M. Xu, N. Duhayon, T. Clarysse, S. Callewaert, W. Vandervorst; Scanning spreading resistance microscopy and spectroscopy for routine and quantitative two-dimensional carrier profiling. *J. Vac. Sci. Technol. B* 1 January 2002; 20 (1): 471–478. https://doi.org/10.1116/1.1424280

[13] Villeneuve-Faure, C.; Boumaarouf, A.; Shah, V.; Gammon, P.M.; Lüders, U.; Coq Germanicus, R. SiC Doping Impact during Conducting AFM under Ambient Atmosphere. *Materials* 2023, *16*, 5401. https://doi.org/10.3390/ma16155401

[14] L. W. Aukerman, M. F. Millea, M. McColl; Diffusion Lengths of Electrons and Holes in GaAs. *J. Appl. Phys* **1967**; 38 (2): 685–690. https://doi.org/10.1063/1.1709396

[15] Tejedor, P.; Díez-Merino, L.; Beinik, I.; Teichert, C. Conductive Atomic Force Microscopy Study of InAs Growth Kinetics on Vicinal GaAs (110). *Applied Physics Letters* **2009**, *95* (12), 123103. https://doi.org/10.1063/1.3232234.

[16] Jongjin Lee, Jaemin Kong, Heejoo Kim, Sung-Oong Kang, Kwanghee Lee; Direct observation of internal potential distributions in a bulk heterojunction solar cell. *Appl. Phys. Lett.* **2011**; 99 (24): 243301. https://doi.org/10.1063/1.3669533

[17] Jaemin Kong, Jongjin Lee, Yonkil Jeong, Maengjun Kim, Sung-Oong Kang, Kwanghee Lee; Biased internal potential distributions in a bulk-heterojunction organic solar cell incorporated with a $TiO_x$ interlayer. *Appl. Phys. Lett.* **2012**; 100 (21): 213305. https://doi.org/10.1063/1.4722802

[18] Saive, R., Scherer, M., Mueller, C., Daume, D., Schinke, J., Kroeger, M. and Kowalsky, W., Imaging the Electric Potential within Organic Solar Cells. Adv. Funct. Mater. **2013**, 23: 5854 - 5860. https://doi.org/10.1002/adfm.201301315

[19] Chen, Q., Mao, L., Li, Y. *et al.* Quantitative *o perando* visualization of the energy band depth profile in solar cells. *Nat Commun* **2015** ,6, 7745. https://doi.org/10.1038/ncomms8745

[20] Junqin Zhang, Aofei Liu, Hailong Xing, Yintang Yang; Study on surface leakage current at sidewall in InP-based avalanche photodiodes with mesa structure. *AIP Advances* **2022**; 12 (3): 035336. https://doi.org/10.1063/5.0080656

[21] Kleider, J.-P.; Alvarez, J.; Ankudinov, A. V.; Gudovskikh, A. S.; Gushchina, E. V.; Labrune, M.; Maslova, O. A.; Favre, W.; Gueunier-Farret, M.-E.; Roca I Cabarrocas, P.; Terukov, E. I. Characterization of Silicon Heterojunctions for Solar Cells. *Nanoscale Res Lett* **2011**, *6* (1), 152. https://doi.org/10.1186/1556-276X-6-152.

[22] Centurioni, E.; Iencinella, D. Role of Front Contact Work Function on Amorphous Silicon/Crystalline Silicon Heterojunction Solar Cell Performance. *IEEE Electron Device Letters* **2003**, *24* (3), 177–179. https://doi.org/10.1109/LED.2003.811405.

[23] Glatzel, T.; Gysin, U.; Meyer, E. Kelvin Probe Force Microscopy for Material Characterization. *Microscopy* **2022**, *71* (Supplement_1), i165–i173. https://doi.org/10.1093/jmicro/dfab040.

[24] Tseberlidis, G.; Hasan Husien, A.; Riva, S.; Frioni, L.; Le Donne, A.; Acciarri, M.; Binetti, S. Semi-Transparent Cu2ZnSnS4 Solar Cells by Drop-Casting of Sol-Gel Ink. *Solar Energy* **2021**, *224*, 134–141. https://doi.org/10.1016/j.solener.2021.05.073.

[25] Espindola-Rodriguez, M.; Sylla, D.; Sánchez, Y.; Oliva, F.; Grini, S.; Neuschitzer, M.; Vines, L.; Izquierdo-Roca, V.; Saucedo, E.; Placidi, M. Bifacial Kesterite Solar Cells on FTO Substrates. *ACS Sustainable Chem. Eng.* **2017**, *5* (12), 11516–11524. https://doi.org/10.1021/acssuschemeng.7b02797.

[26] Ferhati, H.; Djeffal, F.; Drissi, B. L. Performance Improvement of Perovskite/CZTS Tandem Solar Cell Using Low-Cost ZnS/Ag/ITO Multilayer Spectrum Splitter. *Superlattices and Microstructures* **2020**, *148*, 106727. https://doi.org/10.1016/j.spmi.2020.106727.

# Chapter 5

# Further examples of the use of KPFM to investigate photovoltaic issues

This final chapter is not concerned with cross-section measurements, but deals with further use and utility of KPFM to support the development of solar cells and to get information on the properties of materials and interfaces. This has been possible thanks to the IPVF framework, where I performed several types of measurements to help colleagues collecting local probe characterization data as a support to their work and as part of the collaborative research programme.
I will focus on two aspects, namely the potential determination of open-circuit voltages from measurements on non-fully processed solar cells, and the tuning of work functions of selective charge transport layers.

## 5.1 Estimating $V_{oc}$ from local non-contact *SPV* measurements

KPFM has been recently demonstrated as a novel method to map the local $V_{OC}$ of half and fully processed photovoltaic devices with nanoscale spatial resolution [1]. When *SPV* measurements are performed on the surface of a structure that involves a buried pn junction, then one has to consider the contribution of the charge separation by this buried junction. In other words, the *SPV* includes the open circuit voltage that is developed under light by the buried pn or np junction. If the top surface of the measured structure is made of a semiconductor, the *SPV* will also include the contribution of the light-induced changes of the surface band bending, as is the case for a simple layer without buried junction. So, the extended relation for the value of *SPV* is expressed as follows:

$$SPV = \left(V_{CPD/light} - V_{CPD/dark}\right) = \pm V_{OC} + \Delta V_{sbb} \ (1).$$

Here $V_{oc}$ is positive and the sign ± depends on whether the buried junction is a np or a pn junction from the bulk towards the surface. $\Delta V_{sbb}$ is the contribution due to the light-induced change in surface band bending [2], which is generally positive if the surface is an n-type semiconductor, and negative if it is p-type (see paragraph 3.2.4.2). In a fully finalized solar cell, i.e. in a structure where the top surface is made by a metal electrode, only the first term, i.e. the open circuit voltage, is relevant. In the following, I will show measurements performed on a fully processed III-V-based solar cell, on which we could make a comparative analysis between the macroscopic $V_{OC}$ and local *SPV* measurements. In a further sub-section, we have applied the *SPV* analysis to an early-stage Mo-detached CIS based solar cell to determine its implied $V_{OC}$ and to discuss the CIS material properties.

### 5.1.1 Comparison of macroscopic $V_{OC}$ and local SPV on a full cell

*SPV* analysis was conducted on the AlGaAs:Be/n-GaInP:Si solar cells presented in Section 4.1. It is essential to note that this analysis was performed on the solar cell prior to the cleaving process for cross-sectional characterization.

For the realization of this analysis, the sample was grounded to the KPFM setup from the back contact. The back contact was also connected to the negative terminal of a sourcemeter (Keithley 2400) whereas the front contact was connected to its positive terminal, allowing to also measure macroscopic $V_{OC}$ values for comparison with the local *SPV* signals. Finally, a 488 nm laser illumination was used at different power; the effective incident power on the sample surface was calculated using a laser power meter. A schematic of the experimental setup is shown in Figure 1.

The laser was intentionally defocused in order to homogeneously illuminate the surface of the sample (0.5 x 0.5 $cm^2$). Finally, *SPV* analysis was performed with the TRIOS platform presented in paragraph 2.2. AR-ROW-EFM $n^+$-Si Pt/Ir coated AFM tips were used, with a resonance frequency at 75 kHz. FM-KPFM mode was selected with a lift (tip/surface distance) of 10 nm.

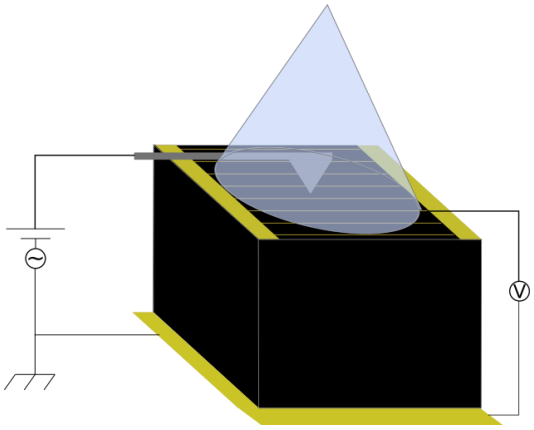


**Figure 1:** Schematic representation of the experimental setup used for comparing local SPV and macroscopic $V_{oc}$ measurements on a p-AlGaAs:Be/n-GaInP:Si based solar cell. The macroscopic $V_{OC}$ of the cell (area of 0.25 $cm^2$) was evaluated by a Keithley 2400 instrument used as a voltmeter (right part) while local *SPV* values were obtained from KPFM scans performed simulatneously.

In Figure 2 the KPFM results obtained in the dark and for a 488 nm laser illumination with a power density of 1.6 mW $cm^{-2}$ are presented together with the I-V characteristics under identical conditions. The I-V curves were acquired directly with the sourcemeter implemented in the TRIOS platform.

The average *SPV* value of 0.88 V results to be very comparable with the corresponding macroscopic $V_{OC}$ of 0.89 V. Nonetheless, as mentioned above and expressed in Eq.(1) the surface bend-banding induced by the illumination can also contribute the SPV signal. In planar configuration, the AFM tip is only sensitive to the band-bending of the upmost layer which in the solar cell is represented by a layer of n-AlInP:Si ($3.9x10^{18}$ $cm^{-3}$) after the etching of the n-GaAs:Si contact layer (see Figure 1 of paragraph 4.1). Therefore,

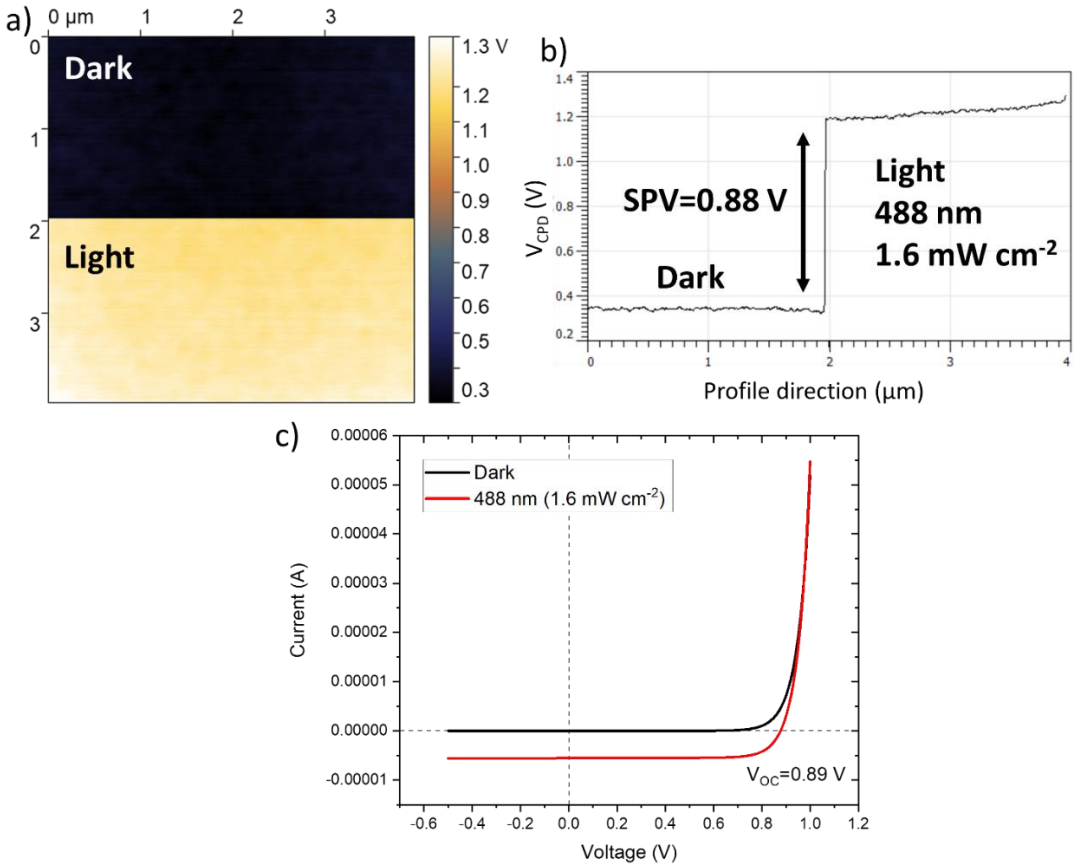


**Figure 2:** a) $V_{CPD}$ image acquired half in dark and half under illumination (488 nm, 1.6 mW cm$^{-2}$) on the AlGaAs-based solar cell b) corresponding averaged $V_{CPD}$ (vertical) profile (averaging of 207 points recorded over a width of 0.7 µm along the x axis) and c) macroscopic *I-V* characteristics of the solar cell in dark conditions and under the same laser illumination.

considering the experimental results shown in Figure 2, due to the relatively high-doping concentration of the n-AlInP:Si layer, the surface band-bending contribution must be negligible or at least considered in the ± 20 mV error associated to ambient conditions KPFM (or in ± 40 mV in SPV analysis due to uncertainty propagation). It is important to recall that in section 3.1.2.5, we have explained the detection of a relatively high SPV value in degenerate n-InP:S layers due to the presence of a strong band-bending induced by surface defects. However, in the case of the InP:S/InP:Fe multilayer sample, the cross-section was obtained by a non-optimized cleaving process. Conversely, in the case of the AlGaAs:Be solar cell, the n-AlInP:Si layer was exposed through a more reliable and well-established etching process. Therefore, the procedure employed for the exposure of the surface can have an impact on the distribution of the surface defects which in turn determines the band-bending.

The $V_{OC}$ and *SPV* comparison was then reiterated for higher laser power illumination. In Figure 3, $V_{OC}$ and *SPV* values are both plotted in function of the laser power. Note that the laser power is presented on a logarithmic scale in order to better observe if there is logarithmic dependence of $V_{OC}$ and *SPV* on the illumination intensity, as would be expected from a simple analysis of the *I-V* curve of a solar cell (see Eq. (2) in Chapter 1), since the photocurrent should depend linearly on light intensity.

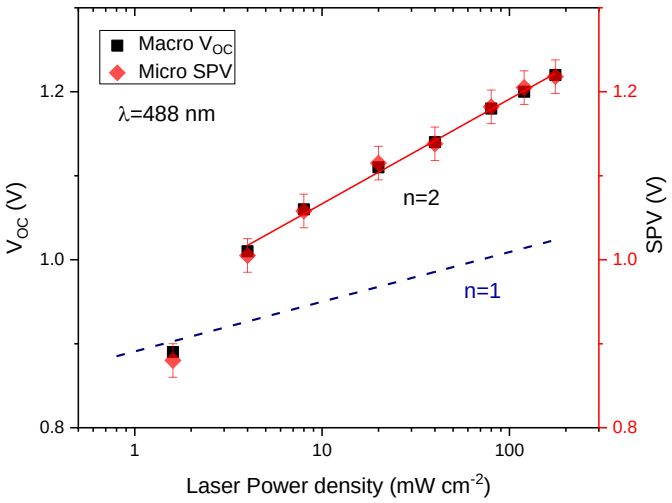


**Figure 3:** *$V_{OC}$* and *SPV* values plotted against laser power density. The ideal case in which n=1 is also reported for reference.

The *SPV* values reported in Figure 3 match the corresponding *$V_{OC}$* values very well, always included in at least the ±40 mV error bar associated with the ambient conditions *SPV* measurements. This confirms results already obtained on other types of structures [1,3], demonstrating the effectiveness of KPFM as a valuable tool for conducting local *$V_{OC}$* measurements. Also we observe in Figure 3 that the data collected at power densities above 10 mW cm$^{-2}$ exhibit a logarithmic dependence on the power density. Considering that the short-circuit current under illumination, $I_L$, should be proportional to the power density, this agrees with the expected behavior,

$$V_{OC} = \frac{nkT}{q} \ln\left(\frac{I_L}{I_0} + 1\right), (2)$$

with an ideality factor *n* equal to 2. At power densities below 10 mWcm$^{-2}$, the data depart from this logarithmic dependence, which could come from the presence of a non-negligible shunt resistance.

We have demonstrated that KPFM-based SPV measurements agree with macroscopic *$V_{OC}$* measurements in fully processed solar cells. However, since *$V_{OC}$* values can be measured using the traditional I-V measurements, there is only limited interest to the use of KPFM-SPV. In contrast, since KPFM is a contactless technique, it can be particularly valuable in monitoring *$V_{OC}$* for incomplete solar cells that may lack metallic contacts or specific conductive layers essential for efficient carrier collection. This will be illustrated in the following section.

### 5.1.2 Estimating *$V_{OC}$* from *SPV* on a cell precursor: application to a Mo-detached CIS solar cell structure

In this paragraph *SPV* analysis for the determination of *$V_{OC}$* values of an unfinalized Mo-detached CIS solar cells under different laser illumination (488 nm, 785 nm, and 980 nm) and power will be presented.
The sample used in this study was provided by Daniel Lincot and his team, as part of a collaborative effort within the IPVF framework. In particular, these samples were made available through the European project

PERCISTAND whose ultimate objective is the realization of a high efficiency (> 30%) perovskite-on-CIS tandem solar cell. The main focus is on the realization of a four terminal (4T) tandem solar cells (Figure 4) and module.

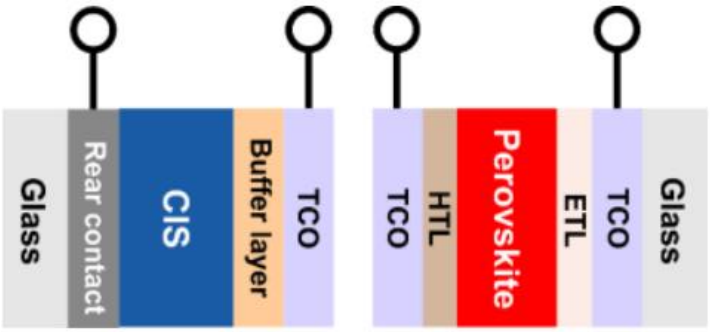


**Figure 4:** Schematic of the 4T perovskite/CIS tandem solar cells (PERCISTAND project)

### 5.1.2.1 Mo-detached CIS sample characteristics

Within the CI(G)S solar cell structure, the diode is established through the formation of a heterojunction that combines p-type CI(G)S and n-type CdS thin film layers. Figure 5 illustrates an example of such a CIGS solar cell, reported from reference [4].

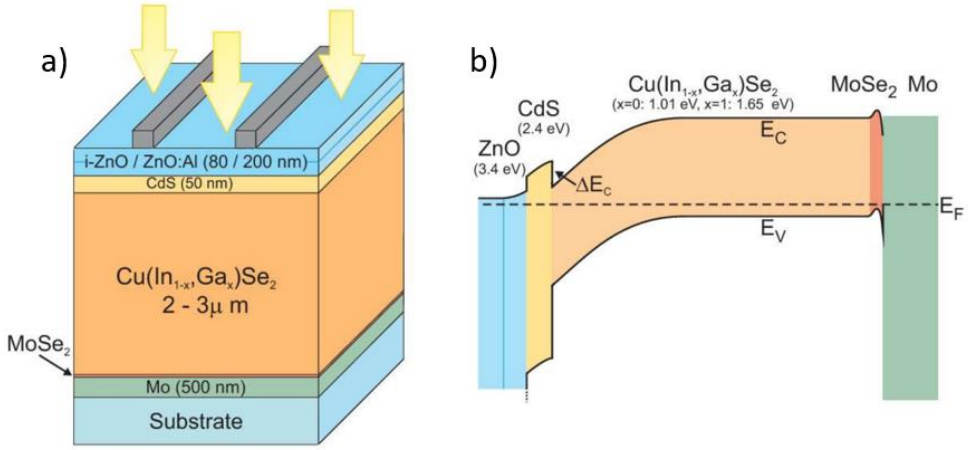


**Figure 5:** a) Illustration of the CIGS device structure and b) the corresponding band diagram. The bandgap of the different materials is also indicated. Reported from reference [4].

The sample under investigation was an early-stage CIS solar cell comprising only three layers: Mo/CIS/CdS. As depicted in Figure 4, this intermediate sample lacked the Zinc oxide (ZnO) layer, the aluminum-doped zinc oxide (AZO) layer and the metallic top contact. The ZnO and AZO layers are essential as transparent conducting oxide layers in a fully functional solar cell since they play a crucial role in enabling sunlight transmission while facilitating efficient collection and extraction of photogenerated carriers. Additionally, ZnO and AZO function as buffer layers, optimizing device performance by minimizing recombination losses and improving band alignment [4].

After detaching the CIS layer from the Mo substrate, the sample was flipped and glued to a glass substrate from the CdS layer using silver paste. This sample configuration allows the silver paste to serve as a metallic contact for subsequent characterization purposes.

Nevertheless, it is imperative to acknowledge that the sample in this current configuration is clearly not optimized. Specifically, both the CIS and CdS layers may exhibit low conductivity, leading to potential challenges in ensuring ohmic contacts. In the case of the top CIS layer, a native oxide layer is likely to be present due to its exposure to air. This limitation may impede the efficient collection of charge carriers, thereby posing difficulties in the characterization process.

As an initial step, the sample was characterized by *I-V* analysis. The back contact was taken directly on the silver paste layer (thus contacting the CdS layer), while the top contact was taken by placing a metallic needle directly onto the CIS layer. The resulting *I-V* curve under both dark and 1-Sun illumination conditions is presented in Figure 6.

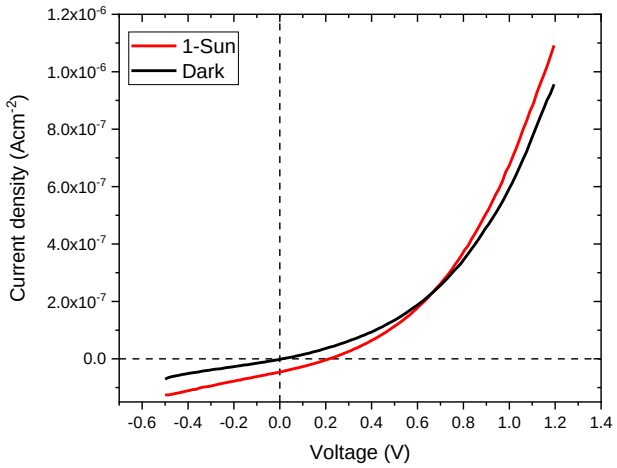


**Figure 6:** *I-V* curve of the analyzed Mo-detached CIS sample in dark (black) and under 1-Sun illumination (red).

The sample exhibited a diode-like *I-V* curve; however, its photovoltaic PV performance was notably poor, as indicated by an $I_{SC}$ value in the order of 1.59 nA cm$^{-2}$ and a $V_{OC}$ value of 0.20 V. This low measured current density can be attributed to challenges in charge carriers collection arising from the non-optimized nature of the device or directly to the presence of a diode with poor characteristics. It is important to note that the extremely low value of the current prevented us from performing an EQE analysis, as the sample signal was hidden in the noise signal. Thus we used the c-AFM and KPFM techniques for further investigations.

### 5.1.2.2 Mo-detached CIS: local probe analysis

As a first step in local probe analysis, c-AFM was used to ascertain whether the observed low PV properties stem from a deficient diode or from potential issues arising due to an elevated top contact resistance between the metallic needle and the CIS surface as a consequence of the high resistivity of the CIS layer at the surface. In particular, Resiscope analysis was conducted on the top surface of the CIS layer. The resulting voltage map, along with the mean values of the calculated local resistance, is presented in Figure 7. It is important to note that the first half of the voltage map corresponds to a negative voltage of -1 V applied between the sample and the tip, while the second half represents the results obtained with a positive voltage of +1 V applied. In this configuration, the sample was connected to the instrument ground via the silver paste layer and the front contact is established between the AFM tip and the CIS layer. A similar schematic of the experimental setup is shown in Figure 9 of Chapter 4, and it will not be repeated

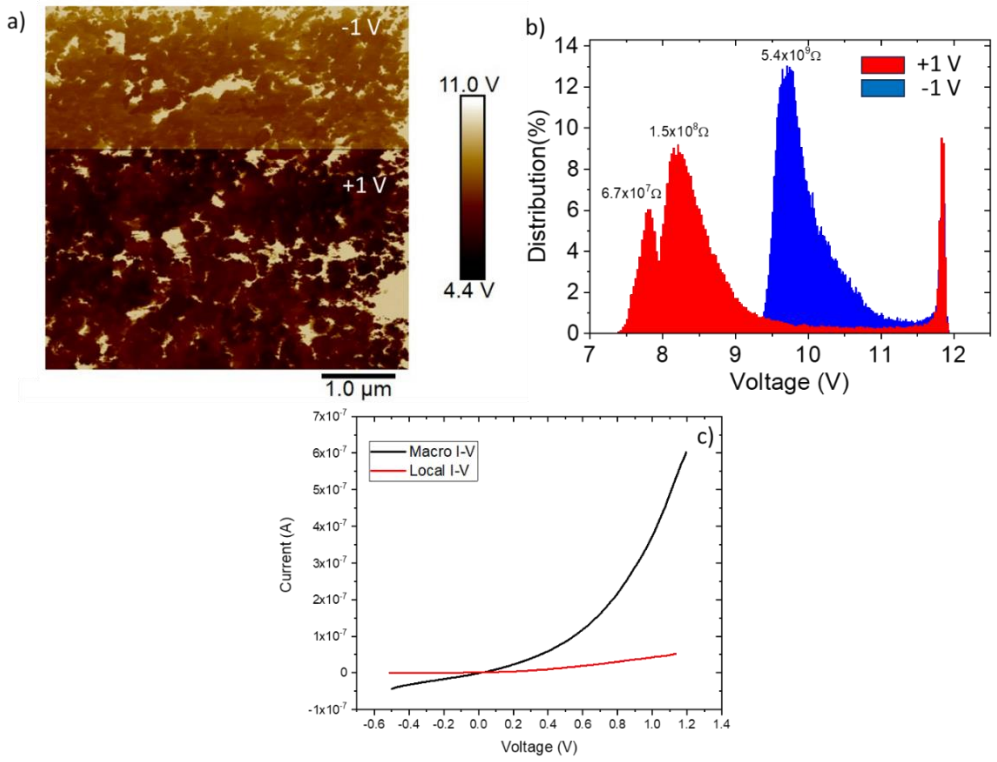


**Figure 7:** a) Voltage map acquired on the CIS surface by Resiscope analysis. The first half of the image was acquired applying -1 V whereas the second half applying + 1 V between the back of the sample (connected to the CdS layer) and the AFM tip. b) Distribution of the voltage values of Figure 7a. Note that in the distribution we have already considered the +2 factor for resistance calculation (see paragraph 2.6.1). c) Local *I-V* curve acquired with the Resiscope system compared to the macro *I-V* shown in Figure 6.

here for brevity. The contact interaction forces were in the range of 700-1000 nN and highly doped diamond coated $n^+$-Si (9.5 N/m) were used.

As hypothesized, the measured resistance for the CIS layer is significantly high, with local resistance values in the range of $10^7$ - $10^{10}$ Ω as shown in Figure 7b in which the calculated resistance values are reported in the voltage values distribution image. Such a high resistance may be related to the presence of an oxide layer on top of the CIS layer, as mentioned above, which likely contributes to the observed poor PV performance due to compromised charge carrier collection. Therefore, the low apparent conductivity suggested by the Resiscope measurements on the surface of the CIS layer, may not reflect the real conductivity of the "bulk" CIS layer.

Additionally, the local *I-V* curve depicted in Figure 7c aligns with the resistance values indicated in the distribution shown in Figure 7b, demonstrating higher current values for the +1 V polarization compared to the -1 V polarization. Nonetheless, in Chapter 4 we have demonstrated that the measured local resistance depend on the applied bias, e.g., rectifying behavior due to the Schottky nature of the electrical contact between the AFM tip and the semiconductor. However, conversely to the simple p and n-GaAs substrates analyzed in section 4.1.4, we wondered whether the different local resistances obtained for opposite polarities are a consequence of the vertical diode originated by the pn CIS/CdS junction.

The local *I-V* curve exhibits different characteristics compared to the macro *I-V* curve (Figure 7c, black curve); specifically, for reverse bias the macro *I-V* results to be more shunted than the local *I-V* indicating

that the rectifying behavior observed in Figure 7c is likely associated with the Schottky contact rather than the buried pn junction. However, there is a possibility that both factors might jointly have an effect.
In the previous section, we have successfully demonstrated that *SPV* analysis can be employed to estimate the open-circuit voltage, so we investigated the *SPV* of this sample using our KPFM setup. During the analysis, the sample was connected to the KPFM ground via the silver paste layer, while the front remained unconnected and floating, ensuring the sample remained in the open-circuit condition throughout the entire analysis. A schematic of the experimental setup is shown in Figure 8. *SPV* analysis was performed with the TRIOS platform presented in section 2.2. ARROW-EFM $n^+$-Si Pt/Ir coated AFM tips were used, with a resonance frequency at 75 kHz. Finally, FM-KPFM mode was selected with a tip/surface distance of 30 nm.

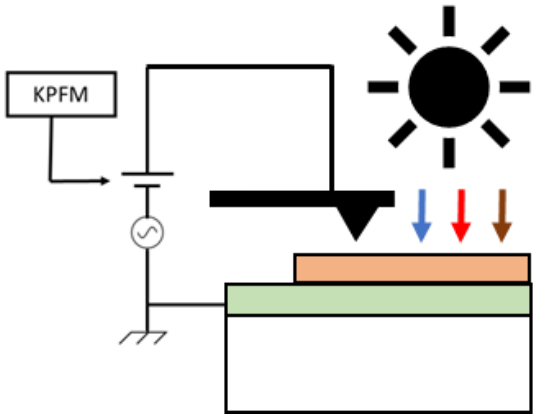


**Figure 8:** Schematic of the KPFM experimental setup used for SPV analysis of the detached CIS/CdS sample. Note that the white rectangle represents the glass substrate, the green rectangle the CdS layer and the orange rectangle the CIS layer, respectively. The contact to the CdS layer through silver paste is not shown. The three arrows with different colors indicate the different laser illumination used during the analysis (488 nm, 785 nm, and 980 nm). The area of the CIS layer is around 0.7 x 0.9 $cm^2$.

In order to avoid local $V_{CPD}$ variations caused by the granular and rough topography of the CIS layer and to mitigate possible inadvertent contacts of the tip with the sample surface during scanning (see paragraph 2.4.2), once a small region characterized by a smooth topography was identified, the tip scan motion was deactivated. In particular, our KPFM setup allows to deactivate the motion of the AFM tip along the y-axis continuously scanning the same line along the x-axis ensuring a more reliable $V_{CPD}$ analysis with reduced dependence on local topography variations. A $V_{CPD}$ image acquired under this new experimental configuration is shown in Figure 9 in which the surface of the CIS laser was illuminated with a 488 nm laser at different powers. The measurement was started in dark (0;0) and after every laser illumination (yellow stripes), the dark conditions (blue stripes) were re-evaluated.
It is important to mention that, although the AFM tip always scans the same sample line along the x-axis, the resulting $V_{CPD}$ image still presents a y-axis expressed in µm. This is related to the internal software of the AFM setup. The y-axis should thus be interpreted as a time dependent coordinate. Specifically, a scan rate of 0.4 Hz was chosen for this analysis and therefore a total of 2.5 seconds was necessary to acquire $V_{CPD}$ along one line. To be more precise, a distance of 1 µm along the y-axis corresponds to 96 lines along the x-axis, which translates to a time of 4 minutes required to cover 1 µm along the y-axis.

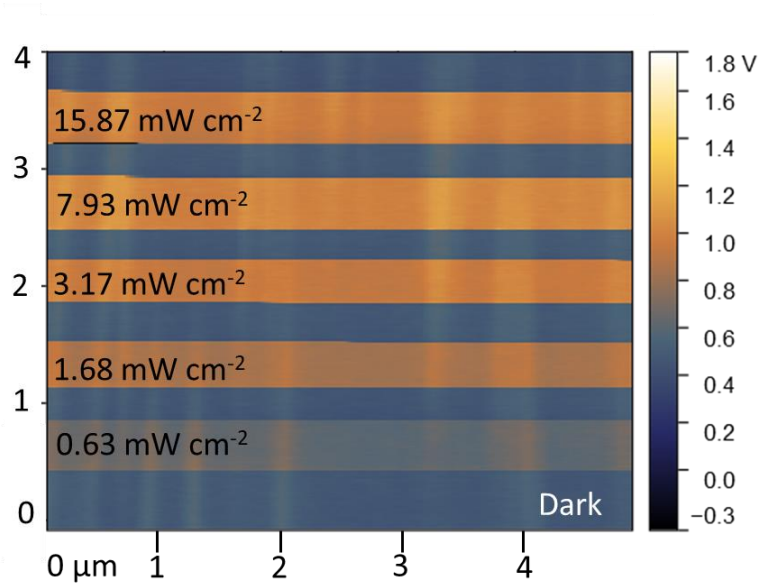


**Figure 9:** $V_{CPD}$ "map" acquired on the CIS surface under increasing 488 nm laser power. The same horizontal line was actually scanned without spatial Y variation. The vertical axis here is a way to show the evolution of the signal when scanning several times the same line under various consecutive repetitions of dark/illuminated sequences with increasing power densities, which values are also indicated.

The $V_{CPD}$ profiles obtained under laser illumination at wavelengths of 488 nm, 785 nm, and 980 nm are presented in Figure 10. The incident power values for each laser were determined using a thermal power sensor S401C from Thorlabs, and these values are displayed in the corresponding profiles. The laser was deliberately defocused during the measurements (see Figure 1) in order to illuminate the whole area of the device.

The maximum SPV values recorded were 0.52 V, 0.65 V, and 0.67 V for the laser illuminations at 488 nm, 785 nm, and 980 nm, respectively. As described in section 2.3.1, a ± 40 mV error is associated to the SPV values due to ambient conditions KPFM.

The highest $V_{CPD}$ value measured under the 488 nm laser illumination was obtained for a laser power illumination of 7.93 mW cm$^{-2}$ instead for 15.87 mW cm$^{-2}$. However, this can be related to a shift of the reference of $V_{CPD}$ (dark) as can be seen after switch-off (at the position of 3.75 µm in Figure 10a).

Interestingly, under 488 nm illumination, the maximum SPV ($V_{OC}$) value results to be smaller than the SPV values obtained under 785 nm and 980 nm lasers illumination. Specifically, as reported in reference [5], in CIS-based materials the penetration depth for the 488 nm wavelength is less than 0.1 µm. Conversely, for the 785 nm and 980 nm wavelengths, the penetration depths reach values in the order of 1 µm and 4 µm, respectively. Hence, the absorption of photons coming from the 488 nm laser illumination occurs in a region that is very close to the surface of the CIS. However, we have previously demonstrated the poor quality of the CIS surface by Resiscope analysis (Figure 7), probably due to the presence of an oxide layer. Besides, the now exposed CIS surface was previously in contact with the Mo layer. For this reason, the detachment procedure may also have introduced surface states that can have an active role on enhancing

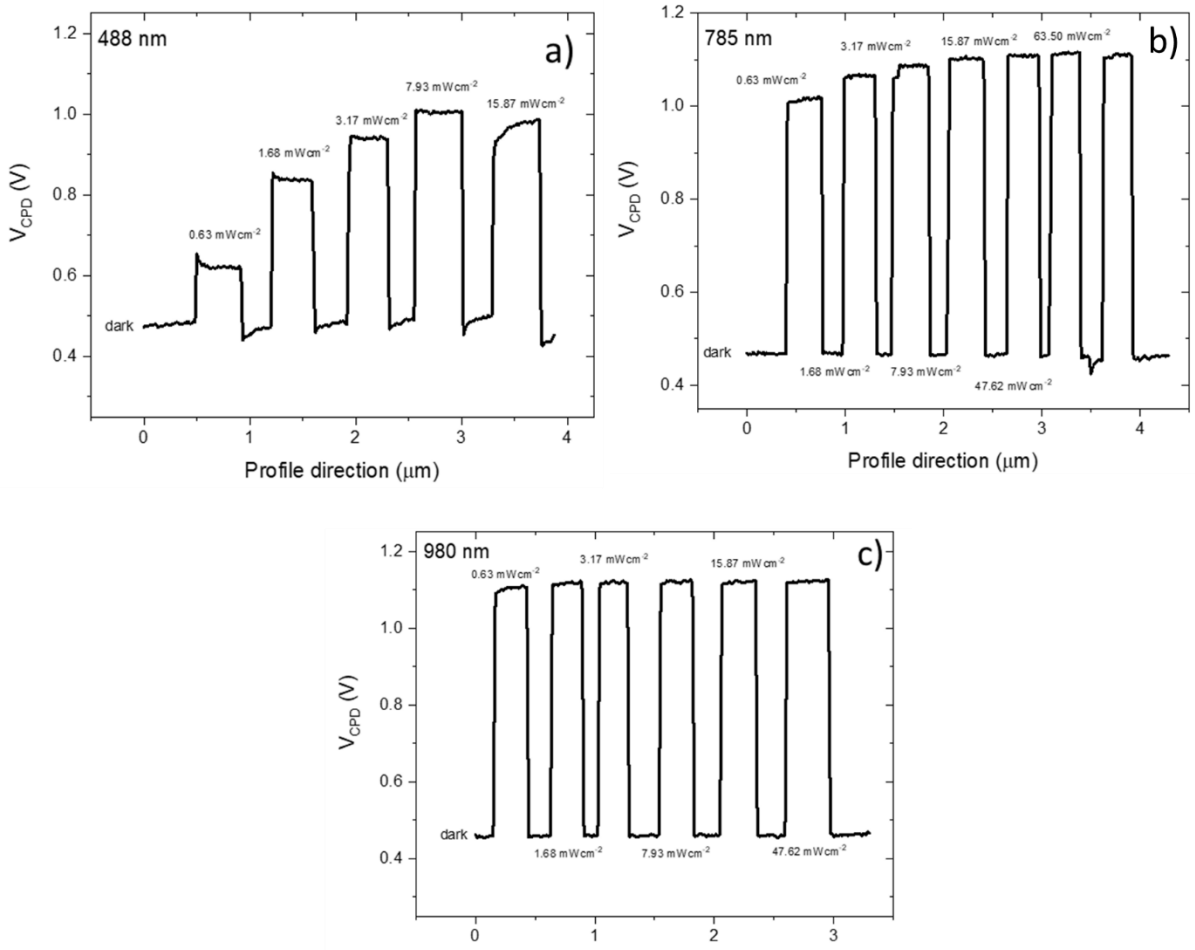


**Figure 10:** *SPV* analysis performed on the surface of the CIS layer at different laser wavelength a) 488 nm, b) 785 nm and c) 980 nm) and illumination power. The laser power densities are also reported. The profile direction corresponds to the Y axis in Figure 9, it does not correspond to a true spatial direction but should be understood as a time dependence, as explained in the caption of Figure 9 and in the text.

recombination phenomena thus leading to lower *SPV*. Notably, these problematics result to be attenuated for the other two wavelengths thanks to the higher penetration depth inside the CIS layers. Additionally, conversely to a typical CIS solar cell (Figure 5), the pn junction is now placed at the back side while the lasers still illuminate the front CIS surface. Therefore, carrier collection and separation can result to be generally deteriorated with respect to an optimized solar cell, especially for the carriers photogenerated near the surface.

Additionally, the experimental *SPV* values were plotted against the power densities (in log scale) and shown in Figure 11. As described in paragraph 5.1.1, if the material was homogeneous and in the ideal theory of pn junctions, one could expect a linear dependence of the SPV in function of the logarithm of illumination power density, with a slope depending on the ideality factor of the pn junction. Such a linear dependence is hardly visible, whatever the illumination wavelength and whatever the illumination power range.

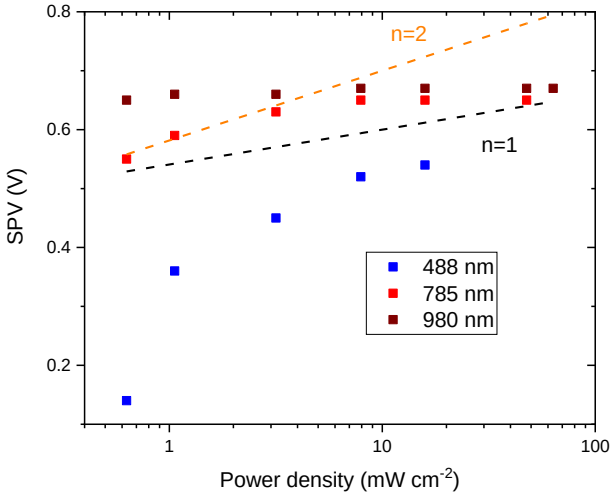


**Figure 11:** Experimental SPV values reported in Figure 10 plotted against the illumination power density. The cases in which n=1,2 are also reported for reference.

As previously explained, when exposed to 488 nm illumination, photon absorption predominantly occurs near the very surface. Consequently, charge carriers need to reach the back pn junction for separation and collection, explaining the low *SPV* values and the strong increase with power density. A non-homogeneous defect concentration from the top surface (corresponding to the detached Mo interface) toward the back CdS layer may also contribute to the strong increase with power density. Additionally, since CIS is a p-type semiconductor, one can also expect a downward surface band bending at the top air interface, which contributes negatively to the *SPV* and can decrease the positive contribution expected from the pn junction.
All these effects are mitigated when photons can be absorbed more deeply in the layer, as at 785 nm and 980 nm. At these wavelengths, a saturation of the *SPV* signal occurs. This phenomenon could be related to a flattening of the bands at the pn junction leading to less efficient carrier separation, however it is surprising that such effect is already visible at relatively low power densities, and more investigations, with the help of numerical modelling, would be required to fully explain the observed experimental saturation and complete behaviors at the various wavelengths.

In conclusion, this study showcases the applicability of KPFM as an effective tool for the characterization of unfinalized solar devices. Through *SPV* analysis, we successfully accessed reasonable $V_{OC}$ values [6] of the Mo-detached CIS solar cell, which would have been challenging to estimate using conventional techniques such as *I-V* and *EQE*.
Nonetheless, as a next step, modeling can be integrated for a better interpretation of experimental results. Specifically, the investigated sample could be modeled as a CIS solar cell with a buried pn junction placed close to the back electrode. In this situation, it would be possible to estimate the carrier lifetime and in turn the carrier diffusion length. Additionally, it would be possible to introduce surface defects at the CIS surface evaluating their impact on carrier recombination near the surface and how this translates to the *SPV* signal.

## 5.2 Tuning the work function of selective electron transport layers for perovskite solar cells

In the PV field, a selective charge transport layer is defined as a component that is able to efficiently extract and transport one type of photogenerated charge carriers, while blocking and avoiding recombination of the other type, thus improving the efficiency of a solar cell energy by minimizing recombination losses. A charge transport layer is defined as Electron Transporting Layer (ETL) when it primarily facilitates the flow of electrons while impeding the transport of holes. Conversely, it is designated as a Hole-Transporting Layer (HTL) when its main function is to support the transport of holes while inhibiting the flow of electrons.

Perovskite solar cells (PSCs) have gained tremendous attention due to their impressive PV performance, rivaling that of commercially available Si or CIGS thin-film solar cell technologies [7]. In fact, perovskite (PVK) devices have achieved remarkable power conversion efficiencies surpassing 25% [6]. The typical PSC structure comprises multiple layers, with a perovskite-based photoactive layer situated between the ETL and the HTL, complemented by front and back electrodes to facilitate efficient charge collection, as illustrated in Figure 12. The correct operation, stability and overall performance of PSCs are highly dependent on the properties of each functional layer and their compatibility with those of adjacent layers. Therefore, understanding and optimizing these individual layers and their interfaces is crucial to improve the efficiency and stability of PSCs.

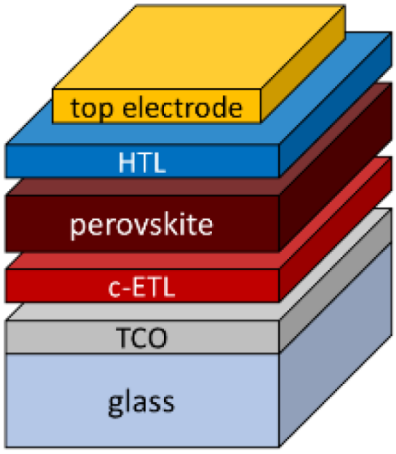


**Figure 12:** Typical structure of a perovskite solar cell. Note that TCO stands for transparent conductive oxide.

We report here some additional insight into the operation of the TCO/ETL/PVK stack. In particular, the use of FTO (Fluorine Tin Oxide) and ITO (Indium Tin Oxide) as a transparent conductive electrode in perovskite solar cells presents a challenge due to their high work function. As a matter of fact, typical reported values range from 4.4 eV to 5 eV [8] and from 4.2 eV to 5 eV [9], for FTO and ITO, respectively. This leads to an unfavorable conduction band alignment with the PVK, hindering efficient electron extraction and charge collection. Therefore other materials can be introduced as ETLs with the objective of improving band alignment between the TCO and the PVK, the more commonly used being titanium dioxide ($TiO_2$), zinc oxide (ZnO) and tin oxide ($SnO_2$) [7].

As described in section 2.2, KPFM is a valuable investigative approach since it provides information on the $V_{CPD}$ of a sample that in turn can be related to its work function. For this reason, in the pursuit of enhancing solar cell performance, we have explored two different possibilities. In particular, the first study involves the evaluation of WFs changes induced by the incorporation of $SnO_2$ and $SnO_2$/NaF on FTO, with the aim of tailoring its electronic properties to improve charge transport and collection. The second study delves into WF modification of $SnO_2$ via $Al_2O_3$, employing a modulation doping concept.

## 5.2.1 Evaluation of the surface potential changes of FTO induced by $SnO_2$ and $SnO_2$/NaF

In this study, the surface potential changes induced by $SnO_2$ and $SnO_2$/NaF layers have been evaluated by means of KPFM measurements in planar conditions. The analyzed samples were provided by Celia Aider as part of a collaborative effort within the IPVF framework.

### 5.2.1.1 Reducing the $SnO_2$ work function through a NaF layer: a brief introduction

In a very recent article Sadegh et al. demonstrated the beneficial impact of a thin layer of NaF deposited between the FTO and the PVK on the quality of the perovskite layer and in turn on the overall solar cell efficiency [10].

Specifically, NaF is an inorganic compound with water solubility. Due to its relatively high dipole moment (8.156 ± 0.001 D), NaF can efficiently create a dipole layer on conductive surfaces. This dipole layer improves PSC performance in several ways. The migration of $Na^+$ ions into the bulk perovskite layer contributes to the spontaneous passivation of the perovskite, enhancing its stability. Moreover, $F^-$ ions, possessing higher electronegativity compared to other halogen ions, create a larger dipole moment that effectively reduces the surface work function of the perovskite.

The interfacial dipole layer and steep band-bending generated by NaF treatment significantly improve the electron transport ability, leading to reduced energy losses and suppressed charge recombination at the substrate/perovskite interface.

Most notably, the NaF modification plays a crucial role in inhibiting moisture-induced degradation of the perovskite films. This effect is attributed to the reduced density of grain boundaries in the active layer and the healing of electronic defects at the FTO/perovskite interface. Consequently, the use of NaF is promising for the production of high-performance and stable perovskite solar cells in the near future.

### 5.2.1.2 $SnO_2$ and $SnO_2$/NaF samples: KPFM analysis and results

In the scope of this study, three distinct samples were analyzed. The first sample consists of bare FTO, the second sample integrates FTO coated with $SnO_2$, and the third sample involves FTO with a bilayer structure of $SnO_2$ and NaF, denoted as FTO/$SnO_2$/NaF. It is noteworthy that the NaF layer was intentionally maintained really thin with specific thickness of 4 nm.

The samples were analyzed with the TRIOS platform described in section 2.2. ARROW-EFM $n^+$-Si Pt/Ir coated AFM tips were used, with a resonance frequency at 75 kHz. Finally, FM-KPFM mode was selected with a tip/surface distance of 30 nm. A schematic of the experimental setup is shown in Figure 13.

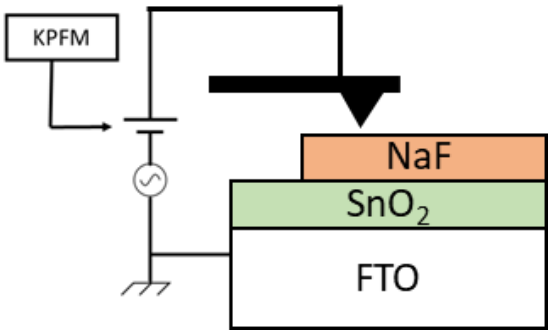


**Figure 13:** Schematic of the KPFM experimental setup used for $V_{CPD}$ analysis of ETL stacks for perovskite solar cells. For each analyzed sample the KPFM ground was connected to the FTO layer as reference.

For each sample, the KPFM ground was connected to the FTO layer. Therefore, the bare FTO sample is used as reference frame to evaluate the change in WF induced by the deposition of the additional layers, as shown in Figure 6 of section 2.2.
In Figure 14 the KPFM results acquired on the three different samples are shown. Specifically, the topography and $V_{CPD}$ map in Figure 14a and 14b refer to the bare FTO sample, the ones in Figure 14c and 14d to the FTO/$SnO_2$ sample and finally the ones in Figure 14e and 14f to the FTO/$SnO_2$/NaF sample.
Note that the results depicted in Figure 14 represent only a single instance of the various $V_{CPD}$ maps acquired during the entirety of this research investigation. To be precise, a total of five separate scans were conducted for each sample, executed at different positions across the surface of the samples. These multiple scans provide a comprehensive view of the spatial distribution of potential variations across the samples under investigation.
Before conducting the KPFM analysis and after each sample characterization, the work function of the scanning tip was assessed by measuring the $V_{CPD}$ value of a freshly exfoliated surface of highly ordered pyrolytic graphite (HOPG) [11]. The successive measurements of $V_{CPD}$ consistently displayed negligible variations, resulting in a calculated work function of 4.9 eV.
The averaged $V_{CPD}$ values over the five different scans for each samples are: 230 mV, 405 mV and 570 mV for the FTO, the $SnO_2$ and the $SnO_2$/NaF samples, respectively.
Remember that due to the ambient conditions, an experimental error of ±20 mV may be associated with each reported value. Thus, the experimental results unequivocally show an increase of surface potential for the FTO/$SnO_2$ and FTO/$SnO_2$/NaF samples with respect to the bare FTO (reference frame).
An increase of surface potential was expected for the FTO/$SnO_2$ sample with respect to the bare FTO sample since the properties of $SnO_2$ as an ETL are well known [12]. Interestingly, the FTO/$SnO_2$/NaF sample presents an even higher surface potential, indicating the beneficial role of the NaF layer to decrease the WF, which should be favorable for achieving higher photovoltage in the device. Overall, the improved electron extraction, fastened charge transport, and suppressed recombination may provide prominent potential to boost photovoltaic performances.

In summary, the KPFM technique was successfully utilized to evaluate the surface potential changes in FTO due to the introduction of $SnO_2$ and $SnO_2$/NaF. Our findings indicate a rise in surface potential, indicating a reduction in the work function (WF) caused by the presence of these additional layers.

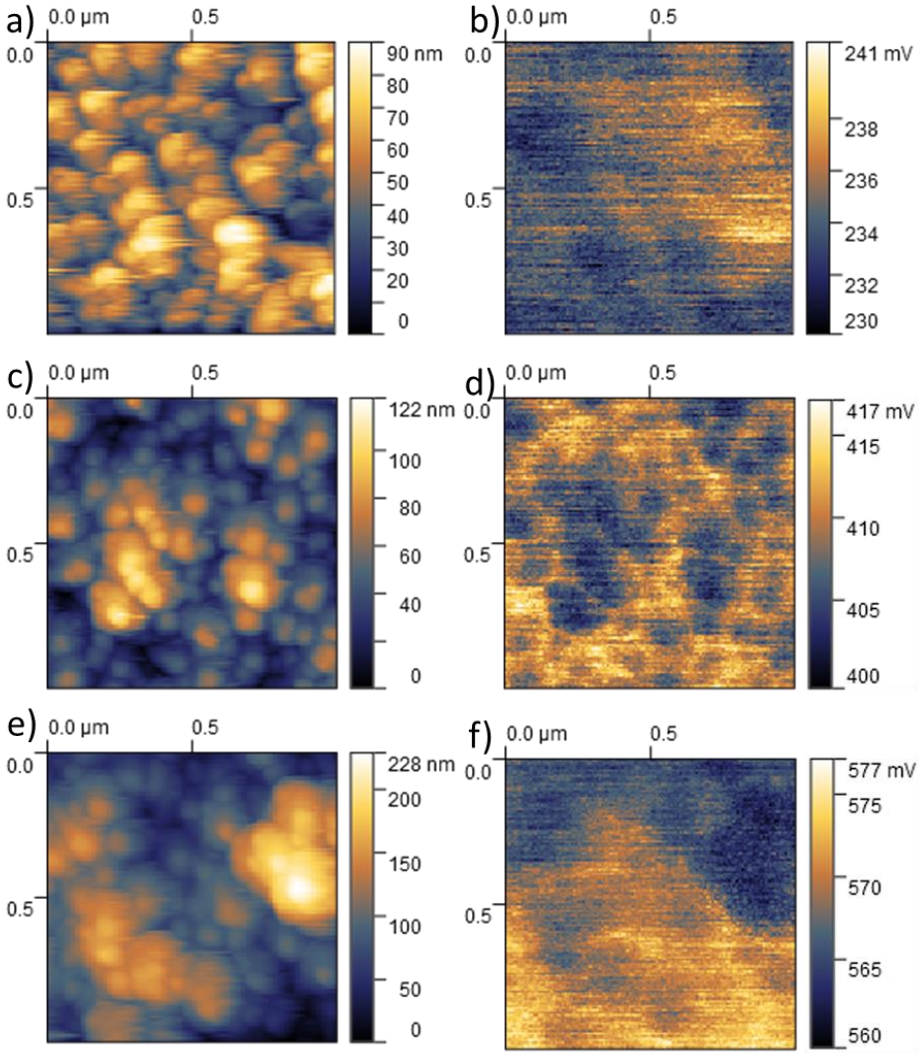


**Figure 14:** Topography and $V_{CPD}$ images of the a), b) bare FTO sample, c), d) FTO/$SnO_2$ sample and finally e), f) of the FTO/$SnO_2$/NaF sample.

## 5.2.2 Evaluation of the surface potential changes of ITO induced by $SnO_2$ and $SnO_2/Al_2O_3$

In a study similar to the one presented in the previous section, KPFM analysis was used to evaluate the surface potential changes induced by $Al_2O_3$ on $SnO_2$ deposited on ITO. The analyzed samples were provided by Shanting Zhang as part of a collaborative effort within the IPVF framework.

### 5.2.2.1 Reducing the $SnO_2$ work function through an $Al_2O_3$ layer: a brief introduction

The controlled introduction of dopants into semiconductors is essential for the advancement of modern technology. However, conventional substitutional doping has its limitations due to material-specific doping restrictions, arising from the creation of compensating defects influenced by the Fermi level-dependent defect formation energies [13]. Furthermore, the traditional doping method involving elemental substitution leads to a simultaneous decrease in charge carrier mobility ($\mu$) as the charge carrier density increases, attributed to ionized impurity scattering.

The advent of the modulation doping technique has presented a solution to overcome the constraint on charge carrier mobility in heavily doped semiconductors. This approach involves spatially separating the dopant impurities from the transport layer; by creating an interface between a low-doped and a highly doped semiconductor with distinct bandgaps, it becomes feasible to mitigate the limitations previously encountered [14].

The impact of defect modulation doping by applying a layer of defective and amorphous insulator material ($Al_2O_3$) onto a polycrystalline wide bandgap, transparent oxide semiconductor ($SnO_2$) has been shown by Weidner et al. [15]. The objective is to induce conduction electrons in the interface-proximal region of the $SnO_2$ substrate. Unlike traditional substitutional doping methods, the modulation doping effect in the $SnO_2$ substrate is achieved through the pinning of the Fermi level within the defective $Al_2O_3$ layer. This layer is deposited at a low process temperature and forms an interface with $SnO_2$, leading to the desired effects (Figure 15).

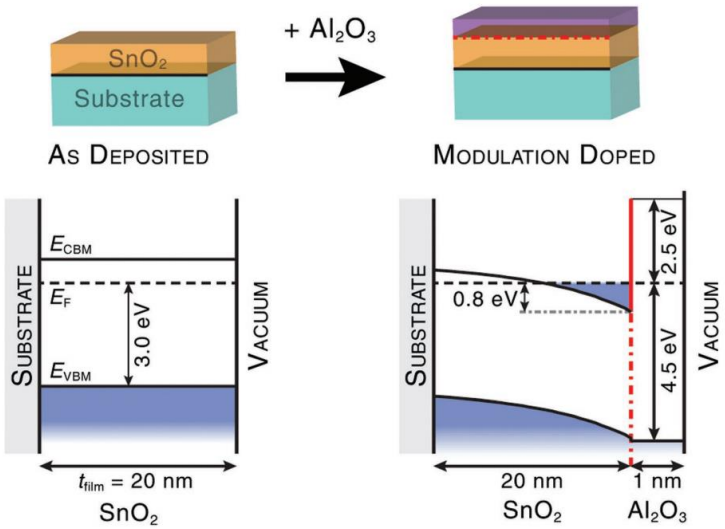


**Figure 15:** Band diagram of a 20 nm $SnO_2$ film before (left) and after (right) deposition of a 1 nm $Al_2O_3$ modulation layer. Reproduced from [15].

#### 5.2.2.2 $SnO_2$ and $SnO_2/Al_2O_3$ samples: KPFM analysis and results

Within the IPVF framework, modulation doping presents a viable approach to enhance the efficiency of perovskite solar cells. We thus investigated a set of nine distinct samples. Among these, a bare ITO sample serves as the reference for comparison with other analyzed samples. The remaining samples comprise two variations of ITO/$SnO_2$: one in its "as-deposited" state and the other subjected to annealing at 180 °C to enhance the crystallinity of $SnO_2$. Additionally, for each $SnO_2$ sample, three ITO/$SnO_2$/$Al_2O_3$ samples were provided. The $Al_2O_3$ layer was deposited using Atomic Layer Deposition (ALD) [16], and the three ITO/$SnO_2$/$Al_2O_3$ samples differ in the number of ALD deposition cycles applied, specifically 1, 2, and 3 ALD deposition cycles.

For KPFM analysis, we used the same configuration as described in section 5.2.1.2 and shown in Figure 13. As in the previous study described in section 5.2.1.2, a total of five separate scans were performed for each sample, executed at different positions across the surface of the samples. Therefore, the following reported $V_{CPD}$ values represent an average calculated over these 5 different scans.

As a first step, the bare ITO sample was characterized, the topography and corresponding $V_{CPD}$ map are reported in Figure 16a and 16b, respectively. The averaged measured $V_{CPD}$ value was equal to 116 mV. Prior to this measurement, the WF of the tip was evaluated [11] and found equal to 4.9 eV. With the reported data, the WF of the ITO would be equal to 4.78 eV, which falls well in the range of values of 4.2 to 5 eV reported in the literature for the WF of ITO [9].

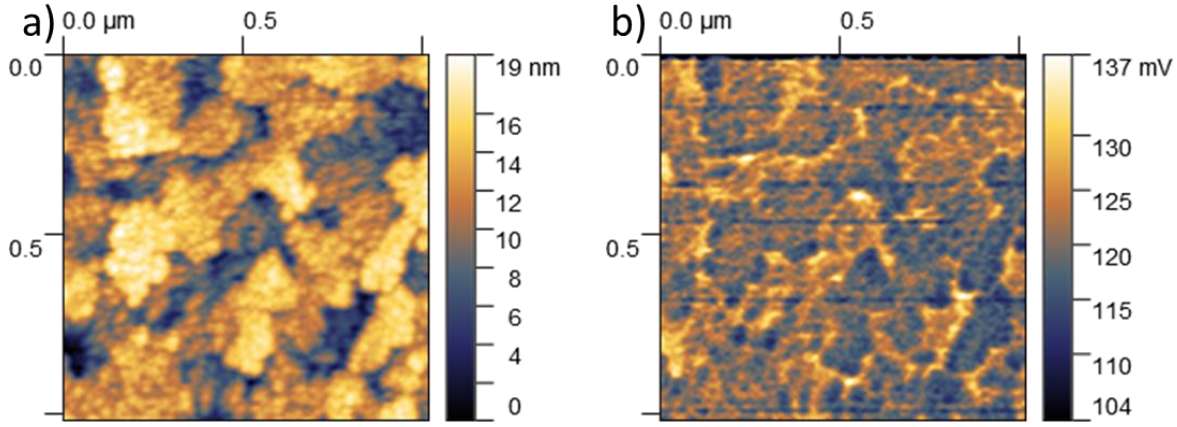


**Figure 16:** Topography a) and $V_{CPD}$ map of the bare ITO sample.

The ITO/$SnO_2$ and ITO/$SnO_2$/$Al_2O_3$ samples were analyzed by connecting the ITO layer to the KPFM ground. Therefore, the bare ITO sample is used as reference frame to evaluate the change in WF induced by the deposition of the additional layers, as shown in Figure 6 of section 2.2.

First, the samples referenced “as deposited” were analyzed. The corresponding topography and $V_{CPD}$ images are reported in Figure 17. The averaged $V_{CPD}$ values obtained after KPFM analysis were 516 mV for the ITO/$SnO_2$ sample (Figure 17a and 17b), 560 mV for the ITO/$SnO_2$/$Al_2O_3$ 1 ALD cycle sample (Figure 17c and 17d), 570 mV for the ITO/$SnO_2$/$Al_2O_3$ 2 ALD cycles sample (Figure 17e and 17f), and 590 mV for the for the ITO/$SnO_2$/$Al_2O_3$ 3 ALD cycles sample (Figure 17g and 17h).

Based on the acquired $V_{CPD}$ values, we demonstrate that the $Al_2O_3$ layer is able to increase the measured surface potential and thus to induce a decrease of WF. Interestingly, the highest $V_{CPD}$ value was obtained for the sample which underwent 3 cycles of ALD, suggesting that the optimal $Al_2O_3$ layer thickness must be in the order of a couple of nm as reported in [15].

However, in the samples labeled as "as deposited," the $SnO_2$ layer was grown at a relatively low temperature of 100 °C, resulting in an amorphous structure. Therefore we questioned whether an improved degree of crystallinity could have an effect on the consequent $Al_2O_3$ modulation doping. For this reason, the same KPFM characterization was performed on a corresponding set of samples for which the $SnO_2$ layer was grown at 180 °C, anticipating a higher degree of crystallinity [18]. Unfortunately, X-ray diffraction (XRD) data to evaluate the impact of the annealing on the crystallinity of the $SnO_2$ are not available.

The KPFM results obtained on the “annealed” set of samples are reported in Figure 18. The averaged $V_{CPD}$ values obtained after KPFM analysis were 500 mV for the ITO/$SnO_2$ sample (Figure 18a and 18b), 650 mV for the ITO/$SnO_2$/$Al_2O_3$ 1 ALD cycle sample (Figure 18c and 18d), 670 mV for the ITO/$SnO_2$/$Al_2O_3$ 2 ALD cycles sample (Figure 18e and 18f), and 690 mV for the for the ITO/$SnO_2$/$Al_2O_3$ 3 ALD cycles sample (Figure 18g and 18h).

Interestingly, the higher deposition temperature did not affect much the $V_{CPD}$ of the $SnO_2$ layer since in both cases they present comparable $V_{CPD}$ values (around 500 mV), but it had a greater impact on the $Al_2O_3$ layers. As a matter of fact, the same surface potential increase trend is found again but the $V_{CPD}$ reached

higher values, suggesting that the crystallinity of the $SnO_2$ layer plays an effective role in the modulation doping of the $Al_2O_3$ layer.

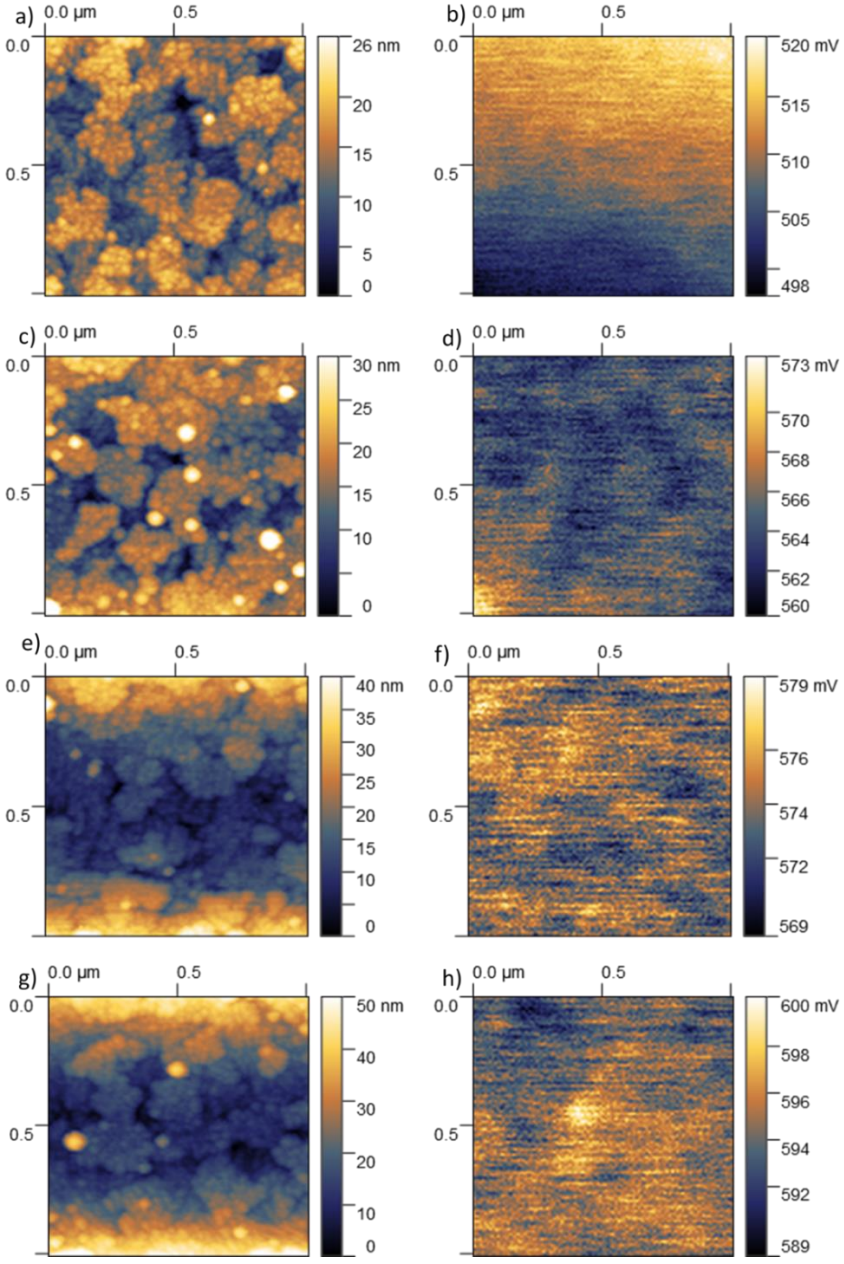


**Figure 17:** Topography and $V_{CPD}$ images acquired on the set of samples denoted "as deposited". Specifically, a) and b) refer to the ITO/$SnO_2$ sample, c) and d) refer to the ITO/$SnO_2$ sample with one ALD deposition of $Al_2O_3$, e) and f) refer to the ITO/$SnO_2$ sample with two ALD deposition of $Al_2O_3$, g) and h) refer to the ITO/$SnO_2$ sample with three ALD deposition of $Al_2O_3$.

In conclusion, KPFM technique was effectively employed to assess the surface potential change of TCOs resulting from the incorporation of $SnO_2$, $SnO_2$/NaF and $SnO_2$/$Al_2O_3$ layers. Our results demonstrate an increase in surface potential, signifying a decrease in the work function (WF) induced by these additional layers. However, it is essential to validate the proposed approach for enhancing the efficiency of perovskite solar cells through the production of finalized devices. Currently, device fabrication is pending as this study

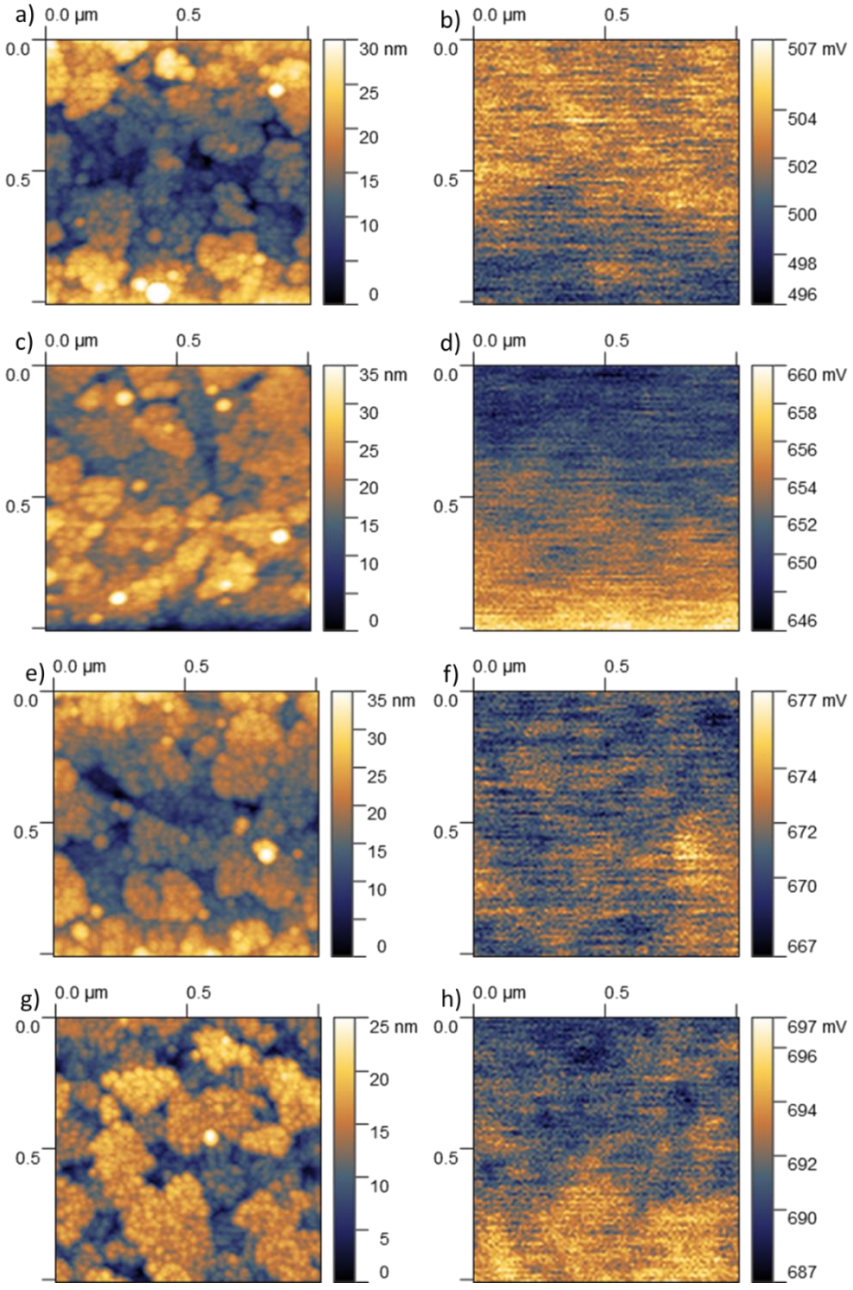


**Figure 18:** Topography and $V_{CPD}$ images acquired on the set of samples denoted "annealed". Specifically, a) and b) refer to the ITO/$SnO_2$ sample, c) and d) refer to the ITO/$SnO_2$ sample with one ALD deposition of $Al_2O_3$, e) and f) refer to the ITO/$SnO_2$ sample with two ALD deposition of $Al_2O_3$, g) and h) refer to the ITO/$SnO_2$ sample with three ALD deposition of $Al_2O_3$.

is still in its initial stages. Additionally, in the case of the annealed $SnO_2$ set of samples (section 5.2.2.2), it will be important to perform XRD in order to assess the degree of crystallinity of the $SnO_2$ layer.

## 5.3 Conclusions

In Chapter 5 we have shown the applicability of KPFM as an effective tool for the characterization of unfinalized solar devices. Specifically, through *SPV* analysis, we successfully accessed reasonable $V_{OC}$ values of a Mo-detached CIS solar cell, which would have been challenging to estimate using conventional techniques such as *I-V* and *EQE*. Nonetheless, as a next step, modeling can be integrated for a better interpretation of experimental results. Specifically, the investigated sample could be modeled as a CIS solar cell with a buried pn junction placed close to the back electrode. In this situation, it would be possible to estimate the carrier lifetime and in turn the carrier diffusion length. Additionally, by introducing surface defects at the CIS surface it could be possible to evaluate their impact on carrier recombination near the surface and how this translates to the *SPV* signal.

Moreover, KPFM technique was effectively used to assess $V_{CPD}$ of transparent conductive oxides resulting from the incorporation of $SnO_2$, $SnO_2$/NaF and $SnO_2/Al_2O_3$ layers. Our results demonstrate an increase in surface potential, signifying a decrease in the work function induced by these additional layers. However, it is essential to validate the proposed approach for enhancing the efficiency of perovskite solar cells through the production of finalized devices. Currently, device fabrication is pending as these studies is still in its initial stages.

## Bibliography

[1] Garrett, J. L.; Tennyson, E. M.; Hu, M.; Huang, J.; Munday, J. N.; Leite, M. S. Real-Time Nanoscale Open-Circuit Voltage Dynamics of Perovskite Solar Cells. *Nano Lett.* **2017**, *17* (4), 2554–2560. https://doi.org/10.1021/acs.nanolett.7b00289.

[2] C. Marchat, Caractérisation électrique et optoélectronique de nouveaux matériaux et composants photovoltaïques à partir de techniques AFM, Université Paris-Saclay, **2020**.

[3] Tennyson, E. M., Garrett, J. L., Frantz, J. A., Myers, J. D., Bekele, R. Y., Sanghera, J. S., Munday, J. N., Leite, M. S. (2015). Nanoimaging of Open-Circuit Voltage in Photovoltaic Devices. *Adv. Energy Mater.* **2015**, 5: 1501142. https://doi.org/10.1002/aenm.201501142

[4] Salhi, B. The Photovoltaic Cell Based on CIGS: Principles and Technologies. *Materials* **2022**, *15*, 1908. https://doi.org/10.3390/ma15051908

[5] Oliveira, A.J.N., Teixeira, J.P., Ramos, D., Fernandes, P.A. and Salomé, P.M.P. (2022), Exploiting the Optical Limits of Thin-Film Solar Cells: A Review on Light Management Strategies in $Cu(In,Ga)Se_2$. Adv. Photonics Res., 3: 2100190. https://doi.org/10.1002/adpr.202100190

[6] Green, MA, Dunlop, ED, Siefer, G, et al. Solar cell efficiency tables (Version 61). *Prog Photovolt Res Appl*. **2023**; 31(1): 3-16. https://doi.org/10.1002/pip.3646

[7] Rong, Y.; Hu, Y.; Mei, A.; Tan, H.; Saidaminov, M. I.; Seok, S. I.; McGehee, M. D.; Sargent, E. H.; Han, H. Challenges for Commercializing Perovskite Solar Cells. *Science* **2018**, *361* (6408), eaat8235. https://doi.org/10.1126/science.aat8235.

[8] M. G. Helander, M. T. Greiner, Z. B. Wang, W. M. Tang, Z. H. Lu; Work function of fluorine doped tin oxide. *J. Vac. Sci. Technol.* **2011**; 29 (1): 011019. https://doi.org/10.1116/1.3525641

[9] Nehate, S. D.; Prakash, A.; Mani, P. D.; Sundaram, K. B. Work Function Extraction of Indium Tin Oxide Films from MOSFET Devices. *ECS J. Solid State Sci. Technol.* **2018**, *7* (3), P87. https://doi.org/10.1149/2.0081803jss.

[10] Sadegh, F.; Akman, E.; Prochowicz, D.; Tavakoli, M. M.; Yadav, P.; Akin, S. Facile NaF Treatment Achieves 20% Efficient ETL-Free Perovskite Solar Cells. *ACS Appl. Mater. Interfaces* **2022**, *14* (34), 38631–38641. https://doi.org/10.1021/acsami.2c06110.

[11] Garrillo, P. F.; Grevin, B.; Chevalier, N.; Borowik, Ł. Calibrated Work Function Mapping by Kelvin Probe Force Microscopy. *Review of Scientific Instruments* **2018**, *89* (4), 043702.https://doi.org/10.1063/1.5007619.
[12] Dkhili, M.; Lucarelli, G.; De Rossi, F.; Taheri, B.; Hammedi, K.; Ezzaouia, H.; Brunetti, F.; Brown, T. M. Attributes of High-Performance Electron Transport Layers for Perovskite Solar Cells on Flexible PET versus on Glass. *ACS Appl. Energy Mater.* **2022**, *5* (4), 4096–4107. https://doi.org/10.1021/acsaem.1c03311.
[13] Zhang, S. B.; Wei, S.-H.; Zunger, A. Microscopic Origin of the Phenomenological Equilibrium ``Doping Limit Rule'' in n-Type III-V Semiconductors. *Phys. Rev. Lett.* **2000**, *84* (6), 1232–1235. https://doi.org/10.1103/PhysRevLett.84.1232.
[14] Harris, J. J.; Pals, J. A.; Woltjer, R. Electronic Transport in Low-Dimensional Structures. *Rep. Prog. Phys.* **1989**, *52* (10), 1217. https://doi.org/10.1088/0034-4885/52/10/002.
[15] Weidner, M.; Fuchs, A.; Bayer, T. J. M.; Rachut, K.; Schnell, P.; Deyu, G. K.; Klein, A. Defect Modulation Doping. *Advanced Functional Materials* **2019**, *29* (14), 1807906. https://doi.org/10.1002/adfm.201807906.
[16] George, S. M. Atomic Layer Deposition: An Overview. *Chem. Rev.* **2010**, *110* (1), 111–131. https://doi.org/10.1021/cr900056b.
[17] Li, Y.; Musaev, O. R.; Wrobel, J. M.; Kruger, M. B. Crystallization by Laser Annealing of Amorphous SnO2 Films on the Si (100) Surface. *Appl. Phys. A* **2018**, *124* (7), 499. https://doi.org/10.1007/s00339-018-1919-4.

# CONCLUSIONS AND PERSPECTIVES

Over the past four decades, the atomic force microscopy (AFM) technique has demonstrated its capability to create micron and submicron-scale mappings, as well as to observe intricate details at the nanoscale. Various extensions have been developed, particularly the "electrical" extensions, which enable the measurement of diverse electrical signals alongside topographical data. For instance, the extension involving Conductive Atomic Force Microscopy (c-AFM) facilitates localized current and resistance measurements [1,2], and when applied to photovoltaic devices (PV), it allows for assessing photocurrent and current-voltage (I-V) characteristics [3]. Another extension known as Kelvin Probe Force Microscopy (KPFM) enables the assessment of surface potential [4], and when employed on PV devices, it provides insights into the open-circuit potential ($V_{OC}$) [5,6]. Furthermore, KPFM holds the unique capability to provide insight into the distribution of surface potential under operando conditions of a photovoltaic device. This ability to investigate potential variations during device operation offers valuable information for understanding and optimizing device performance, and it will also be useful to study reliability and aging issues of various PV technologies, which are going to be more and more important in the future.
The research conducted throughout this thesis centered on the utilization of an AFM microscopy platform (TRIOS/AIST-NT), with a primary emphasis on its electrical extension KPFM and c-AFM (Resiscope). These extensions were employed to investigate photovoltaic devices and/or their constituent elements (absorber and junctions) to extract localized electrical properties. The research can be segmented into three distinct studies, the outcomes of which are detailed in chapters 3, 4, and 5 of this manuscript.

The first study is detailed in Chapter 3 in which the capability of cross-sectional KPFM for the study of III-V multilayer stacks in ambient conditions was investigated. Specifically, KPFM analysis was performed on two different III-V multilayer samples: an InP:S/InP:Fe and an InP:Zn/GaInAs(P):Zn multilayer structure with layers of different widths and doping concentrations.
With the first analysis performed on the InP:S/InP:Fe multilayer stack it is shown that KPFM is a valuable technique to investigate with high spatial resolution III-V multilayer samples in ambient conditions. In particular, KPFM provided the detection of the entire stack after a surface deoxidation by an HF based chemical treatment. KPFM revealed a strong dependence on the local doping concentration providing a complete detection of the InP:S and InP:Fe layers which exhibited different color contrast in the $V_{CPD}$ image. Moreover, we showed that $V_{CPD}$ contrast between the InP:S and InP:Fe layers could even be significantly improved when KPFM measurements were performed under illumination. The analysis of $V_{CPD}$ profiles showed that InP:S and InP:Fe layers of different but similar thickness tend to show different $V_{CPD}$, which can be attributed to the band-bending induced by the space charge due to the different doping densities of the InP:S and InP:Fe layers. Our findings were also supported by modelling of the energy bands profiles of the analyzed structure.
The $V_{CPD}$ profiles extrapolated from different regions of the same scan showed the same qualitative behaviour but presented minor variations. For this reason, a thorough analysis and description of the many factors that influence KPFM measurements was proposed. Conclusively, examination of the surface photovoltage (SPV) across the structure revealed a noteworthy observation: notably positive *SPV*, reaching several hundred millivolts, was identified even in the highly doped InP:S layers, which is rather intriguing and unexpected, but could be attributed to a considerable density of surface state defects, that could induce substantial upward band-bending effects.
In light of these findings, it was clear that the surface defects plays a central role on the experimental value of $V_{CPD,}$ and thus their comprehension is crucial for a quantitative understanding of the experimental data. For this reason, before presenting the cross-sectional KPFM analysis on the InP:Zn/GaInAs(P):Zn

multilayer sample, a thorough description of the theory of surface defects was addressed derived from extensive analysis of three distinct sources [7-9] with the addition of original simulations performed with KELSCAN software.
The last section of Chapter 3 deals with KPFM results on the cross section of the InP:Zn/GaInAs(P):Zn sample, both in dark conditions and under illumination. To ensure the originality of this study with respect to the one presented in the first section of Chapter 3, KP modeling was extensively included to offer a comprehensive and quantitative analysis of the experimental findings.
The analysis of the surface potential profile identified the presence of space charge regions and, thus, the formation of several junctions along the stack. The complexity of the analyzed structure combined with the ambient operating conditions caused challenges in the identification of the real position of the junctions in the $V_{CPD}$ image. KPFM measurements are significantly affected by surface defects and other surface inhomogeneities. In particular, numerical modelling and analysis indicated that surface defects are responsible for a significant departure of the magnitude of the surface potential from the value in the bulk material. Also, we showed that the observed potential profile along the cleaved surface of the n-InP/InP:nid/p-InP:Zn heterojunction stack can be explained by large surface defect densities in the highly doped n-InP and p-InP:Zn layers, with a much lower defect density in the InP:nid buffer layer providing a quantitative interpretation of the experimental surface potential profiles.

In Chapter 4, the local probe characterization was extended to finalized solar cells. In particular, Chapter 4 delves into the core of our research, presenting and analyzing the outcomes of KPFM and c-AFM measurements conducted on the cross-section of diverse photovoltaic technologies, along with the challenges associated with such characterizations.
The first two sections of Chapter 4 present c-AFM and KPFM cross-sectional analysis performed on a p-AlGaAs:Be/n-GaInP:Si heterojunction solar cell. C-AFM analysis was firstly performed on the unfinalized multilayer structure applying either +1 or -1 V between the sample and the AFM tip. This technique allowed the identification of the different region along the structure. Nonetheless, our experimental findings demonstrated that it is not possible to consider the contact between the AFM tip and the sample as an ohmic contact but it must be considered as a Schottky contact, in agreement with results from the literature. In other terms, an electrostatic potential barrier will always form at the semiconductor surface due to the contact with the AFM tip. For this reason, the polarity applied during c-AFM analysis becomes a significant parameter since it can modulate the potential barrier in the semiconductor hindering or facilitating the collection of charges which in turn it determines the local measured resistance.
However, the Schottky characteristics of the electrical contact introduce substantial complications to the acquisition of quantitative results and data interpretation. The electrostatic potential barrier in the semiconductor depends on a multitude of different parameters that comprise the physical properties of a material, such as doping concentration, and also surface defects distributions (e.g., surface band-bending) Additionally, even the experimental conditions play an active role in the form of the applied polarity, applied forces and work function of the AFM tip. Furthermore, c-AFM measurements were also performed in dark and under illumination on the finalized solar cell. Under illumination, c-AFM detected a decrease of the resistance along the AlGaAs:Be absorber and n-type region of the device. Interestingly, the resistance profile revealed the possibility of the presence of a space charge region at Gr AlGaAs/absorber interface which may act as a barrier for carriers.
KPFM was performed under real device operating condition thanks to the use of a sourcemeter (Keithley 2400). The sample was analyzed in short-circuit and open-circuit conditions both in the dark and under illumination conditions. Additionally, the surface potential was evaluated under forward and reverse applied bias in dark conditions. Once more, it can be observed that surface defects play a role in

diminishing the potential variance compared to the anticipated behavior based on the nominal doping concentration of the constituent layers forming the structure. Additionally, it is shown experimentally that the amount of applied external bias is not found in the $V_{CPD}$ image; specifically, only the application of |1| V could effectly change the surface potential distribution. Therefore, through modeling we have also demonstrated that due to surface defects charge carriers could become trapped within the semiconductor material, influencing the overall charge distribution, and leading to non-linear changes in the space charge width with applied bias. Interestingly, we were able to point out that the application of an external bias equal to the open-circuit voltage is able to produce a quasi-Fermi level splitting that is comparable to the one induced as a consequence of the illumination.
The third section of Chapter 4 concerns the cross-section analysis of an n-cSi/p-µcSiO$_x$ Si heterojunction. Specifically, we have used this sample in order to propose different solutions to a peculiar V-shaped potential near the edge of the sample that had been encountered during cross-sectional KPFM analysis. The presence of this V-shaped potential complicates the interpretation of the experimental $V_{CPD}$ profile since it adds uncertainty in the localization of the real edge of the cross-section. This peculiar $V_{CPD}$ signal could arise from interactions between the body of the tip and/or the cantilever and the sample surface. For this reason, we have explored a new experimental configuration in which the whole cantilever is located outside the sample. This new configuration allowed the elimination of the V-shaped potential enabling a more straightforward identification of the edge of cross-section in the $V_{CPD}$ image. Additionally, we have shown that the acquisition of additional signals during analysis, such as Mag, phase and Dmag can also aid in a more precise identification of the real edge of the cross-section.
Finally, it is important to mention that the V-shaped potential is only responsible of complicating the identification of the edge of the cross-section and thus by identifying the physical boundaries of the sample it is still possible to exploit surface potential measurements even when the potential profile shows a V-shape.
The fourth and final section of Chapter 4 deals with the characterization of a CZTGS solar cell using cross-sectional KPFM offering experimental evidence of the unsatisfactory PV performance of this CZTGS device under illumination. The poor PV performance was attributed to the highly sulfurized Mo back contact. Specifically, in kesterite-based solar cell, the Mo acts as back contact and acts as collecting electrode for holes. The increase of potential registered from the $MoS_2$ towards the Mo acts as barrier for the collection of holes and additionally it may also induce electron accumulation at the Mo/$MoS_2$ interface promoting recombination phenomena. These results provided compelling evidence of the charge extraction issues related to a thick $MoS_2$ layer.

Finally, Chapter 5 addresses supplementary projects undertaken during the course of the PhD thesis. In the first section of Chapter 5, *SPV* measurements were successfully correlated with the macro-$V_{OC}$ of the p-AlGaAs:Be/n-GaInP:Si solar cell. Therefore, in the second section of Chapter 5, the applicability of KPFM as an effective tool for the characterization of unfinalized solar devices was demonstrated. It is important to mention that the Mo-detached CIS sample was not optimized and additionally, through c-AFM measurements, we have demonstrated that the CIS layer presented high local resistivity values at the surface due to the presence of an oxide layer at the surface. For these reasons, the *I-V* curve the was collected by placing a metallic needle directly on the CIS surface revealed an open-circuit voltage of only 0.20 V under 1-Sun illumination and moreover the extremely low value of the current prevented us from performing an EQE analysis, as the sample signal was hidden in the noise signal. This was a consequence of the high resistivity of the CIS layer and the resulting poor carrier collection. Nonetheless, through *SPV* analysis, the potential open-circuit voltage of an Mo-detached CIS solar cell was successfully determined to be in the order of 0.55 V and thus KPFM allowed us to overcome these limitations and gain valuable

insights into the real PV performance of the sample.
Finally, in the last section of Chapter 5, the KPFM technique was effectively employed to assess the potential change of FTO and ITO resulting from the incorporation of $SnO_2$ and $SnO_2$/NaF layers and of $SnO_2$ and $SnO_2/Al_2O_3$ layers, respectively. In both cases, the findings unambiguously demonstrated an increase in surface potential, signifying a decrease in the work function (WF) induced by these additional layers.

## Perspectives

This thesis brings forth several perspectives, with a focal point being the potential enhancements to the cleaving process. This enhancement aims to facilitate and improve the quality of local probe analysis. Notably, Chapter 3 underscores the profound impact of surface defects on the electrical and physical attributes of semiconductor surfaces. Consequently, the utilization of specialized equipment designed for the cleaving procedure (such as Focused Ion-Beam FIB) could yield outcomes that are more reliable and reproducible. However, it is worth noting that the acquisition of such equipment comes with a significant financial investment. In light of this, IPVF could explore collaboration agreements with laboratories equipped with these resources.
This possibility could potentially streamline cross-sectional characterization at IPVF, even for samples that are challenging to cleave, such as those fabricated on glass substrates. This advancement could enable an in-depth analysis of perovskite materials, which stands as the ultimate objective of IPVF.
Additionally, implementing a controlled atmosphere at the sample level would enable control and minimization of air effects. This addition is complex due to the open structure of the equipment and would require the use of a sample holder cell from the manufacturer to apply an inert gas atmosphere. It would facilitate electrical measurements by reducing band-bending due to the presence of gas compounds adsorbed on the surface, extend the time window of characterization of those samples that deteriorate in ambient environment, and also by decreasing oxidation effects during c-AFM measurements. In this regard, scanning probe microscopy equipment are generally placed in a glove box to perform analysis in a controlled atmosphere which can add significant difficulties in the positioning of the AFM probe and samples. For this reason, it is worth noting that during these three years of PhD, Horiba started the development of a custom cell that allows to perform local probe analysis under inert $N_2$ atmosphere. In this respect, a prototype cell was provided only near to the end of the PhD project with which some tests on simple silicon-based samples were performed. However, due to the early-stage development of the $N_2$ cell, it revealed to be not fully operational yet. Nonetheless, once the $N_2$ cell will reach its final stage of development, it will offer a new and advantageous experimental configuration for local probe analysis under controlled atmosphere with a relative easier procedure with respect to the glove box.
Additionally, with reference to the experimental results presented in section 5.2, it will be crucial to validate the proposed approaches for work function tuning of transparent conductive oxides by producing perovskite-based finalized solar cell and evaluating their impact on the power conversion efficiency.
Ultimately, a substantially expanded utilization of modeling techniques will facilitate a more profound comprehension of the outcomes derived from experimental investigations. For instance, one possibility lies in the definition of precise surface states distributions within the energy gap of the studied materials. As a consequence, it will then be feasible to obtain a more quantitative reproducibility of the experimental results by modeling. Moreover, an exciting perspective consists in the possibility of the estimation of surface states distributions from local resistance profiles acquired by c-AFM measurements. Specifically, by evaluating the impact of surface states on the free charge carriers concentrations it would be possible to calculate the expected resistivity profile and compare it with the experimental resistance profile.

Ultimately, by dedicating significant efforts, it would be possible to achieve a comprehensive two-dimensional (2D) representation of a cross-section of a solar cell during operation. This involves the ability to thoroughly understand the alterations in potential profiles in response to applied bias or exposure to light both within the bulk and at the surface in the presence of surface defects.

## Bibliography


[1] S. Morita, T. Ishizaka, Y. Sugawara, T. Okada, S. Mishima, S. Imai, N. Mikoshiba, Surface conductance of metal-surfaces in air studied with a force microscope, Japanese Journal of Applied Physics Part 2-Letters & Express Letters. 28 (1989) L1634–L1636. https://doi.org/10.1143/JJAP.28.L1634

[2] M. Salmeron, G. Neubauer, A. Folch, M. Tomitori, D.F. Ogletree, P. Sautet, Viscoelastic and electrical properties of self-assembled monolayers on gold (111) films, Langmuir. 9 (1993) 3600–3611. https://doi.org/10.1021/la00036a041.

[3] D. Mikulik, M. Ricci, G. Tutuncuoglu, F. Matteini, J. Vukajlovic, N. Vulic, E. AlarconLlado, A. Fontcuberta i Morral, Conductive-probe atomic force microscopy as a characterization tool for nanowire-based solar cells, Nano Energy. 41 (2017) 566–572. https://doi.org/10.1016/j.nanoen.2017.10.016.

[4] M. Nonnenmacher, M.P. O'Boyle, H.K. Wickramasinghe, Kelvin probe force microscopy, Applied Physics Letters. 58 (1991) 2921–2923. https://doi.org/10.1063/1.105227.

[5] A. Doukkali, S. Ledain, C. Guasch, J. Bonnet, Surface potential mapping of biased pn junction with kelvin probe force microscopy: application to cross-section devices, Applied Surface Science. 235 (2004) 507–512. https://doi.org/10.1016/j.apsusc.2004.03.249.

[6] E.M. Tennyson, J.L. Garrett, J.A. Frantz, J.D. Myers, R.Y. Bekele, J.S. Sanghera, J.N. Munday, M.S. Leite, Nanoimaging of Open-Circuit Voltage in Photovoltaic Device

[7] Lüth, H. *Solid Surfaces, Interfaces and Thin Films*; Graduate Texts in Physics; Springer: Berlin, Heidelberg, 2010. https://doi.org/10.1007/978-3-642-13592-7.

[8] Wandelt, K. *Surface and Interface Science*; Wiley VCH: Weinheim, 2005.

[9] Ibach, H. *Physics of Surfaces and Interfaces*; Springer Berlin Heidelberg, 2006. https://doi.org/10.1007/3-540-34710-0.

[10] Kleider, J.-P.; Alvarez, J.; Ankudinov, A. V.; Gudovskikh, A. S.; Gushchina, E. V.; Labrune, M.; Maslova, O. A.; Favre, W.; Gueunier-Farret, M.-E.; Roca I Cabarrocas, P.; Terukov, E. I. Characterization of Silicon Heterojunctions for Solar Cells. *Nanoscale Res Lett* **2011**, *6* (1), 152. https://doi.org/10.1186/1556-276X-6-152.

# APPENDIX A

In appendix A we provide more details concerning the physics of space charge layers at a semiconductor surface. Note that the numbering of references follows the one of the corresponding chapter.
Due to the surface band-bending, the local potential of electrons and holes varies along the Z-axis. It is thus suitable to define a *position-dependent potential energy* which depend on the variation of the $E_i$ from $E_F$:

$$e\phi(z) = E_F - E_i \quad (3)$$

Clearly, ϕ is equal to zero in flat band-bending. Additionally, we can define $\phi_s$ and $\phi_b$ as the ϕ values at the surface and in bulk, respectively. Note that $\phi_b$ is defined by the bulk doping concentration.
Having introduced these quantities, the local band deformation can be expressed as:

$$V(z) = \phi(z) - \phi_b \quad (4)$$

The potential at the surface, where the band-bending is maximum, is given by:

$$V_S = \phi_s - \phi_b \quad (5)$$

Finally, it is also convenient to introduce dimensionless potentials u and v:

$$u = \frac{e\phi}{kT}, v = \frac{eV}{kT} \quad (6)$$

These same quantities are denoted as $u_s$ and $v_s$ at the very surface.
Considering the fundamental relations for electrons and hole concentrations in non-degenerate semiconductors, it is possible to define the spatially varying carrier concentrations in a space charge layer:

$$n(z) = n_i e^{u(z)} = n_b e^{v(z)} \quad (7)$$

$$p(z) = n_i e^{-u(z)} = p_b e^{-v(z)} \quad (8)$$

Note that, the form of the space charge layer and the band-bending can be calculated directly using the fundamental Poisson's equation:

$$\frac{d^2V}{dz^2} = -\frac{\rho(z)}{\epsilon\epsilon_0} \quad (9)$$

This equation directly relates the band curvature to the space charge density ρ(z).
The solution of the Poisson's equation with appropriate boundary conditions gives a theoretical description of the space charge layers. However, this may not be an easy task since ρ(z) itself is a function of V(z). For this reason, in the next sections are reported some theoretical cases in which is possible to obtain approximate analytic solutions of the Poisson's equation.

## Depletion space-charge layer

As a first example, the case of semiconductors with strong depletion layers ($|eV_S| >> kT$) is considered. Again, an n-type semiconductor is treated (Figure 10); the p-type case is found by changing the corresponding charge sign.
As described above, the positive $Q_{SC}$ in the depletion layer derives from the ionized bulk donors ($N_D$ and $N^+_D$ if ionized). Thanks to the $|eV_S| >> kT$ assumption, the free electrons density within the space charge layer can be neglected.
At room temperature the shape of the fermi distribution is not perfectly a step function, but it results blunted at the edges. In particular, the occupation of the bulk donor levels changes from nearly 1 to approximately 0 within an energy of around 4kT.

In the case of strong band-bending, the occupation variation responsible of the initial slope increasing (or decreasing) of the energy bands in proximity of the surface occurs over a short distance with respect to the thickness of the whole depletion layer.
As a consequence, the space charge density ρ itself can be approximated to a step function and the space charge can be expressed as:

$$Q_{SC} = eN_D^+ d \approx eN_D d \quad (10)$$

Since in the space charge region the donors are assumed to be entirely ionized. Under these assumptions, Poisson's equation becomes:

$$\frac{d^2\phi}{dz^2} = \frac{d^2V}{dz^2} = -\frac{dE}{dz} = -\frac{\rho(z)}{\epsilon\epsilon_0} = -\frac{eN_D}{\epsilon\epsilon_0} \quad (11)$$

Integrating with respect to z is possible to obtain an expression of the electrical field E(z):

$$E(z) = \frac{eN_D}{\epsilon\epsilon_0}(z-d), 0 \le z \le d \quad (12)$$

Integrating again, an expression of the potential ϕ(z) is obtained:

$$\phi(z) = \phi_b - \frac{eN_D}{\epsilon\epsilon_0}(z-d)^2, 0 \le z \le d \quad (13)$$

And the highest potential $V_S$, e.g., maximum band-bending, is given by:

$$V_s = \phi_s - \phi_b = -\frac{eN_D d^2}{\epsilon\epsilon_0} \quad (14)$$

The result for a hole depletion layer on a p-type material is equivalent but the sign must be inverted, and $N_D$ substituted with $N_A$.

$$V_s = \phi_s - \phi_b = \frac{eN_A d^2}{\epsilon\epsilon_0} \quad (15)$$

Equations 14 and 15 underline that the band-bending and the spatial extension of the space charge layer are proportional.
As a real example, a cleaved n-type ($n=10^{17}$ cm$^{-3}$) GaAs (110) surface presenting an upward bend-bending of 0.7 eV is considered. Assuming a $N_{SS}$ of $10^{12}$ cm$^{-2}$, it is possible to estimate the thickness of the space charge is in the order of around 100 nm. It is worth to mention that relatively low surface-state densities can induce a significant band-bending of about half the band-gap energy.
Additionally, typical strong depletion layers can extend up to several hundreds of nm inside the semiconductor bulk. As a consequence, the presence of surface states can have a long-range impact on the electronic structure.

## Weak space-charge layers

Another simple solution of Poisson's equation can be obtained by considering the other limiting case of weak space charge layers (either accumulation or depletion). In this case $|eV_S|$ is smaller than kT and the potential ϕ(z) is defined by mobile free charges (electrons or holes based on considered semiconductor). Again, an n-type semiconductor with a weak accumulation layer is considered to perform the calculation. Under these assumptions, the total space charge density ρ(z) is composed by the free electrons in the conduction band n(z) and the density of ionized donors $N_D^+(z)$:

$$\rho = -e[n(z) - N_D^+(z)] \quad (16)$$

The electron concentration is expressed as $n = N_C e^{(-\frac{E_C - E_F}{kT})}$ and the density of ionized donors is defined by Fermi's occupation statistics:

$$N_D^+ = N_D - N_D \frac{1}{1 + \exp\left[\frac{E_D - E_F}{kT}\right]} \quad (17)$$

$$\approx N_D \exp\left[\frac{E_D - E_F}{kT}\right] for\ E_D - E_F >> kT \quad (18)$$

The space charge density can be rewritten as:

$$\rho = -e\left[N_{eff}^C \exp\left(-\frac{E_C(z) - E_F}{kT}\right) - N_D \exp\left(\frac{E_D(z) - E_F}{kT}\right)\right] \quad (19)$$

This expression of the space charge density can be rewritten in terms of bulk conduction band minimum and donor energy respectively:

$$\rho = -e\left[N_{eff}^C e^v \exp\left(-\frac{E_C^b - E_F}{kT}\right) - N_D e^{-v} \exp\left(\frac{E_D^b - E_F}{kT}\right)\right] \quad (20)$$

It is worth recalling that v(z) represents the normalized band-bending.
The bulk electron concentration is equal to:

$$n_b = N_{eff}^C \exp\left(-\frac{E_C^b - E_F}{kT}\right) \quad (21)$$

and to:

$$n_b = N_D \exp\left(\frac{E_D^b - E_F}{kT}\right) \quad (22)$$

Since in a bulk n-type semiconductor the donors are not completely ionized and therefore $n_b$ depends only one the ionized ones.
Substituting the lasts equation in the expression of the space charge density:

$$\rho = -en_b\left(e^{v(z)} - e^{-v(z)}\right) \approx -2en_b v(z)\ for\ |v| << 1 \quad (23)$$

(e.g., small band-bending).
Poisson's equation becomes:

$$\frac{d^2v}{dz^2} = \frac{v}{L_D^2} \quad (24)$$

Where $L_D$ is the Debye length, and it is defined as:

$$L_D = \sqrt{\frac{kT\epsilon\epsilon_0}{2e^2 n_b}} \quad (25)$$

The solution of the Poisson's equation is in the form of an exponentially decaying band-bending:

$$v(z) = \frac{eV(z)}{kT} = v_s e^{-z/L_D} \quad (26)$$

Note that deep in the bulk ($z \to \infty$) the potential v and the space charge density ρ are equal to zero.
Finally, the normalized band-bending at the surface ($v_s$) is determined by the charge neutrality conditions:

$$-Q_{SS} = Q_{SC} = \int_0^\infty \rho(z)dz \approx -2en_b v_s \int_0^\infty e^{-z/L_D} dz = -2en_b v_s L_D \quad (27)$$

It follows that due to the charge neutrality condition, the charge density in the surface states ($Q_{SS}$) entirely defines the normalized band-bending at the surface $v_s$ when the bulk doping level ($n_b$) is known.

Here the take home message is that for weak band-bending, either due to accumulation or depletion layers, the spatial extent of the space charge is determined by the Debye length, or, in other terms, by the bulk carrier concentration $n_b$.

## Space charge layers on degenerate semiconductors

Up to now, only non-degenerate semiconductors have been considered. The description of the space charge layer in degenerate semiconductors in non-trivial since the Boltzmann approximation is no longer valid and therefore the full Fermi distribution must be used.

A strongly degenerate n-type semiconductor is considered under the assumption of |eVS|>>kT and |eψF|>>kT. This case is reported in Figure 1.

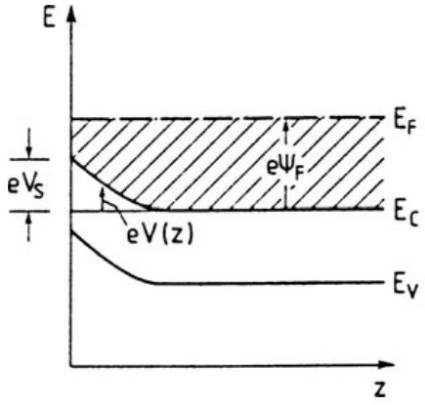


**Figure 12:** Band scheme of a depletion space-charge layer in a highly degenerate n-type semiconductor. Figure 1 was reproduced from [26].

In this case, it is possible to assume that the bulk free electron concentration $n_b$ and the donor concentration $N_D$ follows:

$$n_b = N_D \propto \psi_F^{\frac{3}{2}} \quad (28)$$

As in the case of a free electron gas in a square potential but in this case applied to the bulk electron concentration ($n_b$) and to the donor concentration ($N_D$).

The real concentration n(z) at a variable z distance from the surface can be expressed as:

$$n(z) \propto [\psi_F - V(z)]^{\frac{3}{2}} \quad (29)$$

And therefore, the space charge density ρ(z) is:

$$\rho(z) = -eN_D[1 - (1 - \frac{V}{\psi_F})^{3/2}] \quad (30)$$

Once ρ(z) is defined, an approximate Poisson's equation can be written as:

$$\frac{d^2V}{dz^2} = \frac{1}{2}\frac{d}{dV}(\frac{dV}{dz})^2 = -\frac{\rho(z)}{\epsilon\epsilon_0} = \frac{eN_D}{\epsilon\epsilon_0}\left[1 - \left(1 - \frac{V}{\psi_F}\right)^{\frac{3}{2}}\right] \quad (31)$$

Since by the very definition, the electrical field is defined as the minus derivate of the potential with respect to the position, one integration of the Poisson's equation yields the electrical field in the space charge layer:

$$E^2 = \frac{eN_D}{\epsilon\epsilon_0}\int [1-(1-\frac{V}{\psi_F})^{3/2}]\, dV \quad (32)$$

By imposing the boundary condition such that $E^2(V=0)=0$, an expression of the space-charge field is obtained:

$$E(z) = \sqrt{\frac{2eN_D}{\epsilon\epsilon_0}}\{V(z) - \frac{2}{5}\psi_F + \frac{2}{5}\psi_F\left[1-\left(1-\frac{V(z)}{\psi_F}\right)^{\frac{5}{2}}\right]\}^{1/2} \quad (33)$$

And by defining the electrical field at the very surface as $E_s = E(z=0)$, the space charge can be written in the form of:

$$Q_{SC} = \epsilon\epsilon_0 E_s = \sqrt{2eN_D\epsilon\epsilon_0}\{V(z) - \tfrac{2}{5}\psi_F + \tfrac{2}{5}\psi_F\left[1-\left(1-\tfrac{V(z)}{\psi_F}\right)^{\frac{5}{2}}\right]\}^{1/2} \quad (34)$$

Finally, the spatial dependance of the potential V(z) and the space charge capacitance can be respectively calculated by integrating again equation 33 and by differentiating $Q_{SC}$ ($C_{sc} = dQ_{sc}/dV_s$).

## Fermi level pinning

As mentioned above, the general case of a space-charge layer cannot be described in a closed mathematical form *(if it solves a given problem in terms of functions and mathematical operations from a given generally-accepted set)*.

However, it is convenient to rewrite the Poisson's equation in terms of reduced potential v(z):

$$\frac{d^2v}{dz^2} = -\frac{e^2}{kT\epsilon\epsilon_0}(n_b - p_b + p_b e^{-v} - n_b e^{v}) \quad (35)$$

By defining an effective Debye length as:

$$L = \sqrt{\frac{kT\epsilon\epsilon_0}{e^2(n_b p_b)}} \quad (36)$$

And using equation 36, Poisson's equation can be expressed as:

$$\frac{d^2v}{dz^2} = \frac{1}{L^2}[\frac{\sinh(u_b+v)}{cosh(u_b)} - tanh(u_b)] \quad (37)$$

By multiplication of both side by $2\left(dv/_{dz}\right)$ and integrating the equation with the boundary condition of $dv/_{dz}$ at v=0, one obtains:

$$\frac{dv}{dz} = \pm\frac{F(u_b,v)}{L} \quad (38)$$

Where the + when v>0 and – when v<0, and

$$F(u_b,v) = \sqrt{2}[\frac{\cosh(u_b+v)}{cosh(u_b)} - vtanh(u_b) - 1]^{\frac{1}{2}} \quad (39)$$

A further integration is necessary to calculate the band-bending in function of the z position v(z):

$$\frac{z}{L} = \int_{v_s}^{v}\frac{dv}{\pm F(u_b,v)} \quad (40)$$

In order to formulate some important considerations, here below it is reported the results of a numerical integration of equation 40 directly from [26].

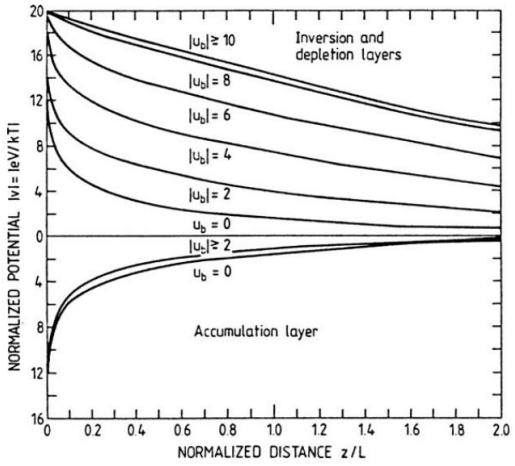


**Figure 2:** The shape of the normalized band bending $v = \frac{eV}{kT}$ as a function of the normalized distance from the surface $z/L$ for various values of the bulk potential $|u_b|$. Figure 13 was reproduced from [26].

In Figure 2, the normalized potential barrier |v| is plotted versus the distance from the surface z divided by the effective Debye length L. Note that the bulk potential $u_b$ ($u_b = E_F - E_i^b/kT$) is a parameter.
The accumulation layers curves with a $|u_b \geq 2|$ will be similar to the intrinsic one ($u_b$=0). Conversely, depletion and inversion layers characterized by high $u_b$ will extend much deeper into the semiconductor bulk. The reason of this opposite behavior can be found in the different nature of the involved charges. In particular, in accumulation layers mobile charge carriers (either electrons or holes) are responsible of the shape of the potential v(z). These free carriers can more easily form narrower space charge layers than the spatially fixed ionized atoms (e.g., the charges responsible of v(z) in depletion or inversion layers).
Again, in order to further develop some important aspects, the absolute band-bending as a function of the surface state density is reported below.

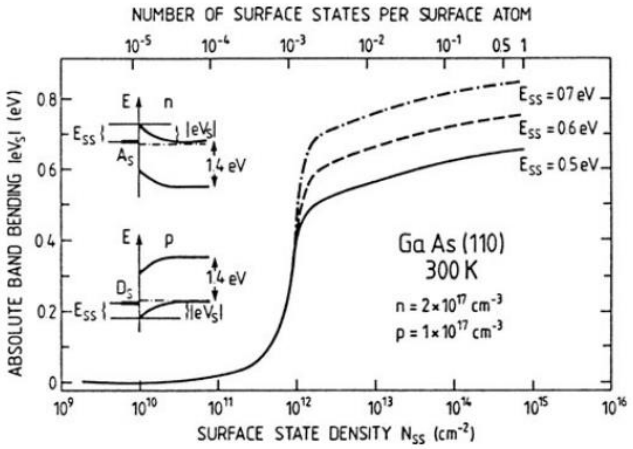


**Figure 3:** Calculated absolute band bending |eVs| due to an acceptor surface-state level ($A_S$) and a donor level ($D_S$) for n and p-type GaAs. |Vs| is plotted versus the surface state density $N_{SS}$ (lower scale) and related to the number of surface states per surface atom (upper scale). Figure 14 was reproduced from [26].
In this example, acceptor-type and donor-type surface states are described by single energy levels separated by $E_{SS}$ from the conduction band minimum and valence band maximum, respectively. Clearly, these

surface states are responsible of the formation of depletion layers in n-type and p-type semiconductors, respectively. The surface band-bending directly depends on the density of surface states.
From Figure 3, it is clear that the band-bending is quite small up to a surface-state density of $5 \cdot 10^{11}$ cm$^{-2}$. However, the band-bending begins to change very rapidly with increasing surface-state density (around $10^{12}$ cm$^{-2}$).
The final saturation band-bending, which depends on the position $E_{SS}$ of the surface-state level, is approached at a surface state occupation of $5 \cdot 10^{12}$ cm$^{-2}$.
Here the key point is that the band-bending stop increasing even though the density of states reaches higher values (1 or 2 order of magnitude more).
This is because the surface states are now energetically located near the Fermi level $E_F$ and to an increase of their density $N_{SS}$ corresponds only an infinitesimal increase in band bending |eVs| and a concurrent discharging of states, to which corresponds a stabilization of the $E_F$. This effect is called *pinning* of the Fermi level.
It follows that a narrow surface-state band with a relative low density (around $10^{12}$ cm$^{-2}$) is able to induce a surface band-bending which is already similar to the maximum achievable value for higher surface state densities. In other terms, the band-bending reaches is maximum (saturates) when the $E_F$ crosses the surface state band and for sufficiently high surface state density the $E_F$ becomes pinned near the surface state.
Furthermore, even a broad surface states density distribution that extends on the energy scale within the energy gap can pin the $E_F$. In this case, the neutrality level $E_n$ separates acceptor-type and donor-type surface states and if the surface state around $E_n$ is high enough (around $10^{12}$ as seen before) then the $E_F$ will be pinned near $E_n$.
An example of a depletion layer in a n-type semiconductor is reported in the Figure below:

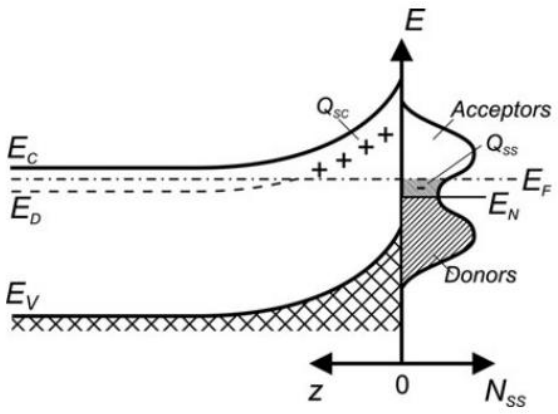


**Figure 4:** Qualitative explanation of $E_F$ pinning on an n-type semiconductor surface. A broad band of surface states ($N_{SS}$), donor-like in the lower and acceptor-like in the upper energy range, has a neutrality level $E_n$. The Fermi energy at the surface is fixed somewhat above $E_n$ such that negatively charged surface acceptors (surface state charge $Q_{SS}$) compensate the positive space charge $Q_{SC}$ arising from ionized bulk donors. Figure 15 was reproduced from [26].

As widely explained before, the $E_F$ has to cross the surface state distribution near the neutrality level $E_n$ in order to minimize the surface charge carried by the surface states (charge neutrality). The consequence in an upward band-bending and the formation of a depletion layer, e.g., the positive charge carried by the ionized bulk donors compensate the negative surface charged carried by surface states.

In this case the $E_F$ must cross the surface state distribution slightly above the neutrality level. If the surface states density around $E_n$ is high enough, $E_F$ will result pinned to $E_n$.

# APPENDIX B

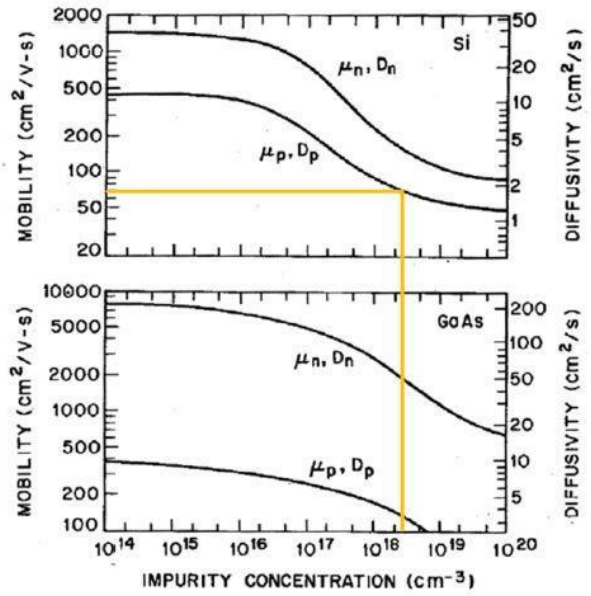


**Figure 5:** Mobility and diffusivity in Si and GaAs at 300K as a function of impurity concentration.

# APPENDIX C

Lu et al., [11] investigated n- and p-type GaAs epitaxial "staircase" structures with doping concentrations ranged from $10^{15}$ to $10^{19}$ $cm^{-3}$ by Scanning Spreading Resistance Microscopy (SSRM) [12] applying opposite polarities of +1 V and -1 V. Their findings are shown in Figure 5 which is directly reported from [11]. Note that the results reported from Lu et al., cannot be quantitatively compared with our own experimental results since higher forces were used (≈ tens of μN) and they employed another investigative approach with a different scanning probe equipment. Nonetheless, their findings can be useful to for a qualitative comparison with our experimental results and provide further discussion.

Lu et al., showed that for the case of the n-GaAs sample, only with the application of a bias of -1 V (Figure 5b) was possible to resolve the expected staircase profiles, whereas, for the +1 V case (Figure 5a), only the layers with the higher doping were well-resolved. Interestingly, for the p-GaAs sample, similar results were obtained but the bias dependence was reversed. Therefore, their experimental findings also provide proof of rectifying behavior of the AFM tip/semiconductor contact.

Furthermore, when considering the n-GaAs sample at +1 V, the explanation of the reasonable resolution of the staircase profile exclusively in the highly doped regions ($N_D$ = $10^{18}$ and $19^{19}$ $cm^{-3}$) can be traced to the sharp band-bending induced by degenerately doped layers [5] which facilitates carrier field emission through the thin energy barrier, which in turn produce a lower contact resistance. However, as the doping concentration decreases ($N_D$ < $10^{18}$) a decrease in tunneling current transmission is observed as the surface energy barrier in the semiconductor widens. For the lower n-doped layers, the application of a positive sample bias will increase this depletion layer thickness and the band-bending to the point where large increases in the resistance are measured. Similar considerations hold for the p-GaAs, but the bias dependence is reversed.

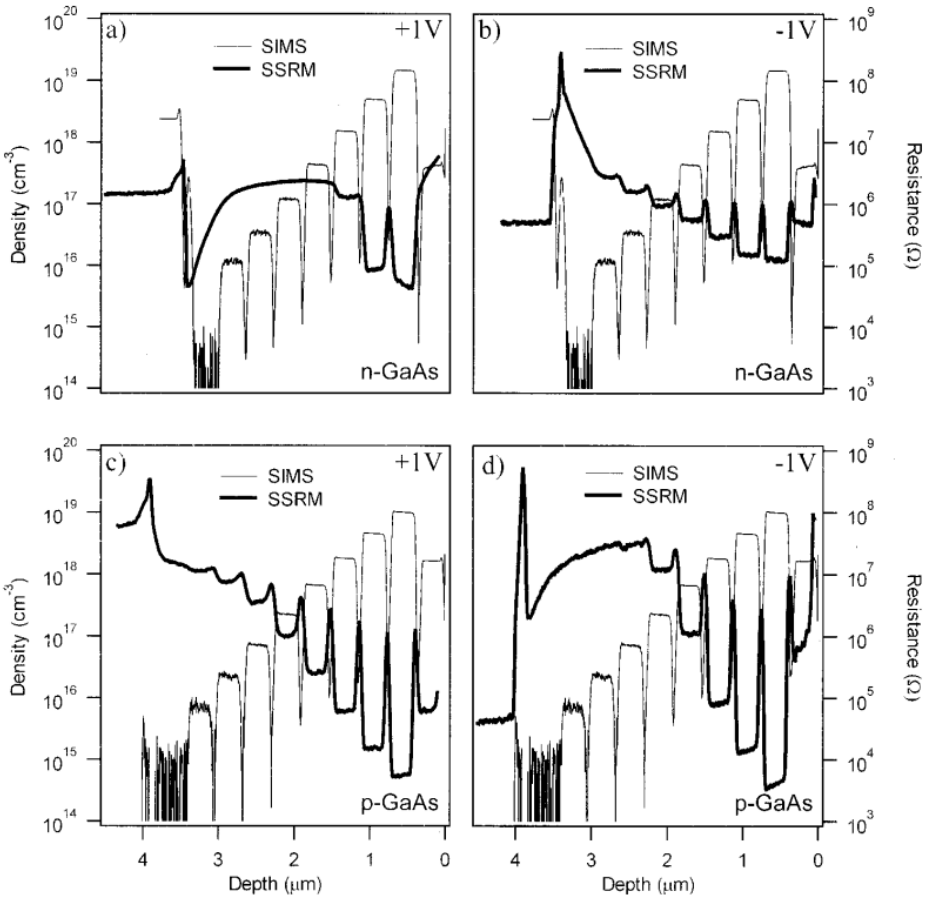


**Figure 5:** Resistance profiles as measured by SSRM, and the dopant concentration profiles as measured by SIMS obtained for n- and p-GaAs "staircase" structures under +1 V and -1V applied bias. Figure 5 was reproduced from [11].

# Appendix D

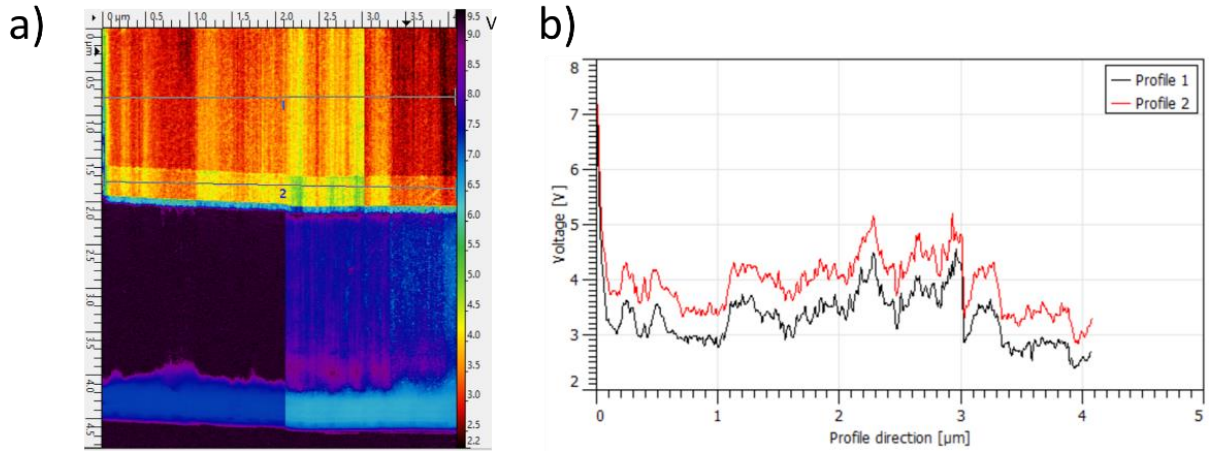


**Figure 6:** Horizontal profiles acquired along the GaAs:Zn substrate and GaAs:Be layer. Note that the illumination did not cause a decrease of the measured resistance in these highly doped p-type layers.

# List of publications

[1] Tseberlidis, G.; Trifiletti, V.; Vitiello, E.; Husien, A. H.; Frioni, L.; **da Lisca, M**.; Alvarez, J.; Acciarri, M.; Binetti, S. O. Band-Gap Tuning Induced by Germanium Introduction in Solution-Processed Kesterite Thin Films. *ACS Omega* **2022**, *7* (27), 23445–23456. https://doi.org/10.1021/acsomega.2c01786.

[2] **da Lisca, M**.; Connolly, J. P.; Alvarez, J.; Mekhazni, K.; Vaissiere, N.; Decobert, J.; Kleider, J.-P. Revealing of InP Multi-Layer Stacks from KPFM Measurements in the Dark and under Illumination. EPJ Photovoltaics **2022**, 13, 19. https://doi.org/10.1051/epjpv/2022017.

[3] Soresi, S.; **da Lisca, M**.; Besancon, C.; Vaissiere, N.; Larrue, A.; Calo, C.; Alvarez, J.; Longeaud, C.; Largeau, L.; Linares, P. G.; Tournié, E.; Kleider, J.-P.; Decobert, J. Epitaxy and Characterization of InP/InGaAs Tandem Solar Cells Grown by MOVPE on InP and Si Substrates. *EPJ Photovolt.* **2023**, *14*, 1. https://doi.org/10.1051/epjpv/2022027.

[4] Donchev, V.; Regaldo, D.; Georgiev, S.; Bojar, A.; **da Lisca, M.**; Kirilov, K.; Alvarez, J.; Schulz, P.; Kleider, J.-P. Surface Photovoltage Study of Metal Halide Perovskites Deposited Directly on Crystalline Silicon. *ACS Omega* **2023**, *8* (9), 8125–8133. https://doi.org/10.1021/acsomega.2c07664.

[5] **da Lisca, M**.; Alvarez, J.; Connolly, J. P.; Vaissiere, N.; Mekhazni, K.; Decobert, J.; Kleider, J.-P. Cross-sectional Kelvin Probe Force Microscopy on III-V epitaxial multilayer stack: challenges and perspectives. *Beilstein J. Nanotechnol.* **2023,** *14,* 725–737. doi:10.3762/bjnano.14.59

# Conferences

JNPV 2021. **Improving the understanding of the KPFM technique through analyses of InP multilayers with associated modelling (Poster)**. Mattia da Lisca, James Connolly, José Alvarez, Nicolas Vaissiere, Jean Decobert, Jean-Paul Kleider.

NC-AFM 2022. **Cross-sectional Kelvin Probe Force Microscopy on III-V epitaxial multilayer stack: challenges and perspectives (Oral presentation).** M. da Lisca, J. Alvarez, J.P. Connolly, K. Mekhazni, N. Vaissiere, J. Decobert, J.-P. Kleider.

WCPEC-8. **Epitaxy and characterization of InP/InGaAs tandem solar cells grown by MOVPE on InP and Si substrates (Poster).** Stefano Soresi, Mattia da Lisca, Nicolas Vaissiere, José Alvarez, Jean-Paul Kleider, Jean Decobert.

WCPEC-8. **Fast External Quantum Efficiency Measurements Using a Fourier Transform-Based Spectroscopy Approach for the Investigation of InGaP/InGaAs/Ge Microcells (Poster)** Herinirina Fanevamampiandra, Christophe Longeaud, Josè Alvarez, Alexandre Jaffre, Mattia da Lisca, Corentin Jouanneau, Thomas Bidaud, Jean-Paul Kleider, Abdelatif Jaouad, Marie-Estelle Gueunier-Farret, Vincent Aimez, Gwenaëlle Hamon, Maxime Darnon.

JNPV 2022. **Local probe microscopies for the study of III-V based solar cells (Poster)** M. da Lisca, J. Alvarez, Amadeo Michaud, Oleksandr Bilousov, J.P. Connolly, Stéphane Collin, J.-P. Kleider.

JNPV 2022. **Modelling investigations of surface photovoltage including surface defects (poster)** J.P. Connolly, M. da Lisca, D. Regaldo, J. Alvarez, S. Georgiev, V. Donchev, J.-P. Kleider.

JNPV 2022. **A Lateral Heterojunction Device as a Tool to Study and Optimize Perovskite-Based Solar Cells (poster)** Davide Regaldo, Pilar Lopez-Varo, Mattia da Lisca, Jean-Baptiste Puel, J Alvarez, Philip Schulz, Jean-Paul Kleider.